

EVIDENCE FOR DECAYS OF THE HIGGS BOSON
TO TAU LEPTONS AT ATLAS

Alexander Tuna

A DISSERTATION

in

Physics and Astronomy

Presented to the Faculties of The University of Pennsylvania
in Partial Fulfillment of the Requirements for the Degree of Doctor of Philosophy
2015

H.H. Williams, Professor, Physics
Supervisor of Dissertation

Marija Drndic, Professor, Physics
Graduate Group Chairperson

Dissertation Committee

I. Joseph Kroll, Professor, Physics
Elliot Lipeles, Associate Professor, Physics
Philip Nelson, Professor, Physics
Burt Ovrut, Professor, Physics
H.H. Williams, Professor, Physics

EVIDENCE FOR DECAYS OF THE HIGGS BOSON
TO TAU LEPTONS AT ATLAS

COPYRIGHT
2015
Alexander Tuna

Acknowledgements

This thesis would not have happened without the help and generosity of many people.

First and foremost, thanks to Brig Williams and Ryan Reece, my advisor and mentor, respectively. I have learned a fantastic amount of physics from you, and I hope I can be helpful to others in the same ways you've been helpful to me.

Thanks to my friends at Penn with whom I worked through classes, including Kurt Brendlinger, Jamie Saxon, Matt Hickman, and Sam Schoenholz. Our time in the Zoo was incredibly fun, and I'm happy to have grown up as a physicist with you.

Thanks to the Penn professors on ATLAS: Brig Williams, Joe Kroll, Evelyn Thomson, and Elliot Lipeles. You've been outstanding caretakers of the Penn Army. I'm sure the group will continue to flourish under your leadership for many years to come. Thanks also to Paul Keener, whose tireless stewardship of the Penn computing cluster aided in much of the work in this thesis.

Thanks to the analyzers from $Z' \rightarrow \tau\tau$, including Will Davey, Andres Florez, Andrew Leister, Gabriel Palacino, Ryan Reece, and Peter Wagner. Thanks especially to Ryan and Will, with whom I worked closely. This was my introduction to ATLAS, and it could not have been more fun.

Thanks to the conveners of tau performance, including Soshi Tsuno, Stan Lai, Stefania Xella, Martin Flechl, Will Davey, and Attilio Andreazza, who helped coordinate a great collection of tau enthusiasts and authored many lovely e-mails. Your feedback and insight was invaluable.

Thanks to the analyzers from $H \rightarrow \tau\tau$ with whom I had the joy of interacting with regularly, including Swagato Banerjee, Quentin Buat, Sofia Consonni, Noel Dawe, Lidia Dell-Asta, Pier-Olivier DeViveiros, Katy Grimm, Keita Hanawa, Louis Helary, Carl Jeske, Koji Nakamura, Henrik Ohman, Nils Ruthmann, Yuki Sakurai, and Michel Trottier-McDonald. Thanks especially to Nils, with whom I worked closely. Thanks to the $H \rightarrow \tau\tau$ conveners, including Sasha Pranko, Stan Lai, Elias Coniavitis, Sinead Farrington and Luca Fiorini, for helping lead our group to a fantastic publication. Thanks also

to the Higgs prospectors, including Olivier Arnaez, Jonathan Long, Leandro Nisanti, Richard Polifka, and Doug Schaefer. Thanks to the entire ATLAS collaboration for operating such an incredible experiment.

Thanks to all the students on ATLAS who wrote theses before me, especially John Alison, Mike Hance, Sarah Heim, Josh Kunkle, Larry Lee, Chris Lester, Chris Meyer, Dominick Olivito, Ryan Reece, Nils Ruthmann, Jamie Saxon, Doug Schaefer, and Jon Stahlman. You helped shape the structure and content of this thesis.

Thanks to the many friends I've made in grad school, especially John Alison, Kurt Brendlinger, Javier Duarte, Dan Guest, Phil Hebda, Sarah Heim, Liz Hines, Tae Min Hong, Tova Holmes, Brett Jackson, Josh Kunkle, Larry Lee, Chris Lester, Mia Liu, Jonathan Long, Zach Marshall, Chris Meyer, Dominick Olivito, Ryan Reece, Jamie Saxon, Doug Schaefer, Sam Schoenholz, Jon Stahlman, Max Swiatlowski, Emily Thompson, Rami Vanguri, and Keisuke Yoshihara. You are an incredibly smart, generous, and kind group of people, and I'm thankful for the privilege of kicking it with you. Thanks especially to the American expat community at CERN, whose company I've enjoyed for many years. Thanks also to my buds from Duke, including Nim Barshad, Olivia Chang, Felix Ho, Ellie Hwang, Sean McCormack, Luke Medhus, and Kevin Wang, for their outstanding and long-lasting friendship.

Thanks to everyone I lived with as a student, including Kurt Brendlinger, Jamie Saxon, Matt Hickman, Ben Wieder, Javier Duarte, Lawrence Lee, and Phil Hebda. Thanks especially to Kurt for being my housemate for the entirety of grad school and not once strangling me. Thanks to everyone in Philadelphia and Geneva whose couch I have crashed on, including Tae Min Hong, Ellie Hwang, Josh Kunkle, Ryan Reece, Sam Schoenholz, and Keisuke Yoshihara.

Thanks to my family: Claire Tuna, Cari Tuna, Carolyn Hughes, and Ishik Tuna. I try to make you proud every day.

ABSTRACT

EVIDENCE FOR DECAYS OF THE HIGGS BOSON
TO TAU LEPTONS AT ATLAS

Alexander Tuna

H.H. Williams

This thesis presents evidence for Higgs decays to tau leptons with the ATLAS experiment at the Large Hadron Collider. Special emphasis is given to the VBF $H \rightarrow \tau_\ell \tau_{\text{had}}$ category of the analysis. The data correspond to 25 fb^{-1} of proton collisions with $\sqrt{s} = 7$ or 8 TeV . The $H \rightarrow \tau\tau$ search strategy, predictions, and results are described. Prospects for the $H \rightarrow \tau\tau$ analysis, both in the near- and long-term, are also discussed.

Contents

Acknowledgements	iii
Abstract	v
Contents	vi
List of Tables	xi
List of Figures	xiii
Preface	xx
1 Introduction	1
2 Theoretical Review	2
2.1 The Standard Model	2
2.2 Search for the Higgs	4
2.3 Shortcomings	6
3 The LHC and the ATLAS detector	8
3.1 The LHC	8
3.1.1 Specifications	9
3.1.2 Operations	11
3.2 The ATLAS detector	12
3.2.1 Inner detector and tracking	15
3.2.1.1 Subdetectors	15
3.2.1.2 Tracking	17

CONTENTS

3.2.2	Calorimeters and clustering	19
3.2.2.1	Subdetectors	20
3.2.2.2	Clustering	20
3.2.3	Muon spectrometry	21
3.3	Particle identification	23
3.3.1	Muons	23
3.3.2	Electrons and photons	24
3.3.3	Hadrons	25
3.3.4	Neutrinos	26
3.4	Triggering	27
3.4.1	L1	28
3.4.2	HLT	29
3.5	Summary	29
4	Tau leptons	31
4.1	Tau leptons	31
4.2	Leptonic tau decays, τ_ℓ	32
4.3	Hadronic tau decays, τ_{had}	32
4.3.1	Reconstruction	32
4.3.2	Identification	35
4.3.3	Leptons mis-identified as τ_{had}	41
4.3.3.1	Electrons	41
4.3.3.2	Muons	43
5	$H \rightarrow \tau_\ell \tau_{\text{had}}$ strategy	47
5.1	Introduction	47
5.1.1	ATLAS Higgs program	47
5.1.1.1	$H \rightarrow$ bosons	48
5.1.1.2	$H \rightarrow$ fermions	48
5.1.2	$H \rightarrow \tau\tau$	49
5.2	Triggers	50
5.3	Physics objects	50
5.3.1	Electrons, muons, and τ_{had}	50
5.3.2	Jets and E_T^{miss}	51

CONTENTS

5.4	Categorization	52
5.4.1	Pre-selection	53
5.4.2	VBF category	55
5.4.3	Boosted category	56
5.5	$\tau\tau$ mass reconstruction	57
5.5.1	$m_{\tau\tau}^{\text{MMC}}$ algorithm	57
5.5.2	Performance	58
5.6	MVA discrimination	60
5.6.1	Inputs	61
5.6.2	Discrimination	67
5.6.3	MVAs in other VBF analyses	70
6	Signal and background predictions	71
6.1	$Z \rightarrow \tau\tau$	71
6.1.1	$Z(\rightarrow \ell\ell) + \text{jets}$ in simulation	71
6.1.2	Embedding	73
6.1.3	Validation	73
6.1.4	Uncertainties	74
6.2	$j \rightarrow \tau_{\text{had}}$ mis-identification	75
6.2.1	$j \rightarrow \tau_{\text{had}}$ in simulation	75
6.2.2	Fakefactor method	79
6.2.2.1	Principle	79
6.2.2.2	Implementation	83
6.2.2.3	Composition of $j \rightarrow \tau_{\text{had}}$ in the SR	85
6.2.3	Validation	88
6.2.4	Uncertainties	88
6.3	top, $Z \rightarrow \ell\ell$, diboson	91
6.3.1	top	91
6.3.2	$Z \rightarrow \ell\ell$ ($\ell \rightarrow \tau_{\text{had}}$), diboson	91
6.4	$H \rightarrow \tau\tau$	92
6.4.1	Samples	92
6.4.2	Uncertainties	94
6.5	Predictions in the signal region	94
6.6	$H \rightarrow \tau_{\text{had}}\bar{\tau}_{\text{had}}$ and $H \rightarrow \tau_\ell\bar{\tau}_\ell$	97

CONTENTS

7 Results	99
7.1 Fit procedure	99
7.1.1 Likelihood function	99
7.1.2 Features	101
7.1.3 Test statistic	101
7.1.4 Impact of uncertainties on μ	101
7.2 Fit results	102
7.3 High score events in data	105
8 Prospects for $H \rightarrow \tau\tau$	109
8.1 Run-II	109
8.1.1 Run-I triggers for $H \rightarrow \tau\tau$	110
8.1.2 Run-II triggers	110
8.1.2.1 Object thresholds	111
8.1.2.2 Topological requirements	111
8.1.2.3 Gains with $\ell + \tau_{\text{had}}$ triggers	114
8.1.3 L1 τ_{had}	118
8.1.3.1 Size	118
8.1.3.2 Isolation	118
8.1.4 Conclusions and contingencies	119
8.2 HL-LHC	121
8.2.1 Selection	122
8.2.2 Emulation of High-Luminosity LHC conditions	123
8.2.2.1 Performance assumptions	124
8.2.2.2 Pileup emulation	124
8.2.2.3 Impact on observables	125
8.2.3 Analysis	126
8.2.3.1 Boosted decision tree training	126
8.2.3.2 Kinematic distributions	126
8.2.4 Results	126
8.2.4.1 Uncertainties assumptions	127
8.2.5 Conclusions	131
9 Conclusions	132

CONTENTS

A Control regions for fakes	133
A.1 Same sign CR	133
A.2 MC SR	133
A.3 $W \rightarrow \ell\nu_\ell$ CR	133
A.4 QCD CR	133
A.5 $Z \rightarrow \ell\ell$ CR	133
A.6 top CR	133
B Inputs to the τ_{had} BDT identifier	146
C Performance of $m_{\tau\tau}$ algorithms	149
Bibliography	152

List of Tables

3.1	The accelerators of the LHC accelerator chain and the speed at which they accelerate protons in 2012.	10
3.2	Features of the subdetectors in the barrel of the Inner Detector: the Pixel detector, the SCT, and the TRT	17
3.3	Approximate average trigger rates and latencies during 2012 data-taking	27
4.1	Discriminating variables used in the τ_{had} identification algorithms	39
4.2	Discriminating variables used in the τ_{had} electron veto . Some variables are also used in the jet discrimination algorithms.	42
4.3	A breakdown of how $\mu \rightarrow \tau_{\text{had}}$ occur, both in the case of all $\mu \rightarrow \tau_{\text{had}}$ and only those which fail the muon reconstruction.	44
5.1	Predicted branching fractions for the Higgs boson of mass 125 GeV	47
5.2	Triggers used in the 8 TeV $H \rightarrow \tau_{\ell}\tau_{\text{had}}$ analysis.	50
5.3	Lepton and τ_{had} criteria used in the 8 TeV $H \rightarrow \tau_{\ell}\tau_{\text{had}}$ analysis.	50
5.4	Jet, b -jet, and $E_{\text{T}}^{\text{miss}}$ criteria used in the 8 TeV $H \rightarrow \tau_{\ell}\tau_{\text{had}}$ analysis.	51
5.5	Pre-selection and categorization criteria in the $H \rightarrow \tau_{\ell}\tau_{\text{had}}$ analysis.	56
5.6	$m_{\tau\tau}$ reconstruction techniques used in ATLAS publications.	57
5.7	Input variables to the $H \rightarrow \tau_{\ell}\tau_{\text{had}}$ BDT discriminators in the boosted and VBF categories.	62
5.8	Measured VBF signal strength in the other major ATLAS analyses: $H \rightarrow \gamma\gamma$, $H \rightarrow ZZ^*$, and $H \rightarrow WW^*$	70
7.1	Data and the predicted yields of signal and background in the VBF $\tau_{\ell}\tau_{\text{had}}$ category after the global fit.	102
8.1	LHC data-taking conditions in 2011 and 2012 compared with the expected data-taking conditions in 2015.	109
8.2	L1 triggers used in the 2012 $H \rightarrow \tau\tau$ analysis, and their expected 2015 versions, grouped by $\tau\tau$ decay channel.	110
8.3	HLT triggers used in the 2012 $H \rightarrow \tau\tau$ analysis, and their expected 2015 versions, grouped by $\tau\tau$ decay channel.	111
8.4	L1 trigger items and rate predictions for 2015 data-taking. A baseline L1 menu is used for calculating the unique rate.	114
8.5	L1 and HLT $\ell + \tau_{\text{had}}$ trigger items operating in 2012.	115

LIST OF TABLES

8.6	Fits of the efficiency for firing the 20 GeV L1 τ_{had} trigger with a Fermi-Dirac distribution for various definitions of the L1 τ_{had} item. No isolation requirement is made.	119
8.7	The τ_{had} L1 menu. A baseline L1 menu is used for calculating the unique rate.	121
8.8	Contingency options for the $H \rightarrow \tau\tau$ section of the τ_{had} L1 menu. The change in unique rate is with respect to the baseline menu. A baseline L1 menu is used for calculating the unique rate.	122
8.9	Event selection and categorization criteria. The $m_T(\ell, E_T^{\text{miss}})$ requirement is relaxed to avoid signal loss due to the degradation of the E_T^{miss} resolution at high $\langle\mu\rangle$	123
8.10	Discriminating variables used for the BDT training.	126
8.11	Yields for signal and background in the VBF category and in the most sensitive BDT bins, as shown in Fig. 8.16.	127
8.12	Uncertainty on the signal strength ($\Delta\mu$) for different scenarios of background uncertainties and signal theory uncertainties.	130
8.13	Uncertainty on the signal strength ($\Delta\mu$) for different scenarios of forward tracking.	131

List of Figures

2.1	Simplified illustration of the fundamental particles of the Standard Model , where the parenthetical note to each particles indicates the year of discovery.	3
2.2	Graph of the discoveries of the fundamental particles of the Standard Model versus time.	4
2.3	Selected Higgs boson production mechanisms and their cross-sections at pp colliders with $\sqrt{s} = 8$ TeV for $m_H = 125$ GeV	5
2.4	Summary of the preferences for the Higgs mass as a result of global fits to precision electroweak data without direct Higgs searches from LEP and the Tevatron (left) and with (right). The fits are done before LHC data-taking.	6
3.1	Aerial view of Geneva with an overlaid drawing of the LHC and associated experiments	9
3.2	The LHC accelerator complex. Before reaching the LHC, protons are accelerated at Linac 2, the Proton Synchrotron Booster (PSB), the Proton Synchrotron (PS), and the Super Proton Synchrotron (SPS)	10
3.3	The peak luminosity as measured in different data-taking periods . The peak Run-I luminosity is $0.8 \times 10^{34} \text{cm}^{-2}\text{s}^{-1}$	11
3.4	Distributions of the recorded luminosity in bins of $\langle\mu\rangle$ (left) and the total integrated luminosity as a function of time (right) . In 2011 (2012), the average $\langle\mu\rangle$ is 9.1 (20.7) and the total integrated luminosity for physics analysis is 4.6 fb^{-1} . (20.3 fb^{-1}).	12
3.5	Cross sections for pp and $p\bar{p}$ processes in the center-of-mass energy regime relevant to the Tevatron and LHC, courtesy of W.J. Stirling	13
3.6	Scale rendering of the ATLAS detector with the various subdetectors highlighted	14
3.7	Transverse schematic view of a wedge of the ATLAS detector. Charged particles leave tracks in the tracker, electrons and photons typically stop in the electromagnetic calorimeter, hadrons like charged pions typically stop in the hadronic calorimeter, and muons are tagged by the muon system as they exit. Neutrinos escape undetected.	15
3.8	A diagram of the barrel of the Inner Detector: the three layers in the Pixels, the four layers in the SCT, and the many layers of the TRT	16
3.9	Event display of a charged particle traveling, from left to right, through three layers of the Pixels detector, four layers of the SCT, and many layers of the TRT . The particle undergoes a material interaction in the TRT and produces multiple additional particles.	18
3.10	Event display of a $Z \rightarrow \mu\mu$ event with 25 reconstructed vertices in 2012 data-taking	18
3.11	A diagram of the ATLAS calorimeters	19

LIST OF FIGURES

3.12	Display of simulated electron (top) and charged pion (bottom) showers, where both particles are 50 GeV and pass through iron	21
3.13	Event display of a jet in the forward calorimeter with cell energies greater than $4\sigma_{\text{noise}}$ (left), $2\sigma_{\text{noise}}$ (center), and with the 4-2-0 topological clustering algorithm	21
3.14	A diagram of the ATLAS muon system (left) and a display of a muon candidate passing through three layers of the RPCs and MDTs (right)	22
3.15	Muon momentum resolution for $ \eta < 1.1$ (left) and $ \eta > 1.7$ (right) for the stand-alone MS and the combination of the MS and inner detector	22
3.16	Validation of the muon energy scale corrections in J/Ψ events (left), Υ events (center), and Z events (right)	24
3.17	Display of an electron traversing the ID, leaving hits in the TRT consistent with transition radiation, and depositing a narrow cluster entirely contained in the EM calorimeter	24
3.18	Data and predictions of m_{ee} before the electron identification algorithm is applied (left) and after (right)	25
3.19	Event display of a displaced vertex consistent with the decay of a B -hadron (left) and efficiency of b -jet identification algorithms measured in simulation as a function of light jet rejection (right)	26
3.20	Resolution of various E_T^{miss} reconstruction algorithms as a function of the number of reconstructed primary vertices in $Z \rightarrow \mu\mu$ events in data (left) and $W \rightarrow e\nu$ events in simulation (right)	27
3.21	Schematic view of the calorimeter granularity available at the L1 trigger	28
3.22	Trigger rate and predicted composition of the lowest unprescaled single muon trigger (left) and single electron trigger (right) in 2012 data-taking.	29
3.23	Summary of cross sections measured at ATLAS in 7 and 8 TeV data-taking	30
4.1	Pie chart of tau lepton decay branching fractions, grouped by hadronic decays (65%) and leptonic decays (35%).	32
4.2	True p_T and reconstructed d_0 for muons from simulated W , Z , and tau lepton decays. Muons from tau lepton decays are shown for $Z \rightarrow \tau\tau$, $H^{\text{ggF}} \rightarrow \tau\tau$, and $H^{\text{VBF}} \rightarrow \tau\tau$ processes.	33
4.3	Track selection efficiency for τ_{had} candidates with the default vertex selection (highest Σp_T^2) versus the dedicated TJVA algorithm, for true 1-track (left) and 3-track (right) τ_{had} , as a function of $\langle \mu \rangle$	34
4.4	τ_{had} energy response curves measured in simulation, for 1-track (left) and 2,3-track (right) τ_{had} , as a function of the reconstructed energy	35
4.5	τ_{had} energy resolution measured, for 1-track (left) and 2,3-track (right) τ_{had} , as a function of the true visible energy	35
4.6	Event display of a $t\bar{t} \rightarrow (b\mu\nu_\mu)(b\tau_{\text{had}}\nu_\tau)$ candidate during 2011 data-taking . The τ_{had} candidate has 3 tracks, the b -jet candidates each have more than 10 tracks, and the muon is in red. The estimated purity of the selection is greater than 75%.	37
4.7	Fit of the predicted τ_{had} track multiplicity to data in a $Z \rightarrow \tau_\mu\tau_{\text{had}}$ event selection before applying tau identification algorithms . The τ_{had} candidates have much lower track multiplicity relative to the large jet background.	38
4.8	Signal and background distributions for two of the discriminating variables in the 1-track τ_{had} jet discrimination algorithm: f_{cent} (left) and $N_{\text{track}}^{\text{iso}}$ (right) . The remaining distributions are shown in Appendix B.	40
4.9	Signal and background distributions for two of the discriminating variables in the 3-track τ_{had} jet discrimination algorithm: R_{track} (left) and $m_{\pi^0+\text{track}}$ (right) . The remaining distributions are shown in Appendix B.	40

LIST OF FIGURES

4.10 Signal efficiency versus inverse background efficiency for 1-track and 3-track τ_{had} jet discrimination algorithms in a lower- p_T regime (left) and higher- p_T regime (right). The loose, medium, and tight operating points are highlighted with red markers.	40
4.11 Correction factors for simulation for the τ_{had} jet discriminant efficiency for 1-track (left) and 3-track (right) τ_{had}	41
4.12 Simulated signal (τ_{had}) and background (e) distributions for the TRT high threshold fraction (left), which is an input to the electron discriminator, and signal efficiency versus inverse background efficiency for the discriminator (right). τ_{had} candidates in both are required to have one reconstructed track, pass the <code>loose</code> jet discriminator, and not overlap with any <code>tight</code> identified electron candidates. The <code>medium</code> operating point is defined to be 85% efficient for signal τ_{had}	43
4.13 The visible mass $m_{e\tau_{\text{had}}}$ in a $Z \rightarrow ee$ selection in data after requiring the τ_{had} candidate pass the medium jet discriminator and not overlap spatially with a tight identified electron (left) and after additionally requiring the τ_{had} pass the loose τ_{had} electron discriminator (right).	43
4.14 The pseudorapidity $\eta(\tau_{\text{had}})$ in a $Z \rightarrow ee$ selection in data after requiring the τ_{had} candidate pass the medium jet discriminator, not overlap spatially with a tight identified electron, and pass the loose τ_{had} electron discriminator from 2012 (left) and 2013 (right). Statistical uncertainty is not shown on the left. The modeling is improved in the forward region for the 2013 discriminator.	44
4.15 True $m_{\mu\mu}$ (left) and $\eta(\mu)$ (right) in $Z \rightarrow \mu\mu$ events where a muon is mis-identified as a τ_{had} . The muons are split into <code>combined</code> muons (black), muons which pass tracking requirements but fail <code>combined</code> requirements (green), are reconstructed but fail tracking requirements (blue), and are not reconstructed (red). A large fraction of non-reconstructed muons have $ \eta \approx 0$, which is a poorly covered region of the muon system.	45
4.16 True $m_{\mu\mu\gamma}$ (left) and $\Delta R(\mu, \gamma)$ (right) in $Z \rightarrow \mu\mu$ events where a muon is mis-identified as a τ_{had} and a true FSR photon is associated to the muon. The muons are split into <code>combined</code> muons (black), muons which pass tracking requirements but fail <code>combined</code> requirements (green), are reconstructed but fail tracking requirements (blue), and are not reconstructed (red).	45
4.17 Data and prediction in a $Z \rightarrow \tau_\mu \tau_{\text{had}}$ selection, where $Z \rightarrow \mu\mu$ ($\mu \rightarrow \tau_{\text{had}}$) is shown in orange, for 2013 (left) and 2014 (right) versions of $\mu \rightarrow \tau_{\text{had}}$ rejection techniques. Overlapping muon candidates in the 2013 version are required to fulfill tracking goodness as a form of identification. The $Z \rightarrow \mu\mu$ ($\mu \rightarrow \tau_{\text{had}}$) is reduced significantly in the 2014 version.	46
5.1 Discovery plots for the $H \rightarrow \gamma\gamma$ (left), $H \rightarrow ZZ^*$ (center), and $H \rightarrow WW^*$ (right) analyses.	48
5.2 Pie chart of di-tau lepton decay branching fractions.	49
5.3 Cartoon depiction of the relevant categories in the $H \rightarrow \tau_\ell \tau_{\text{had}}$ analysis: pre-selection, boosted, and VBF.	52
5.4 Kinematic distributions in the pre-selection category of the 8 TeV $H \rightarrow \tau_\ell \tau_{\text{had}}$ analysis with the requirement on $m_T(\ell, E_T^{\text{miss}})$ removed.	54
5.5 Kinematic distributions in the pre-selection category of the 8 TeV $H \rightarrow \tau_\ell \tau_{\text{had}}$ analysis with the requirement on $m_T(\ell, E_T^{\text{miss}})$ removed.	55
5.6 Cartoon of the $m_{\tau\tau}^{\text{MMC}}$ reconstruction algorithm. Black, filled lines indicate items measured directly (ℓ, τ_{had}). Red, dotted lines indicate items which cannot be measured (neutrinos). The black, dashed line indicates the E_T^{miss} , which is measured indirectly. Blue indicates items which the $m_{\tau\tau}^{\text{MMC}}$ scans to find an optimal solution ($\Delta\phi, E_T^{\text{miss}}$).	58
5.7 Input assumptions of the angle between the visible and invisible tau lepton decay products, for leptonic decays (left), 1-track hadronic decays (center), and 3-track hadronic decays (right)	59

LIST OF FIGURES

5.8	Predicted distributions of $m_{\tau\tau}$ for $Z \rightarrow \tau\tau$ and $H \rightarrow \tau\tau$ for the MMC reconstruction algorithm in the boosted category (left) and VBF category (right).	59
5.9	Efficiency for $H \rightarrow \tau_\ell \tau_{\text{had}}$ versus the efficiency for $Z \rightarrow \tau_\ell \tau_{\text{had}}$ for various $m_{\tau\tau}$ reconstruction algorithms in the boosted category (left) and VBF category (right).	60
5.10	Cartoons of lepton η -centrality (left) and $E_T^{\text{miss}} \phi$ -centrality (right), courtesy of Tae Min Hong.	62
5.11	Predicted signal and background distributions in the boosted category normalized to unit area and overlaid.	63
5.12	Predicted signal and background distributions in the boosted category normalized to unit area and overlaid.	64
5.13	Predicted signal and background distributions in the VBF category normalized to unit area and overlaid.	65
5.14	Predicted signal and background distributions in the VBF category normalized to unit area and overlaid.	66
5.15	Contours of kinematic correlations in the VBF category for VBF $H \rightarrow \tau\tau$ (left), $Z \rightarrow \tau\tau$ (center), and fakes (right).	68
5.16	Contours of kinematic correlations in the VBF category for VBF $H \rightarrow \tau\tau$ (left), $Z \rightarrow \tau\tau$ (center), and fakes (right).	69
5.17	Overlaid shapes of BDT outputs for signal and background processes in the VBF $H \rightarrow \gamma\gamma$, VBF $H \rightarrow ZZ^*$, and VBF $H \rightarrow WW^*$ analyses.	70
6.1	Comparison of data and various predictions of p_T^Z for $Z \rightarrow ee$ (left) and $Z \rightarrow \mu\mu$ (right) in 2011 data-taking. Mis-modeling is observed.	72
6.2	Comparison of data and various predictions in $Z \rightarrow \ell\ell$ events of $\Delta y(jj)$ (left) and m_{jj} (right) in 2011 data-taking. Mis-modeling is observed for all predictions.	72
6.3	Event displays of the three types of events considered in the embedding procedure: a $Z \rightarrow \mu\mu$ event in data (left), a $\tau_{\text{had}}\tau_{\text{had}}$ event in simulation (center), and a hybrid embedding event (right)	74
6.4	Validation of the embedding technique for simulated tau lepton decays in simulated $Z \rightarrow \mu\mu$ events (left) and simulated muons in data $Z \rightarrow \mu\mu$ events (right). Good agreement is observed in both, for the $m_{\tau\tau}^{\text{MMC}}$ (left) and isolation energy (right).	75
6.5	The pre-fit fractional uncertainty on the embedded $Z \rightarrow \tau_\ell \tau_{\text{had}}$ prediction in each bin of the VBF category for uncertainties pertaining to the embedding procedure and τ_{had} performance.	76
6.6	Comparison of data and various predictions of jet track width in dijet (left) and $\gamma + \text{jet}$ (right) events. Mis-modeling is observed for all predictions.	76
6.7	Comparison of data and various predictions in $W(\rightarrow \ell\nu_\ell) + \text{jets}$ events of $\Delta y(jj)$ (top) and m_{jj} (bottom) in 2011 data-taking. Mis-modeling is observed for all predictions.	78
6.8	Data events in the VBF category which fail τ_{had} identification but fulfill all other requirements. The contamination of $Z \rightarrow \tau_\ell \tau_{\text{had}}$ and other processes without $j \rightarrow \tau_{\text{had}}$ is less than 10%.	80
6.9	Data events in the VBF category which fail τ_{had} identification but fulfill all other requirements. The contamination of $Z \rightarrow \tau_\ell \tau_{\text{had}}$ and other processes without $j \rightarrow \tau_{\text{had}}$ is less than 10%.	81
6.10	Correlations between the τ_{had} BDT identification score and event kinematics in data events in the VBF same-sign region which fail τ_{had} identification but fulfill all other requirements. No strong correlations are observed.	82
6.11	Cartoon of the signal, control, and validation regions used which are used in the $j \rightarrow \tau_{\text{had}}$ estimate.	83

LIST OF FIGURES

6.12 Requirements on the τ_{had} jet discriminant, which are defined to have constant signal efficiency as a function of $p_T(\tau_{\text{had}})$, of various operating points for 1-track τ_{had} (left) and 3-track τ_{had} (right).	84
6.13 Predicted flavor composition of $j \rightarrow \tau_{\text{had}}$ in $W(\rightarrow \ell\nu_\ell) + \text{jets}$ simulation for 1-track τ_{had} (left) and 3-track τ_{had} (right).	84
6.14 Fake factors in the VBF category measured in the various control regions in data for 1-track τ_{had} (left) and 3-track τ_{had} (right).	85
6.15 A pie chart of the composition of $j \rightarrow \tau_{\text{had}}$ processes in the anti-identified CR as predicted by simulation and data (left) and the systematic variations on the composition (right).	86
6.16 The composition of $j \rightarrow \tau_{\text{had}}$ processes in the anti-identified CR as predicted by simulation and data as a function of event kinematics.	87
6.17 The composition of $j \rightarrow \tau_{\text{had}}$ processes in the anti-identified CR as predicted by simulation and data as a function of event kinematics.	89
6.18 Fake factors in the VBF category mixed from the various control regions in data for 1-track τ_{had} (left) and 3-track τ_{had} (right). Statistical and systematic uncertainties are shown.	90
6.19 Comparison of data and $j \rightarrow \tau_{\text{had}}$ prediction in the same-sign validation region for various event kinematics. The purity of $j \rightarrow \tau_{\text{had}}$ is $\approx 97\%$. Only statistical uncertainties are shown, and no sign of systematic bias is observed. Additional validation is shown in Appendix A.	90
6.20 Comparison of the prediction of identified taus and the $j \rightarrow \tau_{\text{had}}$ prediction, both in simulation, in the signal region for various event kinematics. Only statistical uncertainties are shown, and no sign of systematic bias is observed. Additional validation is shown in Appendix A.	91
6.21 The pre-fit fractional uncertainty on the $j \rightarrow \tau_{\text{had}}$ prediction in each bin of the VBF category. R_X refers to the uncertainty on the relative contribution of $j \rightarrow \tau_{\text{had}}$ processes.	92
6.22 Data and prediction for the nominal VBF category (left) and without the τ_{had} electron discriminator (right).	93
6.23 The pre-fit fractional uncertainty on the VBF $H \rightarrow \tau_\ell \tau_{\text{had}}$ prediction in each bin of the VBF category for uncertainties pertaining to the jet energy scale (top) and τ_{had} performance, theory, and the luminosity (bottom).	95
6.24 Data and prediction for input variables to the BDT in the $H \rightarrow \tau_\ell \tau_{\text{had}}$ VBF signal region .	96
6.25 Two of the nine input variables to the VBF $H \rightarrow \tau_{\text{had}} \tau_{\text{had}}$ BDT discriminator: $m_{\tau\tau}^{\text{MMC}}$ (left) and m_{jj} (right).	97
6.26 Two of the seven input variables to the VBF $H \rightarrow \tau_\ell \tau_\ell$ BDT discriminator: $m_{\tau\tau}^{\text{MMC}}$ (left) and m_{jj} (right).	98
7.1 The likelihood equation considered for maximization	100
7.2 Distributions of the 8 TeV BDT discriminants in all six analysis categories after the global fit	104
7.3 The fitted signal strength μ split by category, final state, and data-taking period	106
7.4 Plots of data and prediction which emphasize the most sensitive regions . The individual BDT bins from all six categories are ordered by S/B and plotted on a shared axis (left) and entries in the $m_{\tau\tau}^{\text{MMC}}$ distribution are weighted by $\log(1 + S/B)$ (right).	107
7.5 Comparison of the impact of the statistical and systematic uncertainties on the absolute uncertainty on μ	107
7.6 Display of one of the most signal-like events in the $H \rightarrow \tau_\ell \tau_{\text{had}}$ VBF category in data . The blue track matched to the green cluster indicates an electron, the green track matched to the yellow cluster indicates a τ_{had} , the pink dotted line indicates the E_T^{miss} in the transverse plane, and the turquoise cones indicates the VBF jets. The reconstructed $m_{\tau\tau}^{\text{MMC}} = 127$ GeV and $m_{jj} = 1.53$ TeV.	108

LIST OF FIGURES

7.7	Display of one of the most signal-like events in the $H \rightarrow \tau_{\text{had}}\tau_{\text{had}}$ VBF category in data . The green tracks matched to the yellow clusters indicate the τ_{had} , the pink dotted line indicates the $E_{\text{T}}^{\text{miss}}$ in the transverse plane, and the turquoise cones indicates the VBF jets. The reconstructed $m_{\tau\tau}^{\text{MMC}} = 123$ GeV and $m_{jj} = 1.02$ TeV.	108
8.1	Tau trigger rates in 2012 data-taking as a function of instantaneous luminosity for L1 (left) and HLT (right)	110
8.2	Significance (p_0) of the $H \rightarrow \tau\tau$ VBF category in 2012 for the $H \rightarrow \tau_{\text{had}}\tau_{\text{had}}$ (left) and $H \rightarrow \tau_{\ell}\tau_{\text{had}}$ (right) analyses as a function of offline or L1 threshold for various objects.	112
8.3	Topological distributions at L1 for $H \rightarrow \tau_e\tau_{\text{had}}$ MC versus high-pileup ($\langle \mu \rangle = 81$) minimum bias MC.	113
8.4	L1 angular resolution for τ_{had} in simulation and data	113
8.5	Momentum resolution for τ_{had} in simulation and data at L1 (left) and HLT (right). The resolution is significantly improved at HLT	114
8.6	Kinematic distributions in the $\ell + \tau_{\text{had}}$ category of the 8 TeV VBF $H \rightarrow \tau_{\ell}\tau_{\text{had}}$ analysis.	116
8.7	Kinematic distributions in the $\ell + \tau_{\text{had}}$ category of the 8 TeV VBF $H \rightarrow \tau_{\ell}\tau_{\text{had}}$ analysis.	117
8.8	Efficiency for firing the 20 GeV L1 τ_{had} trigger as a function of offline $p_{\text{T}}(\tau_{\text{had}})$ for no isolation requirement (left) and the 2012 isolation requirement (right) for various definitions of the L1 τ_{had} item. The current definition (2×1 EM, 2×2 had.) has the slowest efficiency turn-on. Fits are performed with a Fermi-Dirac distribution.	118
8.9	L1 rate for the di- τ_{had} trigger in 14 TeV minimum bias MC for various p_{T}^{L1} -dependent isolation definitions relative to the 2012 definition: $p_{\text{T}}^{\text{L1,iso}} \leq 4$ GeV. Many options give the same rate (white color). The rate is calculated irrespective of the lowest unprescaled single τ_{had} trigger (left) and with a logical OR of it (right).	120
8.10	Efficiency for firing the L1 τ_{had} trigger for various p_{T}^{L1} -dependent isolation definitions which have similar rates, as derived from Fig. 8.9. The 2012 definition is the black line. The efficiency is calculated irrespective of the lowest unprescaled single τ_{had} trigger (left) and with a logical OR of it (right).	120
8.11	Degradation of $E_{\text{T}}^{\text{miss}}$ -related observables at HL-LHC conditions for VBF $H \rightarrow \tau_{\ell}\tau_{\text{had}}$: the $E_{\text{T}}^{\text{miss}}$ resolution (left) and reconstructed $m_{\tau\tau}^{\text{MMC}}$ (right) . The underflow of the $m_{\tau\tau}^{\text{MMC}}$ shows the fraction of events which fail the mass reconstruction.	125
8.12	Signal efficiency versus background efficiency for scenarios of generic forward tracker coverage and rejection power (left) and zoomed in to lower signal efficiency (right) . A BDT is trained in the VBF category for each scenario.	127
8.13	Signal and background HL-LHC predictions of (a) leading jet p_{T} , (b) sub-leading jet p_{T} , (c) leading jet η , (d) sub-leading jet η , (e) $\Delta\eta_{jj}$, (f) m_{jj} , (g) $\eta_{\text{leadjet}} \times \eta_{\text{sub-leadjet}}$ and (h) $E_{\text{T}}^{\text{miss}}$. The last bin contains the overflow events.	128
8.14	Signal and background HL-LHC predictions of (a) $p_{\text{T}}(\tau_{\text{had}})$, (b) $p_{\text{T}}(\text{lepton})$, (c) $\eta(\tau_{\text{had}})$, (d) $\eta(\text{lepton})$, (e) $\Delta R(\tau_{\text{had}}, \text{lepton})$, (f) MMC (g) $m_{\tau\tau}^{\text{vis.}}$ and (h) $m_{\text{T}}(\ell, E_{\text{T}}^{\text{miss}})$. The last bin contains the overflow events.	129
8.15	Signal and background HL-LHC predictions of (a) $E_{\text{T}}^{\text{miss}}$ ϕ -centrality, (b) lepton η -centrality and (c) $p_{\text{T}}^{\text{Total}}$. The last bin contains the overflow events.	130
8.16	Signal and background HL-LHC predictions of the BDT spectrum in the (a) full range and (b) highest bins range . Signal and background are overlaid in (a) and stacked in (b).	130
A.1	Comparison of data and $j \rightarrow \tau_{\text{had}}$ prediction in the same sign CR for various event kinematics. Only statistical uncertainties are shown.	134
A.2	Comparison of data and $j \rightarrow \tau_{\text{had}}$ prediction in the same sign CR for various event kinematics. Only statistical uncertainties are shown.	135

LIST OF FIGURES

A.3 Comparison of the prediction of identified taus and the $j \rightarrow \tau_{\text{had}}$ prediction, both in simulation, in the signal region for various event kinematics. Only statistical uncertainties are shown.	136
A.4 Comparison of the prediction of identified taus and the $j \rightarrow \tau_{\text{had}}$ prediction, both in simulation, in the signal region for various event kinematics. Only statistical uncertainties are shown.	137
A.5 Comparison of data and $j \rightarrow \tau_{\text{had}}$ prediction in the $W \rightarrow \ell\nu_\ell$ CR for various event kinematics. Only statistical uncertainties are shown.	138
A.6 Comparison of data and $j \rightarrow \tau_{\text{had}}$ prediction in the $W \rightarrow \ell\nu_\ell$ CR for various event kinematics. Only statistical uncertainties are shown.	139
A.7 Comparison of data and $j \rightarrow \tau_{\text{had}}$ prediction in the QCD CR for various event kinematics. Only statistical uncertainties are shown.	140
A.8 Comparison of data and $j \rightarrow \tau_{\text{had}}$ prediction in the QCD CR for various event kinematics. Only statistical uncertainties are shown.	141
A.9 Comparison of data and $j \rightarrow \tau_{\text{had}}$ prediction in the $Z \rightarrow \ell\ell$ CR for various event kinematics. Only statistical uncertainties are shown.	142
A.10 Comparison of data and $j \rightarrow \tau_{\text{had}}$ prediction in the $Z \rightarrow \ell\ell$ CR for various event kinematics. Only statistical uncertainties are shown.	143
A.11 Comparison of data and $j \rightarrow \tau_{\text{had}}$ prediction in the top CR for various event kinematics. Only statistical uncertainties are shown.	144
A.12 Comparison of data and $j \rightarrow \tau_{\text{had}}$ prediction in the top CR for various event kinematics. Only statistical uncertainties are shown.	145
B.1 Signal and background distributions for the full set of the discriminating variables in the 1-track τ_{had} jet discrimination algorithm	147
B.2 Signal and background distributions for the full set of the discriminating variables in the 3-track τ_{had} jet discrimination algorithm	148
C.1 Simulated predictions of $m_{Z \rightarrow \tau_\ell \tau_{\text{had}}}$ and $m_{H \rightarrow \tau_\ell \tau_{\text{had}}}$ in the boosted category for various $m_{\tau\tau}$ reconstruction algorithms.	150
C.2 Simulated predictions of $m_{Z \rightarrow \tau_\ell \tau_{\text{had}}}$ and $m_{H \rightarrow \tau_\ell \tau_{\text{had}}}$ in the VBF category for various $m_{\tau\tau}$ reconstruction algorithms.	151

Preface

My time as a graduate student has been an incredible journey of Higgs bosons and tau leptons. I am forever indebted to the Penn Army, the ATLAS Collaboration, my friends, and my family for their help and support. Let's keep the party going in Run-II.

Alexander Tuna
CERN, April 2015

CHAPTER 1

Introduction

This thesis documents the evidence of Higgs boson decays to tau leptons with the ATLAS experiment at the LHC. Special emphasis is given to the VBF $H \rightarrow \tau_\ell \tau_{\text{had}}$ subset of the analysis. The data correspond to 25 fb^{-1} of proton collisions with $\sqrt{s} = 7$ or 8 TeV .

Chapter 2 gives a brief overview of the Standard Model of particle physics to provide theoretical context for searches for the Higgs boson. Chapter 3 describes the LHC and the ATLAS detector, which are the experimental apparatuses used here, and the process by which detector outputs are interpreted and classified as particles. Chapter 4 describes tau leptons and their experimental signatures at ATLAS. Details of classifying hadronic tau lepton decays are presented, especially discrimination against jets, electrons, and muons.

Chapter 5 discusses the search strategy for $H \rightarrow \tau\tau$ at ATLAS and motivates the use of machine learning. Chapter 6 reviews how physics processes relevant to the search are predicted, including a thorough description of the prediction of jets mis-identified as hadronic tau lepton decays. Chapter 7 gives the results of the searches and presents evidence for decays of the Higgs boson to tau leptons at ATLAS.

Chapter 8 discusses future prospects for $H \rightarrow \tau\tau$ analysis at ATLAS, both in the near- and long-term. Chapter 9 concludes this thesis with a synopsis.

Much of the work in this thesis is included in publications by the ATLAS experiment, including a description of hadronically decaying tau leptons at ATLAS [1] and evidence for decays of the Higgs boson to tau leptons at ATLAS [2].

CHAPTER 2

Theoretical Review

The Standard Model of particle physics is described in brief. It is the preeminent theory describing the behavior of subatomic particles, and it is the result of generations of experimental observations and theoretical interpretations. Until recently, only one fundamental particle of the theory had not been observed: the Higgs boson. The particle was first observed by the ATLAS and CMS experiments at the LHC in 2012.

2.1 The Standard Model

The Standard Model (SM) describes how particles in nature interact in the electroweak and quantum chromodynamic (QCD) sectors. These interactions are encoded in the SM Lagrangian written in the language of a quantum field theory, where particles are represented by quantum fields. The SM Lagrangian is a non-abelian gauge theory with the symmetry group $SU(3) \times SU(2) \times U(1)$.

The gauge invariance of $SU(3)$, $SU(2)$, and $U(1)$ implies the existence of eight gluon fields, three W^i bosons, and a B boson which together mediate the QCD and electroweak sectors. All of these bosons are predicted to be massless, though, which presents a problem since the weak forces are known to be short range, i.e., their mediating boson ought to be massive.

This problem was remedied independently by Brout and Englert [3], Higgs [4, 5], and Guralnik, Hagen, and Kibble [6] in the 1960s. They proposed the symmetry be spontaneously broken by a new scalar field whose accompanying particle has been dubbed the Higgs boson, and the result of this breaking are the massive W^\pm and Z fields, which are superpositions of the massless W^i and B bosons. The symmetry breaking also provides mass terms for the fermions in concert with a Yukawa-style interaction with the Higgs boson. The theory of electromagnetic and weak interactions was coherently unified by Glashow [7], Weinberg [8], and Salam [9] in the late 1960s.

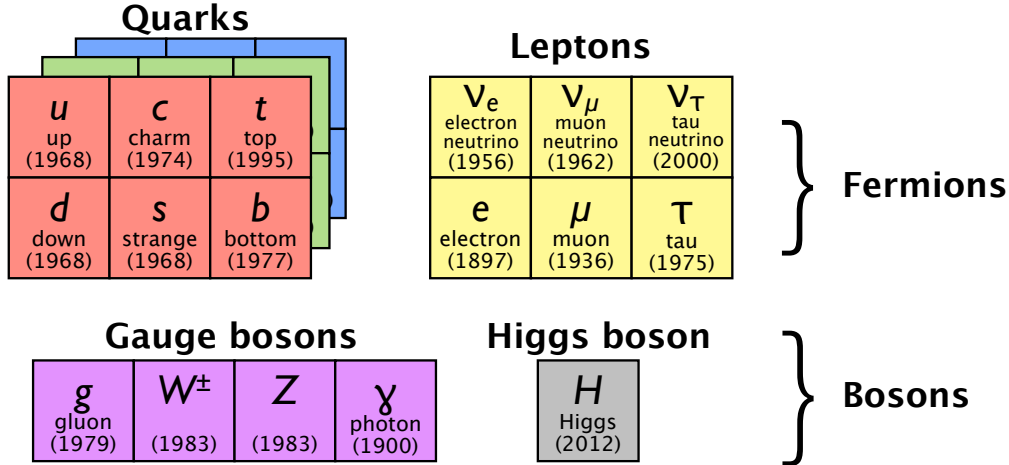


Figure 2.1: Simplified illustration of the fundamental particles of the Standard Model [19], where the parenthetical note to each particles indicates the year of discovery.

Among the first strong evidence for the electroweak theory was the observation of weak neutral current interactions by Gargamelle at CERN [10, 11, 12]. These were a manifestation of the massive Z boson despite not having sufficient energy to produce them directly. A handful of additional experiments could also measure the mixing angle θ_W , which is a parameter of the electroweak theory governing the mixing of the B and the W into the Z and photon. This measurement [13, 14] can be used to make predictions of the masses of the bosons, especially the ratio of their masses: $\cos(\theta_W) = m_W/m_Z$. The UA1 and UA2 experiments at CERN first observed the massive bosons in 1983 [15, 16, 17, 18], and the measured masses were exactly compatible with the prediction of the broken electroweak symmetry. This provided compelling motivation for the existence of the Higgs boson.

The collection of fundamental SM particles, including the Higgs boson, are shown in Figs. 2.1 and 2.2. The bosons of the SM are mediators of the theory, and the fermions compose the matter we observe. The fermions are grouped into the quarks, which compose objects like protons and neutrons, and the leptons, such as electrons. Quarks have fractional electric charge and three possible color charges, typically called red, blue, and green. They therefore interact with all of the SM gauge bosons. The leptons are colorless and only interact with the electroweak gauge bosons. Among the leptons, neutrinos are electrically neutral and thus only participate in weak interactions. They are also have small mass relative to the other SM fermions, though they are not massless. Understanding the properties of neutrinos is an active area of current research.

2. THEORETICAL REVIEW

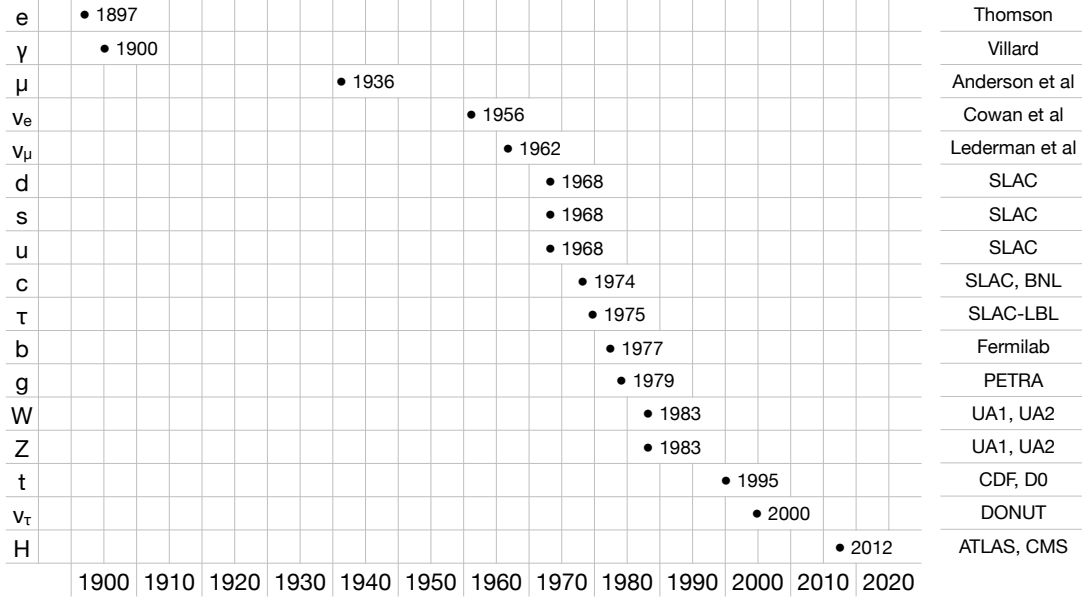


Figure 2.2: Graph of the discoveries of the fundamental particles of the Standard Model versus time.

2.2 Search for the Higgs

Despite the strong motivation for the existence of the Higgs boson, it was not verified for nearly fifty years after its initial proposal. The topic of experimental observation and general phenomenology of the Higgs boson was approached by Ellis, Gaillard, and Nanopoulos, who decided “we do not want to encourage big experimental searches for the Higgs boson” [20] because its mass was an unknown parameter and its couplings to other particles “are probably all very small” [20].

Nonetheless, big experimental searches ensued. The largest production modes of the Higgs boson at proton colliders are through gluon fusion (ggF), vector boson fusion (VBF), and production in association with a vector boson (VH) [21], and the cross-sections for these processes are indeed small. The diagrams are shown in Fig. 2.3 with their cross-section for the Higgs mass at 125 GeV. At electron colliders, the ZH production mode dominates.

The Higgs then decays quickly, and experiments are tasked with inferring its presence from its decay products. Many decay channels are allowed because the Higgs couples directly to all massive particles in the SM Lagrangian. The Higgs decay branching fractions [22] are correlated with the mass of the decay products, and it tends to decay to whatever particle is heaviest and kinematically allowed. For example, if the Higgs mass was 100 GeV, it would decay almost exclusively to bb , whereas at 200 GeV, it would decay mostly to WW and ZZ .

gluon-gluon fusion (ggF)	vector boson fusion (VBF)	associated production VH	associated production $t\bar{t}H$

Figure 2.3: Selected Higgs boson production mechanisms and their cross-sections at pp colliders with $\sqrt{s} = 8$ TeV for $m_H = 125$ GeV [23].

The prospect of directly observing the Higgs boson was a major piece of the physics program at the LEP [24] and Tevatron [25] colliders at CERN and Fermilab, respectively. Experiments at both colliders published many searches [26, 27], and their sensitivity was driven by the $H \rightarrow bb$ decay channel because of its high branching fraction. Neither collider reported an observation, and the LEP experiments excluded SM production of the Higgs boson if its mass were below 114 GeV.

The LEP and Tevatron searches, when combined with fits of precision electroweak measurements sensitive to the mass of the Higgs boson, showed a preference for the Higgs boson mass to be between 115 and 200 GeV, as shown in Fig. 2.4. This set the stage for the ATLAS and CMS experiments at the LHC, with a collision energy much higher than the Tevatron, to finally observe or exclude the existence of the Higgs boson in the first few years of data-taking.

The ATLAS and CMS experiments independently announced the observation of the Higgs boson in 2012 [29, 30], using data taken with proton collisions at 7 and 8 TeV. The measured mass was around 125 GeV, consistent with expectations from global electroweak fits and the LEP and Tevatron exclusions. The discovery was driven by the bosonic decay modes: $H \rightarrow \gamma\gamma$, $H \rightarrow ZZ^*$, and $H \rightarrow WW^*$. ATLAS and CMS have only recently unearthed evidence for the fermionic decay modes, driven by the $\tau\tau$ channel, and that is the topic of this thesis.

Two Nobel prizes in physics have been awarded for the theory of electroweak symmetry breaking [31]. Glashow, Salam, and Weinberg were honored in 1979 for the unified theory of electroweak symmetry breaking after the observation of neutral current interactions at Gargamelle. Englert and Higgs were honored in 2013 for the introduction of spontaneous symmetry breaking after the observation of the Higgs boson at ATLAS and CMS.

2. THEORETICAL REVIEW

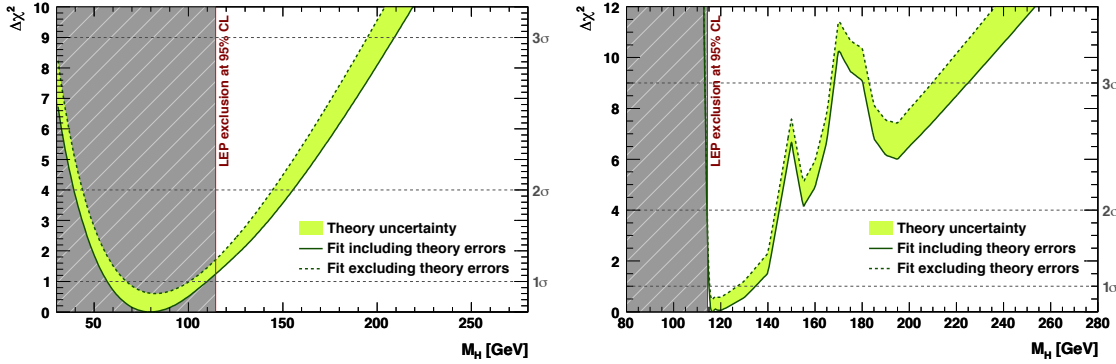


Figure 2.4: Summary of the preferences for the Higgs mass as a result of global fits to precision electroweak data [28] without direct Higgs searches from LEP and the Tevatron (left) and with (right). The fits are done before LHC data-taking.

2.3 Shortcomings

The Standard Model beautifully describes particles physics across many orders of magnitude and in both the electroweak and QCD sectors. However, it is not a complete theory of the universe. There are several aspects of the physical universe for which the SM provides an unsatisfactory description, or no description at all. These are among the strongest reasons for continuing to search for physics beyond the SM. The upcoming years of data-taking at the LHC hope to push the boundaries of our understanding, and to shed light in these uncertain areas.

Dark matter, dark energy

Astrophysical experiments in the past decades [32, 33] have indicated that only around 5% of the universe is composed of observable matter, like protons and electrons. The origin and properties of the remaining 95% are largely unknown. The remainder is generally put into two groups: dark matter, which seems clumped and localized, and dark energy, which seems to permeate all space. Neither dark matter nor dark energy is incorporated into the SM.

Gravity

Gravity is the force which dictates the movement of stars and planets, and keeps humans from floating into space. It is completely missing from the SM. A particle mediating gravity, called the *graviton*, is hypothesized and could probably be accommodated into the SM, but there is no observation of such a particle yet.

Hierarchy and Unification

Nature has so far displayed two fundamental energy scales: the electroweak scale of the Standard

2. THEORETICAL REVIEW

Model (10^2 GeV), and the Planck scale where the effect of gravity on particle interactions cannot be ignored (10^{18} GeV) [34]. Why are these energy scales separated by sixteen orders of magnitude, and what physics exists between them? The SM offers no motivation for these disparate scales, nor does it offer an elegant unification of the fundamental forces. Many popular models of physics beyond the SM, such as supersymmetry, offer more satisfactory descriptions of the high energy regimes [35].

CHAPTER 3

The LHC and the ATLAS detector

The Large Hadron Collider (LHC) and ATLAS detector are described. The LHC is among the largest scientific facilities in the history of humanity. It smashes more protons, at higher speeds, than any previous physics experiment. The ATLAS detector records these collisions and translates detector signals into physics phenomena. These are the experimental apparatuses which provide data for this thesis.

3.1 The LHC

The Large Hadron Collider (LHC) [36] is the most powerful particle accelerator ever built. It was first conceived in the 1980s with the purpose of finding the Higgs boson and discovering physics beyond our current understanding. It became operational in the early 2010s.

The LHC is a circular hadron collider 27 kilometers in circumference and 100 meters underground, near Geneva, Switzerland. It straddles the border of Switzerland and France. It is operated by the European Organization for Nuclear Research (CERN¹) and occupies the underground tunnel originally constructed for the Large Electron Positron collider (LEP) for use in the 1990s. The construction costs of the LHC are approximately five billion USD.

The LHC collides hadrons at high energies to probe the boundaries of our understanding of particle physics. These collisions are observed by four major experiments situated along the LHC ring: ATLAS [37], CMS [38], ALICE [39], and LHCb [40]. ATLAS and CMS are general purpose particle detector experiments built for discovering physics of and beyond the Standard Model. ALICE is designed to observe heavy ion (lead nuclei) collisions and study the physics of quark-gluon plasma. LHCb specializes in the study of b -hadrons. An aerial view of the experiments is shown in Fig. 3.1.

¹Conseil Européen pour la Recherche Nucléaire

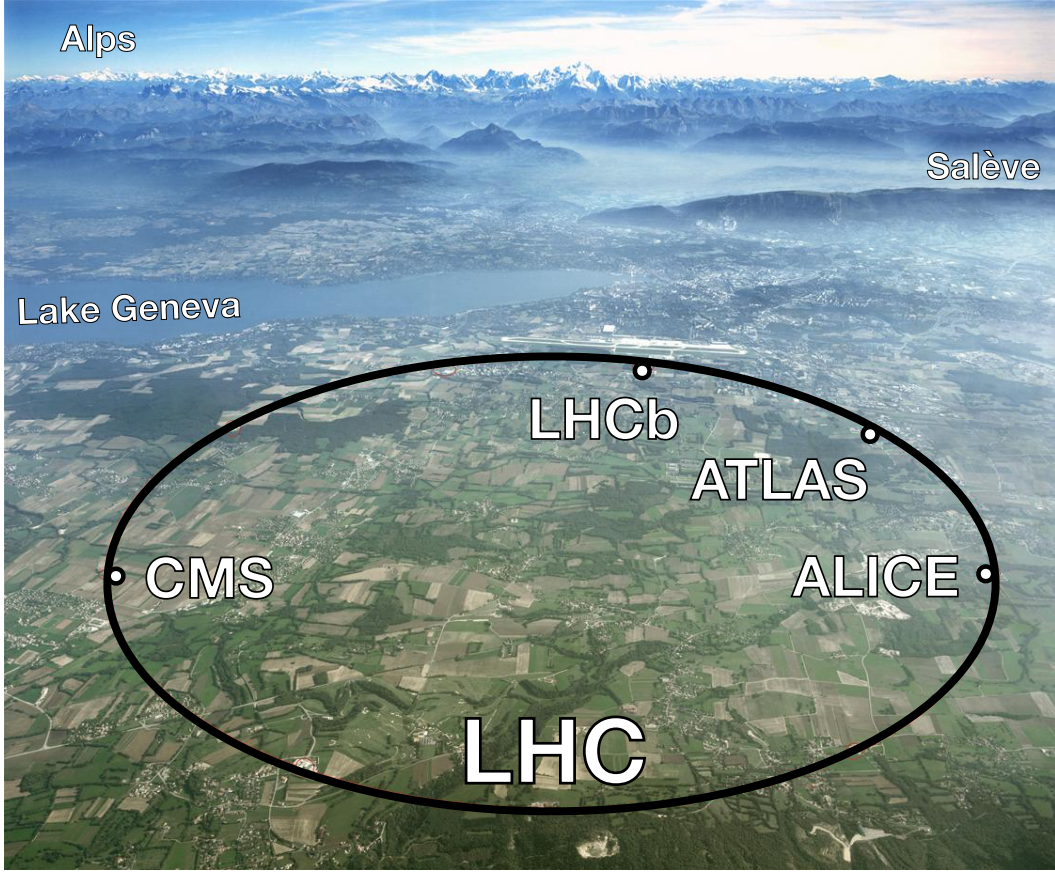


Figure 3.1: Aerial view of Geneva with an overlaid drawing of the LHC and associated experiments [41].

3.1.1 Specifications

The LHC is last step of a multi-stage chain of accelerators called the LHC accelerator complex [42], shown in Fig. 3.2. Protons are first retrieved from hydrogen atoms and accelerated by the Linac 2 linear accelerator to 50 MeV per proton. The protons are then passed successively to the Proton Synchotron Booster (PSB), Proton Synchotron (PS), and Super Proton Synchrotron (SPS) where they are accelerated to 1.4 GeV, 25 GeV, and 450 GeV, respectively. The protons are finally fed into the LHC where they are maximally accelerated to 4 TeV in 2012 operations, yielding a center-of-mass collision energy of 8 TeV. This chain is summarized in Table 3.1. At full energy, the protons will typically circulate the LHC for many hours at a time.

Protons travel around the LHC in two oppositely circulated beams. The proton beams are bent and focused by powerful superconducting electromagnets, which operate cryogenically at an ultracold

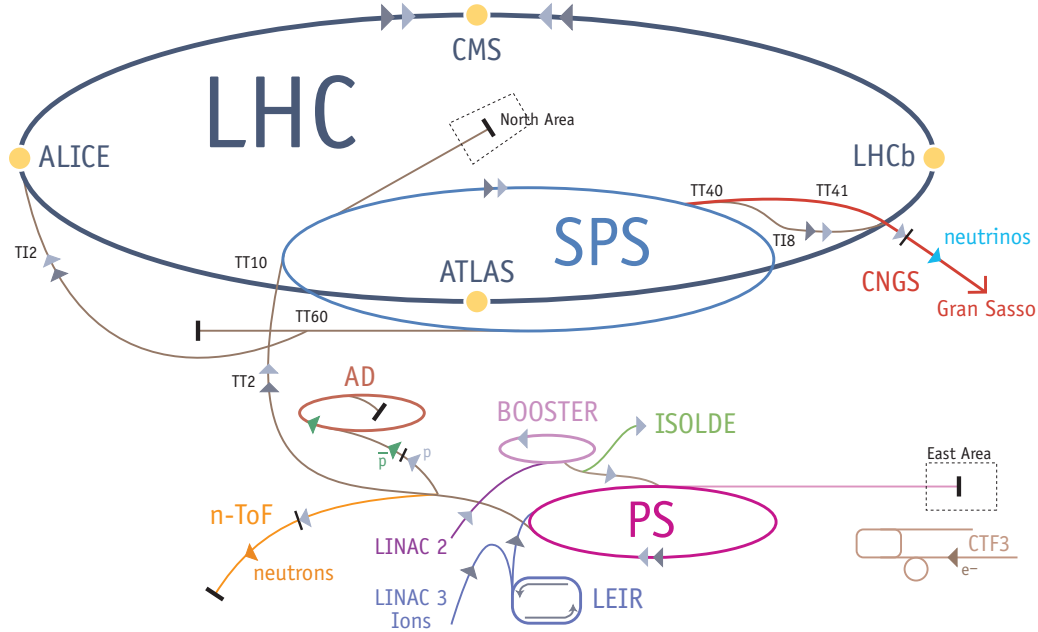


Figure 3.2: The LHC accelerator complex. Before reaching the LHC, protons are accelerated at Linac 2, the Proton Synchrotron Booster (PSB), the Proton Synchrotron (PS), and the Super Proton Synchrotron (SPS) [43].

Table 3.1: The accelerators of the LHC accelerator chain and the speed at which they accelerate protons in 2012. [43].

proton energy (GeV)	speed of light (%)	accelerator
0.05	31.4	Linac 2
1.4	91.6	PSB
25	99.93	PS
450	99.9998	SPS
4000	99.99997	LHC

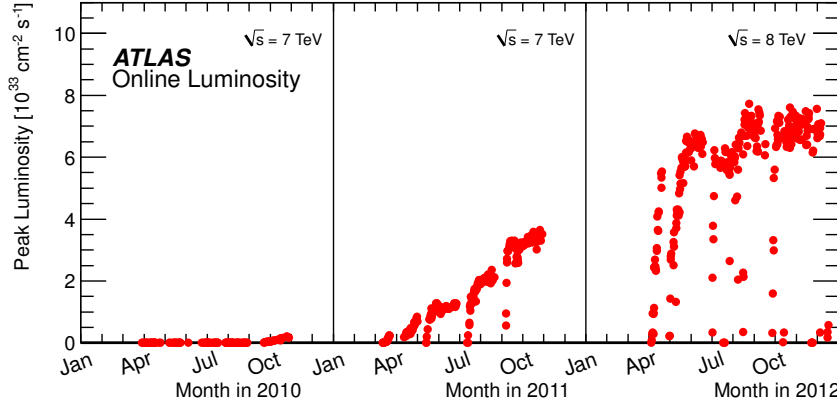


Figure 3.3: The peak luminosity as measured in different data-taking periods [46]. The peak Run-I luminosity is $0.8 \times 10^{34} \text{cm}^{-2}\text{s}^{-1}$.

temperature of 2 K (-456 F). The proton beams are segmented into groups of protons called *bunches*. Each beam contains 2808 bunches, and each bunch contains approximately 10^{11} protons. Many protons are included per bunch to maximize the probability of a proton-proton collision for a given bunch crossing. A bunch crossing happens every 50 nanoseconds during operations in 2012.

3.1.2 Operations

The LHC is designed to collide protons with a center-of-mass energy \sqrt{s} of 14 TeV and an instantaneous luminosity of $10^{34} \text{cm}^{-2}\text{s}^{-1}$. However, while commissioning in 2008, the machine broke due to a faulty electrical connection between two superconducting magnets [44]. The LHC was repaired in 2009 and, to ensure safer operation, began colliding protons below design energy and instantaneous luminosity in late 2009.

The LHC collided protons for physics studies in 2010-2012 at a reduced energy of 7 TeV (2010-2011) and 8 TeV (2012). These years of data-taking are referred to as *Run-I* and include the discovery of the Higgs boson. The peak instantaneous luminosity achieved was $7.7 \times 10^{33} \text{cm}^{-2}\text{s}^{-1}$ in 2012 [45], which doubled the peak luminosity of 2011 data-taking.

To increase the number of collisions recorded, many proton collisions are allowed to occur within a single bunch crossing. This average number of proton collisions per bunch crossing $\langle\mu\rangle$ is referred to as *pileup*. The average $\langle\mu\rangle$ in 2012 is around 20 collisions per crossing and reaches as large as 35-40. Profiles of the pileup are shown in Figs. 3.3 and 3.4.

The LHC, ATLAS, and CMS are undergoing maintenance and upgrades from early 2013 until early 2015. Data-taking is intended to resume in mid-2015 with an increased $\sqrt{s} = 13$ TeV and a

3. THE LHC AND THE ATLAS DETECTOR

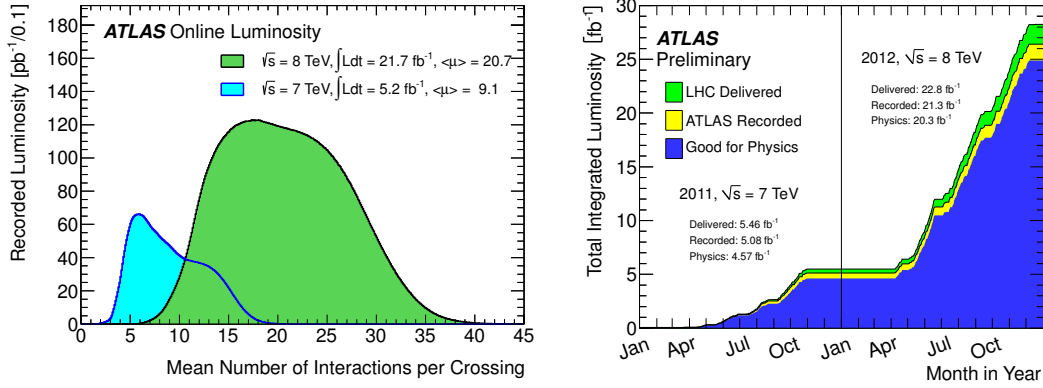


Figure 3.4: Distributions of the recorded luminosity in bins of $\langle \mu \rangle$ (left) and the total integrated luminosity as a function of time (right) [46]. In 2011 (2012), the average $\langle \mu \rangle$ is 9.1 (20.7) and the total integrated luminosity for physics analysis is 4.6 fb^{-1} . (20.3 fb^{-1}).

instantaneous luminosity of $10^{34} \text{ cm}^{-2} \text{s}^{-1}$. The *Run-II* data-taking campaign is intended to last for the next three to four years, until 2017-2018, when another round of upgrades are planned to be installed.

These datasets allow the ATLAS and CMS experiments to probe physics of the Standard Model and beyond unlike any previous experiment in particle physics. Despite operating below design energy and luminosity, the Run-I dataset accesses electroweak processes at unprecedented rates, as shown in Fig. 3.5. This rate will increase again in the Run-II data-taking campaign, thereby offering a new opportunity for discovery.

3.2 The ATLAS detector

The ATLAS² detector is a general purpose cylindrical detector centered on one of the LHC collision points. It is 46 meters in length, 25 meters in diameter, and weighs 7000 tons. Assembly began at CERN in 2003 and was completed in 2008. A schematic rendering is shown in Fig. 3.6.

ATLAS is built to measure and classify particles arising from proton-proton collisions. These particles can be as low energy as a few hundred MeV to as high energy as multiple TeV. To detect such a broad range of phenomena, multiple subdetectors are employed. These are concentric about the proton-proton interaction point (IP) and are designed to observe different classes of particles.

The *inner detector* is closest to the beams and is designed to detect charged particles. The *calorimeters* are outside the inner detector and are designed to stop all particles except muons and

²A Toroidal LHC Apparatus

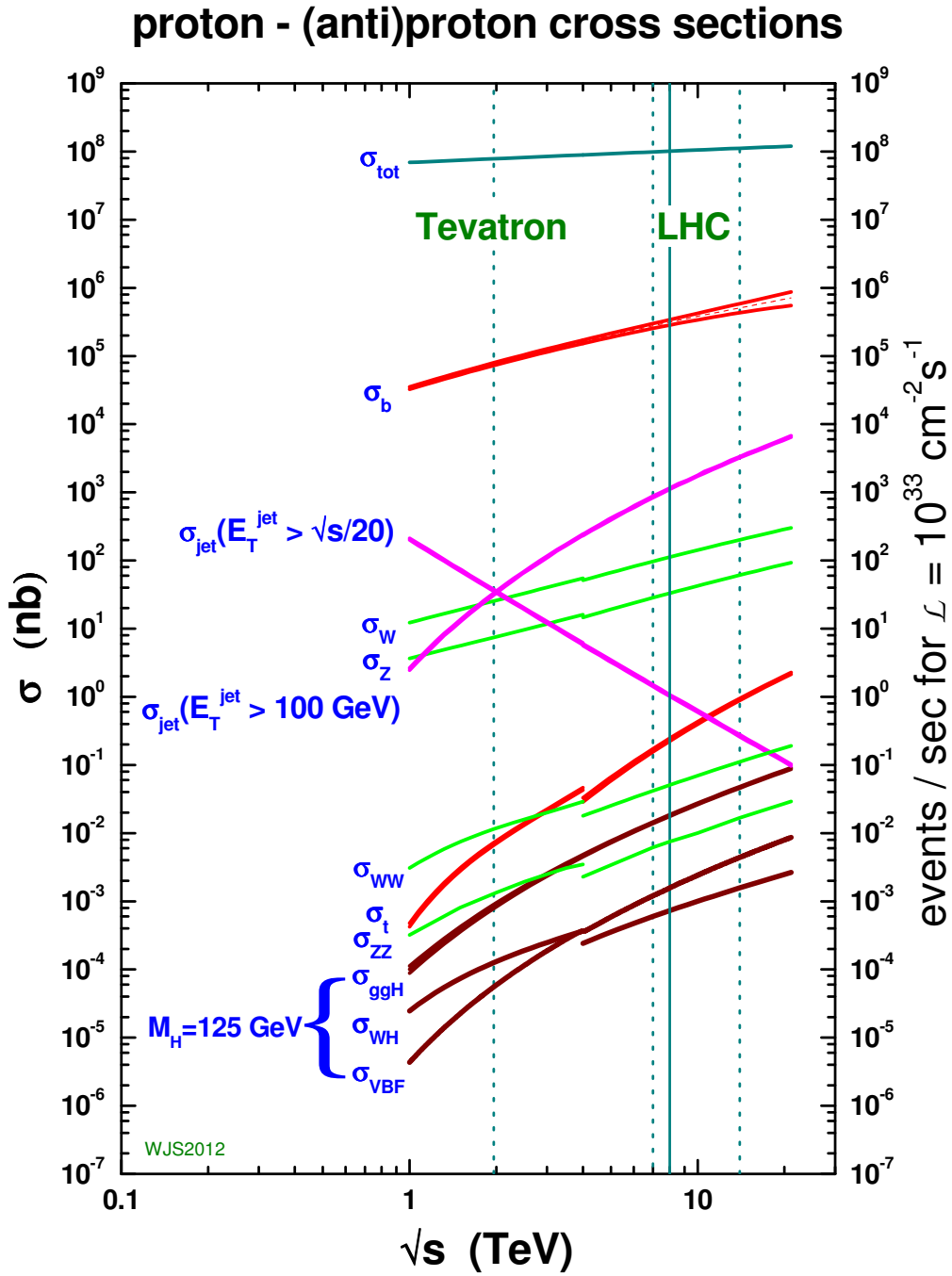


Figure 3.5: Cross sections for pp and $p\bar{p}$ processes in the center-of-mass energy regime relevant to the Tevatron and LHC, courtesy of W.J. Stirling [47].

3. THE LHC AND THE ATLAS DETECTOR

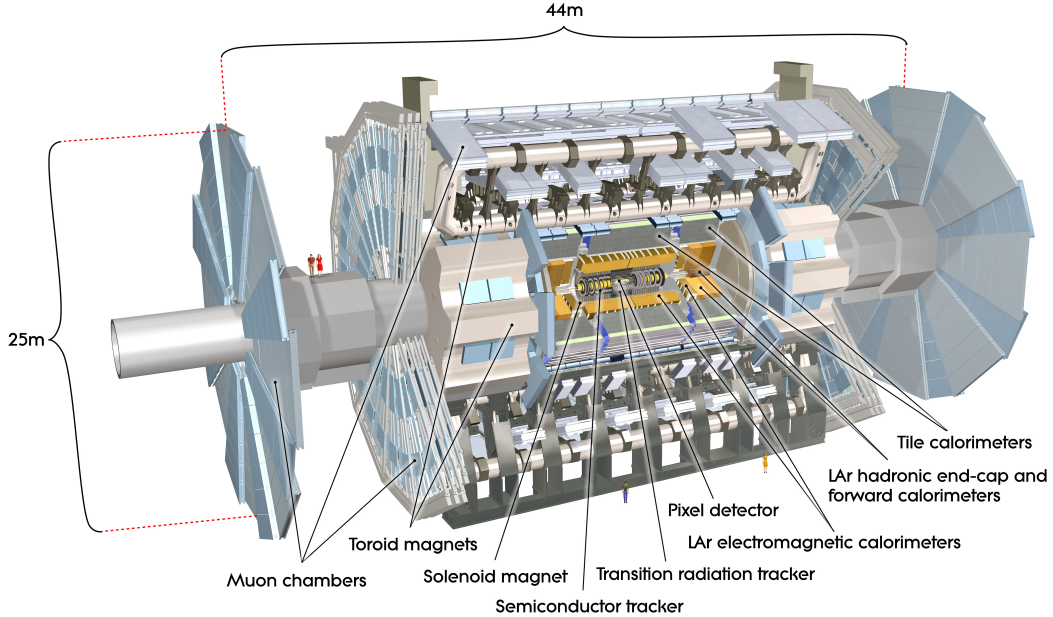


Figure 3.6: Scale rendering of the ATLAS detector with the various subdetectors highlighted [48].

neutrinos. The *muon system* is furthest from the beams and is designed to detect muons as they exit ATLAS.

The inner detector is enclosed by a solenoidal magnet with a field of approximately 2 Tesla. A large toroidal magnet exists within the muon system which has a field of 2 to 8 Tesla. The purpose of these magnets is to bend the trajectory of charged particles as they travel through ATLAS. The momenta of these particles can then be precisely inferred from the measured trajectory according to the classical Lorentz force law.

ATLAS uses a right-handed coordinate system with its origin at the IP in the center of the detector, and the z -axis along the beam line. The x -axis points from the IP to the center of the LHC ring, and the y -axis points upwards. Cylindrical coordinates (r, ϕ) are used in the transverse plane, ϕ being the azimuthal angle around the beam line. The pseudorapidity η is typically used in place of the polar angle θ and is defined as $\eta = -\ln(\tan \frac{\theta}{2})$ [29].

The ATLAS collaboration was formed in 1992, and as of 2011, it includes over 3000 scientists from 174 institutions and 38 countries. It is one of the largest scientific collaborations in the world.

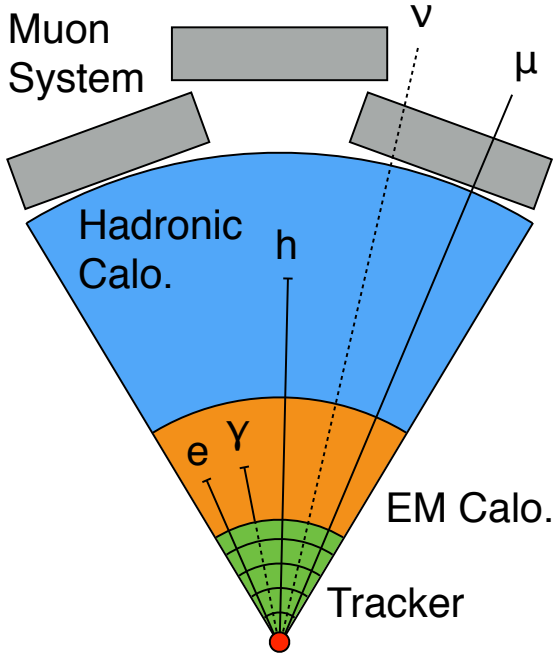


Figure 3.7: Transverse schematic view of a wedge of the ATLAS detector. Charged particles leave tracks in the tracker, electrons and photons typically stop in the electromagnetic calorimeter, hadrons like charged pions typically stop in the hadronic calorimeter, and muons are tagged by the muon system as they exit. Neutrinos escape undetected.

3.2.1 Inner detector and tracking

The inner detector (ID), also called the *tracker*, is designed to precisely measure the trajectory and momentum of charged particles as they pass through the 2 T magnetic field provided by the solenoid, such as electrons, muons, and charged pions [37]. The ID is composed of three independent but complementary subdetectors: the Pixel detector, the Semiconductor Tracker (SCT), and the Transition Radiation Tracker (TRT). These are shown in Fig. 3.8. The subdetectors are split into barrel and endcap components, have full 2π coverage in ϕ , and have at least coverage in $|\eta|$ up to 2.0. Information from all three subdetectors is used to reconstruct tracks and vertices.

3.2.1.1 Subdetectors

The Pixel detector exists closest to the interaction point and employs three layers of silicon pixels [37]. The pixels have fine granularity and are designed to deliver precise measurement of tracking parameters close to the IP, which are useful for secondary vertexing. The intrinsic resolution of the pixels in the barrel are $10 \mu\text{m}$ in $r\phi$ and $115 \mu\text{m}$ in z . The Pixel detector has 80×10^6 channels, by far the

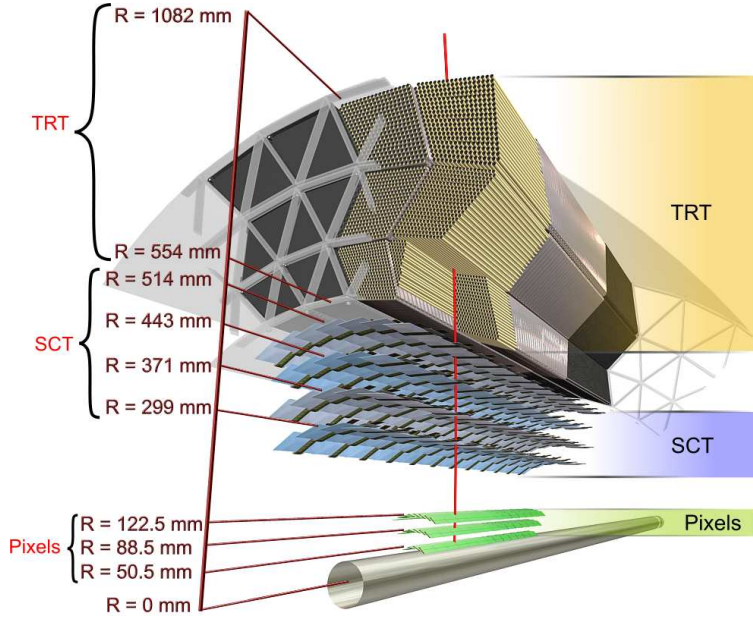


Figure 3.8: A diagram of the barrel of the Inner Detector: the three layers in the Pixels, the four layers in the SCT, and the many layers of the TRT [49].

most of any ATLAS subdetector, and usually provides three measurements per charged particle. The track resolution is $10 \mu\text{m}$. The Pixel detector has coverage up to $|\eta| = 2.5$.

The SCT surrounds the Pixel detector and also employs silicon detector elements, using microstrips instead of pixels [37]. The strips are arranged in four double layers, with the pairs arranged at small angles relative to each other, to make a three-dimensional measurement. The intrinsic resolution of the strips in the barrel are $17 \mu\text{m}$ in $r\phi$ and $580 \mu\text{m}$ in z . The SCT has 6.3×10^6 channels and usually provides eight measurements per charged particle. It has coverage up to $|\eta| = 2.5$.

The TRT surrounds the SCT and is the largest of the ID subdetectors [37]. It employs 300,000 straw drift tubes for recording the passage of charged particles. The intrinsic resolution of the TRT in the barrel is $130 \mu\text{m}$ in $r\phi$; the drift tubes cannot make a measurement in z . The TRT has 350,000 channels and usually provides 30 or more measurements per charged particle. It has coverage up to $|\eta| = 2.0$. A comparison of subdetector features is shown in Table 3.2.

The TRT additionally provides information for classifying charged particles as electrons or pions via the detection of transition radiation in the xenon gas mixture in the drift tubes [50]. This radiation is produced when a charged particle crosses the boundary between two media of different dielectric constants and is proportional to the Lorentz γ of a particle. For an electron and charged pion of equal

3. THE LHC AND THE ATLAS DETECTOR

momentum, the electron is therefore much more likely to produce TR than the pion since its mass is 200 times smaller. Transition radiation is observed in the TRT as hits well above the threshold for tracking, which are referred to as *high threshold* hits, as opposed to *low threshold*.

3.2.1.2 Tracking

Information from these three subdetectors are combined to make *tracks*, which have a unique correspondence to charged particles and are meant to describe their trajectory and momentum. As a charged particle travels through the ID, it leaves *hits* in each subdetector along its trajectory, as shown in Fig. 3.9. These are built into tracks with a three-dimensional fit using Kalman filtering tools which can account for multiple scattering as the charged particle traverses the media of the ID [49, 51]. The ATLAS tracking algorithms builds tracks for charged particles as low momentum as a few hundred MeV.

A vertex reconstruction algorithm [53, 51] is used to determine if multiple tracks originate from a single pp collision. The output of the algorithm is a complete set of vertices per event and the association of each track to a vertex. Starting with the set of all tracks passing simple goodness criteria (e.g., requiring a minimum number of hits in the silicon detectors), a vertex seed is derived from the global maximum of z coordinates, and tracks are associated to that seed using a χ^2 fitting algorithm. Tracks incompatible with the vertex are then used as seeds for the next iteration of the vertexing algorithm until all tracks are exhausted.

Vertexing is essential for deciding which tracks (and thus physics objects) originate from the pp collision of interest and which tracks do not. The vertex associated to the collision of interest is called the *primary vertex* and is conventionally the vertex with the highest track p_T^2 associated to it. If a track is not consistent with having been produced in the primary vertex, it is typically ignored as originating from a pileup interaction. This is the best and most intuitive method of ignoring pileup contributions since the calorimeter cannot extrapolate particle trajectories back to the beamline with nearly as good precision. A visualization of the power of tracking for pileup rejection is shown in Fig. 3.10.

Table 3.2: Features of the subdetectors in the barrel of the Inner Detector: the Pixel detector, the SCT, and the TRT [49].

Subdetector	Channels	Element size [μm]	Resolution [μm]	Layer radii [mm]
Pixels	80×10^6	50×400	10×115	50.5, 88.5, 122.5
SCT	6.3×10^6	80×120000	17×580	299, 371, 443, 514
TRT	350×10^3	4000	$130 \times \emptyset$	554 – 1082

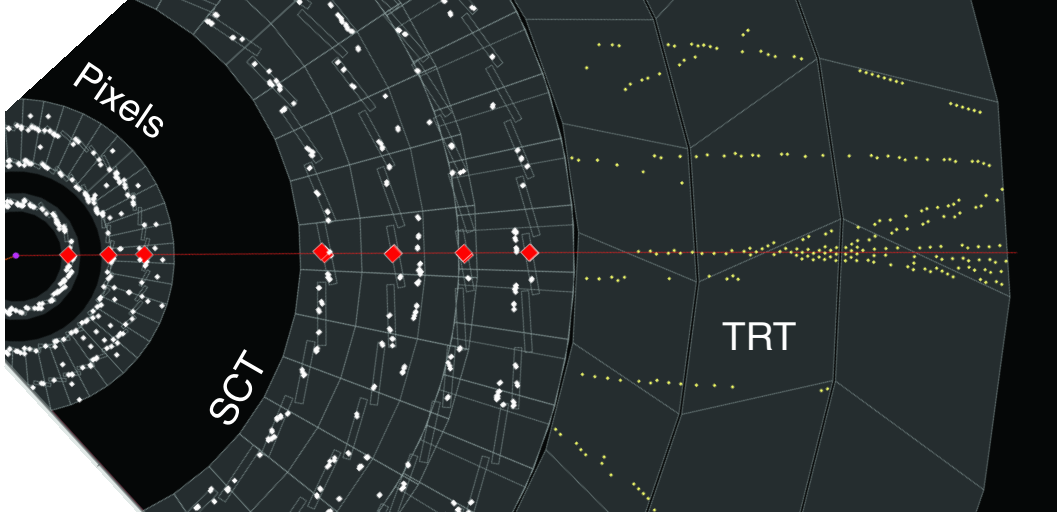


Figure 3.9: Event display of a charged particle traveling, from left to right, through three layers of the Pixels detector, four layers of the SCT, and many layers of the TRT [52]. The particle undergoes a material interaction in the TRT and produces multiple additional particles.

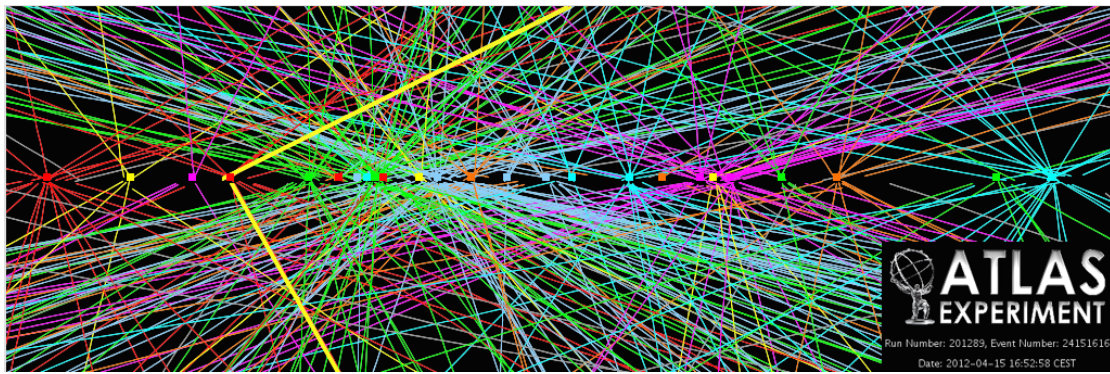


Figure 3.10: Event display of a $Z \rightarrow \mu\mu$ event with 25 reconstructed vertices in 2012 data-taking [54].

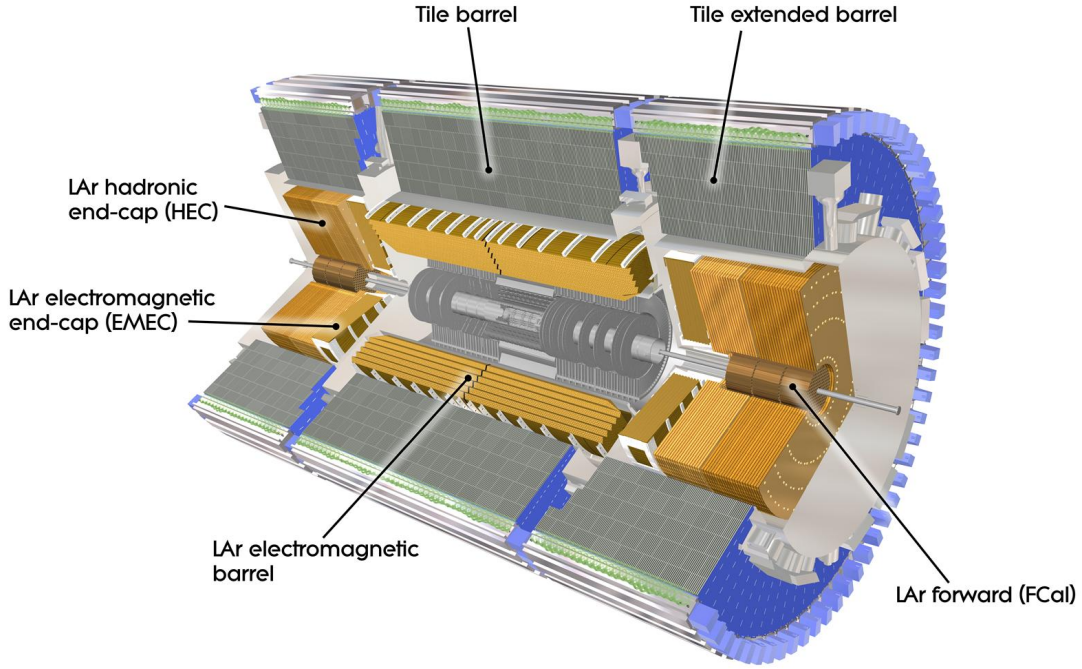


Figure 3.11: A diagram of the ATLAS calorimeters [37].

A track can then be described by five parameters: the transverse impact parameter relative to the primary vertex d_0 , the longitudinal impact parameter z_0 , the azimuthal angle ϕ_0 , the polar angle θ , and the ratio of charge to momentum q/p .

3.2.2 Calorimeters and clustering

The ATLAS calorimeters sit outside the inner detector and the solenoid magnet. They are designed to stop particles like electrons, photons, and pions and to measure their energy. The calorimeters are grouped into electromagnetic (EM) and hadronic calorimeters, where the name describes the class of particle they are designed to stop. Both classes of calorimeters are *sampling* calorimeters, meaning only a fraction of a particle shower energy is observed, and the full shower energy must be inferred. Dense absorber material is used to initiate showers, and interleaved active material is used for detecting the showers.

The calorimeter subdetectors are shown in Fig. 3.11. They are split into barrel and endcap components, have full 2π coverage in ϕ , and have coverage in $|\eta|$ up to 4.9. Information from all subdetectors is used to reconstruct calorimeter clusters.

3.2.2.1 Subdetectors

The EM calorimeters are subdivided into barrel and endcap components, which cover $|\eta| < 1.5$ and $1.4 < |\eta| < 3.2$. An additional presampler exists for $|\eta| < 1.8$ to account for showers starting before the calorimeter. Lead plates are used as the absorber material with liquid argon (LAr) as the active material. An accordion-style geometry is employed for uniform ϕ coverage without azimuthal cracks. The EM calorimeter is radially subdivided into first, second, and third layers away from the beamline. The first and second layers are finely segmented in η for providing detailed descriptions of shower shapes, which are important for particle identification algorithms. The second layer is also the largest layer and usually contains most of the energy of an electromagnetic shower. The third layer measures the leftover energy which is not deposited in the first or second layers.

The hadronic calorimeter is also subdivided into barrel and endcap components. The barrel tile calorimeter uses steel as the absorber material and scintillating tiles as the active material, and it covers the range $|\eta| < 1.7$. The endcap calorimeter uses copper plates as the absorber material and LAr as the active material, and it covers the range $1.5 < |\eta| < 3.2$. The hadronic calorimeters are significantly coarser than the EM calorimeter because electrons and photons typically do not reach the hadronic calorimeters, hence particle identification techniques are less valuable.

Finally, the forward calorimeter (FCal) covers the very forward region $3.1 < |\eta| < 4.9$ and uses LAr as active material. It is typically grouped with the hadronic calorimeters since the identification of electromagnetic objects stops at the boundary of the inner detector ($|\eta| < 2.5$), hence the FCal is most often used in measuring the energy of hadrons.

3.2.2.2 Clustering

EM objects, such as photons and electrons, tend to produce narrow calorimeter showers which are dominantly contained in the EM calorimeters. Hadrons, such as charged pions, tend to produce broader showers and travel through the EM calorimeters and deep into the hadronic calorimeters before stopping. Hadronic showers can also include significant EM deposits from neutral pions which decay to two photons before reaching the calorimeters. A comparison of electron and pion showers is shown in Fig. 3.12. All particles leave a signature of large deposits in adjacent calorimeter cells.

Calorimeter cells from all subdetectors are combined into higher level objects by a three-dimensional topological clustering algorithm [56]. The algorithm uses the iterative 4-2-0 scheme: first, cluster seeds are built from any cell with more than $4\times$ larger deposit than expected from noise. Second, any cell neighboring a seed cell with more than $2\times$ larger deposit than noise is added to the cluster. Last, any cell neighboring the existing cluster with more than $0\times$ larger deposit than noise is added.

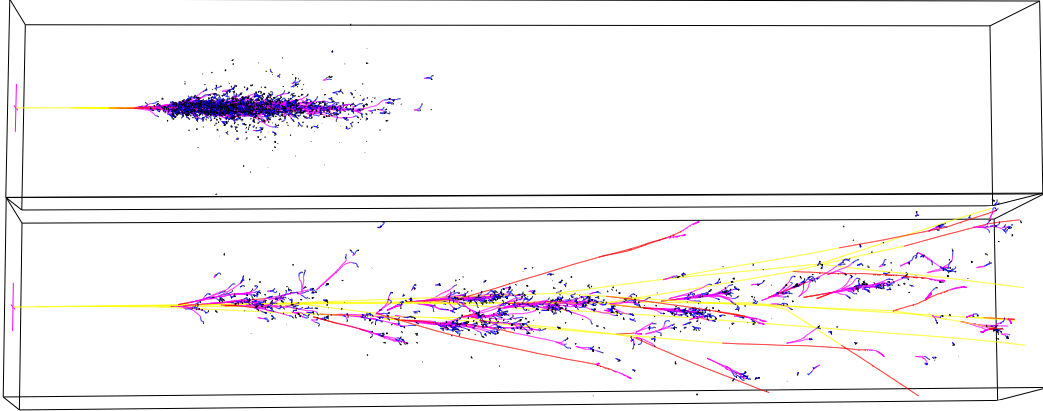


Figure 3.12: Display of simulated electron (top) and charged pion (bottom) showers, where both particles are 50 GeV and pass through iron [55].

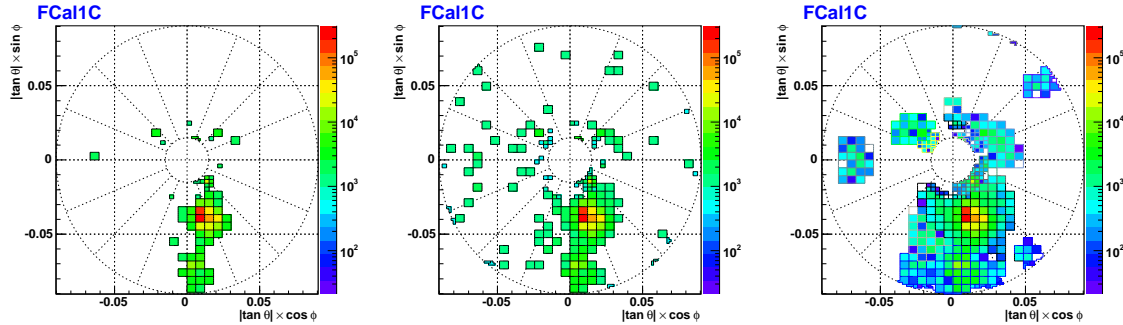


Figure 3.13: Event display of a jet in the forward calorimeter with cell energies greater than $4\sigma_{\text{noise}}$ (left), $2\sigma_{\text{noise}}$ (center), and with the 4-2-0 topological clustering algorithm [57].

Another clustering algorithm, called the *sliding window* algorithm, is used specially for EM objects. The sliding window algorithm uses a small, rectangular tower window to seed clusters in the EM calorimeter since EM objects tend to produce predictably narrow showers.

3.2.3 Muon spectrometry

The muon system (MS), also called the *muon spectrometer*, is designed to measure the trajectory and momentum of muons [58], especially at high p_T . It is furthest from the interaction point, and muons with less than a few GeV of momentum are unable to reach the MS before looping back into the detector due to barrel and endcap toroid magnets, which provide a magnetic field between 2 and 8 Tesla. It detects muons in the same style as the Inner Detector wherein the trajectory of charged

3. THE LHC AND THE ATLAS DETECTOR

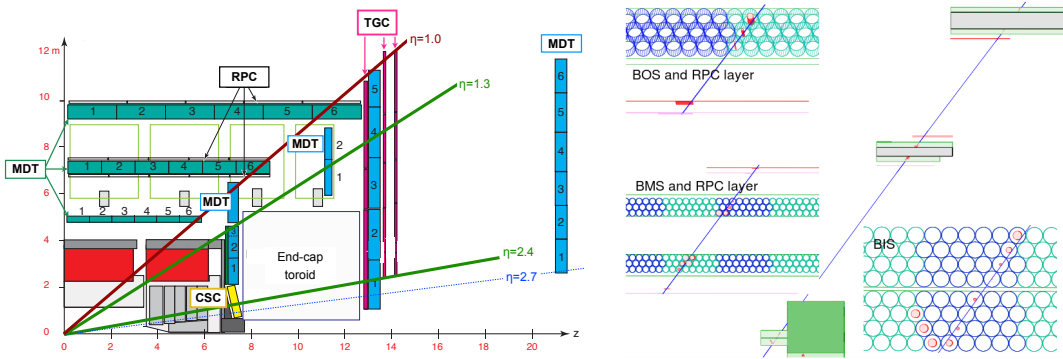


Figure 3.14: A diagram of the ATLAS muon system (left) [59] and a display of a muon candidate passing through three layers of the RPCs and MDTs (right) [54].

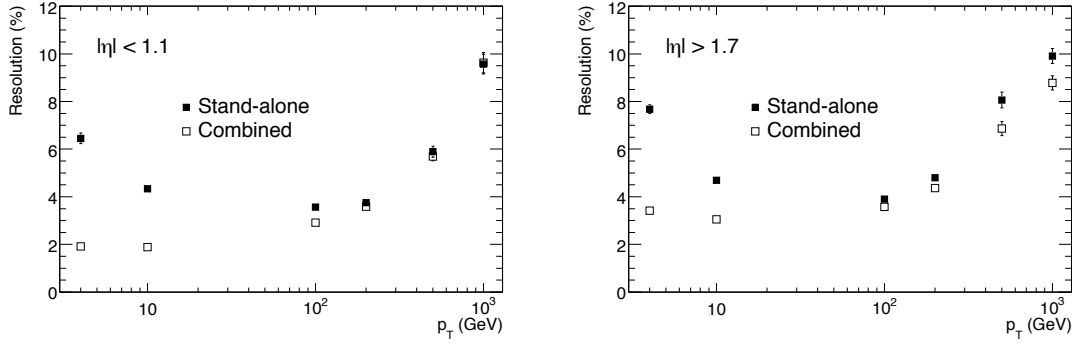


Figure 3.15: Muon momentum resolution for $|\eta| < 1.1$ (left) and $|\eta| > 1.7$ (right) for the stand-alone MS and the combination of the MS and inner detector [37].

particles can be traced through the MS and the momentum can be inferred from the track curvature.

The MS is comprised of four subdetectors: the Monitored Drift Tubes (MDTs), the Cathode Strip Chambers (CSCs), the Resistive Plate Chambers (RPCs), and the Thin Gap Chambers (TGCs), as shown in Fig. 3.14. The MDTs are used for precision measurements of the muon trajectory and momentum, and are used for the full range of the MS, $|\eta| < 2.7$. The CSCs are additionally deployed in the forward region $|\eta| > 2.0$. In the hardware trigger, where fast processing is required, the RPCs are used in the barrel and the TGCs are used in the endcap.

The MS and ID provide independent measurements of muon momenta. These measurements are combined for an overall measurement of muon momentum to exploit the advantages of each subdetector. The MS measurement dominates the combination at muon p_T in the hundreds of GeV and above, as shown in Fig. 3.15.

3.3 Particle identification

One of the major tasks in particle physics is the transformation of low-level detector outputs to high-level physics objects. At ATLAS, this is typically done in two steps referred to as *reconstruction*. First, detector outputs like inner detector hits and calorimeter cells are converted to tracks and clusters, respectively, as discussed previously. Second, combinations of tracks and clusters are converted into physics objects.

In addition to reconstruction, physics objects often require identification and calibration. Identification refers to the determination of which particle is responsible for a given detector signal, e.g., is a deposit in the calorimeter more likely to be from an electron or a charged pion. Calibration refers to the porting of a measured energy in the detector to the energy of a physics object. Calibration accounts for effects like pileup and dead material in the subdetectors.

These physics objects are often meant to exactly represent an individual particle, such as a muon. Otherwise, the physics objects represent a collection of particles which are naturally grouped together. For example, a *jet* represents the group of hadrons produced when a quark or gluon propagates through ATLAS.

3.3.1 Muons

Muons are among the simplest physics objects to reconstruct since a large fraction of ATLAS is built specifically for this purpose. They are minimum ionizing particles and do not deposit significant energy in the calorimeters, hence they are the only particles expected to regularly reach and interact with the MS.

Muons are reconstructed by matching tracks in the MS to tracks in the ID [60], where track quality criteria are required in both subdetectors. This is $\approx 99\%$ efficient for an inclusive collection of muons from $Z \rightarrow \mu\mu$, and it is limited by lack of coverage of the MS at $|\eta| < 0.1$ and $1.1 < \eta < 1.3$. The performance of the muon calibration is shown in Fig. 3.16

Muons are most often used in ATLAS as the decay products of electroweak bosons like the W and Z . They are also produced in the decays of some hadrons, but muons from these processes can be rejected by requiring that the muon be isolated in the detector, both in the inner detector and in the calorimeters. Since the purity of muon reconstruction is already high, additional muon identification techniques are not explored.

3. THE LHC AND THE ATLAS DETECTOR

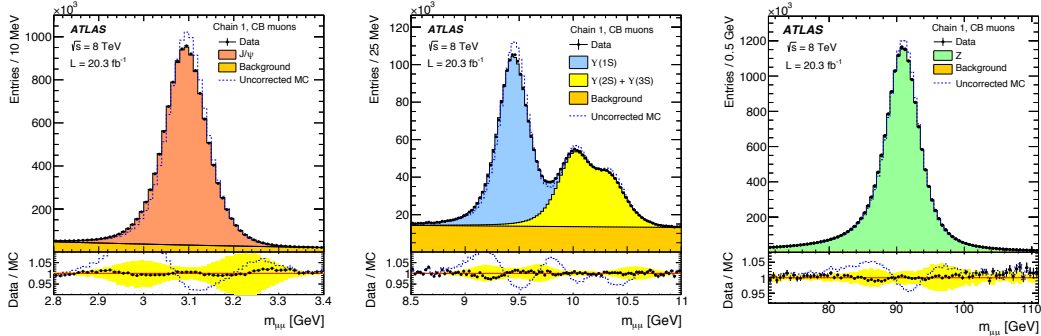


Figure 3.16: Validation of the muon energy scale corrections in J/Ψ events (left), Υ events (center), and Z events (right) [60].

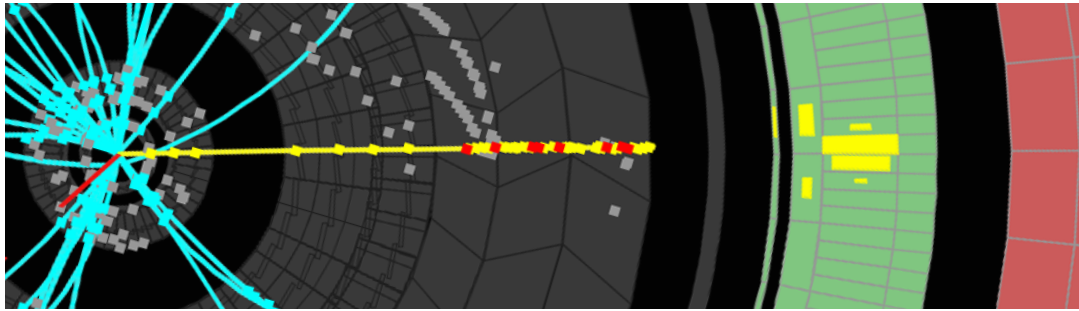


Figure 3.17: Display of an electron traversing the ID, leaving hits in the TRT consistent with transition radiation, and depositing a narrow cluster entirely contained in the EM calorimeter [54].

3.3.2 Electrons and photons

Electrons are reconstructed by matching sliding window calorimeter clusters to ID tracks [61]. This offers no rejection against other charged particles, however, so identification algorithms are built which exploit discriminating features of electrons. Relative to backgrounds, electrons are more likely to leave longitudinally narrow calorimeter deposits in the EM calorimeter, deposit very little energy in the hadronic calorimeter, and be isolated in the ID and the EM calorimeter. Electrons are also more likely to have transition radiation in the TRT. These properties are shown in Fig. 3.17 and allow for huge rejection of backgrounds, as shown in Fig. 3.18.

Photons have similar detector signatures as electrons since their calorimeter deposits are also longitudinally narrow and expected to be contained within the EM calorimeter [62]. Identification algorithm are split into two categories: isolated photons which leave no hits in the ID, and photons which convert into pairs of electrons before reaching the calorimeter.

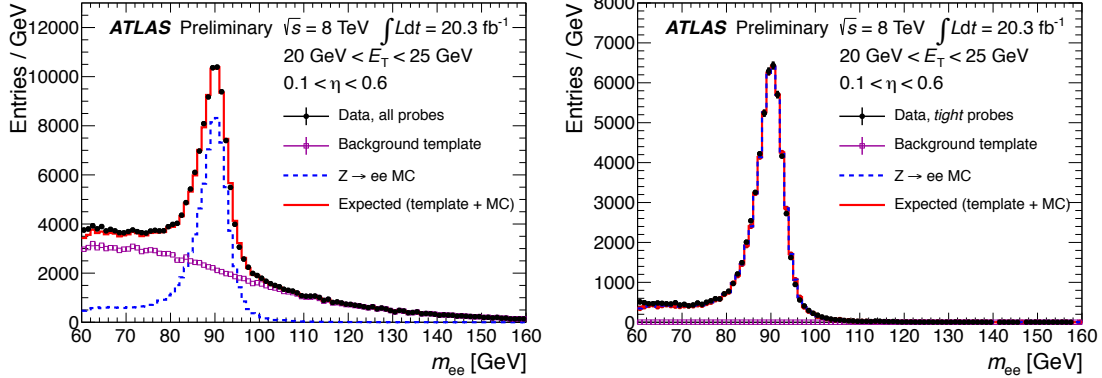


Figure 3.18: Data and predictions of m_{ee} before the electron identification algorithm is applied (left) and after (right) [61].

3.3.3 Hadrons

Instead of attempting to reconstruct individual hadrons, ATLAS reconstructs collimated sprays of hadrons referred to as jets [63]. Jet momenta range from ≈ 10 GeV to multiple TeV, and spatially they are the largest physics objects, though they can be as small as a single pion. Jets are produced copiously at hadron colliders, which can be problematic with significant pileup.

Jets are reconstructed from calorimeter topological clusters using the anti- k_t algorithm [64] with a distance parameter of $R = 0.4$. This is an iterative clustering algorithm which groups topological clusters into jets based on their spatial proximity and momentum. Tracks can be associated to a jet based on simple spatial matching or the more robust ghost association [65]. A slew of corrections are applied to calibrate the energy and position of jets [63, 65]. These correct for effects like pileup, dead material, and the non-compensating nature of the calorimeters. Jets can additionally be classified as hard-scatter or pileup jets based on the fraction of their track momenta consistent with originating from the primary vertex [66].

Jets which arise from the fragmentation of b -quarks, referred to as b -jets, are given special treatment because the significant lifetime of B -hadrons means these jets can be distinguished from jets arising from lighter sources like gluons or u -quarks [67]. Multivariate algorithms are used to look for the signature of a second vertex with some spatial displacement from the primary vertex. An example of a displaced vertex, and the performance of these algorithms, are shown in Fig. 3.19.

Jets which arise from the hadronic decay of tau leptons are also treated specially because their signature in the detector can be distinguished from generic QCD jets. They are characteristically produced with 1 or 3 tracks and are relatively narrow objects in the ID and calorimeters [1]. They

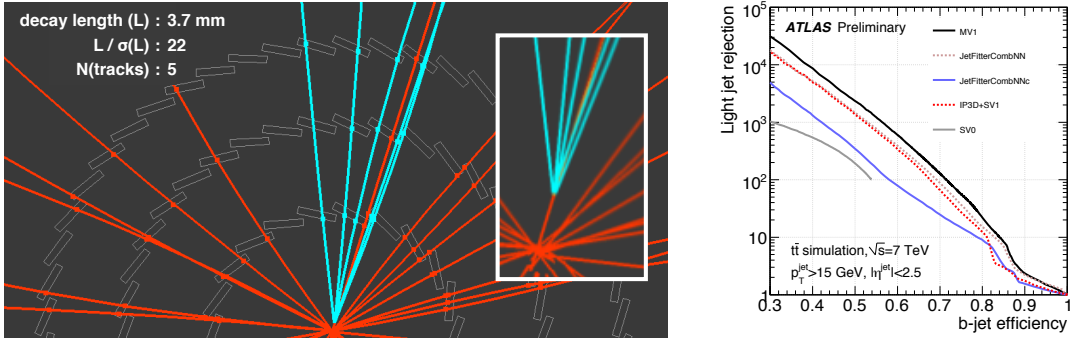


Figure 3.19: Event display of a displaced vertex consistent with the decay of a B -hadron (left) [68] and efficiency of b -jet identification algorithms measured in simulation as a function of light jet rejection (right) [69].

are discussed in greater detail in Section 4.3.

3.3.4 Neutrinos

Neutrinos do not interact with the ATLAS detector and escape undetected. But their presence can be inferred from momentum imbalance since each pp collision should conserve momentum. To measure the momentum imbalance, the negative total vector sum of momenta per collision is calculated, and the transverse projection the sum is interpreted to be the total transverse momentum of the neutrinos in the event. This is referred to as the missing transverse energy, E_T^{miss} .

The calculation of the total momenta in the event is done in two steps. First, the calibrated physics objects in the event, like jets and electrons, are collected and their vector sum is calculated. This is referred to as the *hard term* of the E_T^{miss} calculation. Second, tracks and calorimeter information unassociated to hard objects are combined and form the *soft term* of the E_T^{miss} calculation. The vector sum of the hard and soft terms is the total momentum imbalance of the event [70].

The soft term calculation is challenging because associating calorimeter information to a specific vertex is difficult in the presence of pileup. Hence multiple methods exist for calculating the soft term. A comparison of the E_T^{miss} resolution is shown in Fig. 3.20 as a function of the pileup of the event. Of the options available in 2014, the *STVF* method [71] has the best resolution. The STVF soft term is first calculated with calorimeter topoclusters, and the magnitude of the sum is then weighted down by the fraction of unassociated track momenta arising from the PV to the total unassociated track momenta of the event. This heavily suppresses the calorimeter-based soft term, which has a strong dependence on pileup.

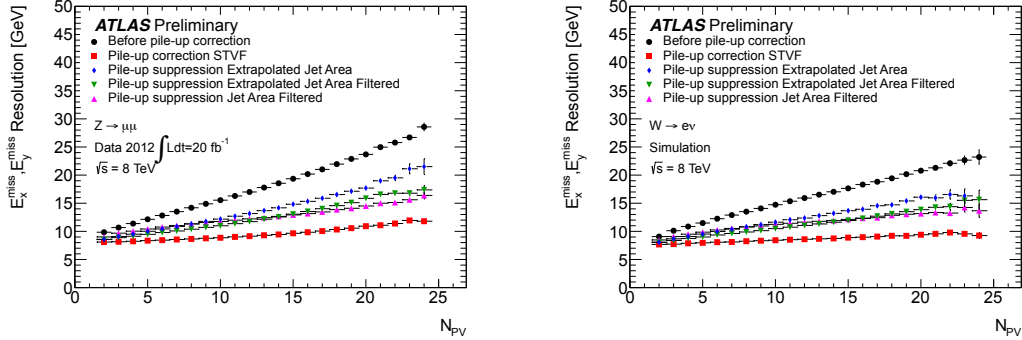


Figure 3.20: Resolution of various E_T^{miss} reconstruction algorithms as a function of the number of reconstructed primary vertices in $Z \rightarrow \mu\mu$ events in data (left) and $W \rightarrow e\nu$ events in simulation (right) [71].

3.4 Triggering

One of the most challenging aspects of physics at hadron colliders is that the vast majority of pp collisions produce low p_T QCD dijets, and these events are mostly uninteresting in searches for new physics. Additionally, ATLAS does not have the computing resources to reconstruct and save 20 MHz of pp collisions. A huge reduction of data is necessary immediately after the collisions occur. This reduction must be careful not to remove events with interesting signatures.

The scheme of fast reduction is called *triggering*. Reconstruction and decision-making in the trigger is referred to as occurring *online*, whereas the nominal ATLAS reconstruction occurs *offline*. The trigger is split into two stages. First, all pp collisions are sent to a hardware trigger with much coarser granularity than offline. Events passing the hardware trigger are then sent to software triggers with granularity comparable to offline. The hardware trigger is called *Level 1* (L1), and the software triggers are called the *High Level Trigger* (HLT). The HLT step is additional split into two stages, *Level 2* (L2) and *Event Filter* (EF). The reduction and latency targets are shown in Table 3.3.

Table 3.3: Approximate average trigger rates and latencies during 2012 data-taking [37, 59, 72].

system	input rate	output rate	reduction	latency
L1	20 MHz	70 kHz	300×	2.5 μs
HLT, L2	70 kHz	5 kHz	15×	75 ms
HLT, EF	5 kHz	700 Hz	7×	1 s

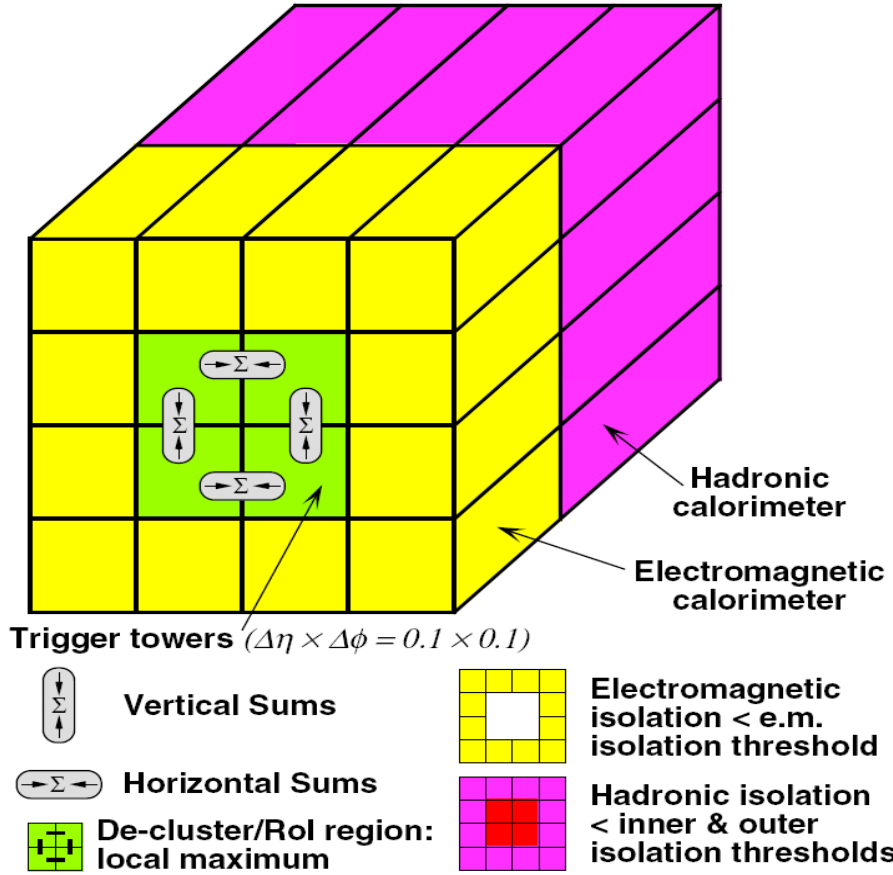


Figure 3.21: Schematic view of the calorimeter granularity available at the L1 trigger [73].

3.4.1 L1

The L1 trigger is the fastest and most reductive step of the trigger system. Only information from the calorimeter and muon subdetectors are available because the inner detector is not equipped to process events at tens of MHz, and because tracking algorithms are currently too slow. Performance is sacrificed for speed in the EM calorimeter and muon system: the granularity of the EM calorimeter is reduced for faster processing, as shown in Fig. 3.21, and only information from the RPCs and TGCs is read out from the muon system.

A consequence of the reduced granularity of the EM calorimeter is that the sophisticated offline identification algorithms cannot be used. For example, the only identification technique available for τ_{had} at L1 is calorimeter isolation. Furthermore, the isolation can only be evaluated in a square annulus with the reduced granularity and cannot be p_T^{L1} -dependent.

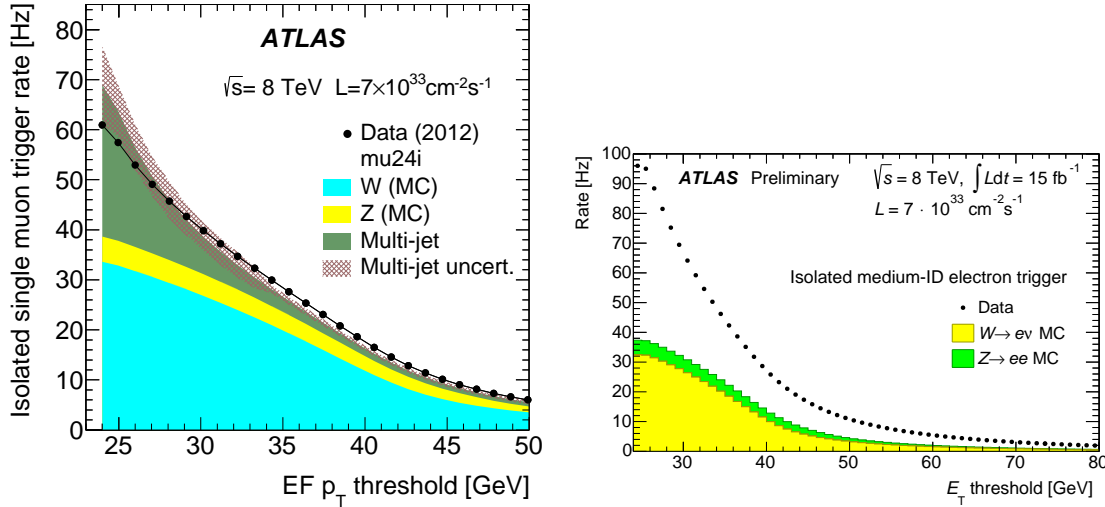


Figure 3.22: Trigger rate and predicted composition of the lowest unprescaled single muon trigger (left) [59] and single electron trigger (right) [74] in 2012 data-taking.

In Run-I, much of the L1 bandwidth is allocated to the inclusive single muon and single electron triggers. These are among the most used triggers in ATLAS physics and performance analyses because of their inclusiveness and because light leptons are characteristic of electroweak physics.

3.4.2 HLT

The HLT latency is much less restrictive than at L1. By the end of the HLT, tracking and topological clustering algorithms are run over a full scan and with the nominal granularity of the detector. Reconstruction, identification, and calibration algorithms closely resemble their offline counterparts, with adaptations to online made as necessary.

Like L1, much of the HLT bandwidth is allocated to the inclusive single muon and single electron triggers. The rate and predicted composition of these HLT triggers are shown in Fig. 3.22. Electrons and muons from W/Z decays are irreducible contributions to the HLT rate and are among the limiting factors.

3.5 Summary

The ATLAS physics program in Run-I of the LHC is a great success of detector operation, performance, and large-scale data analysis. ATLAS has measured cross-sections of processes ranging more than ten orders of magnitude, as shown in Fig. 3.23, including multiple production modes of the

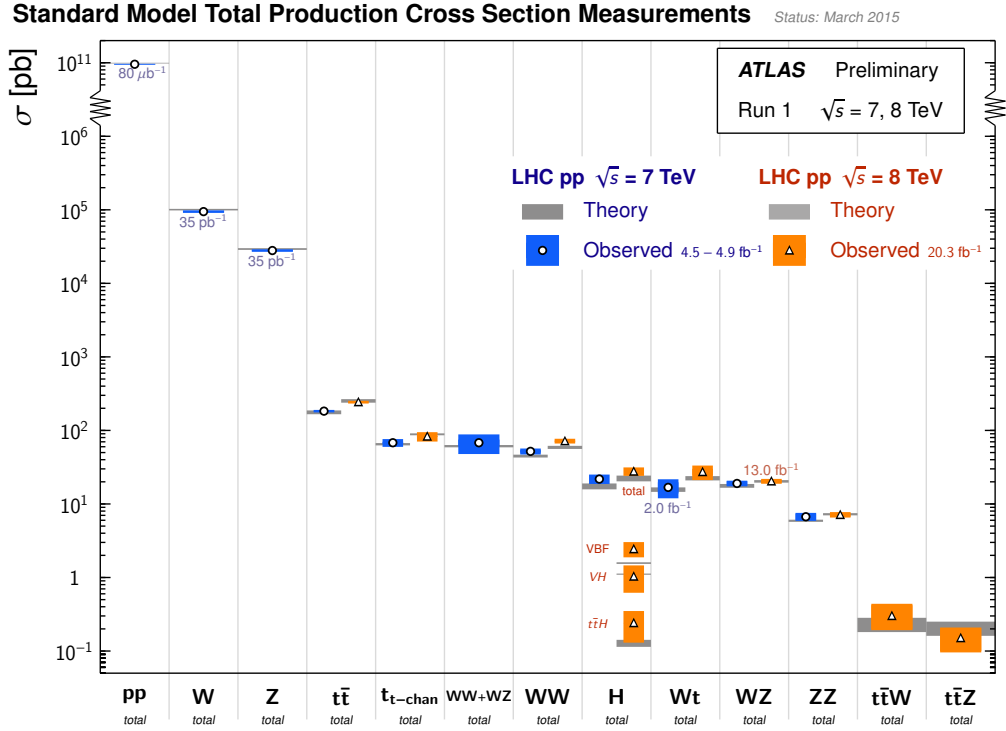


Figure 3.23: Summary of cross sections measured at ATLAS in 7 and 8 TeV data-taking [76].

recently discovered Higgs boson. As of early 2015, the ATLAS collaboration has authored more than 350 peer-reviewed publications [75].

CHAPTER 4

Tau leptons

Tau leptons and their signature in the ATLAS detector are described. This draws from extensive ATLAS documentation on the topic [77, 78, 79], especially the recent publication summarizing the Run-I performance [1]. These are the featured particles of this thesis.

4.1 Tau leptons

Tau leptons were discovered in 1975 by Martin Perl and the SLAC-LBL group at the SPEAR electron-positron collider [80, 81, 82]. They have since been studied in great detail at experiments like Belle [83] and BaBar [84]. The associated tau neutrino was first observed directly at the DONUT experiment in 2000 [85], though its existence was inferred by measurements of the width of the Z boson by experiments at the LEP collider in 1990 [86].

Tau leptons are the heaviest of the charged leptons. Their mass of 1.78 GeV is approximately twenty times larger than the muon mass [87], and their short lifetime $c\tau = 87 \mu\text{m}$ implies tau leptons produced in pp collisions at the LHC typically decay within the ATLAS beam pipe. The ATLAS detector therefore observes only the decay products of the tau lepton, not the particle itself.

Tau leptons decay leptonically ($\tau \rightarrow \ell\nu_\ell\nu_\tau$, $\ell = e, \mu$) in 35% of decays and hadronically ($\tau \rightarrow \text{hadron(s)} \nu_\tau$) in 65%. Among hadronic decays, 72% involve exactly one charged pion and 22% exactly three charged pions. The remaining percentage of hadronic decays dominantly involves kaons or five (or more) charged pions. All tau lepton decays involve at least one neutrino. A pie chart of tau lepton branching fraction is given in Fig. 4.1.

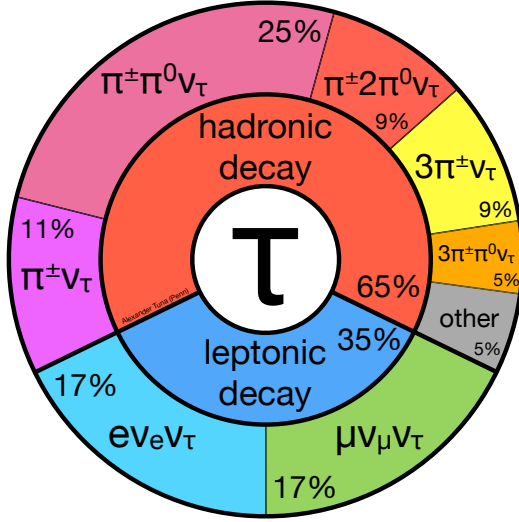


Figure 4.1: Pie chart of tau lepton decay branching fractions, grouped by hadronic decays (65%) and leptonic decays (35%).

4.2 Leptonic tau decays, τ_ℓ

At ATLAS, light leptons from tau lepton decays ($\tau \rightarrow \ell \nu_\ell \nu_\tau$, $\ell = e, \mu$) are largely indistinguishable from prompt leptons from W and Z decays. They are typically less energetic due to the presence of two additional neutrinos in the tau lepton decay (e.g., $W \rightarrow \ell \nu_\ell$ versus $W \rightarrow \tau \nu_\tau \rightarrow \ell \nu_\ell \nu_\tau \nu_\tau$), but for identification purposes, the only distinguishing features arise from the displaced tau vertex. This displacement is often quantified by the transverse distance of closest approach of the light lepton to the primary vertex (d_0). But given the short lifetime of tau leptons, the discrimination power is weak. These properties are shown in Fig. 4.2.

4.3 Hadronic tau decays, τ_{had}

This section follows the recent ATLAS publication describing τ_{had} performance in Run-I [1].

4.3.1 Reconstruction

τ_{had} reconstruction begins with the collection of jets formed by the anti- k_t algorithm with distance parameter $R = 0.4$, as discussed in Section 3.3.3, which groups the set of reconstructed three-dimensional calorimeter topoclusters into jet objects. The topoclusters are calibrated using a local hadronic calibration (LC) [88]. Jets are required to have $p_T > 10$ GeV and $|\eta| < 2.5$ to qualify as a seed for a

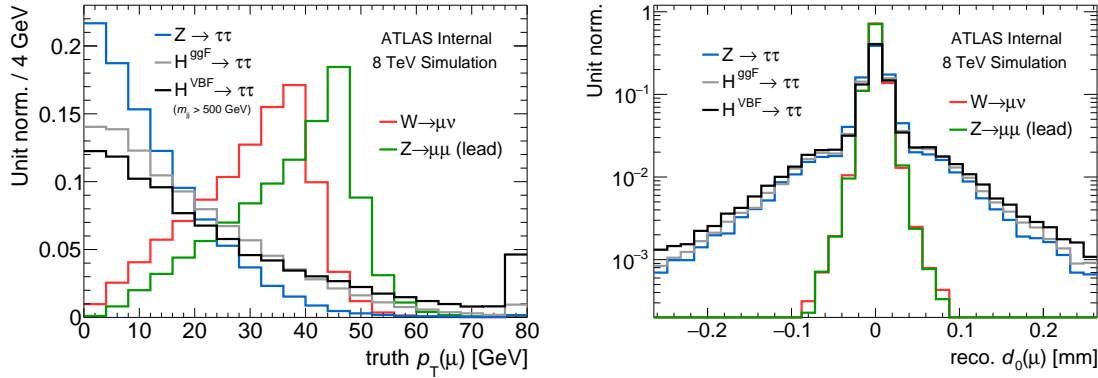


Figure 4.2: True p_T and reconstructed d_0 for muons from simulated W , Z , and tau lepton decays. Muons from tau lepton decays are shown for $Z \rightarrow \tau\tau$, $H^{ggF} \rightarrow \tau\tau$, and $H^{VBF} \rightarrow \tau\tau$ processes.

τ_{had} candidate. The initial τ_{had} four-momentum is calculated by summing the TopoClusters within $\Delta R < 0.2$ of the barycenter of the jet seed, where the τ_{had} mass is assumed to be zero.

Tracking and vertexing for τ_{had} occurs in three steps. First, all tracks are collected within $\Delta R < 0.2$ of the jet seed which pass quality criteria described later, but for which no impact parameter requirements are made. Second, a reconstructed vertex is chosen to estimate from which pp collision the τ_{had} originates, called the tau vertex (TV). It is defined as the vertex which maximizes the fraction of track momenta originating from that vertex versus total track momenta, referred to as the tau vertex fraction:

$$\text{TVF(vertex)} = \frac{\sum p_T^{\tau_{\text{had}}} \text{ tracks associated to vertex}}{\sum p_T^{\tau_{\text{had}}} \text{ tracks}} \quad (4.1)$$

This vertex association is called the Tau Jet Vertex Association (TJVA) algorithm, and it helps ensure robustness against harsh pileup conditions, as shown in Fig. 4.3.

Last, the set of tracks is reduced by making additional impact parameters requirements with respect to the TV. The full set of track selection criteria are:

- $p_T > 1$ GeV,
- at least two hits in the pixel subdetector,
- at least seven hits in the pixel and SCT subdetectors combined,
- $|d_{0,\text{TV}}| < 1.0$ mm,
- $|z_{0,\text{TV}} \sin \theta| < 1.5$ mm

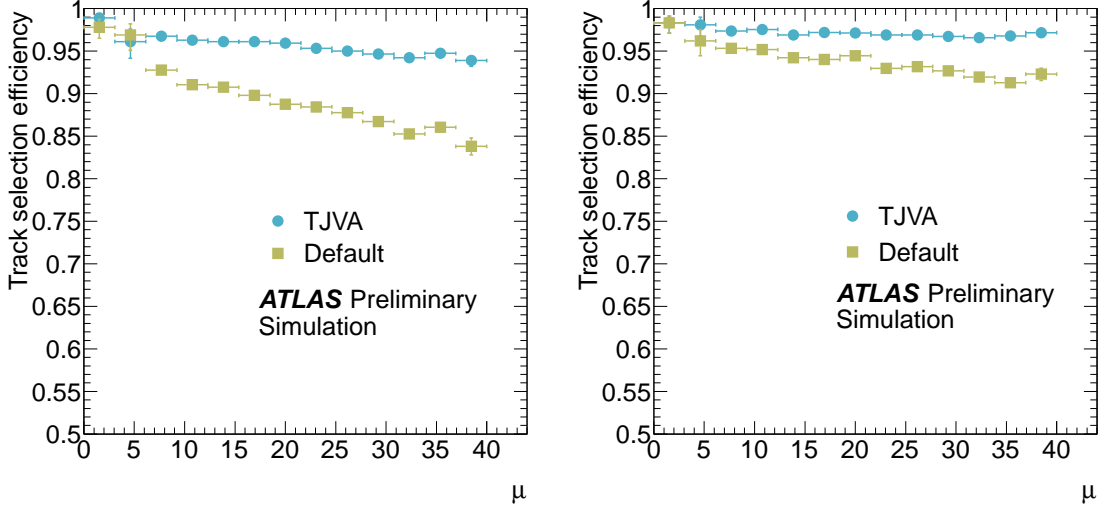


Figure 4.3: Track selection efficiency for τ_{had} candidates with the default vertex selection (highest Σp_T^2) versus the dedicated TJVA algorithm, for true 1-track (left) and 3-track (right) τ_{had} , as a function of $\langle \mu \rangle$ [77].

This set of tracks is used when classifying the τ_{had} candidate track multiplicity. For identification purposes, tracks in the *isolation region* $0.2 < \Delta R < 0.4$ are also required to pass these criteria.

A correction to the τ_{had} energy is applied to account for biases, such as effects from pileup, the underlying event, and clusters falling out of the $\Delta R = 0.2$ cone. This correction is derived in simulated $Z \rightarrow \tau\tau$, $W \rightarrow \tau\nu$, and $Z' \rightarrow \tau\tau$ events where the true visible τ_{had} energy $E_{\text{vis.}}^{\text{true}}$ is known. It is derived as a function of the pre-calibrated τ_{had} energy $E_{\text{LC}}^{\tau_{\text{had}}}$ and η and shown in Fig. 4.4. Small additional corrections are applied to account for biases from pileup and poorly instrumented regions of the detector. The resulting τ_{had} energy resolution is shown in Fig. 4.5.

Data-driven corrections for and uncertainties on the τ_{had} energy calibration are derived in two ways: the *deconvolution* method and the *in-situ* method. The deconvolution method relies on the τ_{had} having a known composition of charged and neutral hadrons such that the response can be decomposed into individual sources. For charged hadrons, the response is estimated from test beam measurements and simulation with varied hadronic shower models. For electromagnetic showers from neutral pion decays, the response is estimated from $Z \rightarrow ee$.

The in-situ method relies on the sensitivity of the visible $m_{\tau\tau}$ in $Z \rightarrow \tau_\ell \tau_{\text{had}}$ events to the τ_{had} energy. Relative to τ_{had} , the lepton energy is precisely calibrated and validated in data with $Z \rightarrow \ell\ell$ events. These events are selected in data by requiring exactly one isolated muon, exactly one identified τ_{had} , and some additional kinematic cuts to suppress non- $Z \rightarrow \tau_\ell \tau_{\text{had}}$ events. The τ_{had} energy is then

4. TAU LEPTONS

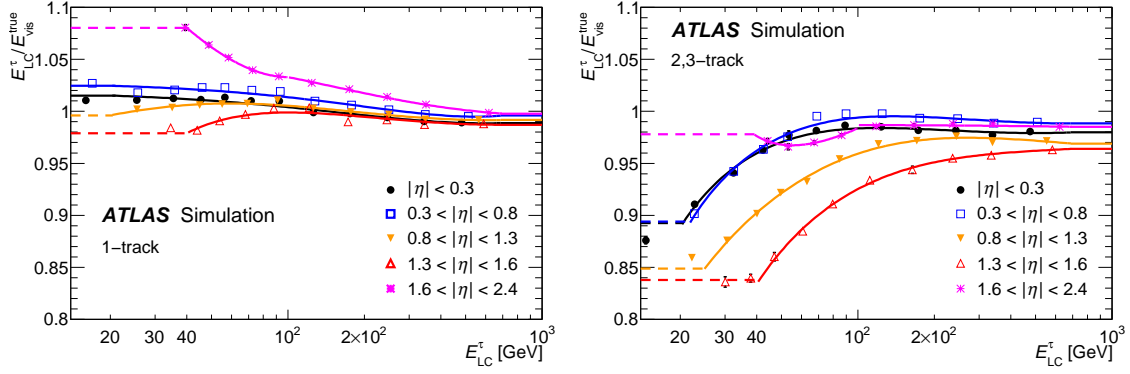


Figure 4.4: τ_{had} energy response curves measured in simulation, for 1-track (left) and 2,3-track (right) τ_{had} , as a function of the reconstructed energy [1].

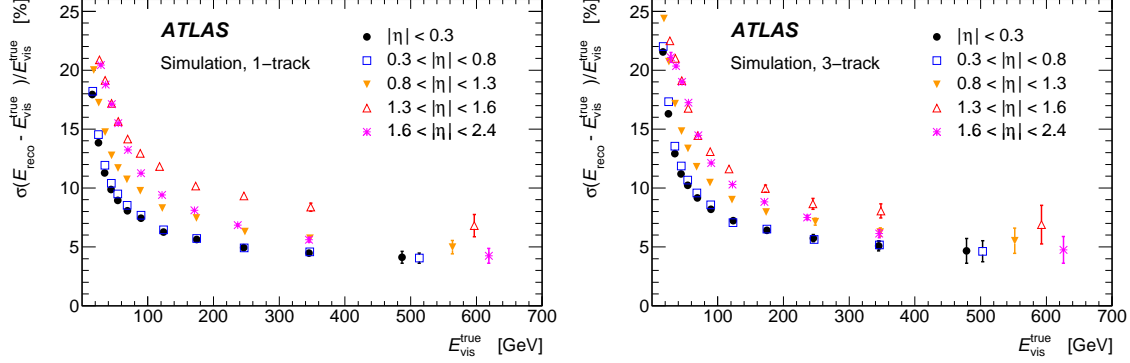


Figure 4.5: τ_{had} energy resolution measured, for 1-track (left) and 2,3-track (right) τ_{had} , as a function of the true visible energy [1].

allowed to float like $(1 + \alpha)E_T$, and the effect is propagated to the visible $m_{\tau\tau}$ spectrum. The data is then adjusted by the parameter α to match the simulated prediction, which has already been corrected to $E_{\text{vis}}^{\text{true}}$. The measured α , called the *TES shift*, is:

$$\begin{aligned} \alpha_{1\text{-track}} &= 0.8\% \pm 1.3\% \text{ (stat.)} \pm 0.6\% \text{ (syst.)} \\ \alpha_{3\text{-track}} &= 1.1\% \pm 1.4\% \text{ (stat.)} \pm 0.7\% \text{ (syst.)} \end{aligned} \quad (4.2)$$

4.3.2 Identification

The overwhelming majority of particles observed at ATLAS are hadrons. Distinguishing QCD jets from τ_{had} is therefore hugely important for physics with tau leptons. The properties with discriminating power can be broadly grouped into three categories:

Track multiplicity:

τ_{had} tend to have 1 or 3 reconstructed tracks, where no such specificity is expected for jets.

Narrowness:

τ_{had} tend to be more narrow in the tracker and calorimeter since tau leptons from electroweak decays are boosted, and τ_{had} do not undergo the same broadening fragmentation as quarks and gluons from QCD processes.

Displaced vertex:

Tracks from τ_{had} tend to be more displaced from the primary vertex than tracks in jets due to the finite tau lepton lifetime.

The track multiplicity and narrowness features are shown qualitatively in Fig. 4.6.

For track multiplicity, reconstructed τ_{had} are required to have exactly 1 or 3 associated tracks. This is effective at rejecting QCD jets which have a broader track multiplicity spectrum. This requirement has significant efficiency loss (20-40%) due to photon conversions from neutral pion decays and pileup, among other effects. The track multiplicity spectrum for τ_{had} and jets is shown in Fig. 4.7 in a $Z \rightarrow \tau_\mu \tau_{\text{had}}$ -rich selection of data.

For narrowness and vertex displacement, discriminating variables are formed using tracking and calorimeter information and combined in multi-variate identification algorithms. These algorithms are typically referred to as τ_{had} identification or jet discriminators. A complete description of the variables used is given in Table 4.1 and Appendix B.

An additional identification algorithm is used to decompose the tau lepton decay into charged and neutral pions. The algorithm is sequential: first, it uses global τ_{had} features measured in the tracker and calorimeter to reconstruct the number of neutral pions associated to the τ_{had} . Second, it creates neutral pion candidates from the most π^0 -like clusters associated to the τ_{had} . These candidates, along with the charged pions measured as associated tracks, make up the decomposed τ_{had} and feed into the jet discriminant. This reconstruction is substantially more difficult than for charged pions which enjoy precision measurements in the tracker with marginal contamination from pileup, the underlying event, and other processes.

Central energy fraction (f_{cent}):

Fraction of transverse energy deposited in the region $\Delta R < 0.1$ out of all energy deposited in the region $\Delta R < 0.2$ around the τ_{had} candidate calculated by summing the energy deposited in all cells belonging to TopoClusters with a barycenter in this region, calibrated at the EM energy

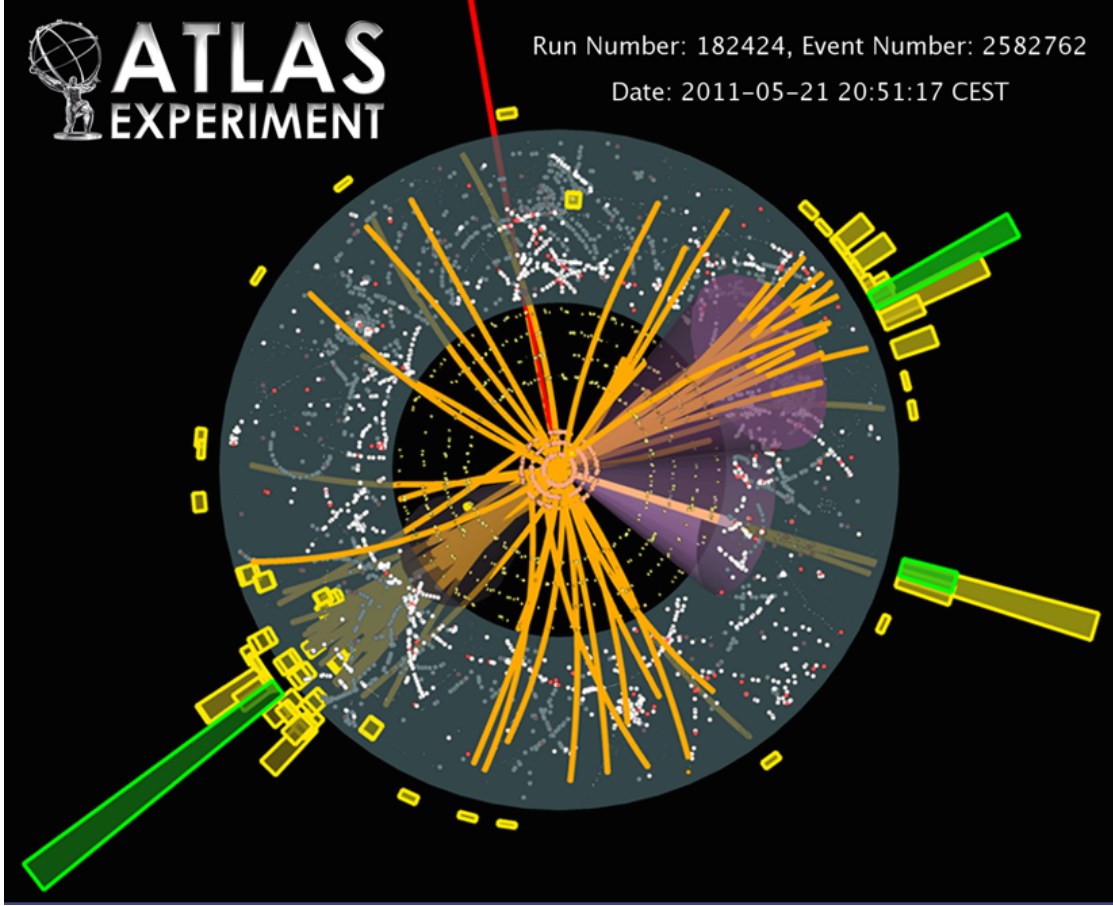


Figure 4.6: Event display of a $t\bar{t} \rightarrow (b\mu\nu_\mu)(b\tau_{\text{had}}\nu_\tau)$ candidate during 2011 data-taking [54]. The τ_{had} candidate has 3 tracks, the b -jet candidates each have more than 10 tracks, and the muon is in red. The estimated purity of the selection is greater than 75%.

scale. Biases due to pile-up contributions are removed using a correction based on the number of reconstructed primary vertices in the event.

Leading track momentum fraction (f_{track}):

The transverse momentum of the highest- p_T charged particle in the core region of the τ_{had} candidate, divided by the transverse energy sum, calibrated at the EM energy scale, deposited in all cells belonging to TopoClusters in the core region. A correction depending on the number of reconstructed primary vertices in the event is applied to this fraction, making the resulting variable pile-up independent.

Track radius (R_{track}):

p_T -weighted distance of the associated tracks to the τ_{had} direction, using all tracks in the core

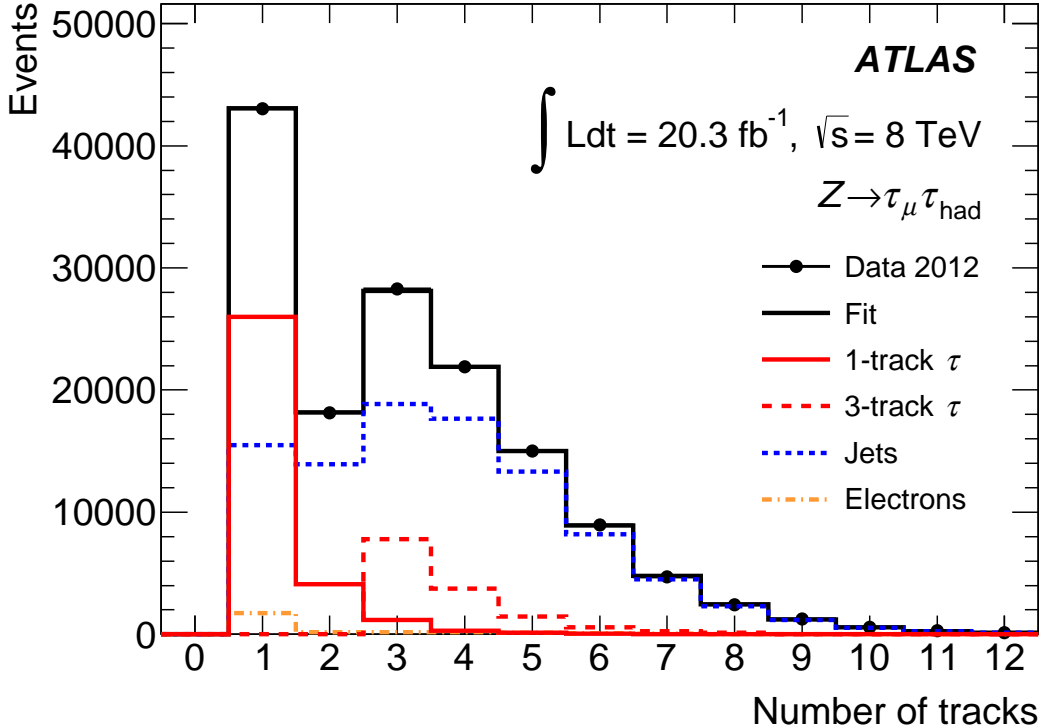


Figure 4.7: Fit of the predicted τ_{had} track multiplicity to data in a $Z \rightarrow \tau_\mu \tau_{\text{had}}$ event selection before applying tau identification algorithms [1]. The τ_{had} candidates have much lower track multiplicity relative to the large jet background.

and isolation regions.

Leading track IP significance ($S_{\text{lead track}}$):

Transverse impact parameter of the highest- p_T track in the core region, divided by its estimated uncertainty.

Number of tracks in the isolation region ($N_{\text{track}}^{\text{iso}}$):

Number of tracks associated to the τ_{had} in the region $0.2 < \Delta R < 0.4$.

Maximum ΔR (ΔR_{max}):

The maximum ΔR between a track associated to the τ_{had} candidate and the τ_{had} direction. Only tracks in the core region are considered.

Transverse flight path significance (S_T^{flight}):

The decay length of the secondary vertex (vertex reconstructed with the tracks associated to the

4. TAU LEPTONS

core region of the τ_{had} candidate) in the transverse plane, divided by its estimated uncertainty. It is defined only for multi-track τ_{had} candidates.

Track mass (m_{tracks}):

Invariant mass of the four-vector sum of the charged particle momenta in the core and isolation regions.

Track-plus- π^0 -system mass ($m_{\pi^0+\text{track}}$):

Invariant mass of the system composed of the tracks and π^0 mesons in the core region.

Number of π^0 mesons reconstructed in the core region (N_{π^0}):

Ratio of track-plus- π^0 -system p_{T} to total τ_{had} p_{T} ($p_{\text{T}}^{\pi^0+\text{track}}/p_{\text{T}}$):

Ratio of estimated p_{T} using track + π^0 information to the calorimeter-only measurement.

The performance of the jet discrimination algorithms is measured in data and simulation in a $Z \rightarrow \tau_{\ell}\tau_{\text{had}}$ selection. A tag-and-probe method is used, where the muon from a tau lepton decay is tagged and a τ_{had} is probed which satisfies topological selections consistent with the $Z \rightarrow \tau_{\ell}\tau_{\text{had}}$ process.

To measure the efficiency, templates are built for signal τ_{had} and background processes of the track multiplicity and fit to data. Correction factors are derived to correct potential mis-modeling in the simulation and shown in Fig. 4.11. No significant mis-modeling is observed.

Table 4.1: Discriminating variables used in the τ_{had} identification algorithms [1].

Variable	Offline		Trigger	
	1-track	3-track	1-track	3-track
f_{cent}	•	•	•	•
f_{track}	•	•	•	•
R_{track}	•	•	•	•
$S_{\text{lead track}}$	•		•	
$N_{\text{track}}^{\text{iso}}$	•		•	
ΔR_{max}		•		•
$S_{\text{T}}^{\text{flight}}$		•		•
m_{tracks}		•		•
$m_{\pi^0+\text{track}}$	•	•		
N_{π^0}	•	•		
$p_{\text{T}}^{\pi^0+\text{track}}/p_{\text{T}}$	•	•		

4. TAU LEPTONS

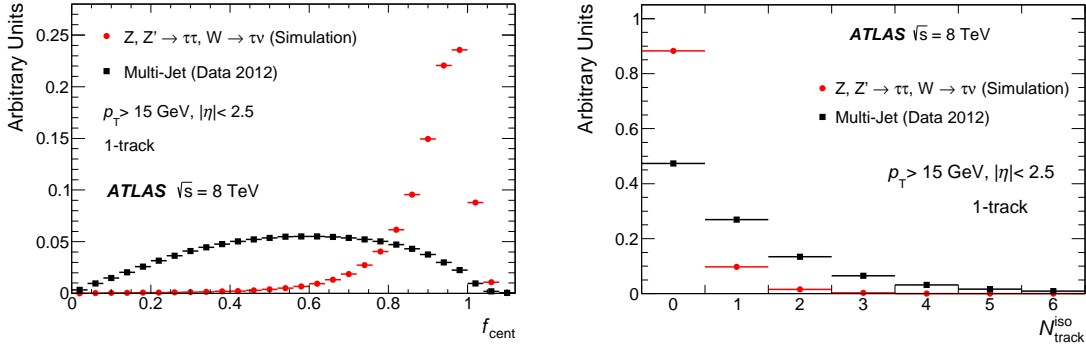


Figure 4.8: Signal and background distributions for two of the discriminating variables in the 1-track τ_{had} jet discrimination algorithm: f_{cent} (left) and $N_{\text{track}}^{\text{iso}}$ (right) [1]. The remaining distributions are shown in Appendix B.

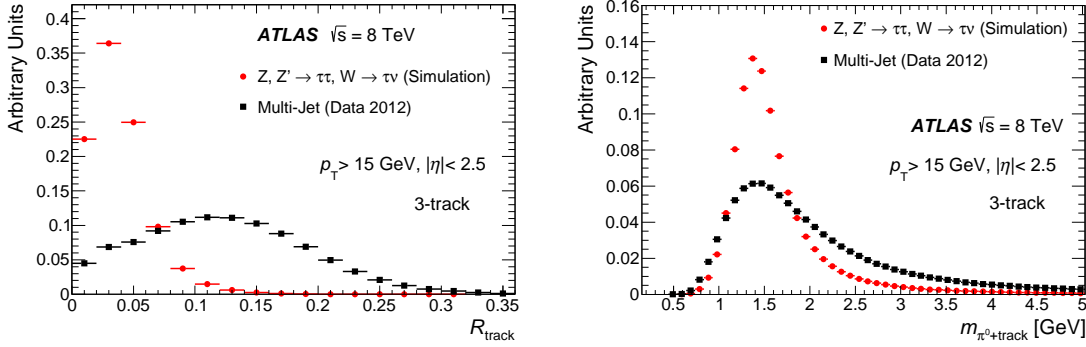


Figure 4.9: Signal and background distributions for two of the discriminating variables in the 3-track τ_{had} jet discrimination algorithm: R_{track} (left) and $m_{\pi^0 + \text{track}}$ (right) [1]. The remaining distributions are shown in Appendix B.

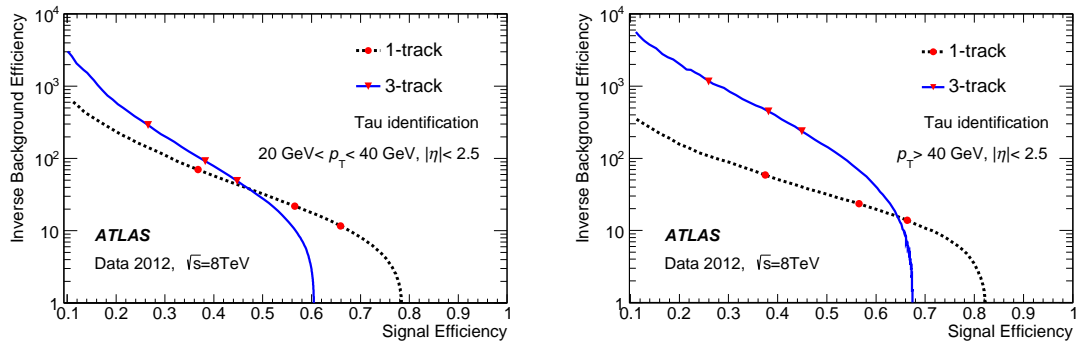


Figure 4.10: Signal efficiency versus inverse background efficiency for 1-track and 3-track τ_{had} jet discrimination algorithms in a lower- p_T regime (left) and higher- p_T regime (right) [1]. The loose, medium, and tight operating points are highlighted with red markers.

4. TAU LEPTONS

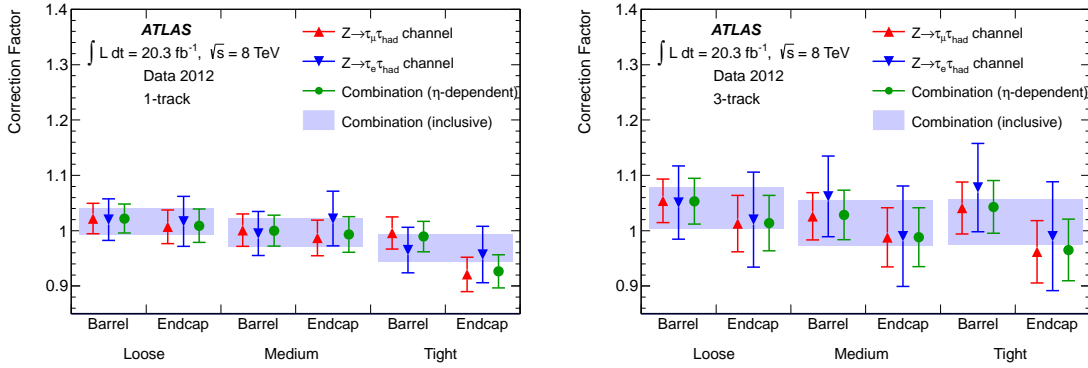


Figure 4.11: Correction factors for simulation for the τ_{had} jet discriminant efficiency for 1-track (left) and 3-track (right) τ_{had} [1].

4.3.3 Leptons mis-identified as τ_{had}

4.3.3.1 Electrons

The characteristic 1-track signature of τ_{had} can be mimicked by electrons, even those which fail dedicated electron identification algorithms. This is problematic for $\tau_e \tau_{\text{had}}$ analyses because $Z \rightarrow ee$ ($e \rightarrow \tau_{\text{had}}$) peaks in $m_{\tau\tau}$ near the $H \rightarrow \tau_e \tau_{\text{had}}$ mass peak and because high-mass $Z/\gamma^* \rightarrow ee$ ($e \rightarrow \tau_{\text{had}}$) can have long tails in $m_{\tau\tau}$.

Despite their similarities, many properties can be used to discriminate electrons from τ_{had} . Electrons tend to produce more transition radiation than τ_{had} , have narrower deposits in the calorimeter, and have shallower deposits in the calorimeter, with rarely any depositions in the hadronic calorimeter. These properties are combined in a multi-variate identification algorithm trained in five regions of $\eta(\tau_{\text{had}})$ to discriminate electrons from simulated $Z/\gamma^* \rightarrow ee$ against τ_{had} from simulated $Z/\gamma^* \rightarrow \tau\tau$. The algorithms are collectively referred to as the electron discriminator or veto.

TRT high threshold fraction ($f_{\text{TRT,HT}}$):

The ratio of high-threshold to low-threshold hits (including outlier hits) in the TRT for the leading track.

Pre-sampler and strip fraction (f_{PS}):

The fraction of cluster energy deposited in the pre-sampler and strips of the EM calorimeter.

Track-cluster $|\Delta\eta|$:

The $|\Delta\eta|$ between the cluster and the leading track.

4. TAU LEPTONS

Track-cluster $|\Delta\phi|$:

The $|\Delta\phi|$ between the cluster and the leading track.

Hadronic leakage ($f_{\text{track}}^{\text{Had},0}$):

The ratio of energy deposited in the zeroth compartment of the hadronic calorimeter to the lead track momentum.

EM fraction (f_{EM}):

The fraction of energy deposited in the EM calorimeter.

Strip maxima ($E_{\text{T},\text{max}}^{\text{strip}}$):

The maximal energy deposited in a 101×3 (η, ϕ) window of the strips.

The performance of the electron discriminators is evaluated in data and simulation using a $Z \rightarrow ee$ tag-and-probe technique, where one identified electron is tagged and a τ_{had} candidate is probed where the mass of the electron- τ_{had} pair is consistent with the Z mass. This measurement can be challenging because few $e \rightarrow \tau_{\text{had}}$ survive the electron discriminator. The characteristic peak in $m_{\tau\tau}^{\text{vis.}}$ is shown in Fig. 4.13 before and after application of the algorithms.

In the 2012 version of the electron discriminator, a mis-modeling in simulation is found in the forward region regarding the energy deposited in the third layer of the EM calorimeter, which propagates to the discriminator via f_{EM} . The mis-modeling is ameliorated in the 2013 version by redefining

Table 4.2: Discriminating variables used in the τ_{had} electron veto [1, 78, 77]. Some variables are also used in the jet discrimination algorithms.

variable	$ \eta(\tau_{\text{had}}) $				
	0.0 – 0.8	0.8 – 1.37	1.37 – 1.52	1.52 – 2.0	> 2.0
$f_{\text{TRT,HT}}$	•	•	•	•	
f_{PS}	•	•	•	•	•
f_{track}	•	•	•	•	•
$ \Delta\phi $	•	•	•	•	•
$ \Delta\eta $	•	•	•	•	•
$f_{\text{track}}^{\text{Had},0}$	•	•	•	•	•
f_{EM}	•	•	•	•	•
$E_{\text{T},\text{max}}^{\text{strip}}/p_{\text{T}}$	•	•			
f_{iso}		•		•	•
f_{cent}	•		•		

4. TAU LEPTONS

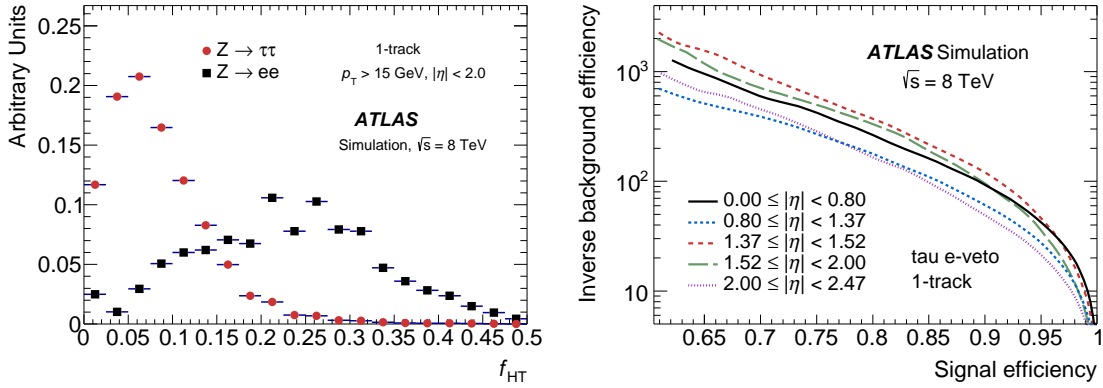


Figure 4.12: Simulated signal (τ_{had}) and background (e) distributions for the TRT high threshold fraction (left), which is an input to the electron discriminator, and signal efficiency versus inverse background efficiency for the discriminator (right) [1]. τ_{had} candidates in both are required to have one reconstructed track, pass the `loose` jet discriminator, and not overlap with any `tight` identified electron candidates. The `medium` operating point is defined to be 85% efficient for signal τ_{had} .

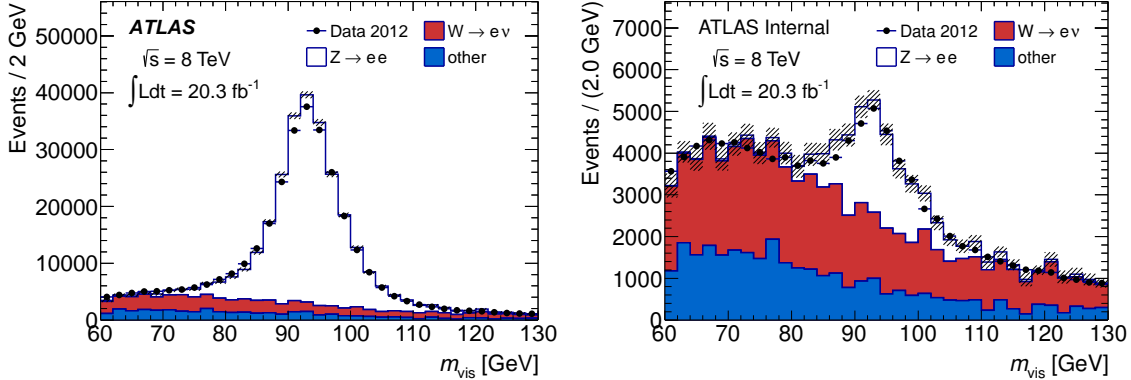


Figure 4.13: The visible mass $m_{e\tau_{\text{had}}}$ in a $Z \rightarrow ee$ selection in data after requiring the τ_{had} candidate pass the medium jet discriminator and not overlap spatially with a tight identified electron (left) [1] and after additionally requiring the τ_{had} pass the loose τ_{had} electron discriminator (right).

f_{EM} to depend less strongly on the third layer deposition, and the modeling is improved, as shown in Fig. 4.14.

4.3.3.2 Muons

The characteristic 1-track signature of τ_{had} can also be mimicked by muons. This is more rare than $e \rightarrow \tau_{\text{had}}$ mis-identification since muons are minimum ionizing particles and do not often deposit

4. TAU LEPTONS

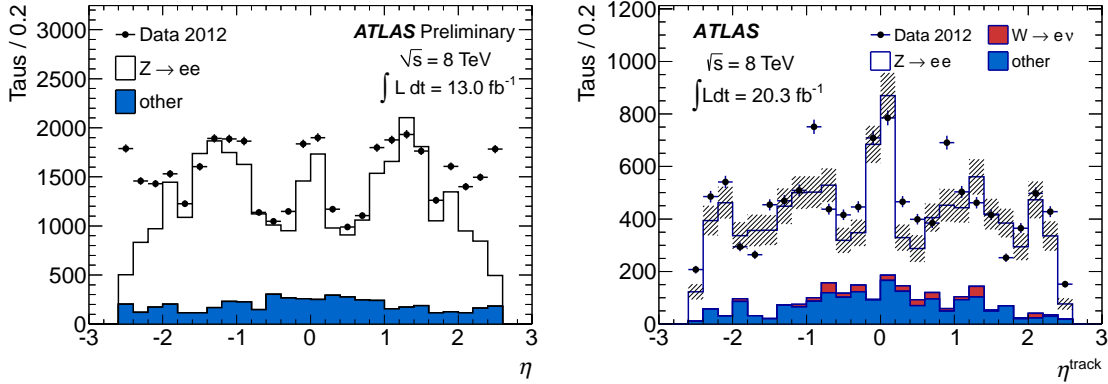


Figure 4.14: The pseudorapidity $\eta(\tau_{\text{had}})$ in a $Z \rightarrow ee$ selection in data after requiring the τ_{had} candidate pass the medium jet discriminator, not overlap spatially with a tight identified electron, and pass the loose τ_{had} electron discriminator from 2012 (left) [78] and 2013 (right) [1]. Statistical uncertainty is not shown on the left. The modeling is improved in the forward region for the 2013 discriminator.

sufficient energy in the calorimeters to seed a τ_{had} candidate. But $Z \rightarrow \mu\mu$ ($\mu \rightarrow \tau_{\text{had}}$) can nonetheless be a problem for $\tau_\mu \tau_{\text{had}}$ final states for the same reasons as $Z \rightarrow ee$ is problematic for $\tau_e \tau_{\text{had}}$ final states.

Studies of $Z \rightarrow \mu\mu$ simulation indicate most (60%) $\mu \rightarrow \tau_{\text{had}}$ have a cluster in the calorimeter from photon FSR. The remaining are assumed to undergo sufficient energy loss in the hadronic calorimeter to create a cluster. Only 2% of $\mu \rightarrow \tau_{\text{had}}$ are not reconstructed as a muon candidate. Most of these $\mu \rightarrow \tau_{\text{had}}$ occur in a region of η which is poorly covered by the muon system, and some occur because they are too low p_T for the muon reconstruction algorithms. These properties are shown in Fig. 4.15 and Fig. 4.16.

In physics analysis, $\mu \rightarrow \tau_{\text{had}}$ are typically rejected by requiring a τ_{had} candidate not overlap with an identified muon and that it pass an additional, dedicated muon veto. These rejection criteria are re-optimized in 2014 for better $\mu \rightarrow \tau_{\text{had}}$ suppression and simultaneously better true τ_{had} efficiency. The updated rejection removes the dedicated muon veto, which costs $\approx 5\%$ efficiency for true τ_{had} ,

Table 4.3: A breakdown of how $\mu \rightarrow \tau_{\text{had}}$ occur, both in the case of all $\mu \rightarrow \tau_{\text{had}}$ and only those which fail the muon reconstruction.

cluster from:				
type of $\mu \rightarrow \tau_{\text{had}}$	FSR γ	detector (e.g., brem.)	$p_T < 5 \text{ GeV}$	$ \eta < 0.1$
all	59%	41%	2%	4%
not reconstructed as μ	60%	40%	20%	60%

4. TAU LEPTONS

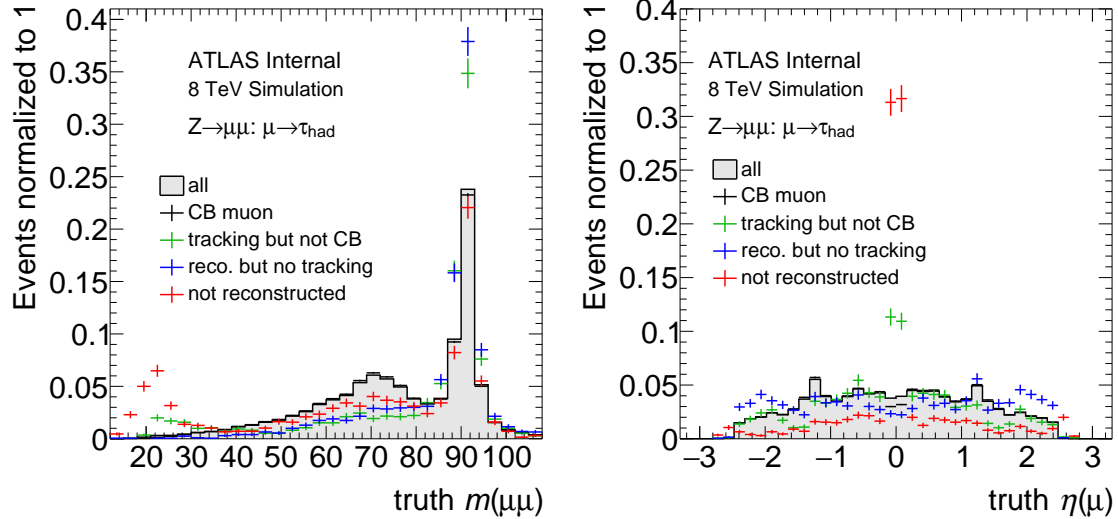


Figure 4.15: True $m_{\mu\mu}$ (left) and $\eta(\mu)$ (right) in $Z \rightarrow \mu\mu$ events where a muon is mis-identified as a τ_{had} . The muons are split into combined muons (black), muons which pass tracking requirements but fail combined requirements (green), are reconstructed but fail tracking requirements (blue), and are not reconstructed (red). A large fraction of non-reconstructed muons have $|\eta| \approx 0$, which is a poorly covered region of the muon system.

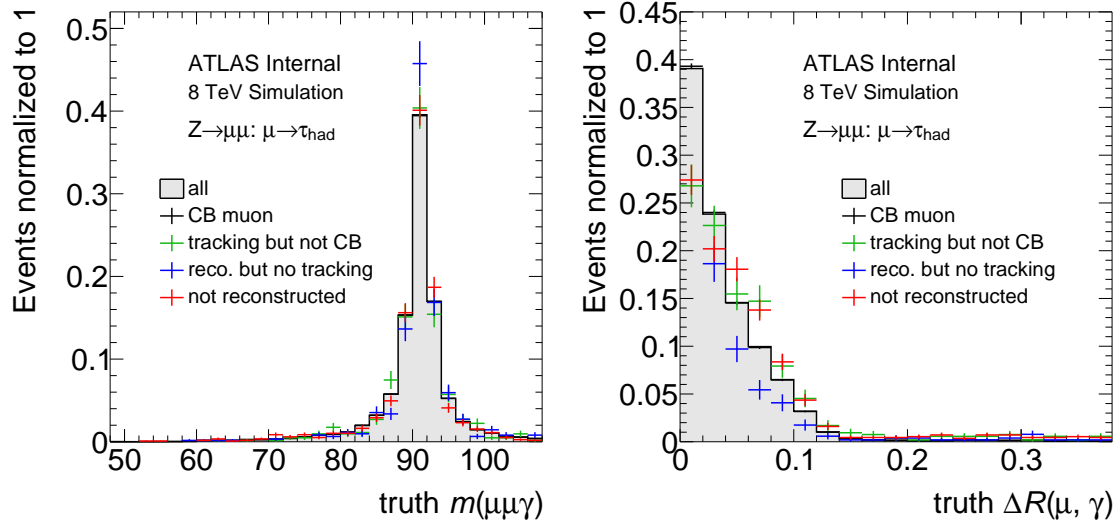


Figure 4.16: True $m_{\mu\mu\gamma}$ (left) and $\Delta R(\mu, \gamma)$ (right) in $Z \rightarrow \mu\mu$ events where a muon is mis-identified as a τ_{had} and a true FSR photon is associated to the muon. The muons are split into combined muons (black), muons which pass tracking requirements but fail combined requirements (green), are reconstructed but fail tracking requirements (blue), and are not reconstructed (red).

4. TAU LEPTONS

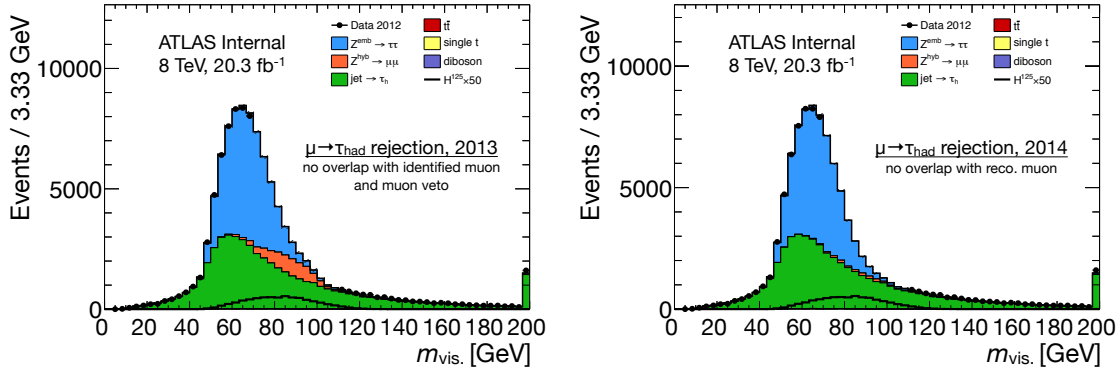


Figure 4.17: Data and prediction in a $Z \rightarrow \tau_\mu \tau_{\text{had}}$ selection, where $Z \rightarrow \mu\mu$ ($\mu \rightarrow \tau_{\text{had}}$) is shown in orange, for 2013 (left) and 2014 (right) versions of $\mu \rightarrow \tau_{\text{had}}$ rejection techniques. Overlapping muon candidates in the 2013 version are required to fulfill tracking goodness as a form of identification. The $Z \rightarrow \mu\mu$ ($\mu \rightarrow \tau_{\text{had}}$) is reduced significantly in the 2014 version.

and tightens the overlap criteria such that τ_{had} candidates are rejected if they overlap with any reconstructed muon above 2 GeV. The improved rejection of this criteria is shown in Fig. 4.17.

CHAPTER 5

$H \rightarrow \tau_\ell \tau_{\text{had}}$ strategy

The strategy of the $H \rightarrow \tau_\ell \tau_{\text{had}}$ analysis is described. This draws from documentation detailing its evolution in recent years [89, 90], especially the recent ATLAS $H \rightarrow \tau\tau$ publication [2].

5.1 Introduction

The search for the Higgs boson has been the major focus of accelerator physics for decades. Though explored in great detail at experiments at LEP [26] and the Tevatron [27], its existence has only recently proven by the ATLAS and CMS experiments at the LHC.

5.1.1 ATLAS Higgs program

The ATLAS Higgs program initially focused on five decay modes expected to have sensitivity to Standard Model Higgs production in the first years of LHC data-taking: $H \rightarrow \gamma\gamma$, $H \rightarrow ZZ^*$, $H \rightarrow WW^*$, $H \rightarrow \tau\tau$, and $H \rightarrow bb$. The $H \rightarrow \gamma\gamma$ and $H \rightarrow ZZ^*$ analyses are appealing for their distinctive signatures, and the $H \rightarrow WW^*$, $H \rightarrow \tau\tau$, and $H \rightarrow bb$ analyses are appealing for their relatively high rates. The predicted Higgs branching fractions for selected decay modes are given in Table 5.1.

Table 5.1: Predicted branching fractions for the Higgs boson of mass 125 GeV [91].

Decay mode	fermions			bosons			
	bb	$\tau\tau$	$\mu\mu$	WW^*	ZZ^*	$\gamma\gamma$	$Z\gamma$
Branching fraction	58%	6.3%	0.022%	22%	2.6%	0.23%	0.15%

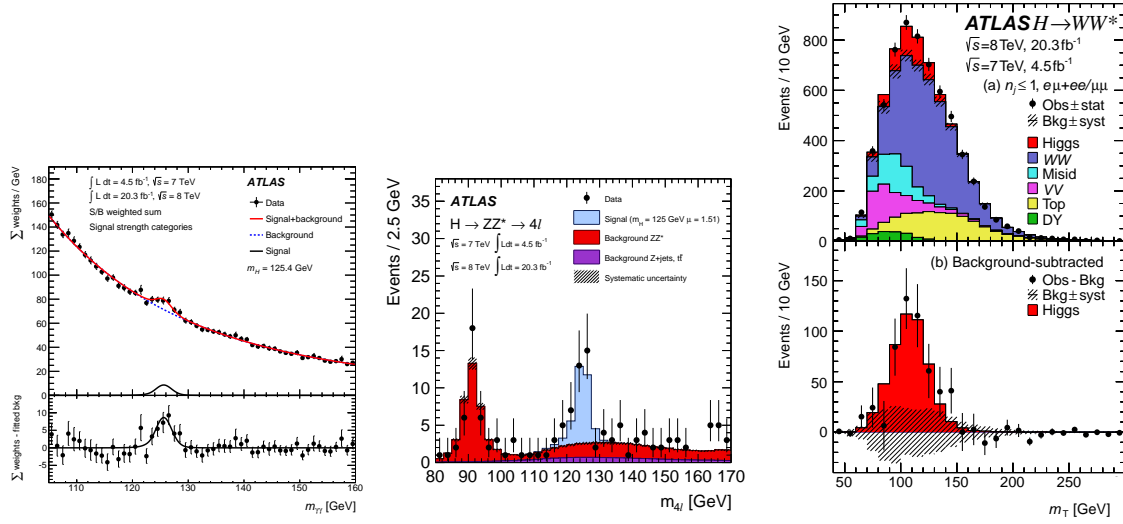


Figure 5.1: Discovery plots for the $H \rightarrow \gamma\gamma$ (left) [92], $H \rightarrow ZZ^*$ (center) [93], and $H \rightarrow WW^*$ (right) [94] analyses.

5.1.1.1 $H \rightarrow \text{bosons}$

The Higgs discovery in 2012-2013 is driven by the bosonic decays. The $H \rightarrow \gamma\gamma$ and $H \rightarrow ZZ^*$ analyses enjoy excellent mass resolution for reconstructing m_H and resonant backgrounds. They measure the Higgs mass to less than one percent uncertainty. The $H \rightarrow WW^*$ analysis utilizes a distinctive final state (two leptons with low $\Delta\phi$) and a relatively high branching fraction. Higgs discovery plots for these analyses can be seen in Fig. 5.1.

Pairs of gauge bosons like γ, W, Z are produced infrequently at the LHC, hence all three bosonic analyses best measure the ggF Higgs production mechanism since it has the highest cross section. Their best discriminating variable is typically the reconstructed Higgs mass because there are no significant resonant backgrounds. This can be fully reconstructed in the $H \rightarrow \gamma\gamma$ and $H \rightarrow ZZ^*$ analyses because there are no neutrinos in the decays. In the $H \rightarrow WW^*$, the Higgs mass can be partially reconstructed by incorporating the E_T^{miss} in a transverse mass m_T .

5.1.1.2 $H \rightarrow \text{fermions}$

With the full Run-I dataset and evolving analysis techniques, the searches for fermionic decays of the Higgs boson become competitive in sensitivity with analyses of the bosonic decays. Among these searches, the $H \rightarrow \tau\tau$ and $H \rightarrow bb$ analyses are the most powerful with the Run-I dataset. The $H \rightarrow \tau\tau$ analysis is described here, especially in the $\tau_\ell \tau_{\text{had}}$ final state. The $H \rightarrow bb$ analysis is described in detail elsewhere [95].

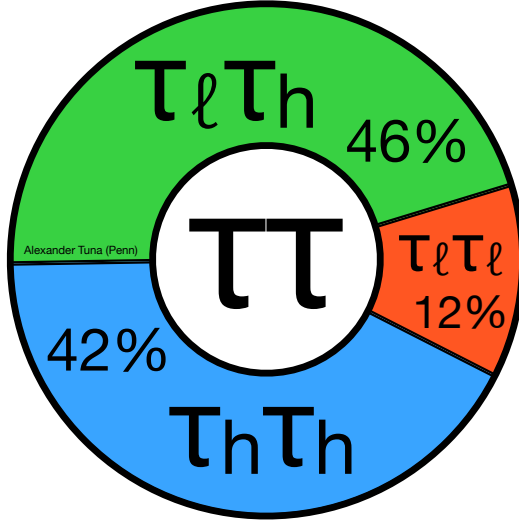


Figure 5.2: Pie chart of di-tau lepton decay branching fractions.

5.1.2 $H \rightarrow \tau\tau$

The $H \rightarrow \tau\tau$ analysis is naturally broken into three final states (or “channels”) given the combinatorics of tau lepton decays: $\tau_\ell \tau_{\text{had}}$, $\tau_{\text{had}} \tau_{\text{had}}$, and $\tau_\ell \tau_\ell$. Their branching fractions are shown in Fig. 5.2. The experimental methods of each final state are conceptually similar though not identical. This thesis describes the $H \rightarrow \tau_\ell \tau_{\text{had}}$ in detail since it was the focus of the author, and the $H \rightarrow \tau_{\text{had}} \tau_{\text{had}}$ and $H \rightarrow \tau_\ell \tau_\ell$ are only briefly summarized.

Unlike the $H \rightarrow$ bosons analyses, the $H \rightarrow \tau\tau$ suffers from a large background of $Z \rightarrow \tau\tau$. This background cannot be easily disentangled from $H \rightarrow \tau\tau$ because multiple neutrinos exist in the decays of the tau leptons and $m_{\tau\tau}$ cannot be fully reconstructed. The cross-section for QCD production for $Z \rightarrow \tau\tau$ is also 10^3 times larger than ggF $H \rightarrow \tau\tau$ production [2], which is the largest production mode.

The cross-section for EW production of $Z \rightarrow \tau\tau$, however, is only 4 times larger than VBF $H \rightarrow \tau\tau$ production [2], which is the second largest production mode and can be tagged via the associated VBF jets. This makes the $H \rightarrow \tau\tau$ analysis a natural candidate for *categorization*, where Higgs production modes are targeted with much smaller cross sections than the inclusive production but with better experimental sensitivity.

5.2 Triggers

The lowest unprescaled single lepton triggers, as described in Section 3.4, are used for the $H \rightarrow \tau_\ell \tau_{\text{had}}$ data sample. These correspond to offline lepton p_T thresholds of 26 GeV in the 8 TeV dataset. $\ell + \tau_{\text{had}}$ triggers are considered to recover data events with leptons below the single lepton trigger thresholds, but they are ultimately not used due to lack of sensitivity and additional complications. The triggers used are shown in Table 5.2.

5.3 Physics objects

5.3.1 Electrons, muons, and τ_{had}

Electrons, muons, and τ_{had} are selected according to the reconstruction, identification, and calibration algorithms described in Sections 3.3 and 4.3. The selection criteria used are summarized in Table 5.3.

Electrons are required to have $p_T > 26$ GeV and pass the `tightPP` identification algorithm and be isolated both in the tracker and the calorimeter. Less than 6% of the magnitude of the electron energy is required to exist in an isolation cone of 0.4 in the tracker and 0.2 in the calorimeter. The recent electron likelihood identification algorithm [61] is explored, and though improvement is observed, time constraints prevent its use in this analysis.

Muons are required to have $p_T > 26$ GeV and to satisfy the `isCombined` reconstruction algorithm

Table 5.2: Triggers used in the 8 TeV $H \rightarrow \tau_\ell \tau_{\text{had}}$ analysis.

channel	L1	HLT
$H \rightarrow \tau_e \tau_{\text{had}}$	EM18VH	e24vhi_medium1
$H \rightarrow \tau_\mu \tau_{\text{had}}$	MU20	mu24i_tight

Table 5.3: Lepton and τ_{had} criteria used in the 8 TeV $H \rightarrow \tau_\ell \tau_{\text{had}}$ analysis.

object	criteria
Electrons	$p_T > 26$ GeV, $ \eta < 2.47$ (excl. crack) <code>tightPP</code> , $f_{\text{isol.}}^{\text{track}} < 0.06$, $f_{\text{isol.}}^{\text{calo.}} < 0.06$
Muons	$p_T > 26$ GeV, $ \eta < 2.5$ <code>isCombined</code> , $f_{\text{isol.}}^{\text{track}} < 0.06$, $f_{\text{isol.}}^{\text{calo.}} < 0.06$
τ_{had}	$p_T > 20$ GeV, $ \eta < 2.47$, $ \eta^{\text{lead track}} < 2.47$ <code>JetBDTSigMedium</code> , no overlap with reco. muon or <code>loosePP</code> electron <code>EleBDTMedium</code> in $\tau_e \tau_{\text{had}}$ channel

and be isolated both in the tracker and the calorimeter. Less than 6% of the magnitude of the muon energy is required to exist in an isolation cone of 0.4 in the tracker and 0.2 in the calorimeter.

τ_{had} are required to have $p_T > 20$ GeV and to pass the `JetBDTSigMedium` jet discriminator. As discussed in Section 4.3, this identification algorithm includes isolation criteria. τ_{had} are also required to not overlap with any reconstructed muon candidates or `loosePP` electron candidates, as discussed in Section 4.3.3. In the $\tau_e \tau_{\text{had}}$ final state, τ_{had} are additionally required to pass the `EleBDTMedium` electron discriminator.

For the purpose of vetoing events with additional light leptons, p_T and identification criteria for electrons (muons) are relaxed to 15 GeV (10 GeV) and `loosePP` (`loose`), respectively.

5.3.2 Jets and E_T^{miss}

Jets, b -jets, and E_T^{miss} are selected according to the reconstruction, identification, and calibration algorithms described in Section 3.3. The selection criteria used are summarized in Table 5.4.

Jets are required to have $p_T > 30$ GeV and pass a requirement of $\text{JVF} > 0.5$ if they are within the tracking volume $\eta(\text{jet}) < 2.4$. Jets are disambiguated from other physics objects by removing the jet if it overlaps with any electron, muon, or τ_{had} passing identification requirements previously discussed. Jets are classified as b -jets if they are within the tracking volume and pass the 70% working point of the MV1 b -tagging algorithm.

E_T^{miss} is calculated with hard objects as selected by the analysis thresholds and with a soft term from the STVF method, as described in Section 3.3.4. No explicit cuts on the E_T^{miss} are made at any stage of the $\tau_\ell \tau_{\text{had}}$ analysis because the E_T^{miss} spectra for $H \rightarrow \tau\tau$ does not strongly discriminate the dominant backgrounds, $Z \rightarrow \tau\tau$ and $W(\rightarrow \ell\nu_\ell) + \text{jets}$, which have neutrinos in the final state. A track-based soft term is explored, and though improvement is observed, time constraints prevent its use in this analysis.

Table 5.4: Jet, b -jet, and E_T^{miss} criteria used in the 8 TeV $H \rightarrow \tau_\ell \tau_{\text{had}}$ analysis.

object	criteria
Jets	$p_T > 30$ GeV, $ \eta < 4.5$ $\text{JVF} > 0.5$ if $ \eta < 2.4$
b -jets	$p_T > 30$ GeV, $ \eta < 2.4$ 70% MV1 b -tag working point
E_T^{miss}	hard term consistent with object selection (ignoring photons) STVF soft term

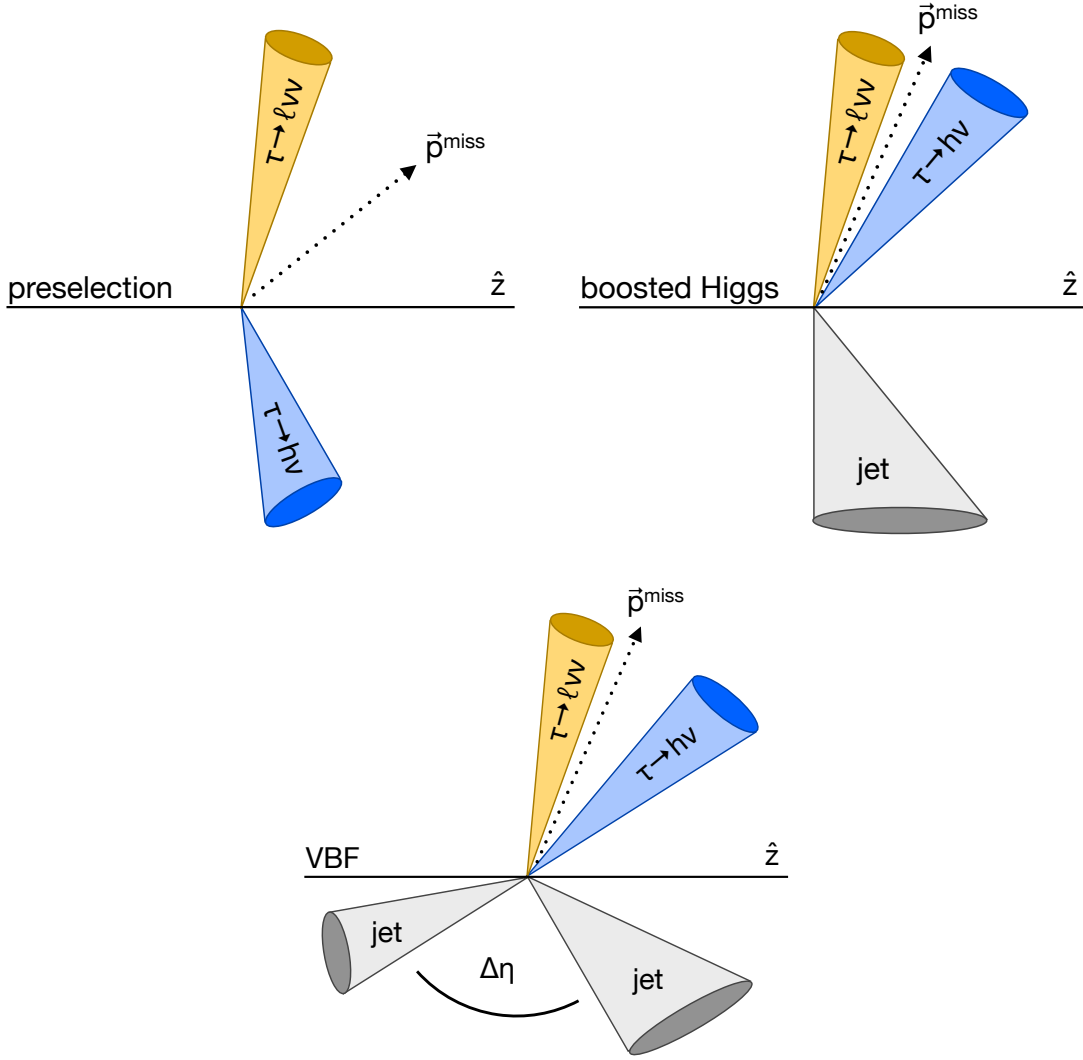


Figure 5.3: Cartoon depiction of the relevant categories in the $H \rightarrow \tau_\ell \tau_{\text{had}}$ analysis: pre-selection, boosted, and VBF.

5.4 Categorization

Event selection is done in two stages: pre-selection and categorization. The first step, pre-selection, is meant to be a simple and pared down event selection on top of which further selections are built. The second step, categorization, adds additional selection to the pre-selection for defining signal regions. A cartoon of the pre-selection and categorizations are shown in Fig. 5.3.

5.4.1 Pre-selection

Pre-selection of the $\tau_\ell \tau_{\text{had}}$ analysis requires exactly one light lepton, exactly one τ_{had} , exactly zero b -tagged jets, and that the lepton and τ_{had} have opposite charges. A requirement of $m_T(\ell, E_T^{\text{miss}}) < 70$ GeV is applied, which reconstructs a transverse W mass and is $\approx 95\%$ efficient for $H \rightarrow \tau\tau$. The pre-selection is summarized in Table 5.5.

This simple selection is shared among all signal regions. Individual pieces of the selection can be reversed to define control regions in data rich in $j \rightarrow \tau_{\text{had}}$. For example, the $m_T(\ell, E_T^{\text{miss}})$ requirement is reversed to defined a $W(\rightarrow \ell\nu_\ell) + \text{jets}$ control region.

Event kinematics for data and prediction at the pre-selection stage are shown in Figs. 5.4 and 5.5. These predictions are discussed in more detail in Chapter 6. Since the selection is very inclusive, many hundreds of thousands of events pass the pre-selection, especially $Z \rightarrow \tau\tau$ and $j \rightarrow \tau_{\text{had}}$.

5. $H \rightarrow \tau_\ell \tau_{\text{had}}$ STRATEGY

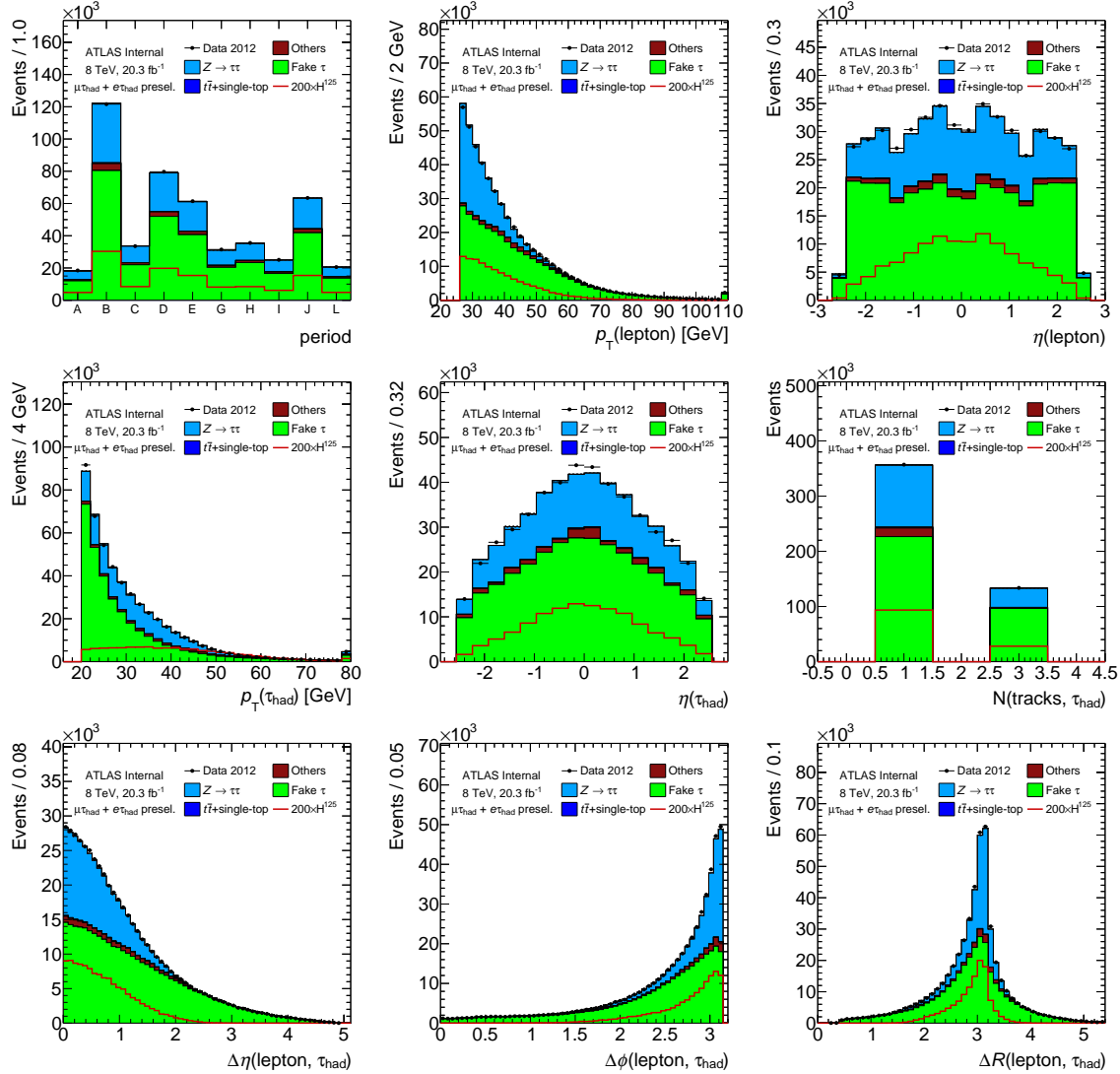


Figure 5.4: Kinematic distributions in the pre-selection category of the 8 TeV $H \rightarrow \tau_\ell \tau_{\text{had}}$ analysis with the requirement on $m_T(\ell, E_T^{\text{miss}})$ removed.

5. $H \rightarrow \tau_\ell \tau_{\text{had}}$ STRATEGY

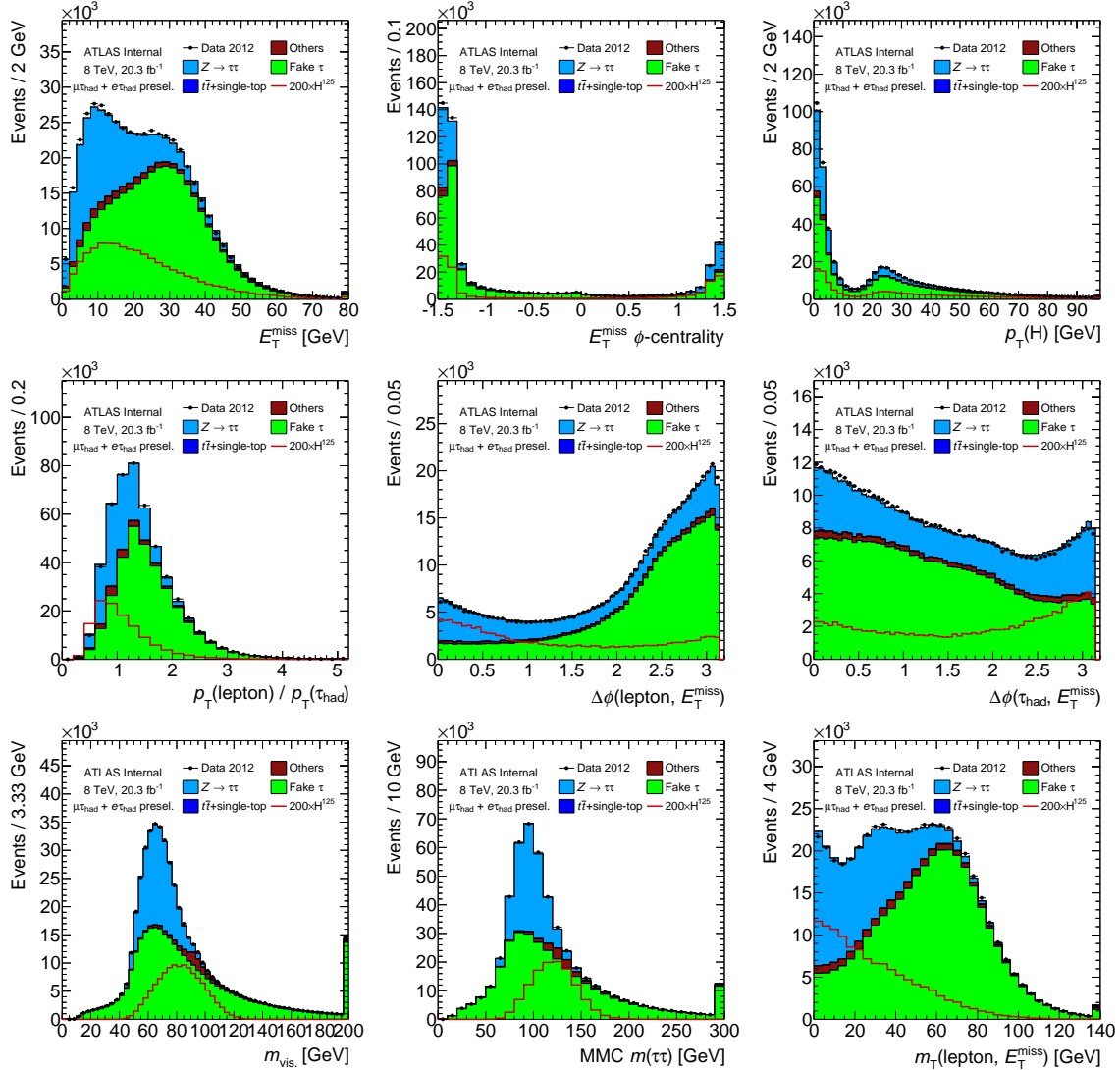


Figure 5.5: Kinematic distributions in the pre-selection category of the 8 TeV $H \rightarrow \tau_\ell \tau_{\text{had}}$ analysis with the requirement on $m_T(\ell, E_T^{\text{miss}})$ removed.

5.4.2 VBF category

Due to the large background from QCD $Z \rightarrow \tau\tau$ and $W(\rightarrow \ell\nu_\ell) + \text{jets}$ production, the most sensitive search for $H \rightarrow \tau\tau$ is via the VBF production mechanism [96]. The signature of this production mechanism is the existence of two jets with large separation in rapidity, and this signature guides the selection criteria of the VBF category.

In addition to the pre-selection criteria, two additional jets are required for the VBF category which satisfy $\Delta\eta(jj) > 3$. The leading and sub-leading jets are assumed to be the VBF jets, and

they are required to satisfy the criteria described in Table 5.4. The threshold on the lead jet is raised to 50 GeV. The visible mass $m_{\tau\tau}^{\text{vis.}}$ is also required to be above 40 GeV because discrepancies are observed between data and prediction at very low mass. The VBF category selection is summarized in Table 5.5, and similar selection criteria are used to define the VBF $H \rightarrow \tau_{\text{had}}\tau_{\text{had}}$ and $H \rightarrow \tau_\ell\tau_\ell$ categories.

5.4.3 Boosted category

The second category considered is the boosted category. This category selects events by the transverse boost of the Higgs candidate, where the Higgs candidate is defined as the vector sum of the lepton, τ_{had} , and E_T^{miss} . It is required to have a boost greater than 100 GeV, and similar selection criteria are used to define the boosted $H \rightarrow \tau_{\text{had}}\tau_{\text{had}}$ and $H \rightarrow \tau_\ell\tau_\ell$ categories.

This selection emphasizes the ggF Higgs production mechanism with a high p_T ISR jet. The sensitivity of the ggF analysis improves with higher $p_T(H)$ because the $m_{\tau\tau}$ mass reconstruction techniques have better resolution at smaller $\Delta\phi(\tau\tau)$. These techniques are discussed in detail in Section 5.5.

Detailed descriptions of analysis techniques in the boosted category are omitted in this thesis. The focus of the author was on the VBF category, which is more sensitive in searching for $H \rightarrow \tau\tau$.

Table 5.5: Pre-selection and categorization criteria in the $H \rightarrow \tau_\ell \tau_{\text{had}}$ analysis.

object	criteria
Pre-selection	exactly one lepton and one τ_{had} with opposite charge no b -tagged jets $m_T(\ell, E_T^{\text{miss}}) < 70$ GeV
VBF category	Pre-selection criteria At least two jets, with $p_T(\text{lead jet}) > 50$ GeV $\Delta\eta(jj) > 3$ $m_{\tau\tau}^{\text{vis.}} > 40$ GeV
Boosted category	Pre-selection criteria $p_T^H > 100$ GeV

5.5 $\tau\tau$ mass reconstruction

Because there are three neutrinos in the final state of a $\tau_\ell \tau_{\text{had}}$ decay, the Higgs four-momentum cannot be fully reconstructed as in the $H \rightarrow \gamma\gamma$ or $H \rightarrow ZZ^*$ analyses. Many options exist for reconstructing $m_{\tau\tau}$, as shown in Table 5.6.

Visible mass, $m_{\tau\tau}^{\text{vis.}}$:

Mass of the visible decay products (lepton and τ_{had}). This is the simplest mass reconstruction and is robust against poor E_T^{miss} resolution. However, it ignores all information about the E_T^{miss} .

Total transverse mass, m_T^{total} :

Transverse mass of the lepton, τ_{had} , and E_T^{miss} . This is another simple mass reconstruction, and it incorporates the E_T^{miss} . However, no prior knowledge of tau lepton decays is utilized.

Collinear mass, $m_{\tau\tau}^{\text{col.}}$:

Mass of the $\tau\tau$ system assuming the neutrinos are exactly collinear with the visible decay products. This is the first attempt at fully reconstructing a $\tau\tau$ resonance.

Missing mass calculator, $m_{\tau\tau}^{\text{MMC}}$:

Mass of the $\tau\tau$ system assuming the neutrinos are approximately collinear with the visible decay products. This is discussed in more detail in Section 5.5.1.

5.5.1 $m_{\tau\tau}^{\text{MMC}}$ algorithm

The Missing Mass Calculator $m_{\tau\tau}^{\text{MMC}}$ is used to fully reconstruct $m_{\tau\tau}$ [98]. This requires solving an underconstrained system of equations for seven unknowns in the $\tau_\ell \tau_{\text{had}}$ final state: x -, y -, and z -components of the momentum carried by the neutrinos for each of the tau leptons in the event, and the invariant mass of the $\nu\nu$ system from the leptonic tau decay. The calculation uses the constraints from the measured x - and y -components of the E_T^{miss} , and the visible masses of both tau lepton decays. A scan is performed over the two components of the E_T^{miss} vector and the yet undetermined variables. Each scan point is weighted by its probability according to the E_T^{miss} resolution and the

Table 5.6: $m_{\tau\tau}$ reconstruction techniques used in ATLAS publications.

$m_{\tau\tau}$	$m_{\tau\tau}^{\text{vis.}}$	m_T^{total}	$m_{\tau\tau}^{\text{col.}}$	$m_{\tau\tau}^{\text{MMC}}$
process(es)	$Z \rightarrow \tau\tau$	$Z' \rightarrow \tau\tau$	$H \rightarrow WW^*$ vs. $Z \rightarrow \tau\tau$	$H \rightarrow \tau\tau$ vs. $Z \rightarrow \tau\tau$
publication	[1]	[97]	[94]	[2]

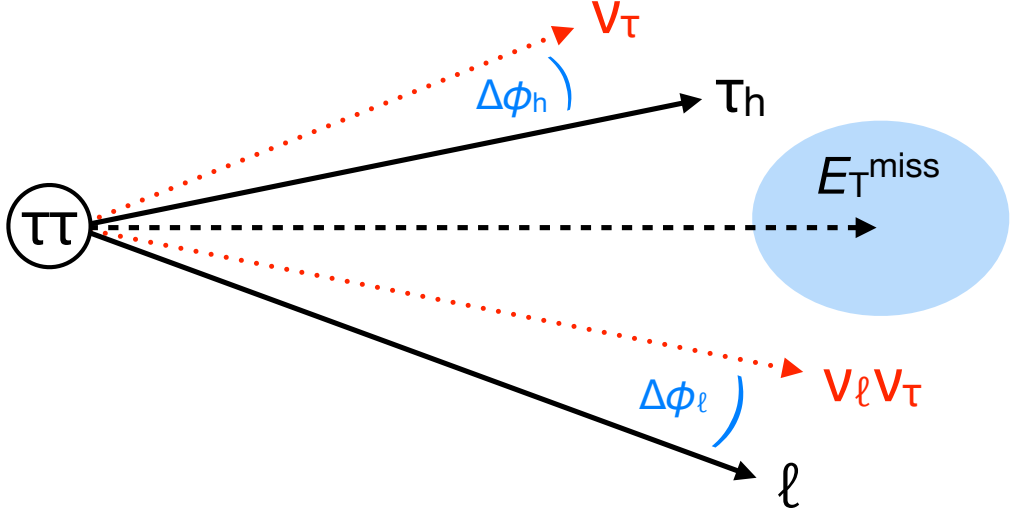


Figure 5.6: Cartoon of the $m_{\tau\tau}^{\text{MMC}}$ reconstruction algorithm. Black, filled lines indicate items measured directly (ℓ , τ_{had}). Red, dotted lines indicate items which cannot be measured (neutrinos). The black, dashed line indicates the E_T^{miss} , which is measured indirectly. Blue indicates items which the $m_{\tau\tau}^{\text{MMC}}$ scans to find an optimal solution ($\Delta\phi$, E_T^{miss}).

tau decay topologies. The estimator for the $m_{\tau\tau}$ is defined as the most probable value of the scan points. A cartoon visualization of the technique is shown in Fig. 5.6.

The multi-dimensional scan requires probability density functions (PDFs) for each dimension, and the final probability is a product of each PDF evaluated at a given scan point. Scans of the x - and y -components of the E_T^{miss} use Gaussian PDFs where the mean is the measured E_x^{miss} and E_y^{miss} , respectively, and the standard deviation is the resolution inferred from the measured ΣE_T of the event. The PDFs of the tau decay topologies are derived from simulated $Z \rightarrow \tau\tau$ events and shown in Fig. 5.7 for a given p_T range.

A similar technique, named SVFIT, is used in the CMS $H \rightarrow \tau\tau$ analysis [100].

5.5.2 Performance

The reconstructed $m_{\tau\tau}^{\text{MMC}}$ is shown in the $\tau_\ell \tau_{\text{had}}$ boosted and VBF categories in Fig. 5.8. Good separation is observed for $Z \rightarrow \tau\tau$ and $H \rightarrow \tau\tau$. For both processes, the efficiency for the MMC algorithm to converge is 99%.

To compare the performance of the various $m_{\tau\tau}$ reconstruction techniques, the efficiency for a requirement $m_{\tau\tau} > X$ is calculated across the mass range for $H \rightarrow \tau\tau$ (signal) and $Z \rightarrow \tau\tau$ (background). An ideal $m_{\tau\tau}$ algorithm would have $\epsilon(H \rightarrow \tau\tau)$ near 1 and $\epsilon(Z \rightarrow \tau\tau)$ near 0 for

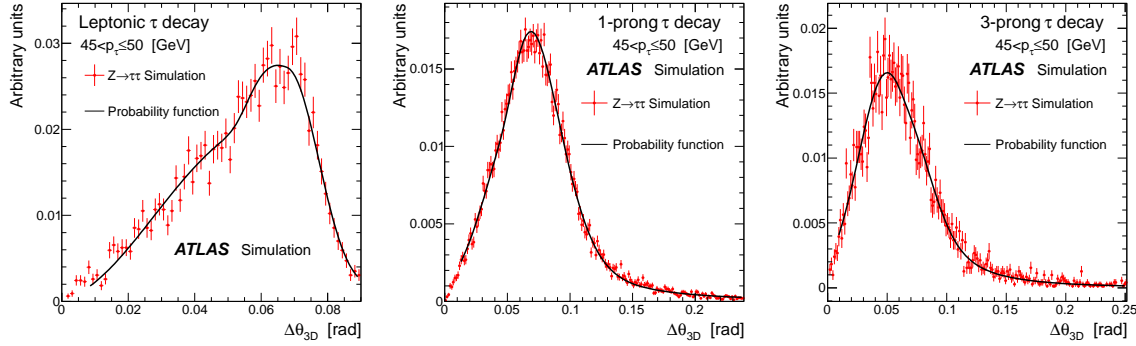


Figure 5.7: Input assumptions of the angle between the visible and invisible tau lepton decay products, for leptonic decays (left), 1-track hadronic decays (center), and 3-track hadronic decays (right) [99].

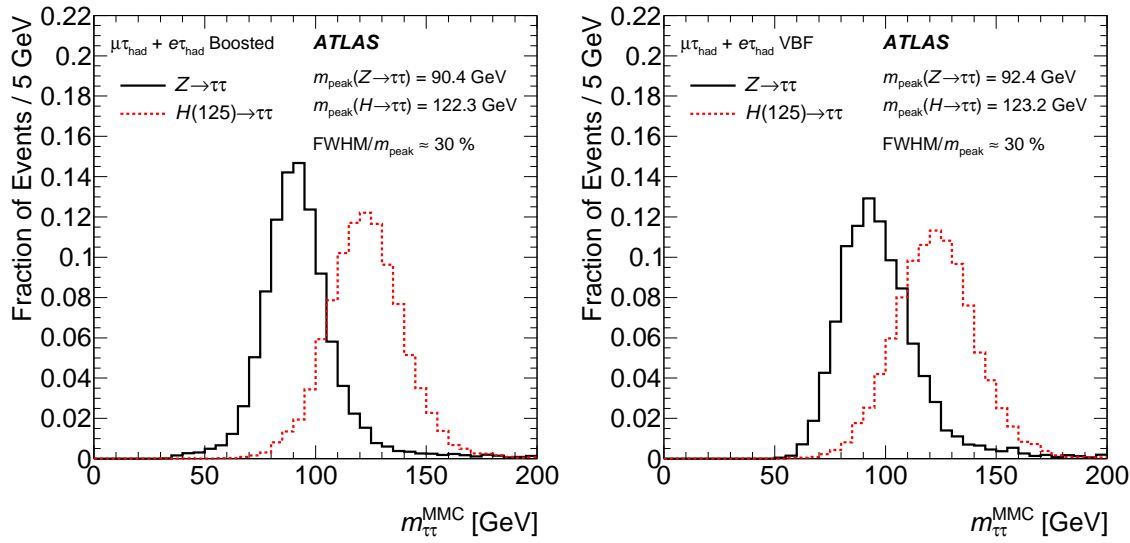


Figure 5.8: Predicted distributions of $m_{\tau\tau}$ for $Z \rightarrow \tau\tau$ and $H \rightarrow \tau\tau$ for the MMC reconstruction algorithm in the boosted category (left) and VBF category (right).

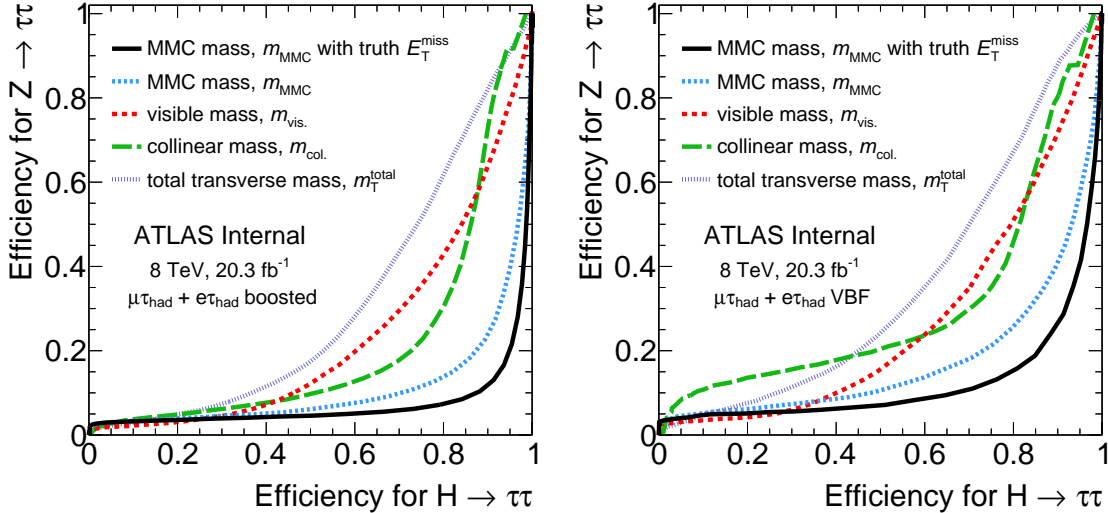


Figure 5.9: Efficiency for $H \rightarrow \tau_\ell \tau_{\text{had}}$ versus the efficiency for $Z \rightarrow \tau_\ell \tau_{\text{had}}$ for various $m_{\tau\tau}$ reconstruction algorithms in the boosted category (left) and VBF category (right).

$m_{\tau\tau} > 100, 110, 120$ GeV. The efficiencies are shown in Fig. 5.9 in the boosted and VBF categories.

The distributions of the various $m_{\tau\tau}$ algorithms are shown in Appendix C.

Of the $m_{\tau\tau}$ algorithms considered, the MMC has the best performance in this metric. The E_T^{miss} reconstruction performance is among the limiting factors of the MMC algorithm.

5.6 MVA discrimination

The Higgs discovery program is driven by final states where the reconstructed Higgs mass is the most powerful variable for discriminating signal from background. This is especially true of the $H \rightarrow \gamma\gamma$ and $H \rightarrow ZZ^*$ analyses, where m_H can be fully reconstructed and no nearby resonant backgrounds exist.

The landscape is not as easy for $H \rightarrow \tau\tau$. The resonant and irreducible $Z \rightarrow \tau\tau$ process is nearby in mass, and the resolution of the $m_{\tau\tau}$ is similar to the difference between the masses due to the presence of neutrinos in the tau lepton decays. Additionally, the distinctive VBF signature provides potentially greater discriminating power than $m_{\tau\tau}$.

For these reasons, a multi-variate (MVA) analysis is chosen where event-level observables like $m_{\tau\tau}^{\text{MMC}}$ and m_{jj} are input to a boosted decision tree (BDT) discriminator [101, 102]. The BDT attempts to classify a given event as signal-like or background-like with a continuous output score judged on the multi-dimensional evaluation of input variables. A score of 1 is most signal-like, and a

score of -1 is most background-like.

5.6.1 Inputs

Inputs to the VBF BDT discriminator can be broadly grouped into two classes: $H \rightarrow \tau\tau$ kinematics and VBF kinematics. $H \rightarrow \tau\tau$ kinematics provide discrimination against non- $H \rightarrow \tau\tau$ decays: for example, the $m_{\tau\tau}^{\text{MMC}}$ discriminates against all backgrounds, and the transverse W -mass $m_T(\ell, E_T^{\text{miss}})$ discriminates against $W(\rightarrow \ell\nu_\ell) + \text{jets}$ events. VBF kinematics provide discrimination against non-VBF produced processes: for example, dijets produced in VBF tend to have larger m_{jj} than QCD $Z \rightarrow \tau\tau$ produced in association with two jets. One of the appealing features of the BDT, however, is that correlations between these groups of variables are exploited in the classification. This is discussed in more detail in Section 5.6.2.

An interesting sub-set of inputs are centrality variables. These are transformations of discrete properties to continuous observables. The first, E_T^{miss} ϕ -centrality, quantifies whether the E_T^{miss} is between the lepton and τ_{had} in the transverse plane. In $\tau\tau$ systems, the E_T^{miss} typically points between the lepton and τ_{had} , whereas non- $\tau\tau$ systems have no such constraint. The E_T^{miss} ϕ -centrality is accordingly maximized when the E_T^{miss} points directly between the lepton and τ_{had} and minimized when it points opposite.

The second centrality variable, lepton η -centrality, quantifies whether the lepton is between the VBF jets in η . In VBF systems, the Higgs decay products typically point between the VBF jets in η , whereas non-VBF systems have no such constraint. Visualization of the allowed values of the centralities are shown in Fig. 5.10.

The choice of variables is optimized to give good separation while keeping the number of inputs small and manageable. The set of inputs used in the $H \rightarrow \tau_\ell \tau_{\text{had}}$ categories is shown in Table 5.7. Distributions of input variables and other kinematics are shown in Figs. 5.11 and 5.12 for the boosted category and Figs. 5.13 and 5.14 for the VBF category. Signal and background predictions are discussed in greater detail in Chapter 6.

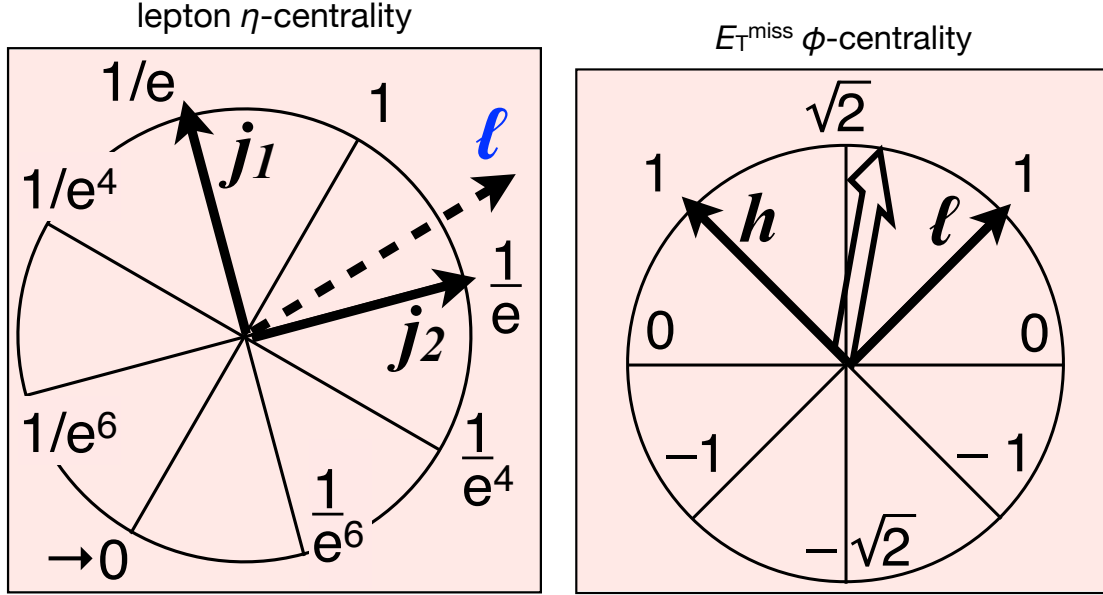


Figure 5.10: Cartoons of lepton η -centrality (left) and E_T^{miss} ϕ -centrality (right), courtesy of Tae Min Hong.

Table 5.7: Input variables to the $H \rightarrow \tau_\ell \tau_{\text{had}}$ BDT discriminators in the boosted and VBF categories.

Variable	VBF	boosted	Description
$m_{\tau\tau}^{\text{MMC}}$	•	•	ditau mass
$\Delta R(\text{lepton}, \tau_{\text{had}})$	•	•	spatial separation of lepton, τ_{had}
$E_T^{\text{miss}} \phi$ -centrality	•	•	ϕ -centrality of E_T^{miss} between lepton, τ_{had}
$m_T(\ell, E_T^{\text{miss}})$	•	•	transverse W mass
$\Delta\eta(jj)$	•		η -separation of VBF jets
m_{jj}	•		mass of VBF jets
$\eta_{j_1} \times \eta_{j_2}$	•		η -product of VBF jets
p_T^{Total}	•		vector sum of lepton, τ_{had} , E_T^{miss} and VBF jets
lepton η -centrality	•		η -centrality of lepton between VBF jets
Σp_T		•	scalar sum of lepton, τ_{had} , and all jets
$p_T^{\text{lepton}}/p_T^{\tau_{\text{had}}}$		•	ratio of lepton p_T to $\tau_{\text{had}} p_T$

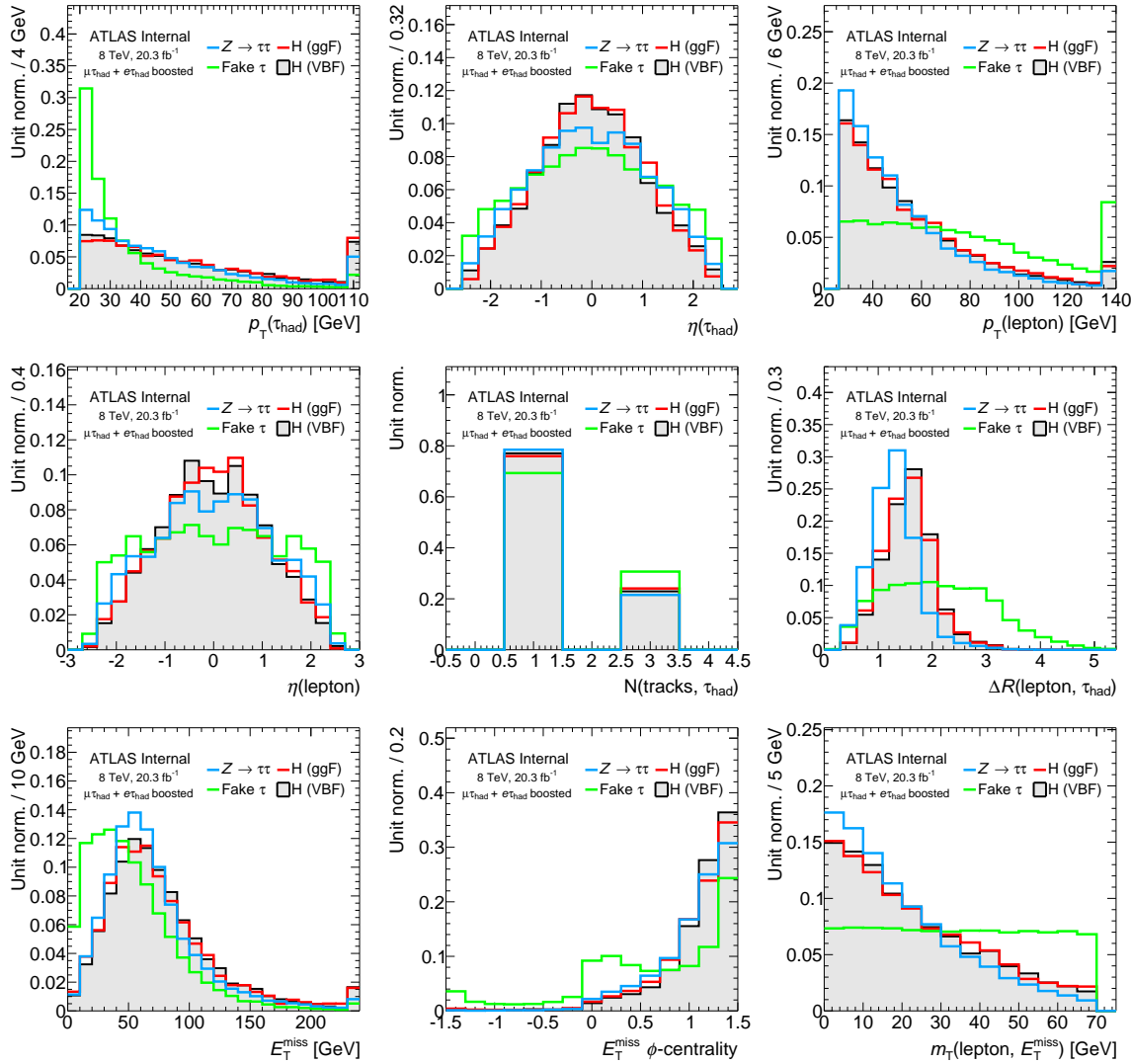


Figure 5.11: Predicted signal and background distributions in the boosted category normalized to unit area and overlaid.

5. $H \rightarrow \tau_\ell \tau_{\text{had}}$ STRATEGY

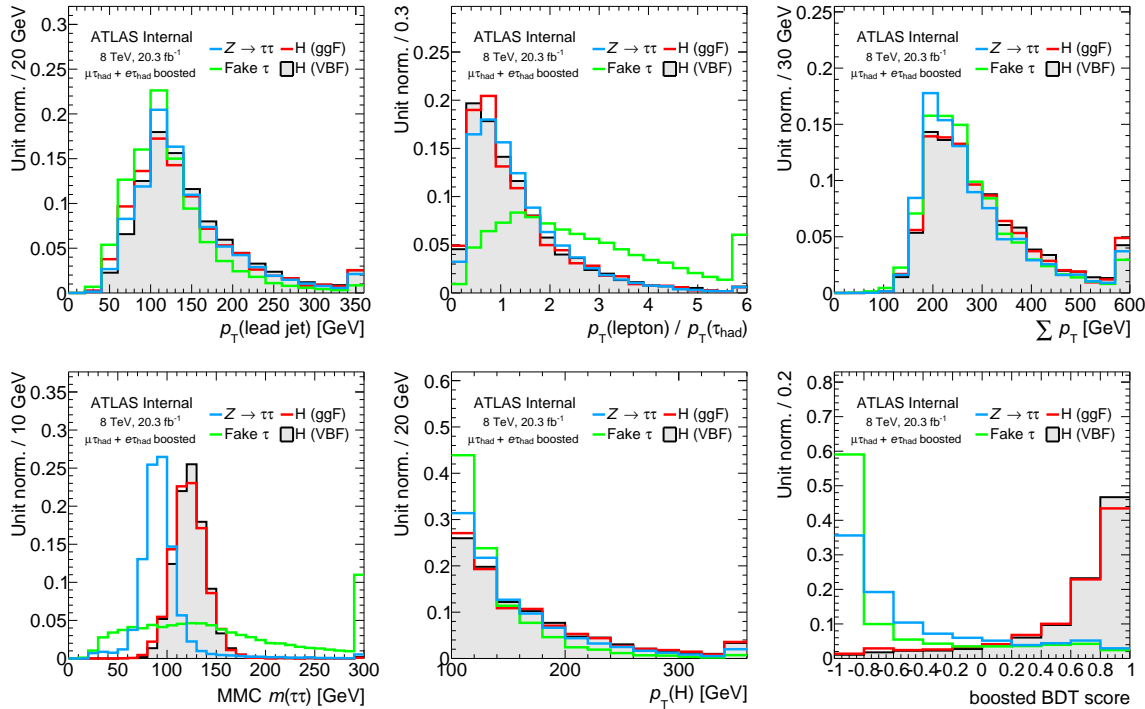


Figure 5.12: Predicted signal and background distributions in the boosted category normalized to unit area and overlaid.

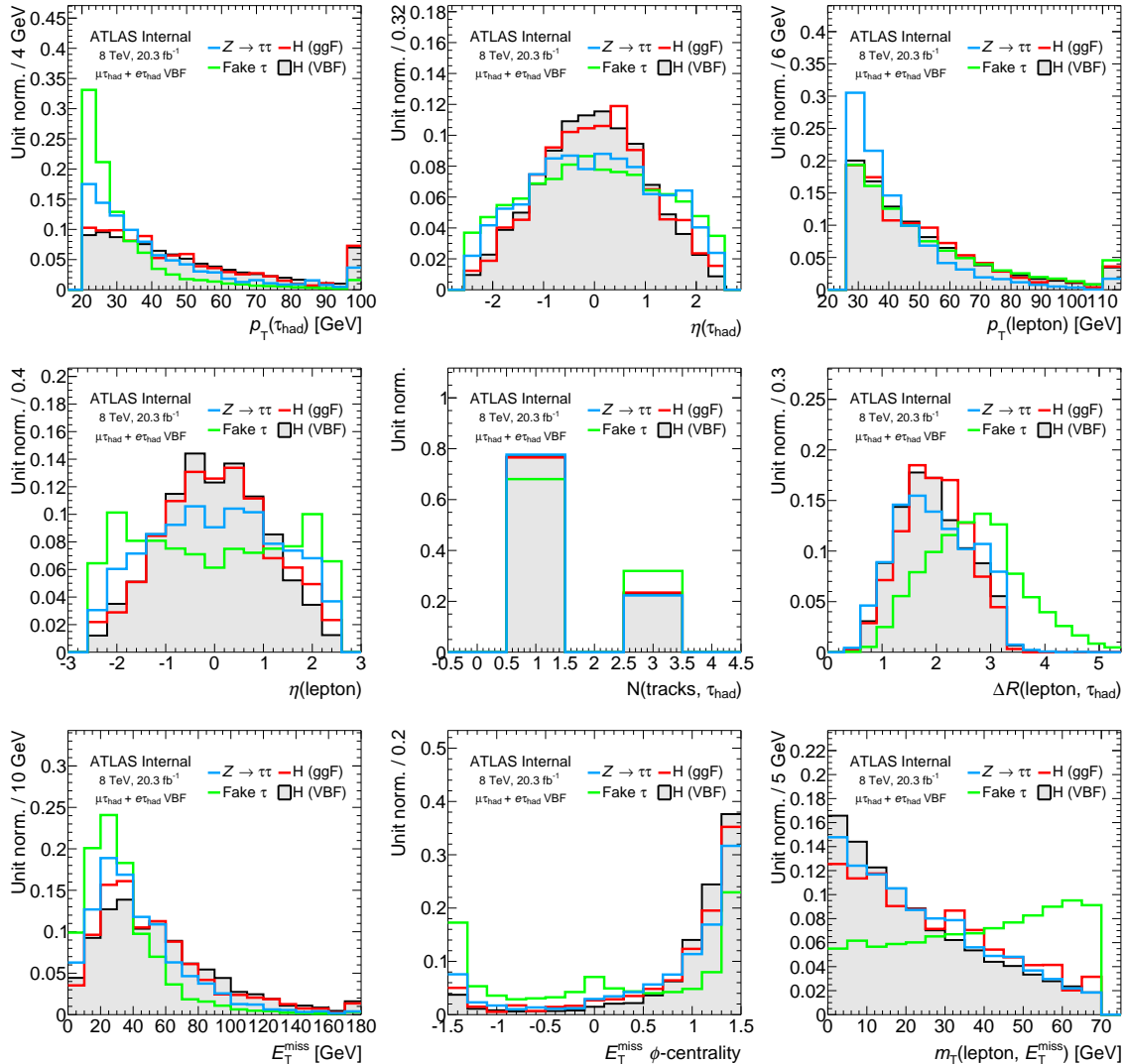


Figure 5.13: Predicted signal and background distributions in the VBF category normalized to unit area and overlaid.

5. $H \rightarrow \tau\ell\tau_{\text{HAD}}$ STRATEGY

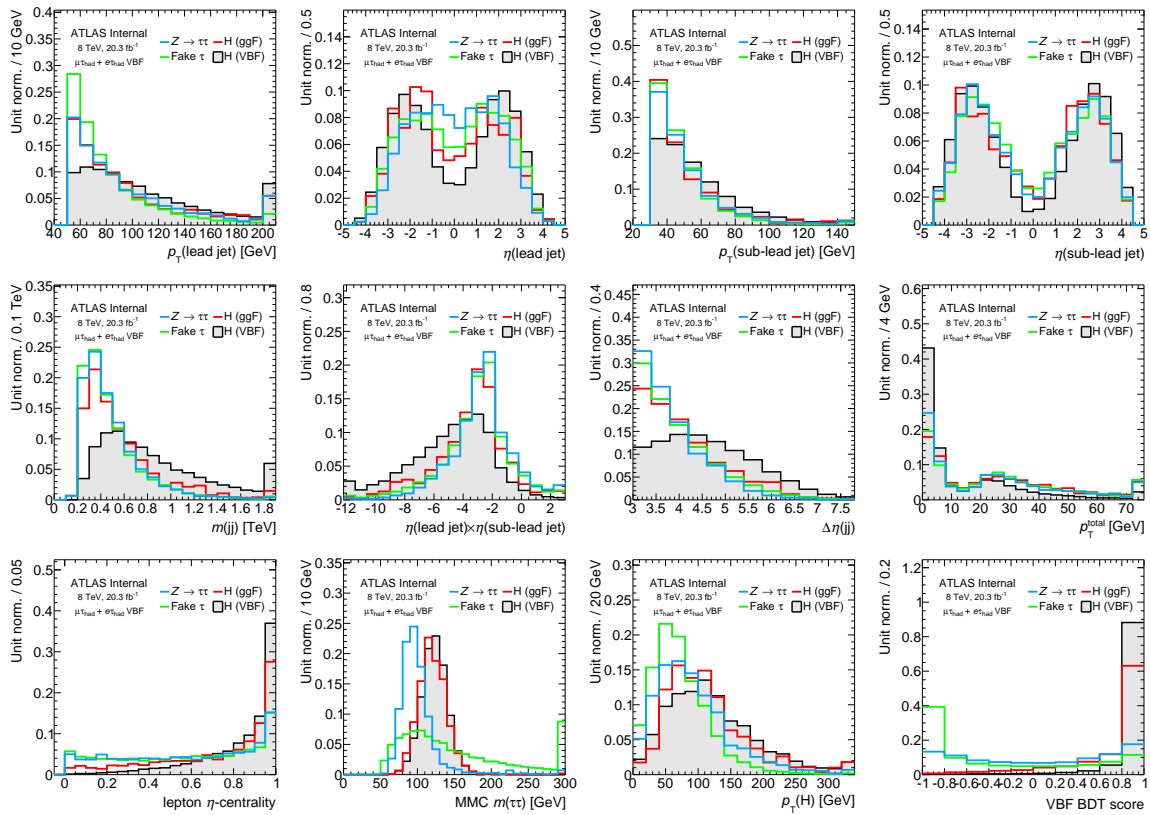


Figure 5.14: Predicted signal and background distributions in the VBF category normalized to unit area and overlaid.

5.6.2 Discrimination

One of the strengths of the BDT analysis is that it can exploit correlations between input variables for better background discrimination. This is especially true in the VBF category where there is interplay between the VBF-oriented variables and the $H \rightarrow \tau\tau$ -oriented variables. Another strength is the BDT can make cuts as hyper-surfaces around weakly discriminating variables instead of rectangular cuts.

Two-dimensional contours of variables of interest are shown in Figs. 5.15 and 5.16 for VBF $H \rightarrow \tau\tau$, $Z \rightarrow \tau\tau$, and $j \rightarrow \tau_{\text{had}}$. The behavior helps demonstrate the utility of the BDT analysis.

$\Delta R(\text{lepton}, \tau_{\text{had}})$ and $m_{\tau\tau}^{\text{MMC}}$:

$m_{\tau\tau}^{\text{MMC}}$ is not strongly correlated with $\Delta R(\text{lepton}, \tau_{\text{had}})$ for $Z/H \rightarrow \tau\tau$ because they are resonant decays. For $j \rightarrow \tau_{\text{had}}$, there is a strong correlation.

$p_T(H)$ and $\Delta R(\text{lepton}, \tau_{\text{had}})$:

$\Delta R(\text{lepton}, \tau_{\text{had}})$ is strongly correlated with $p_T(H)$ for $Z/H \rightarrow \tau\tau$ because their decay products stem from a resonant decay. For $j \rightarrow \tau_{\text{had}}$, the correlation is weaker.

E_T^{miss} ϕ -centrality and $\Delta R(\text{lepton}, \tau_{\text{had}})$:

E_T^{miss} ϕ -centrality is correlated with $\Delta R(\text{lepton}, \tau_{\text{had}})$ for $Z/H \rightarrow \tau\tau$ because as ΔR shrinks, the E_T^{miss} is more spatially constrained. For $j \rightarrow \tau_{\text{had}}$, the E_T^{miss} is more randomly distributed relative to the $\ell + \tau_{\text{had}}$ system.

m_{jj} and $\Delta\eta(jj)$:

For all processes, m_{jj} and $\Delta\eta(jj)$ are strongly but not perfectly correlated, hence additional discrimination power is available.

m_{jj} and $\Delta R(\text{lepton}, \tau_{\text{had}})$:

For $Z/H \rightarrow \tau\tau$, there is correlation between m_{jj} and $\Delta R(\text{lepton}, \tau_{\text{had}})$ because the $\tau\tau$ system is recoiling off of the dijet system. This is an example of interplay between VBF and $\tau\tau$ kinematics.

m_{jj} and $m_{\tau\tau}^{\text{MMC}}$:

For all processes, m_{jj} and $m_{\tau\tau}^{\text{MMC}}$ are not strongly correlated, and their individual discrimination power is comparable. Extracting signal from a fit of the ditau mass is therefore not obviously the best candidate.

5. $H \rightarrow \tau_\ell \tau_{\text{had}}$ STRATEGY

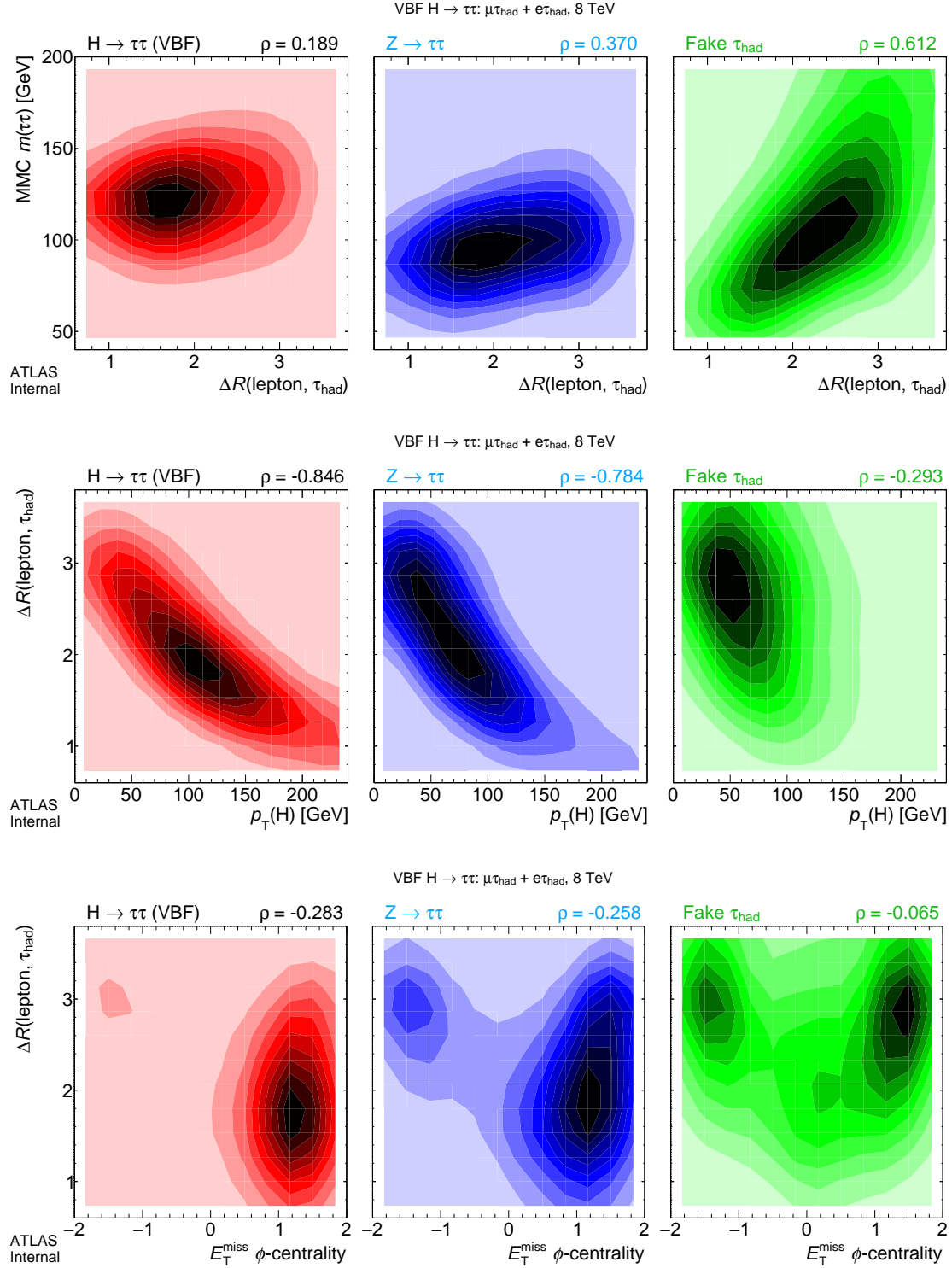


Figure 5.15: Contours of kinematic correlations in the VBF category for VBF $H \rightarrow \tau\tau$ (left), $Z \rightarrow \tau\tau$ (center), and fakes (right).

5. $H \rightarrow \tau_\ell \tau_{\text{had}}$ STRATEGY

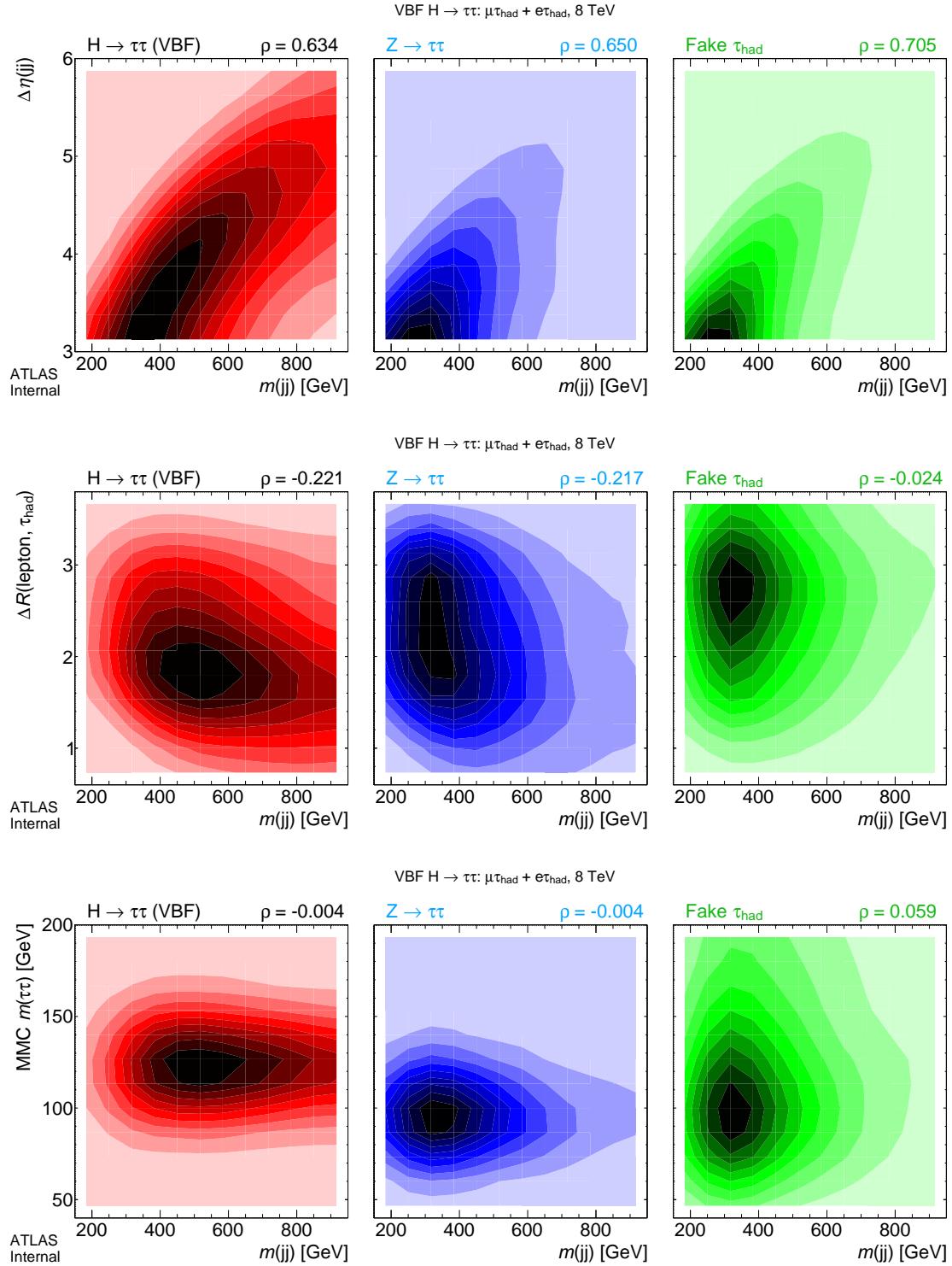


Figure 5.16: Contours of kinematic correlations in the VBF category for VBF $H \rightarrow \tau\tau$ (left), $Z \rightarrow \tau\tau$ (center), and fakes (right).

5. $H \rightarrow \tau_\ell \tau_{\text{HAD}}$ STRATEGY

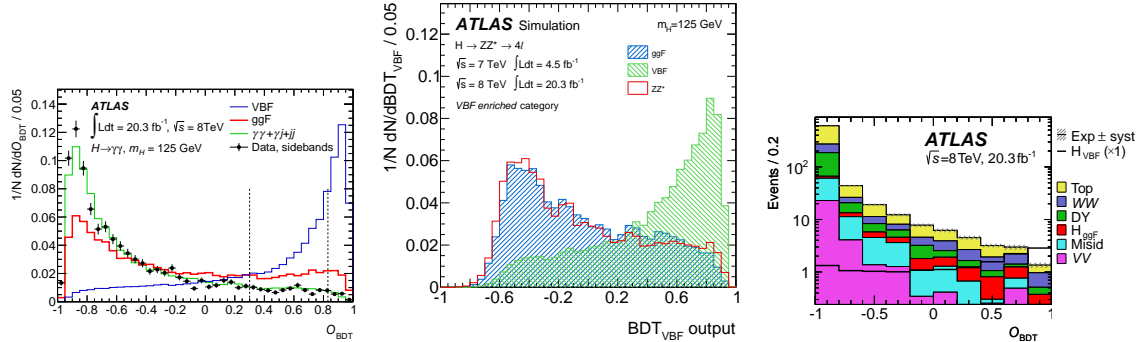


Figure 5.17: Overlaid shapes of BDT outputs for signal and background processes in the VBF $H \rightarrow \gamma\gamma$ [92], VBF $H \rightarrow ZZ^*$ [93], and VBF $H \rightarrow WW^*$ [94] analyses.

5.6.3 MVAs in other VBF analyses

The $H \rightarrow \tau\tau$ analysis is one of many recent VBF Higgs analyses on ATLAS to adopt a MVA approach.

In the $H \rightarrow \gamma\gamma$ and $H \rightarrow ZZ^*$ analyses, a VBF BDT is derived which is meant to be uncorrelated with m_H . These BDT discriminators use similar input variables as the $H \rightarrow \tau\tau$ VBF BDT, such as m_{jj} and $\Delta\eta(jj)$. For $H \rightarrow \gamma\gamma$, a requirement on the output of the BDT discriminator is made ($O_{\text{BDT}} \geq 0.83$) to enrich the VBF $H \rightarrow \gamma\gamma$ process, and the signal is then extracted from a fit of $m_{\gamma\gamma}$. For $H \rightarrow ZZ^*$, the signal is extracted via a two-dimensional fit of the VBF BDT discriminator and $m_{4\ell}$.

The $H \rightarrow WW^*$ MVA analysis takes the same approach as the $H \rightarrow \tau\tau$ analysis. Variables correlated with the reconstructed Higgs mass, including m_T and $m_{\ell\ell}$, are included in the BDT discriminator, and the signal yield is extracted from a fit of the BDT output.

Predicted BDT discriminator outputs are shown in Fig. 5.17 for the $H \rightarrow \gamma\gamma$, $H \rightarrow ZZ^*$, and $H \rightarrow WW^*$ analyses. Good discrimination is found between signal and background processes. The measured signal strength for these analyses is shown in Table 5.8.

Table 5.8: Measured VBF signal strength in the other major ATLAS analyses: $H \rightarrow \gamma\gamma$ [92], $H \rightarrow ZZ^*$ [93], and $H \rightarrow WW^*$ [94].

channel	$H \rightarrow \gamma\gamma$	$H \rightarrow ZZ^*$	$H \rightarrow WW^*$
signal strength	$\mu_{\text{VBF}} = 0.8 \pm 0.7$	$\mu_{\text{VBF}+VH} = 0.3^{+1.6}_{-0.9}$	$\mu_{\text{VBF}} = 1.3 \pm 0.5$

CHAPTER 6

Signal and background predictions

The modeling of physics processes relevant to the $H \rightarrow \tau\tau$ analysis are described, with emphasis on the VBF $H \rightarrow \tau_\ell \tau_{\text{had}}$ channel. This draws from internal documentation of the recent ATLAS $H \rightarrow \tau\tau$ publication [103].

6.1 $Z \rightarrow \tau\tau$

The $Z \rightarrow \tau\tau$ process constitutes a major and irreducible background to all three final states of the $H \rightarrow \tau\tau$ analysis. Its modeling is therefore critical. It is also challenging to validate because the poor mass resolution of $m_{\tau\tau}$ implies finding a region of data orthogonal to the $H \rightarrow \tau\tau$ signal regions but rich in $Z \rightarrow \tau\tau$ events is not possible.

6.1.1 $Z(\rightarrow \ell\ell) + \text{jets}$ in simulation

The simplest approach is to use simulation to model $Z \rightarrow \tau\tau$. Unfortunately, ATLAS has observed in the $Z \rightarrow ee$ and $Z \rightarrow \mu\mu$ processes that mis-modeling is present in various aspects of $Z(\rightarrow \ell\ell) + \text{jets}$ kinematics. These aspects include the $Z p_T$ and dijet kinematics, as shown in Fig. 6.1 and Fig. 6.2, respectively.

These mis-modelings are worrisome for $H \rightarrow \tau\tau$ analyses because they rely on accurate modeling of these kinematics. For example, mis-modeling in p_T^Z is problematic because this variable defines the boosted category of the $H \rightarrow \tau\tau$ analysis. It is also strongly correlated with discriminating variables like $\Delta R(\tau\tau)$. Mis-modeling in dijet kinematics like m_{jj} is of even greater concern because they are among the most powerful and high-profile discriminating variables in the VBF category.

Some versions of the ATLAS $H \rightarrow \tau\tau$ analysis use simulated $Z \rightarrow \tau\tau$ with corrections derived from $Z \rightarrow \ell\ell$ events in data [89]. While helpful, these corrections are one-dimensional and cannot

6. SIGNAL AND BACKGROUND PREDICTIONS

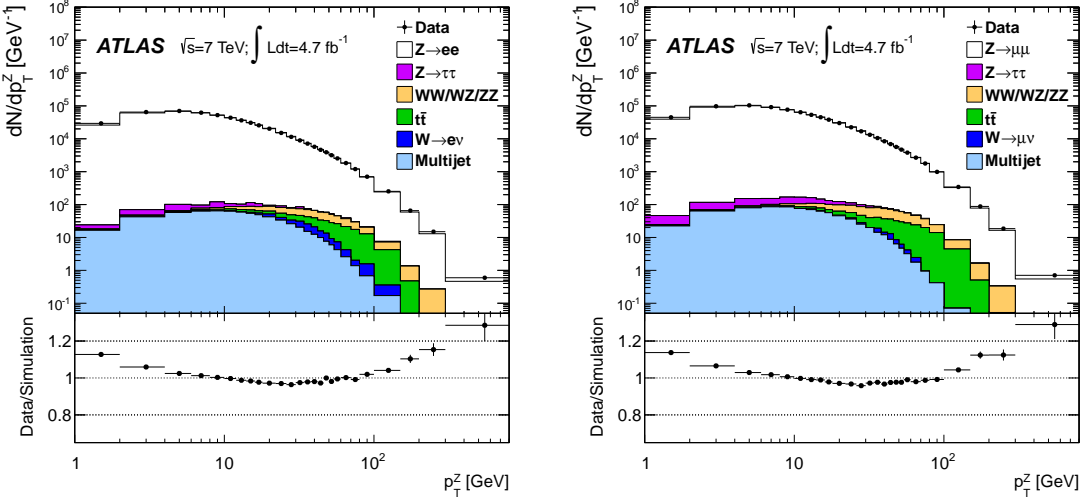


Figure 6.1: Comparison of data and various predictions of p_T^Z for $Z \rightarrow ee$ (left) and $Z \rightarrow \mu\mu$ (right) in 2011 data-taking [104]. Mis-modeling is observed.

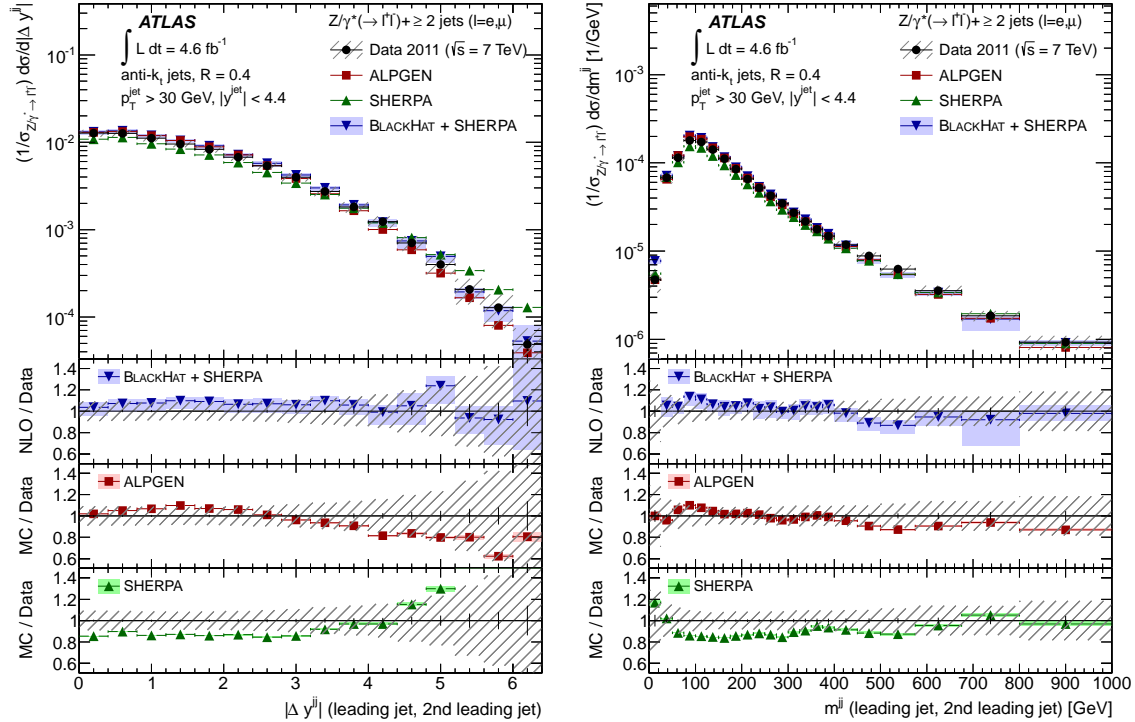


Figure 6.2: Comparison of data and various predictions in $Z \rightarrow \ell\ell$ events of $\Delta y(jj)$ (left) and m_{jj} (right) in 2011 data-taking [105]. Mis-modeling is observed for all predictions.

6. SIGNAL AND BACKGROUND PREDICTIONS

account for potential correlations in the mis-modeling. For these reasons, this approach is not used in the recent publication.

6.1.2 Embedding

A more data-driven approach to modeling $Z \rightarrow \tau\tau$ is used wherein $Z \rightarrow \mu\mu$ events are tagged in data and the muons are replaced with simulated tau lepton decays. This exploits lepton universality in Z decays and has the great advantage of taking all $Z + \text{jets}$ features directly from data, such as $Z p_{\text{T}}$, dijet kinematics, and soft hadronic activity. Only the tau lepton decays and the detector response of the decay products are taken from simulation. The former is measured with excellent precision at B -factories [106], and the latter is an ongoing area of study within ATLAS detector performance groups.

$Z \rightarrow \mu\mu$ events are selected in data by requiring an event fire the lowest unprescaled dimuon trigger and have at least two reconstructed muons with $p_{\text{T}} > 15$ GeV and $|\eta| < 2.5$. All possible pairs of muons are then considered which satisfy $p_{\text{T}}^{\text{lead}} > 20$ GeV, muon isolation requirements, have opposite charges, and have $m_{\mu\mu} > 40$ GeV. The pair which has mass closest to the Z mass is then chosen as the Z decay products.

Tau lepton decays are then simulated with TAUOLA with the same four-momenta as the muons associated to the Z decay and sent through the full ATLAS detector simulation, digitization, and reconstruction. The decays can be set to whatever final state desired (e.g., $\tau_e \tau_{\text{had}}$) within TAUOLA.

The simulated $\tau\tau$ system is then merged with the data $Z \rightarrow \mu\mu$ event by removing tracks and calorimeter cells associated to the muons and inserting tracks and cells from the tau lepton decays. For subtracting the calorimeter cells, deposited cell energies are derived from a simulated $Z \rightarrow \mu\mu$ event with the same kinematics as the data $Z \rightarrow \mu\mu$ event. The hybrid event, with a simulated $\tau\tau$ system and a $Z + \text{jets}$ event from data, is then re-run through the ATLAS reconstruction, yielding the so-called *embedded* $Z \rightarrow \tau\tau$ event. Event displays of this procedure is shown in Fig. 6.3.

6.1.3 Validation

Various steps of the embedding procedure are validated with creative choices of output and input datasets of the embedding algorithms. For example, to test the subtraction of data muons, the embedding procedure is run on data $Z \rightarrow \mu\mu$ events merged with simulated $Z \rightarrow \mu\mu$ decays, and the output is compared with the original data $Z \rightarrow \mu\mu$ events. For a global test of the fidelity of the method, the embedding procedure is run on simulated $Z \rightarrow \mu\mu$ events merged with simulated $Z \rightarrow \tau\tau$

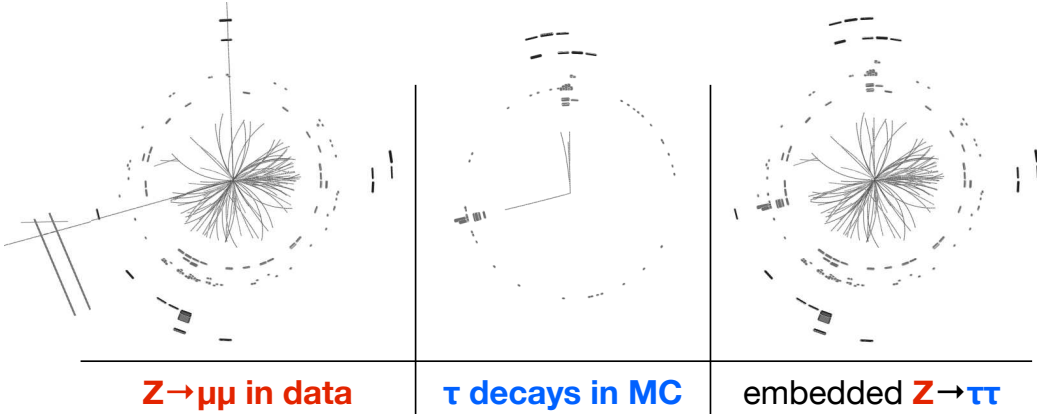


Figure 6.3: Event displays of the three types of events considered in the embedding procedure: a $Z \rightarrow \mu\mu$ event in data (left), a $\tau_{\text{had}}\tau_{\text{had}}$ event in simulation (center), and a hybrid embedding event (right) [107].

decays, and the output is compared with simulated $Z \rightarrow \tau\tau$ events. The results are shown in Fig. 6.4, and no significant biases are observed.

6.1.4 Uncertainties

Since all Z kinematics are taken directly from data, no uncertainties regarding to Z or jet kinematics are considered. However, uncertainties regarding the response of simulating tau decay products and the embedding procedure itself are considered. The uncertainty on the detector response is implemented via the typical collection of uncertainties pertaining to the measured identification efficiency and energy calibration of simulated leptons and τ_{had} at ATLAS.

Two uncertainties regarding the embedding procedure are considered. First, the isolation criteria on the data muons are either relaxed or tightened to test the dependence of the prediction on the $Z \rightarrow \mu\mu$ selection criteria. Second, the amount of cell energy subtracted when removing the data muons is varied by 20%, which is commensurate with the observed differences in the isolation energy between simulated $Z \rightarrow \mu\mu$ events merged with simulated $Z \rightarrow \tau\tau$ decays and simulated $Z \rightarrow \tau\tau$ events.

The pre-fit impact of these uncertainties on the $Z \rightarrow \tau\tau$ prediction is shown in each bin of the VBF discriminator in Fig. 6.5. The largest uncertainty at high VBF BDT score is the nearly 30% statistical uncertainty on the prediction, which is an inevitable limitation of the embedding procedure

6. SIGNAL AND BACKGROUND PREDICTIONS

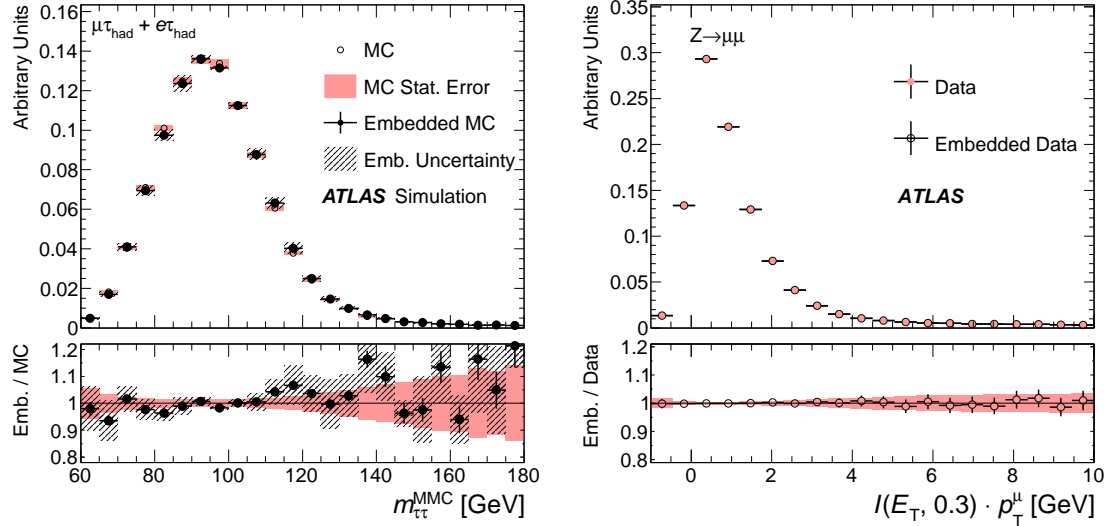


Figure 6.4: Validation of the embedding technique for simulated tau lepton decays in simulated $Z \rightarrow \mu\mu$ events (left) and simulated muons in data $Z \rightarrow \mu\mu$ events (right) [2]. Good agreement is observed in both, for the $m_{\tau\tau}^{\text{MMC}}$ (left) and isolation energy (right).

since it relies on the finite number of $Z \rightarrow \mu\mu$ events in data. The largest systematic uncertainties are components of the τ_{had} energy scale uncertainty, which are each 10-15%. These propagate directly to shifts of the $m_{\tau\tau}^{\text{MMC}}$.

6.2 $j \rightarrow \tau_{\text{had}}$ mis-identification

The largest background in the VBF $H \rightarrow \tau_\ell \tau_{\text{had}}$ analysis is from events where a jet is mis-identified as a τ_{had} ($j \rightarrow \tau_{\text{had}}$), also called *fakes*. The use of data-driven approaches to the prediction is therefore crucial. Unlike the $Z \rightarrow \tau\tau$ background, many regions of data exist which are rich in $j \rightarrow \tau_{\text{had}}$, and these regions can be exploited for prediction and validation. The largest sources of $j \rightarrow \tau_{\text{had}}$ are $W(\rightarrow \ell\nu_\ell) + \text{jets}$, QCD, top, and $Z(\rightarrow \ell\ell) + \text{jets}$ events.

6.2.1 $j \rightarrow \tau_{\text{had}}$ in simulation

Like the $Z \rightarrow \tau\tau$ background, simulation is a simple but deficient means of predicting the $j \rightarrow \tau_{\text{had}}$ background. ATLAS observes mis-modeling in descriptions of jet shapes like the track width and track multiplicity [108], as shown in Fig. 6.6, which τ_{had} jet discriminators rely heavily on. This is especially problematic for τ_{had} because the identification algorithms emphasize tails of distributions like track width, not the bulk, hence detailed corrections to the simulation can be statistically limited.

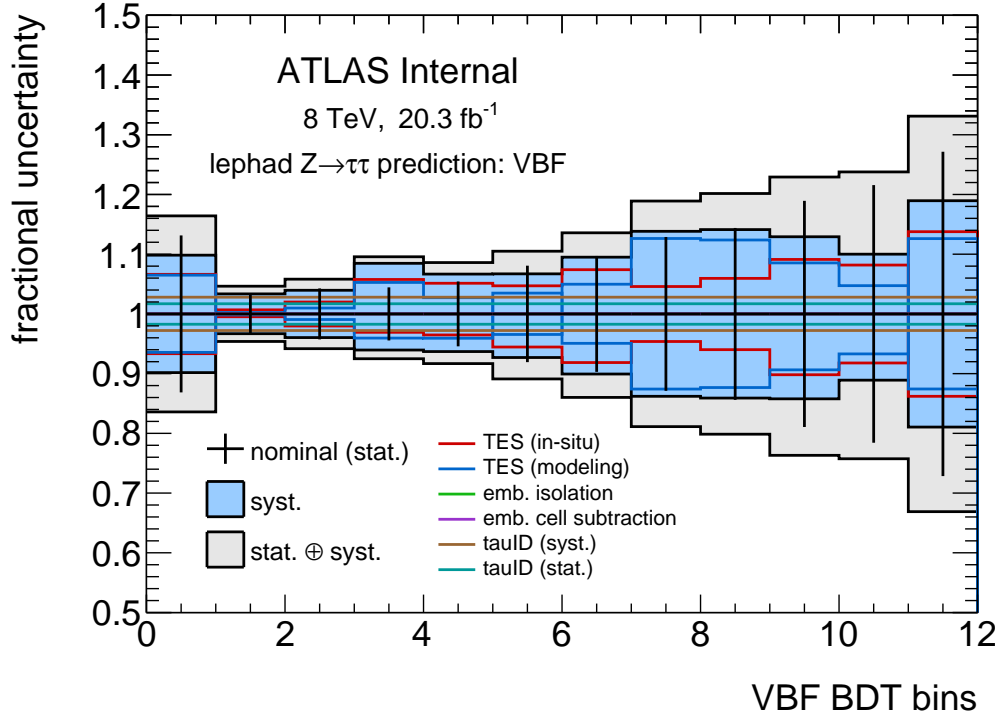


Figure 6.5: The pre-fit fractional uncertainty on the embedded $Z \rightarrow \tau\tau_{\text{had}}$ prediction in each bin of the VBF category for uncertainties pertaining to the embedding procedure and τ_{had} performance.

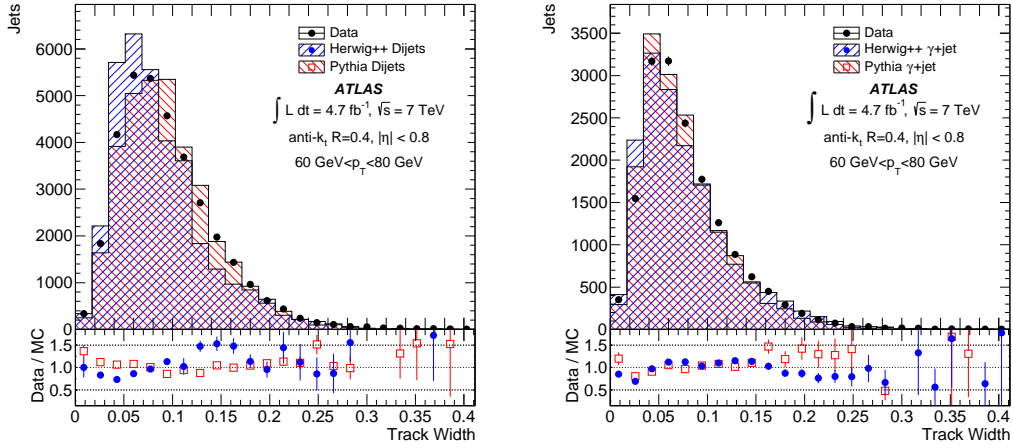


Figure 6.6: Comparison of data and various predictions of jet track width in dijet (left) and $\gamma + \text{jet}$ (right) events [108]. Mis-modeling is observed for all predictions.

6. SIGNAL AND BACKGROUND PREDICTIONS

Additionally, the event kinematics of $W(\rightarrow \ell\nu_\ell) + \text{jets}$ and $Z(\rightarrow \ell\ell) + \text{jets}$ events have known mis-modeling in simulation. The mis-modeling of $Z(\rightarrow \ell\ell) + \text{jets}$ events is discussed in Section 6.1.1, and ATLAS observes comparable mis-modeling in dijet kinematics of $W(\rightarrow \ell\nu_\ell) + \text{jets}$ events, as shown in Fig. 6.7. The mis-modeling of variables like $\Delta y(jj)$ and m_{jj} is of concern since the VBF discriminators depend heavily on these kinematics.

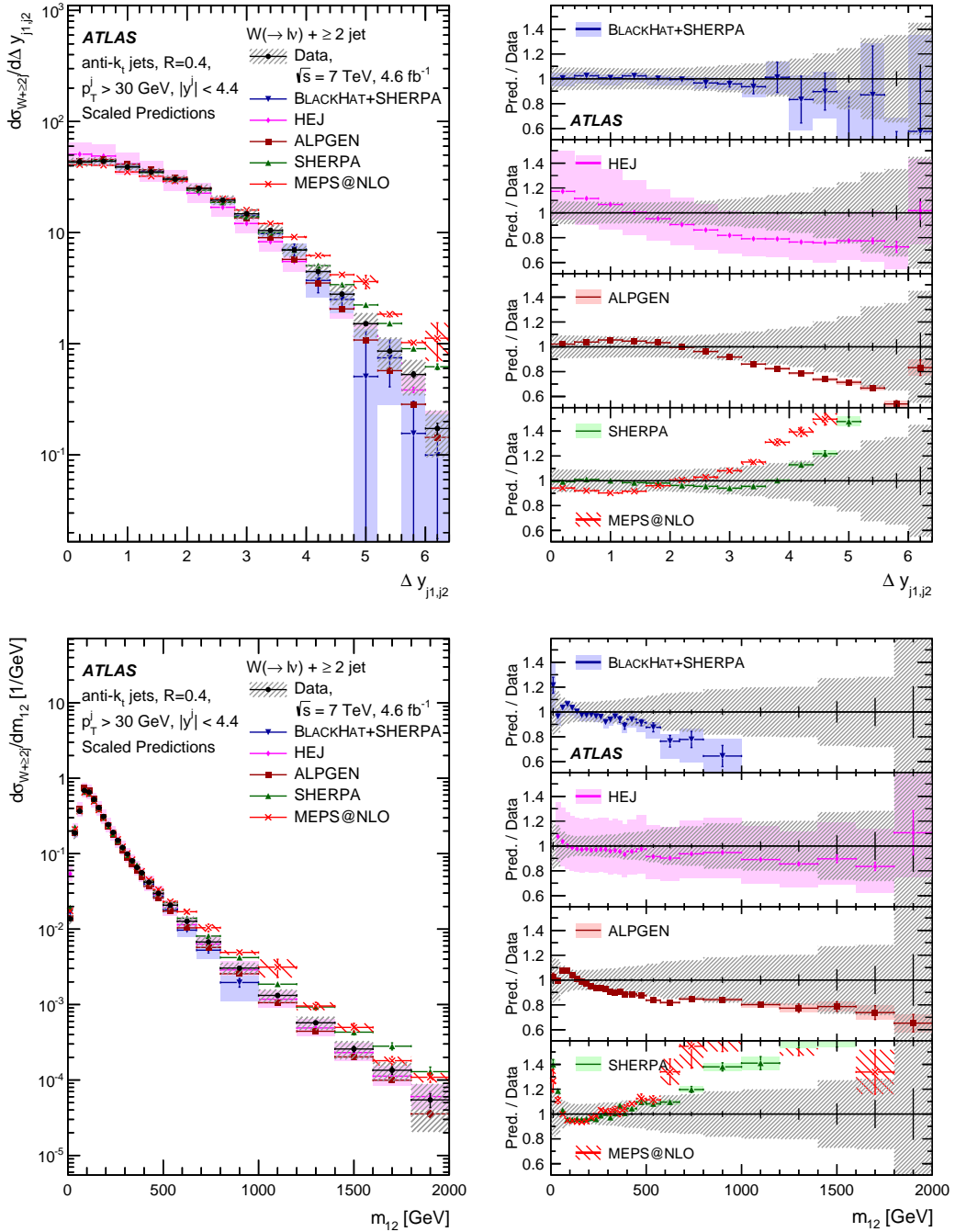


Figure 6.7: Comparison of data and various predictions in $W(\rightarrow \ell\nu\ell) + \text{jets}$ events of $\Delta y(jj)$ (top) and m_{jj} (bottom) in 2011 data-taking [109]. Mis-modeling is observed for all predictions.

Previous ATLAS $H \rightarrow \tau\tau$ analyses have used simulated $W(\rightarrow \ell\nu_\ell) + \text{jets}$, $Z(\rightarrow \ell\ell) + \text{jets}$, and top events with corrections derived from data, in conjunction to same-sign data events, to model $j \rightarrow \tau_{\text{had}}$ [110, 89]. While helpful, these corrections are one-dimensional and cannot account for potential correlations in the mis-modeling, and the same-sign data sample has large statistical uncertainties. For these reasons, this approach is not used in the recent publication.

6.2.2 Fakefactor method

6.2.2.1 Principle

An alternative data-driven approach is taken wherein events in data which pass all the signal region requirements, but fail the τ_{had} identification algorithm, are used to predict $j \rightarrow \tau_{\text{had}}$. The principle of this extrapolation is that τ_{had} identification is uncorrelated with event kinematics like m_{jj} . The kinematics of events where the τ_{had} fails identification criteria then provide an unbiased prediction of $j \rightarrow \tau_{\text{had}}$ kinematics in events where the τ_{had} passes identification.

The anti-identified data sample has a high purity of $j \rightarrow \tau_{\text{had}}$, as shown in Figs. 6.8 and 6.9. The residual contamination of $Z \rightarrow \tau_\ell \tau_{\text{had}}$ and other processes without $j \rightarrow \tau_{\text{had}}$ is nonetheless subtracted from the data to form the $j \rightarrow \tau_{\text{had}}$ estimate. The high purity is helpful because uncertainties on the predicted contamination (e.g., the tau energy scale uncertainty for $Z \rightarrow \tau_\ell \tau_{\text{had}}$) are evaluated to have a negligible impact on the $j \rightarrow \tau_{\text{had}}$ estimate and can be ignored.

The correlation between the τ_{had} identifier and event-level kinematics is checked in data in the VBF same-sign region, as shown in Fig. 6.10. No strong correlations are observed for any event-level kinematic variable, including the final BDT discriminator.

6. SIGNAL AND BACKGROUND PREDICTIONS

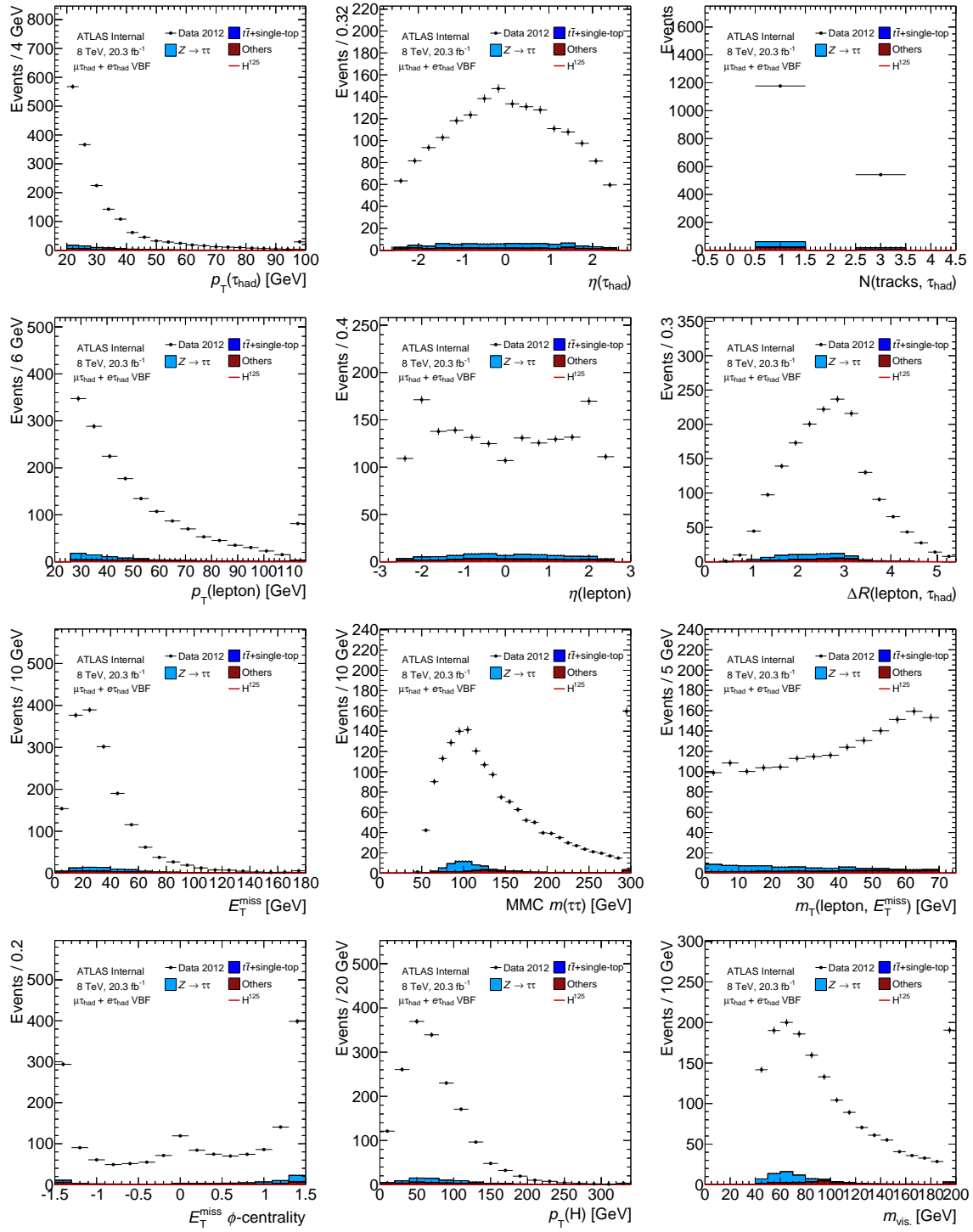


Figure 6.8: Data events in the VBF category which fail τ_{had} identification but fulfill all other requirements. The contamination of $Z \rightarrow \tau_\ell \tau_{had}$ and other processes without $j \rightarrow \tau_{had}$ is less than 10%.

6. SIGNAL AND BACKGROUND PREDICTIONS

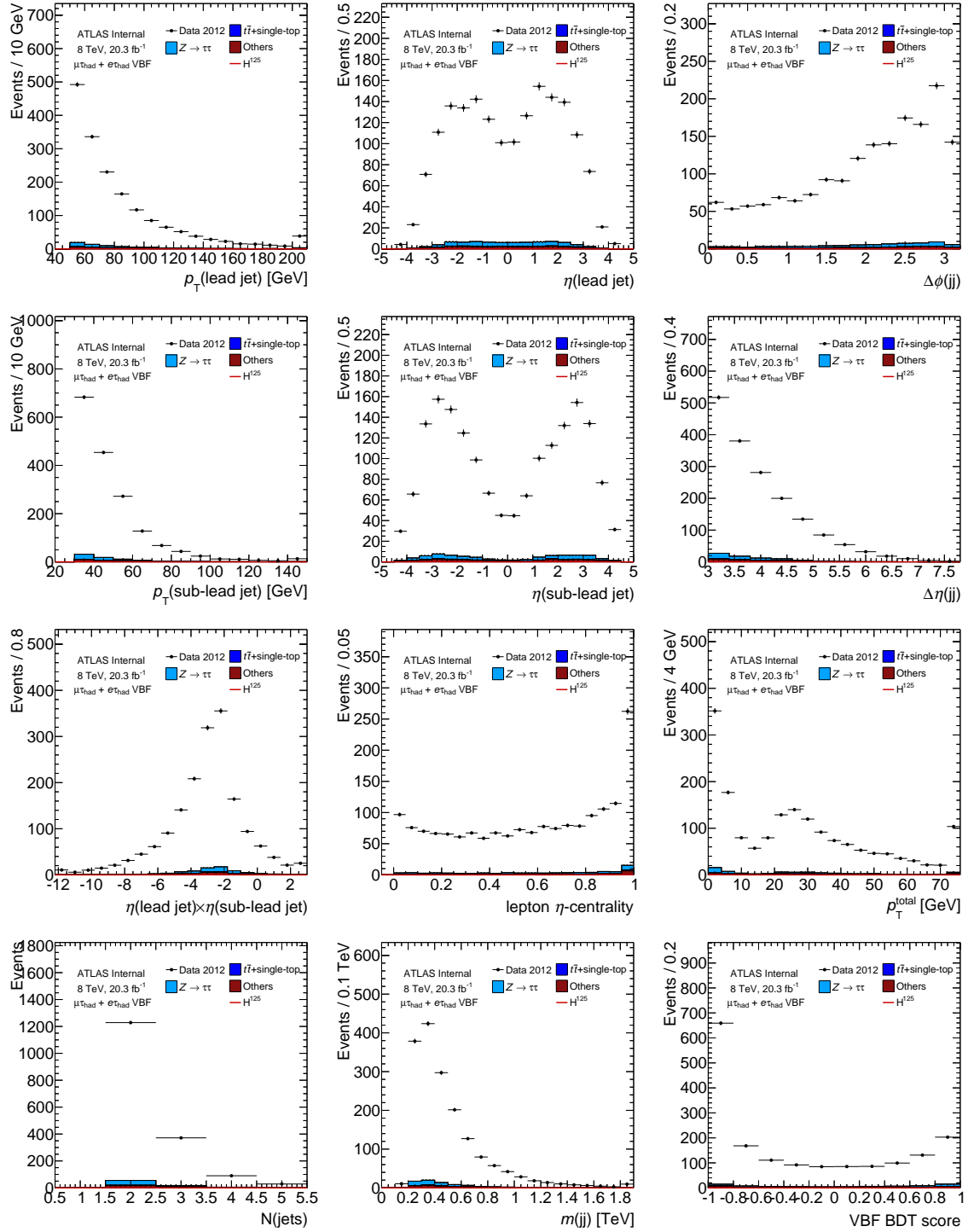


Figure 6.9: Data events in the VBF category which fail τ_{had} identification but fulfill all other requirements. The contamination of $Z \rightarrow \tau_\ell \tau_{\text{had}}$ and other processes without $j \rightarrow \tau_{\text{had}}$ is less than 10%.

6. SIGNAL AND BACKGROUND PREDICTIONS

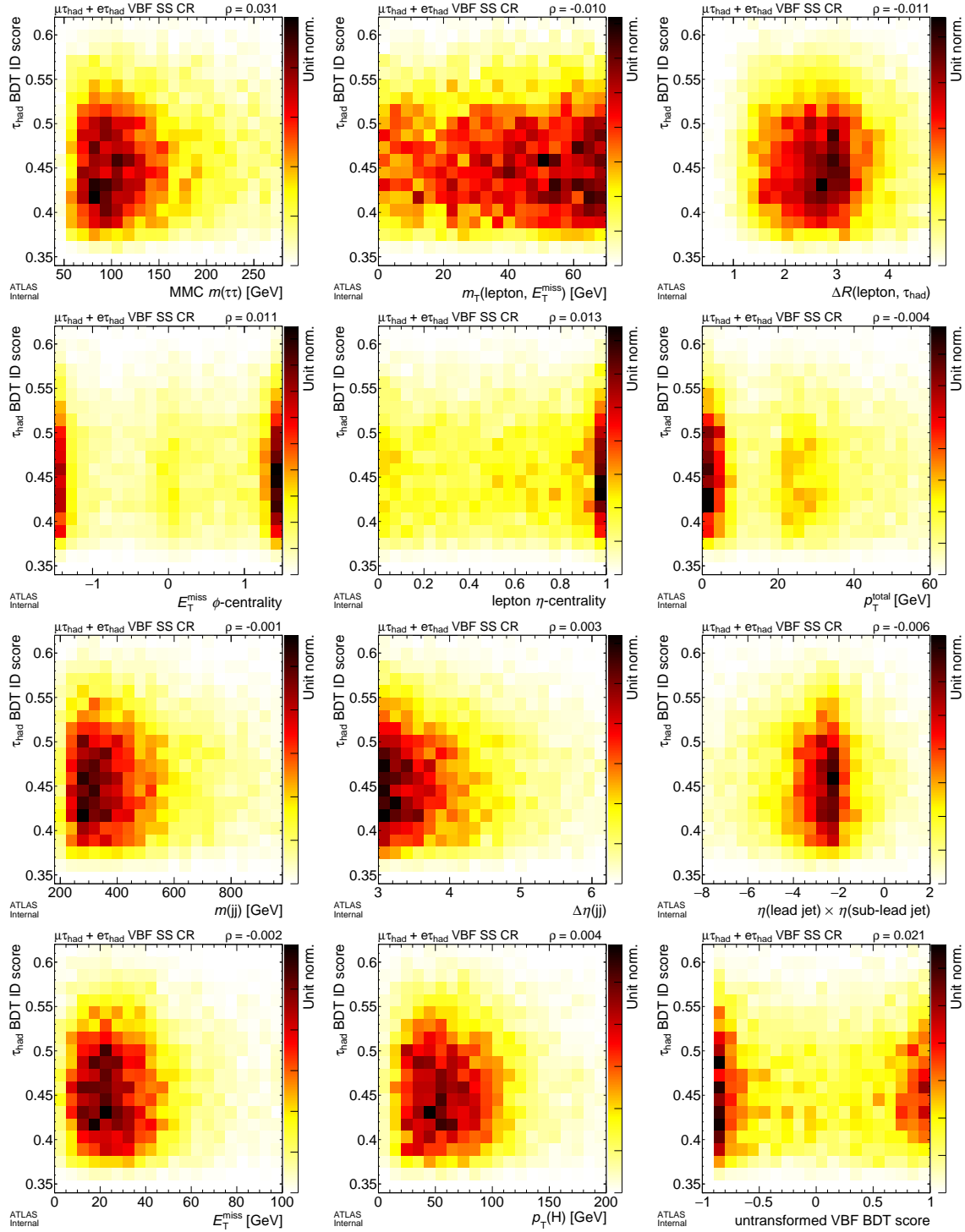


Figure 6.10: Correlations between the τ_{had} BDT identification score and event kinematics in data events in the VBF same-sign region which fail τ_{had} identification but fulfill all other requirements. No strong correlations are observed.

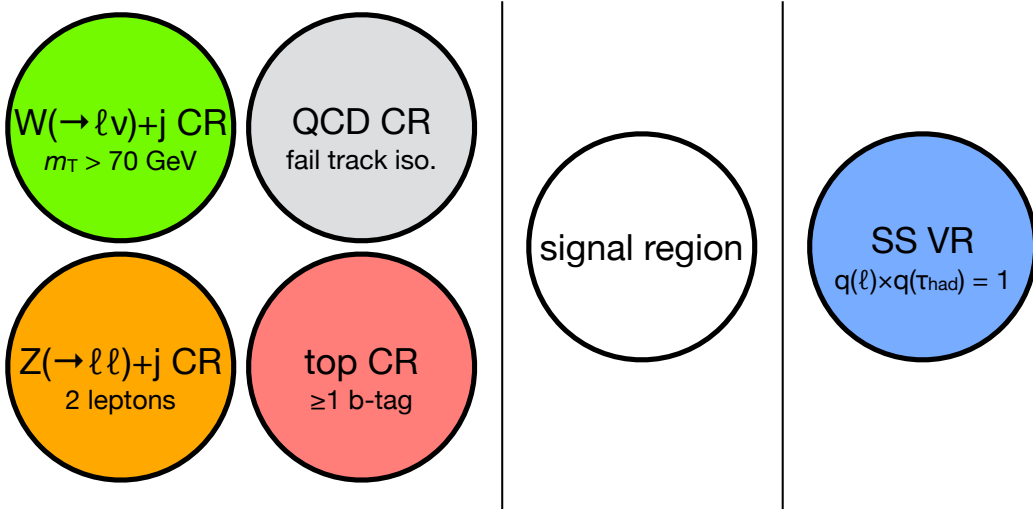


Figure 6.11: Cartoon of the signal, control, and validation regions used which are used in the $j \rightarrow \tau_{\text{had}}$ estimate.

6.2.2.2 Implementation

The $j \rightarrow \tau_{\text{had}}$ prediction is written as:

$$N_{j \rightarrow \tau_{\text{had}}} = (N_{\text{data}}^{\text{fail ID}} - N_{Z \rightarrow \tau\tau \text{ et al.}}^{\text{fail ID}}) \times \text{FF}_{\text{SR}} \quad (6.1)$$

where the number of predicted $j \rightarrow \tau_{\text{had}}$ events $N_{j \rightarrow \tau_{\text{had}}}$ is derived in each bin of any kinematic variable, like m_{jj} . The transfer factor needed to weight data events which fail τ_{had} identification is called the fakefactor (FF). It is parameterized in the number of tracks associated to the τ_{had} and $p_T(\tau_{\text{had}})$, and it is derived in a variety of regions rich in different $j \rightarrow \tau_{\text{had}}$ processes:

$$\text{FF}_{\text{region}} = \left. \frac{\left(N_{\text{data}}^{\text{pass ID}} - N_{Z \rightarrow \tau\tau \text{ et al.}}^{\text{pass ID}} \right)}{\left(N_{\text{data}}^{\text{fail ID}} - N_{Z \rightarrow \tau\tau \text{ et al.}}^{\text{fail ID}} \right)} \right|_{\text{region}} \quad (6.2)$$

where the regions considered here are rich in $j \rightarrow \tau_{\text{had}}$ from $W(\rightarrow \ell \nu_\ell) + \text{jets}$, QCD, $Z(\rightarrow \ell \ell) + \text{jets}$, or top events, or the same-sign region, which is a blend of $j \rightarrow \tau_{\text{had}}$ processes. These regions are shown pictorially in Fig. 6.11.

To protect against potential extrapolation biases, τ_{had} candidates failing identification criteria are required to pass a looser-than-**loose** requirement. This requirement is optimized to minimize the extrapolation without sacrificing the statistics of the estimate, and a requirement of **loose** $\times 0.7$ is chosen. For example, if the **loose** identification criteria requires the τ_{had} BDT score greater than

6. SIGNAL AND BACKGROUND PREDICTIONS

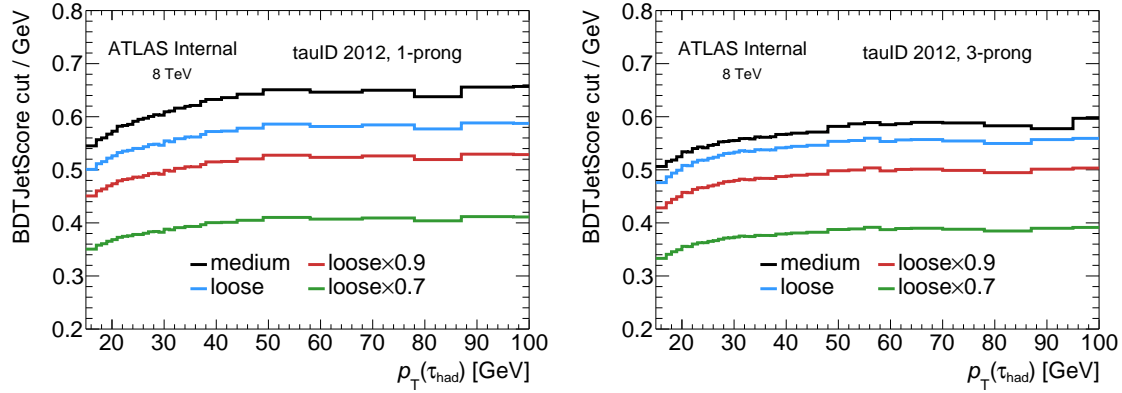


Figure 6.12: Requirements on the τ_{had} jet discriminant, which are defined to have constant signal efficiency as a function of $p_T(\tau_{\text{had}})$, of various operating points for 1-track τ_{had} (left) and 3-track τ_{had} (right).

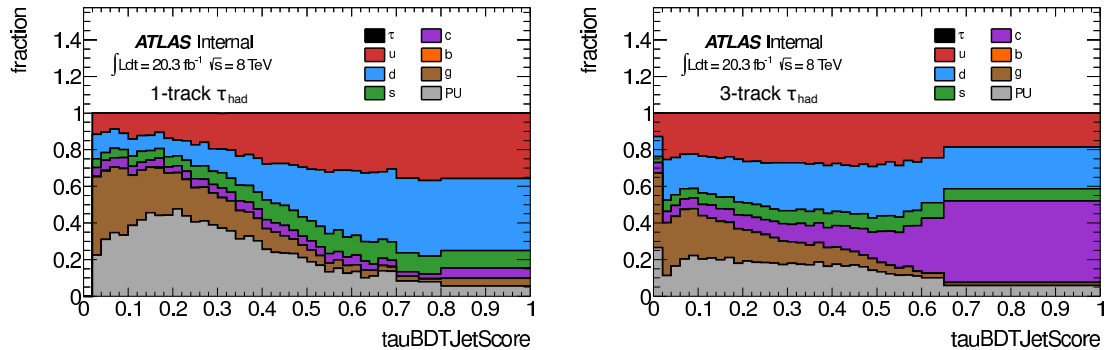


Figure 6.13: Predicted flavor composition of $j \rightarrow \tau_{\text{had}}$ in $W(-\rightarrow \ell\nu_\ell) + \text{jets}$ simulation for 1-track τ_{had} (left) and 3-track τ_{had} (right).

0.5, the **loose** $\times 0.7$ identification criteria requires greater than 0.35. The $p_T(\tau_{\text{had}})$ dependence of this requirement is shown in Fig. 6.12.

The impact of requiring **loose** $\times 0.7$ can be seen by considering the response of various flavors of $j \rightarrow \tau_{\text{had}}$ to the tau identification BDT, as shown in $W(-\rightarrow \ell\nu_\ell) + \text{jets}$ simulation in Fig. 6.13. This requirement reduces the pileup and gluon content of the anti-identified region and gives it a closer flavor resemblance to the identified region.

The fakefactors measured in data in the $W(-\rightarrow \ell\nu_\ell) + \text{jets}$, QCD, $Z(-\rightarrow \ell\ell) + \text{jets}$, and top control regions are shown in Fig. 6.14 for 1-track and 3-track τ_{had} in the VBF category. The measured fakefactors do not show systematic differences between regions given the statistical uncertainty.

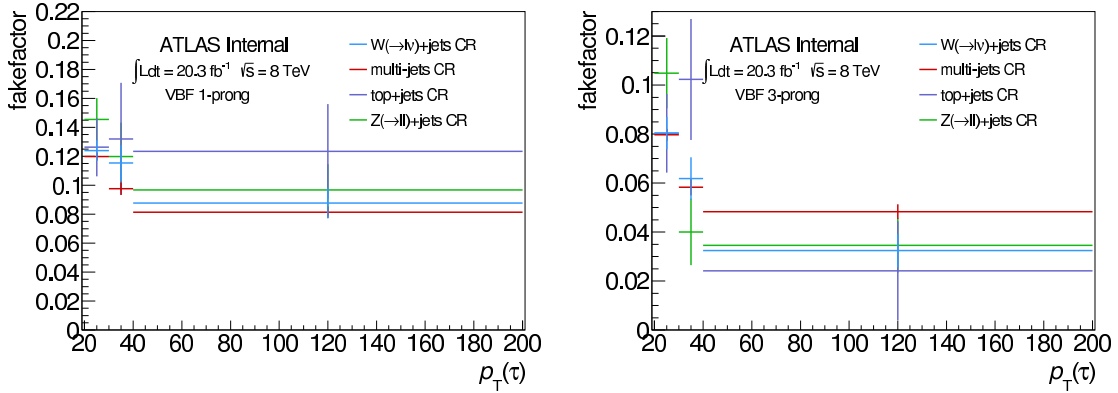


Figure 6.14: Fake factors in the VBF category measured in the various control regions in data for 1-track τ_{had} (left) and 3-track τ_{had} (right).

6.2.2.3 Composition of $j \rightarrow \tau_{\text{had}}$ in the SR

A fakefactor for the signal region can be derived from fakefactors measured in the control regions by using simulation to predict the relative contributions of the $W(\rightarrow \ell\nu_\ell) + \text{jets}$, top, and $Z(\rightarrow \ell\ell) + \text{jets}$ processes in the anti-identified region. The remaining difference between data and prediction is then assumed to be from QCD.

The overall relative contributions are shown in Fig. 6.15, and the differential contributions are shown in Figs. 6.16 and 6.17. No strong dependence on the final VBF BDT discriminator is observed, though dependencies are observed on distributions like $p_T(\text{lepton})$ and E_T^{miss} .

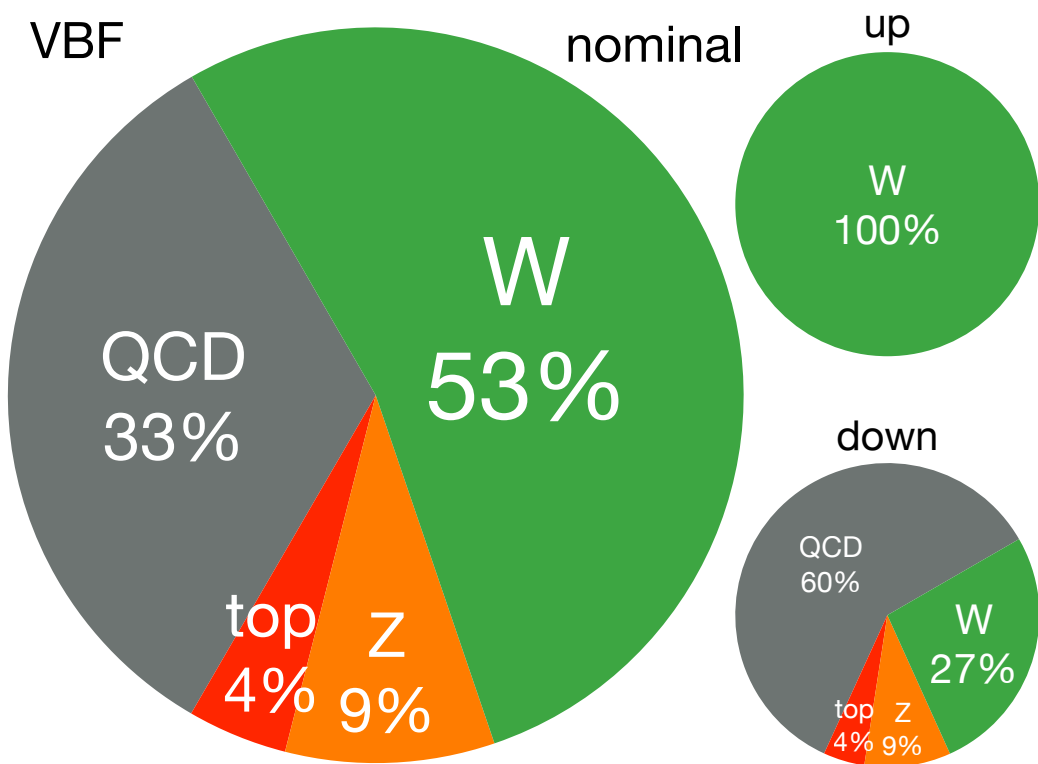


Figure 6.15: A pie chart of the composition of $j \rightarrow \tau_{\text{had}}$ processes in the anti-identified CR as predicted by simulation and data (left) and the systematic variations on the composition (right).

6. SIGNAL AND BACKGROUND PREDICTIONS

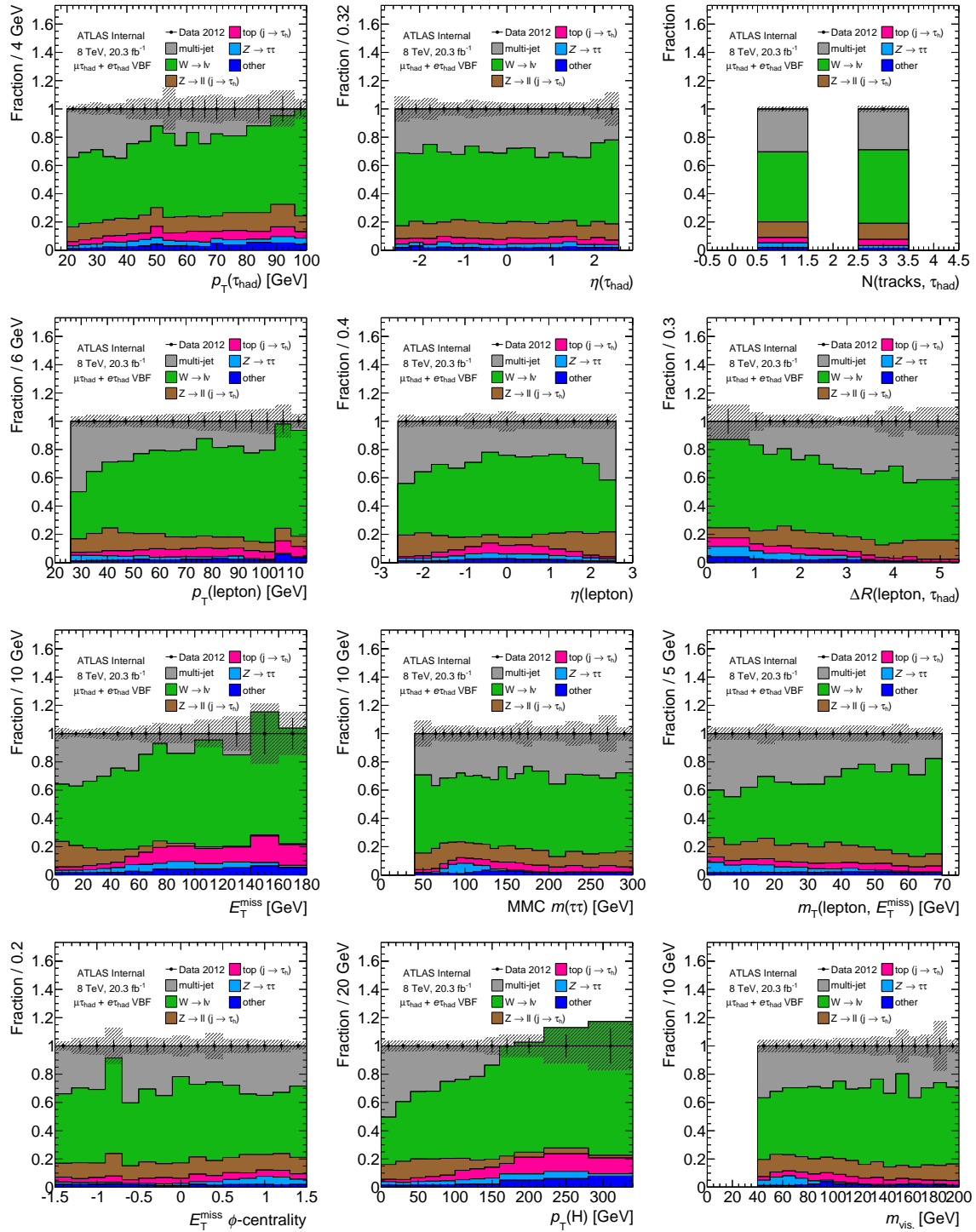


Figure 6.16: The composition of $j \rightarrow \tau_{\text{had}}$ processes in the anti-identified CR as predicted by simulation and data as a function of event kinematics.

6. SIGNAL AND BACKGROUND PREDICTIONS

The signal region fakefactors are then derived as a linear combination of control region fakefactors weighted by the expected contributions. The systematic uncertainties on these contributions is shown in Fig. 6.15. A conservative approach is taken due to the mistrust of simulated $j \rightarrow \tau_{\text{had}}$, and the contribution from $W(\rightarrow \ell\nu_\ell) + \text{jets}$ is allowed to double or halve as the two variations.

The signal region fakefactors are shown in Fig. 6.18. These are also referred to as mixed fakefactors. Since the control region fakefactors do not have significant differences between them, the dominant uncertainty on the signal region fakefactors is typically statistical.

6.2.3 Validation

The fakefactor method is validated by checking predictions of event-level kinematics, especially the BDT discriminant, in the control and validation regions. It is additionally validated by following the same fakefactor procedure in $W(\rightarrow \ell\nu_\ell) + \text{jets}$, top, and $Z(\rightarrow \ell\ell) + \text{jets}$ simulated events in the signal region, where dedicated $\text{FF}_{\text{SR}}^{\text{MC}}$ are derived.

Data and prediction in the same-sign validation region are shown in Fig. 6.19. Data and prediction in the various control regions are further shown in Appendix A. Predictions with simulation are shown in Fig. 6.20. In all plots, good agreement is observed and no systematic biases are uncovered.

6.2.4 Uncertainties

Multiple sources of uncertainties to the fake factor method are considered. First, the statistical uncertainty on the fake factors measured in control regions is propagated to the uncertainty on the signal region fakefactor. Second, the uncertainty on the relative contributions of the different $j \rightarrow \tau_{\text{had}}$ processes are varied and propagated to the signal region fakefactor calculation. Third, the fidelity of using control region fakefactors in the signal region is tested by comparing fakefactors measured in simulation in control regions versus the signal region. No significant difference is found, and the uncertainty is ignored. Fourth, the closure of the method is tested with predictions in the same sign validation region and in the signal region in simulation. No signs of systematic bias in the BDT score prediction are found, and the closure uncertainties are ignored.

The pre-fit impact of these uncertainties on the $j \rightarrow \tau_{\text{had}}$ prediction is shown in each bin of the VBF discriminator in Fig. 6.21. The largest uncertainty at high VBF BDT score is the 15% statistical uncertainty on the prediction. This could be ameliorated by relaxing the `loose` $\times 0.7$ requirement on anti-identified τ_{had} , though this would risk introducing systematic bias of increasing the extrapolation. The largest systematic uncertainty is on the relative contribution of $j \rightarrow \tau_{\text{had}}$ processes, and this only propagates to a 3% uncertainty on the prediction.

6. SIGNAL AND BACKGROUND PREDICTIONS

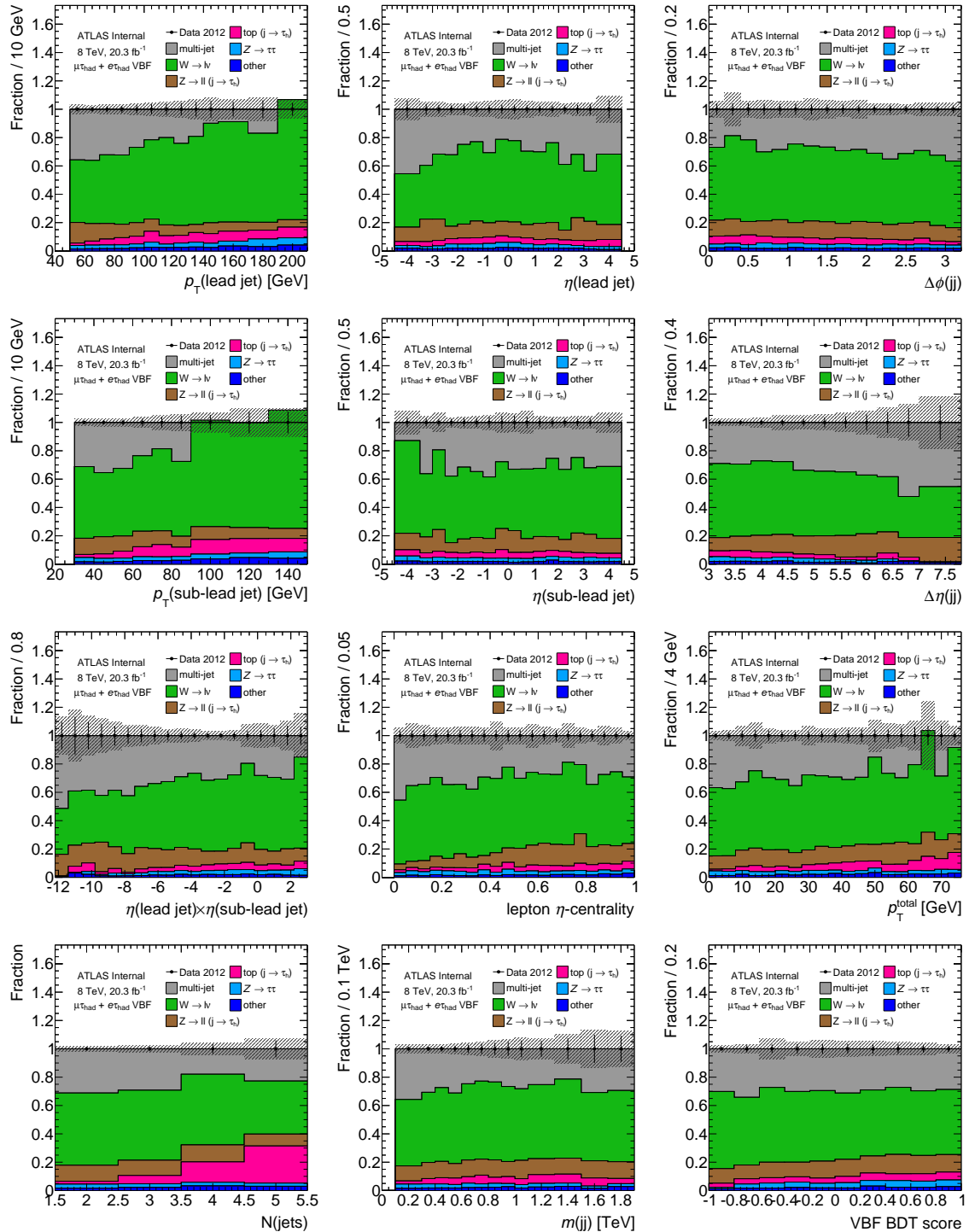


Figure 6.17: The composition of $j \rightarrow \tau_{\text{had}}$ processes in the anti-identified CR as predicted by simulation and data as a function of event kinematics.

6. SIGNAL AND BACKGROUND PREDICTIONS

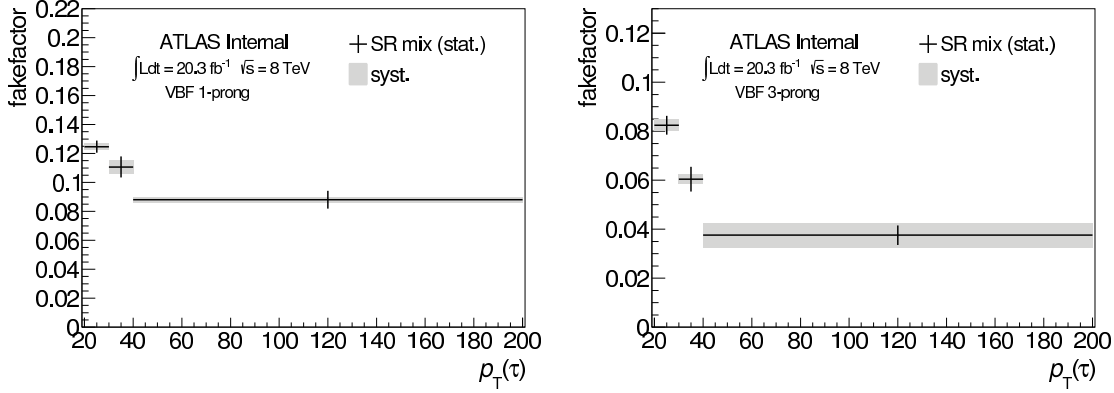


Figure 6.18: Fake factors in the VBF category mixed from the various control regions in data for 1-track τ_{had} (left) and 3-track τ_{had} (right). Statistical and systematic uncertainties are shown.

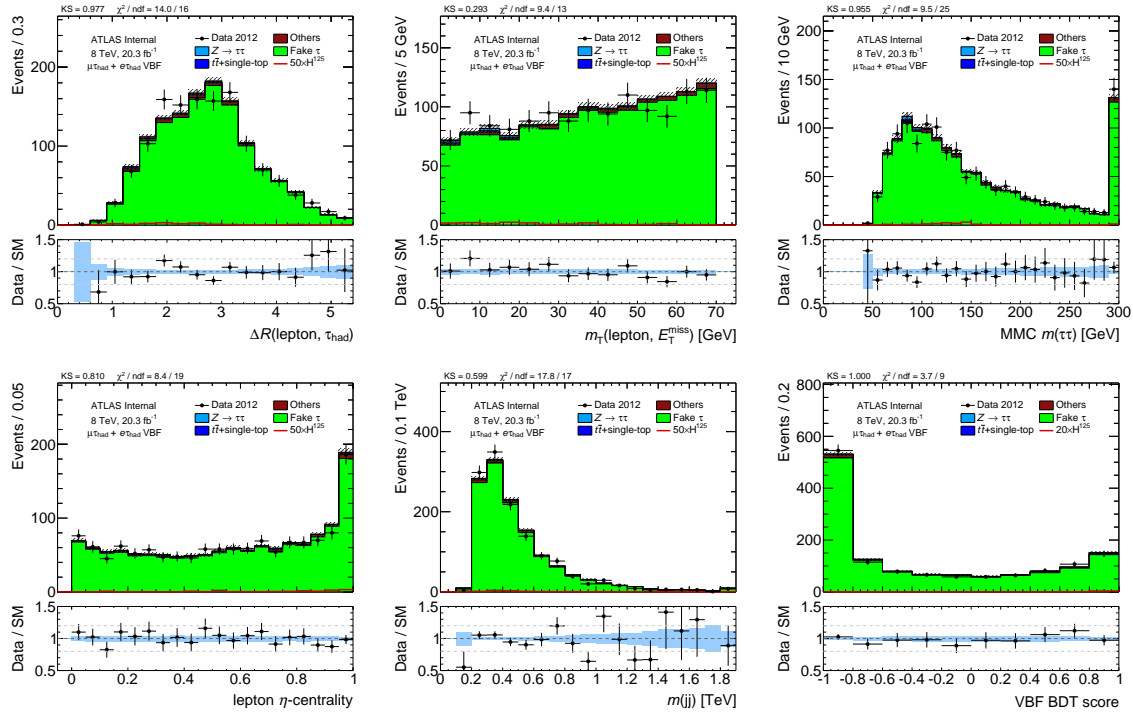


Figure 6.19: Comparison of data and $j \rightarrow \tau_{\text{had}}$ prediction in the same-sign validation region for various event kinematics. The purity of $j \rightarrow \tau_{\text{had}}$ is $\approx 97\%$. Only statistical uncertainties are shown, and no sign of systematic bias is observed. Additional validation is shown in Appendix A.

6. SIGNAL AND BACKGROUND PREDICTIONS

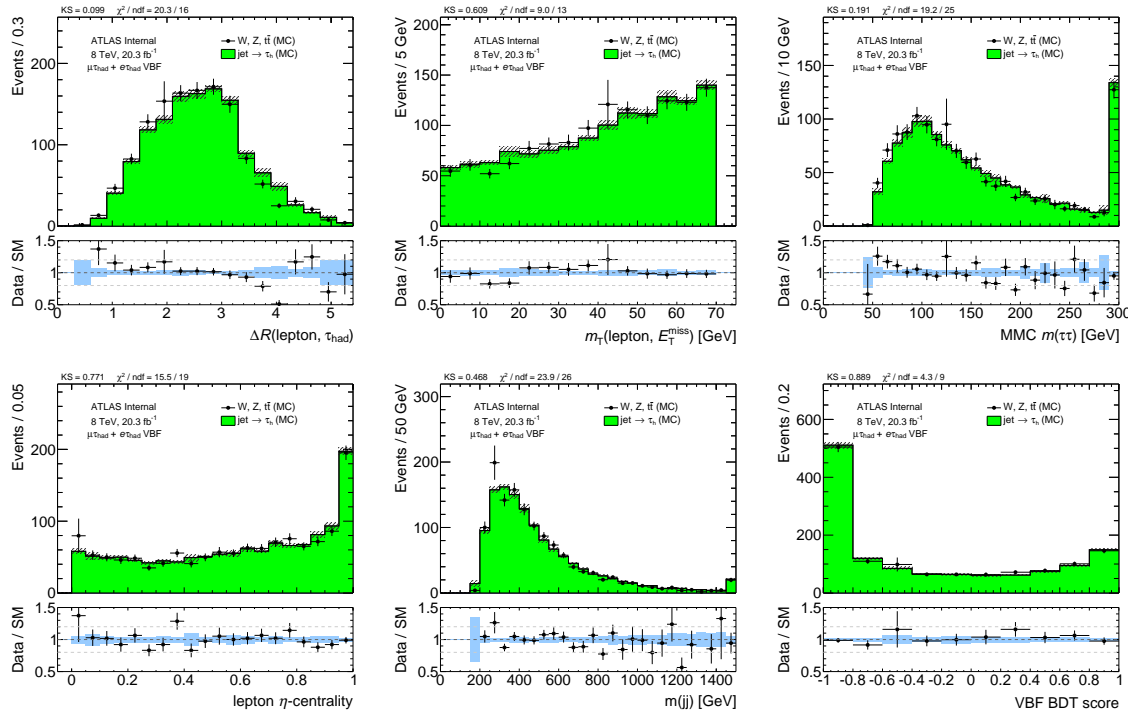


Figure 6.20: Comparison of the prediction of identified taus and the $j \rightarrow \tau_{\text{had}}$ prediction, both in simulation, in the signal region for various event kinematics. Only statistical uncertainties are shown, and no sign of systematic bias is observed. Additional validation is shown in Appendix A.

6.3 top, $Z \rightarrow \ell\ell$, diboson

6.3.1 top

Top events with a true τ_{had} or $\ell \rightarrow \tau_{\text{had}}$ are estimated with simulation and object-level corrections prescribed by the τ_{had} performance group. These include $t\bar{t}$ and single top processes. The normalization is constrained using a top-enriched control region, but detailed corrections to the simulation are not sought because the background is sub-dominant. These top processes only comprise 5% of the background prediction in the VBF category and in the most sensitive bin of the VBF BDT discriminator.

6.3.2 $Z \rightarrow \ell\ell (\ell \rightarrow \tau_{\text{had}})$, diboson

$Z \rightarrow \ell\ell$ events where a lepton is mis-identified as a τ_{had} and diboson events (WW, WZ, ZZ) are estimated with simulation and object-level corrections prescribed by the τ_{had} performance group. Control

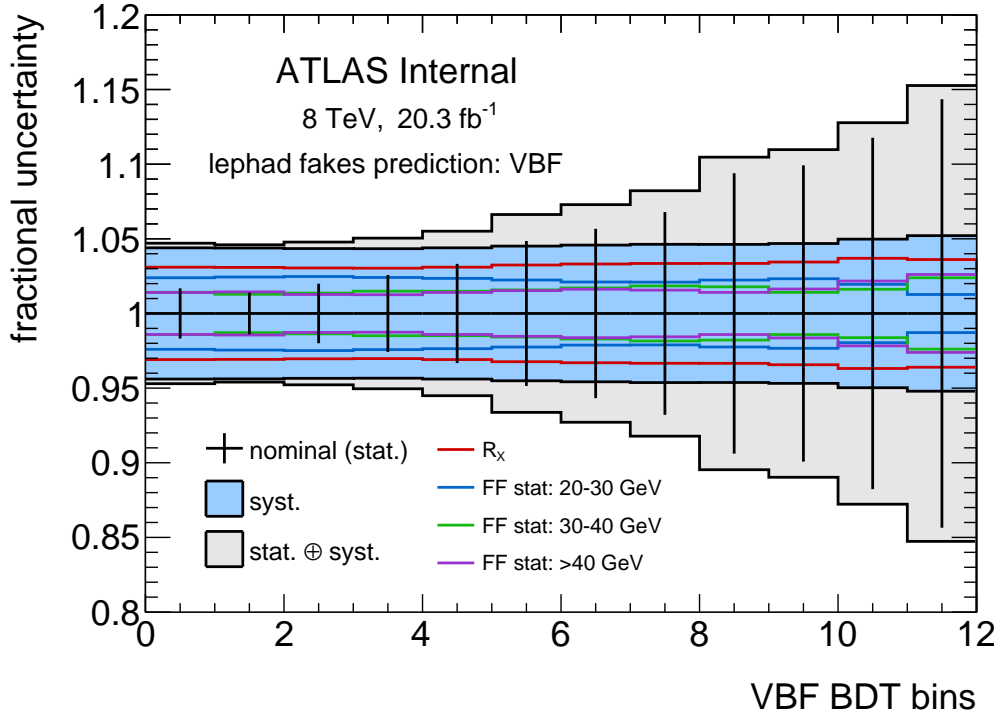


Figure 6.21: The pre-fit fractional uncertainty on the $j \rightarrow \tau_{\text{had}}$ prediction in each bin of the VBF category. R_X refers to the uncertainty on the relative contribution of $j \rightarrow \tau_{\text{had}}$ processes.

regions for these processes are not sought because the processes are too small to find meaningful regions for comparing data with simulation. Detailed corrections to the simulation are also not sought because each processes comprises less than 5% of the background prediction in the VBF category and in the most sensitive bin of the VBF BDT discriminator.

The τ_{had} electron discriminator reduces the $Z \rightarrow ee$ background from problematic to negligible, as shown in Fig. 6.22. Without the electron discriminator, the VBF $Z \rightarrow ee$ background would be difficult to distinguish from VBF $H \rightarrow \tau\tau$ and potentially of comparable magnitude.

6.4 $H \rightarrow \tau\tau$

6.4.1 Samples

The signal $H \rightarrow \tau\tau$ processes are simulated with POWHEG+PYTHIA (ggFH, VBFH) and PYTHIA (WH, ZH, ttH) [2], though the VH and ttH processes are generally negligible in the signal regions considered. The overall normalisation of the ggF process is taken from a calculation at next-to-next-

6. SIGNAL AND BACKGROUND PREDICTIONS

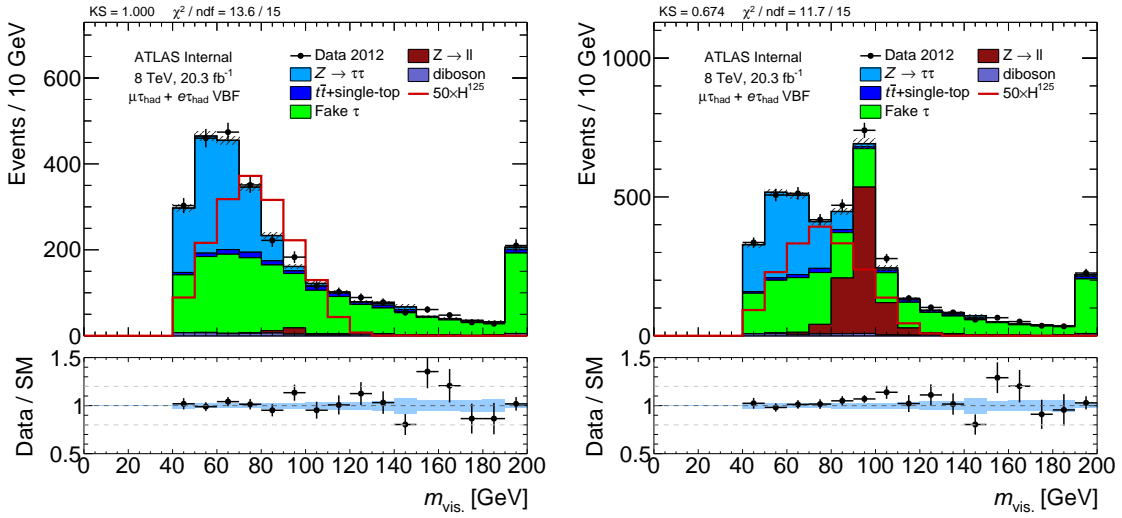


Figure 6.22: Data and prediction for the nominal VBF category (left) and without the τ_{had} electron discriminator (right).

to-leading-order (NNLO) in QCD, including soft-gluon resummation up to next-to-next-to-leading logarithm terms (NNLL). Next-to-leading order (NLO) EW corrections are also included. Production by VBF is normalized to a cross section calculated with NLO QCD and EW corrections with an approximate NNLO QCD correction applied.

Additional corrections to the shape of the generated p_T distribution of Higgs bosons produced via ggF are applied to match the distribution from a calculation at NNLO including the NNLL corrections provided by the HRES2.1 program [2]. In this calculation, the effects of finite masses of the top and bottom quarks are included and dynamical renormalisation and factorisation scales, $\mu_R, \mu_F = \sqrt{m_H^2 + p_T^2}$, are used. A reweighting is performed separately for events with no more than one jet at particle level and for events with two or more jets. In the latter case, the Higgs boson p_T spectrum is reweighted to match the MINLO HJJ predictions. The reweighting is derived such that the inclusive Higgs boson p_T spectrum and the p_T spectrum of events with at least two jets match the HRES2.1 and MINLO HJJ predictions respectively, and that the jet multiplicities are in agreement with (N)NLO calculations from JETVHETO. A similar p_T -dependent weighting is derived for NLO EW corrections of the VBFH production using HAWK, though the corrections are small in the p_T ranges considered here [2].

6.4.2 Uncertainties

Uncertainties regarding the detector response of all physics objects is considered for the signal $H \rightarrow \tau\tau$. This is implemented via the typical collection of uncertainties pertaining to the measured identification efficiency and energy calibration of simulated leptons, τ_{had} , jets, and $E_{\text{T}}^{\text{miss}}$ at ATLAS. The uncertainties on the VBF Higgs production kinematics are generally smaller than the experimental uncertainties.

The pre-fit impact of these uncertainties on the VBF $H \rightarrow \tau\tau$ prediction is shown in each bin of the VBF discriminator in Fig. 6.23. The largest uncertainty at high VBF BDT score is the jet energy scale (JES) uncertainty including uncertainties in the forward region, which are large relative to JES uncertainties within the tracker. JES uncertainties are also the largest class of uncertainties, though no single component propagates to an uncertainty larger than 10% on the VBF $H \rightarrow \tau\tau$ prediction.

6.5 Predictions in the signal region

Predictions in the signal region of the VBF $H \rightarrow \tau_{\ell}\tau_{\text{had}}$ analysis are shown in Fig. 6.24. These input variables feed into the BDT discriminator from which the signal is extracted, which is discussed in Chapter 7. The largest background is from $j \rightarrow \tau_{\text{had}}$, the second largest background is from $Z \rightarrow \tau\tau$, and the remaining backgrounds are individually less than 5% of the total background prediction.

Good agreement between data and prediction is observed for all input variables. This agreement is evaluated with visual inspection and with quantitative measures like $\chi^2/\text{N(D.O.F)}$ and the Kolmogorov-Smirnov test.

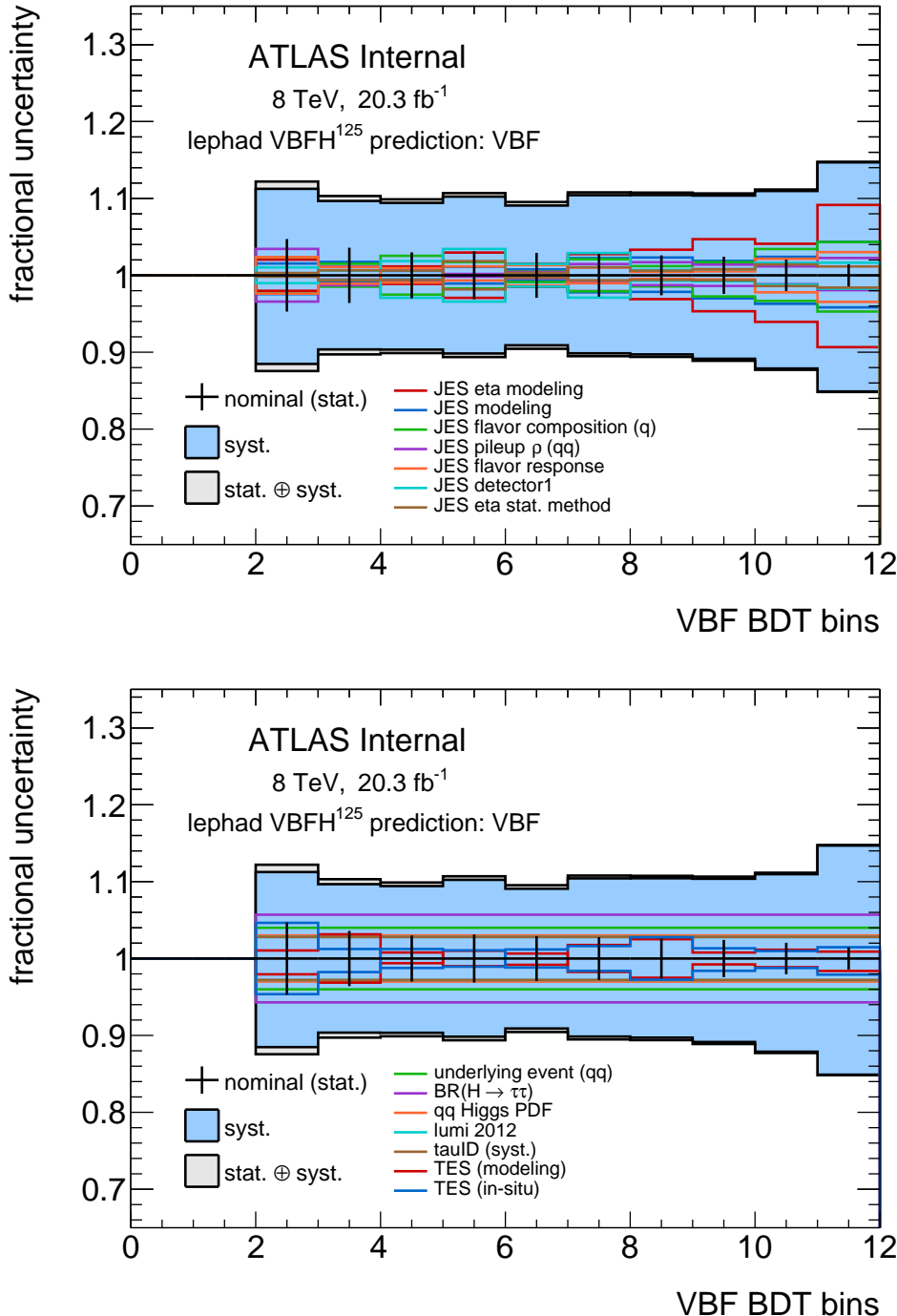


Figure 6.23: The pre-fit fractional uncertainty on the VBF $H \rightarrow \tau_\ell \tau_{\text{had}}$ prediction in each bin of the VBF category for uncertainties pertaining to the jet energy scale (top) and τ_{had} performance, theory, and the luminosity (bottom).

6. SIGNAL AND BACKGROUND PREDICTIONS

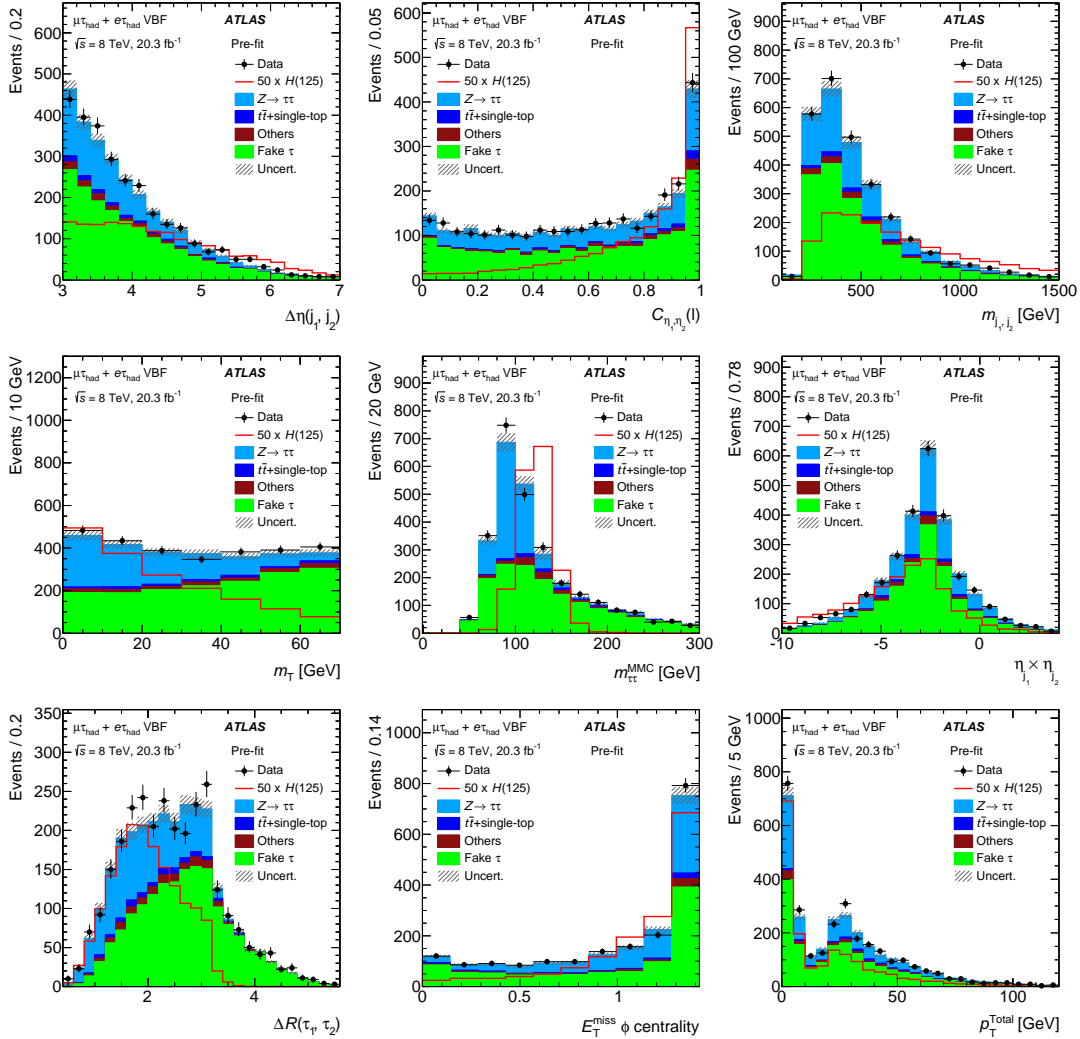


Figure 6.24: Data and prediction for input variables to the BDT in the $H \rightarrow \tau\ell\tau_{\text{had}}$ VBF signal region [2].

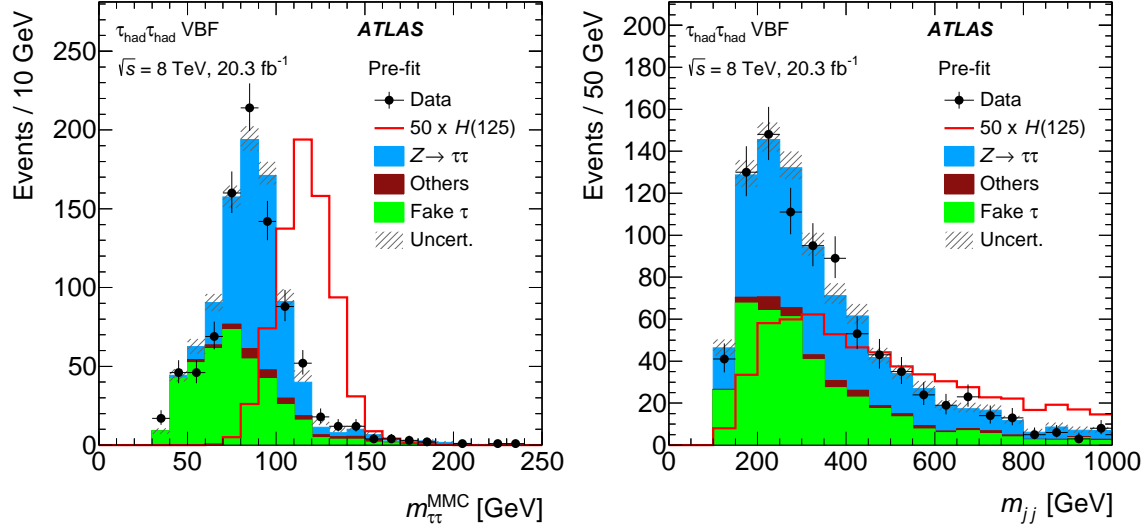


Figure 6.25: Two of the nine input variables to the VBF $H \rightarrow \tau_{\text{had}}\tau_{\text{had}}$ BDT discriminator: $m_{\tau\tau}^{\text{MMC}}$ (left) and m_{jj} (right). [2].

6.6 $H \rightarrow \tau_{\text{had}}\tau_{\text{had}}$ and $H \rightarrow \tau_\ell\tau_\ell$

Selected predictions in the signal regions of the VBF $H \rightarrow \tau_{\text{had}}\tau_{\text{had}}$ and $H \rightarrow \tau_\ell\tau_\ell$ analyses are shown in Figs. 6.25 and 6.26. Good agreement between data and prediction is observed for the input variables.

The background predictions are conceptually similar to the predictions in the $H \rightarrow \tau_\ell\tau_{\text{had}}$ analysis: $Z \rightarrow \tau\tau$ is predicted with the embedding, mis-identified backgrounds ($j \rightarrow \tau_{\text{had}}$, $j \rightarrow \ell$) are predicted with regions of data topologically similar to the signal region but with object-level identification criteria reversed, and the remaining backgrounds are predicted with simulation. The background predictions in these are discussed in greater detail in the accompanying publication [2].

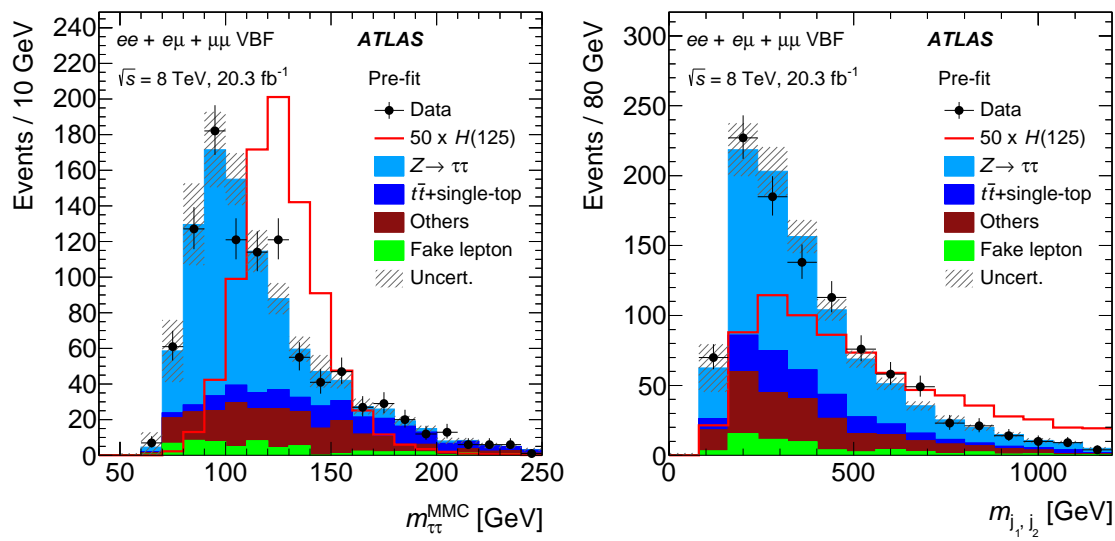


Figure 6.26: Two of the seven input variables to the VBF $H \rightarrow \tau_\ell \tau_\ell$ BDT discriminator: $m_{\tau\tau}^{\text{MMC}}$ (left) and m_{jj} (right). [2].

CHAPTER 7

Results

Results of the $H \rightarrow \tau\tau$ analysis are discussed. This is described in additional detail in the recent ATLAS $H \rightarrow \tau\tau$ publication [2]. The description of the fit procedure draws heavily from the recent ATLAS $H \rightarrow WW^*$ publication [94].

The yields of signal and background processes are extracted from a statistical analysis of the data and the predictions described in Chapters 5 and 6. A likelihood function is maximized which provides the “best fit” of the prediction to the data in each bin of the BDT discriminators within their prescribed uncertainties.

The likelihood contains the data and prediction from six signal regions: three final states and two categories. Control regions are also used to constrain some background uncertainties. For example, a region of data rich in top events is used in the $\tau_\ell\tau_{\text{had}}$ analysis to constrain the normalization on the portion of the top background predicted with simulation.

7.1 Fit procedure

The statistical analysis maximizes a likelihood function \mathcal{L} which depends on the signal strength μ , the set of uncertainties (or nuisance parameters) θ_i , and the observed number of data events N . The signal strength is defined as the measured $H \rightarrow \tau\tau$ cross-section divided by the predicted $H \rightarrow \tau\tau$ cross-section. A measured $\mu = 1$ would imply exactly the same number of $H \rightarrow \tau\tau$ events are observed as expected.

7.1.1 Likelihood function

The likelihood function is shown in Fig. 7.1. It is the product of four terms.

7. RESULTS

$$\mathcal{L} = \underbrace{\prod_{i,b} f\left(N_{ib} \mid \mu \cdot S_{ib} \cdot \prod_r \nu_{br}(\theta_r) + \sum_k \beta_k \cdot B_{kib} \cdot \prod_s \nu_{bs}(\theta_s)\right)}_{\text{Poisson for SR with signal strength } \mu; \text{ predictions } S, B} \cdot \underbrace{\prod_l f\left(N_l \mid \sum_k \beta_k \cdot B_{kl}\right)}_{\text{Poisson for profiled CRs}} \cdot \underbrace{\prod_t g(\vartheta_t \mid \theta_t)}_{\text{Gauss. for syst.}} \cdot \underbrace{\prod_k f(\xi_k \mid \zeta_k \cdot \theta_k)}_{\text{Poiss. for MC stats}}$$

Figure 7.1: The likelihood equation considered for maximization [94].

The first term of the likelihood is a Poisson function, in each bin b of each category i , describing the probability of observing N events given the predicted number of signal events S and background events B . The number of signal events is scaled by the signal strength μ which is shared among bins and categories. The number of background events is scaled by a parameter β_k which can be category-dependent. The signal and background predictions are modified by response functions $\nu(\theta)$ for each nuisance parameter θ .

The response function for bin-wise systematic uncertainties is given by $\nu(\theta) = 1 + \theta \cdot \frac{\Delta_\theta}{N}$, where Δ_θ is the given uncertainty on θ in units of N , i.e., $N \cdot \nu(\theta = \pm 1) = N \pm \Delta_\theta$ for $N = S, B$. The response function for statistical uncertainties on the predictions is $\nu(\theta) = \theta$.

The second term is a Poisson function, in each control region l , describing the probability of observing N events given the predicted number of background events B . The number of background events is scaled by a parameter β_k which is shared with the first term. The statistical power of the control region data is then used to constrain the background normalization in the signal region.

The third term is a Gaussian function, for each systematic uncertainty, describing the probability of a given nuisance parameter being pulled away from its nominal value. This is a penalty term for choosing a less likely value of the nuisance parameter than the nominal value. The choice of Gaussian function to describe the uncertainty is convention.

The fourth term is a Poisson function, in each bin of each category, describing the uncertainty due to finite sample size of the signal and background predictions. This is especially relevant for predictions which have natural statistical limitations, e.g., predicting the $Z \rightarrow \tau\tau$ background with $Z \rightarrow \mu\mu$ events from data.

To extract the observed μ and other quantities, the likelihood is maximized with respect to μ and the associated nuisance parameters θ . This maximization yields the most probable μ . The likelihood is evaluated at $\vartheta = 0$ and $\xi = \zeta$ which imposes that the most probable value of each systematic nuisance parameter is zero and statistical nuisance parameter is one.

7. RESULTS

7.1.2 Features

The first term of the likelihood is maximized when the prediction exactly matches the observed data events in a given bin. The prediction is allowed to change within the maximization as the nuisance parameters are pulled. This allowed change is restricted by the Gaussian constraints imposed on these uncertainties, which are maximized when the nuisance parameters are unchanged from their pre-fit prediction. For example, the jet energy scale is allowed to be moved by $+1\sigma$, but this incurs a penalty in the likelihood of $\frac{g(1|0,1)}{g(0|0,1)} \approx 0.6$.

The normalization of the embedded $Z \rightarrow \tau\tau$ is allowed to float freely within each final state, i.e., there is no constraint beyond the signal region statistics. In the $\tau_\ell\tau_{\text{had}}$ channel, a single normalization nuisance parameter is used for $Z \rightarrow \tau\tau$ which is shared in each BDT bin of each category. This is sensible because the defining features of the categories – dijet kinematics and p_T^Z – are expected to be well predicted by the embedding method.

The likelihood maximization extracts many fitted parameters, including the signal strength μ , the pulls of the nuisance parameters θ_i , and the uncertainties on the nuisance parameters in units of the pre-fit uncertainties (i.e., $\Delta_{\theta,\text{pre-fit}} = 1$).

7.1.3 Test statistic

The test statistic is defined as:

$$q(\mu) = -2 \ln \left(\frac{\mathcal{L}(\mu, \theta_i)}{\mathcal{L}_{\max.}} \right) \Bigg|_{\theta_i=\hat{\theta}_{i,\mu}} \quad (7.1)$$

and is evaluated as a function of μ . The denominator $\mathcal{L}_{\max.}$ is the unconditional maximum of the likelihood as a function of μ and the nuisance parameters θ_i and is therefore just a number. The numerator $\mathcal{L}(\mu, \theta_i)$ is the conditional maximum for a given μ as a function of the nuisance parameters, thereby asking which signal strength is most likely.

The fitted uncertainty on a nuisance parameter is defined as the distance $\theta_{\text{right}} - \theta_{\text{left}}$ such that $q(\mu) = 1$ when scanning a given nuisance parameter to the right and left of the fitted θ . If \mathcal{L} follows a Gaussian distribution, the integral from θ_{left} to θ_{right} corresponds to 68% (1σ) of the distribution.

7.1.4 Impact of uncertainties on μ

The post-fit *impact* of a given nuisance parameter on the signal strength is defined as:

$$\Delta_{\hat{\mu},i} = \hat{\mu} \left(\hat{\theta}_i \pm \Delta_{\hat{\theta}_i} \right) - \hat{\mu} \quad (7.2)$$

7. RESULTS

where hats indicate post-fit values. $\hat{\mu}(\hat{\theta}_i \pm \Delta_{\hat{\theta},i})$ indicates the fitted μ of the full fit but with θ_i fixed to its post-fit value $\hat{\theta}$ varied by the post-fit uncertainty $\pm \Delta_{\hat{\theta},i}$, where all other nuisance parameters are floating. If the fitted μ is robust against changes to a nuisance parameter, its impact will be small.

7.2 Fit results

The data and fitted signal and background predictions are shown in Fig. 7.2. The majority of bins in the BDTs are dominated by background, and good modeling is observed. In the signal-like regime of BDT output near 1, the predicted contribution from $H \rightarrow \tau\tau$ signal is visible in the VBF category of each final state, and the signal hypothesis is favored over the background-only hypothesis.

The yields in the VBF $H \rightarrow \tau_\ell \tau_{\text{had}}$ category and in the most signal-like regime are shown in Table 7.1 after the global fit. In the highest BDT bin, the signal hypothesis is favored over the background-only hypothesis.

At the value of the Higgs boson mass obtained from the combination of the ATLAS $H \rightarrow \gamma\gamma$ and $H \rightarrow ZZ^*$ measurements, the signal strength obtained is 1.4 ± 0.3 (syst.) ± 0.3 (stat.) ± 0.1 (theo.). The signal strength breakdown by category and channel is shown in Fig. 7.3.

The probability p_0 of obtaining a result at least as signal-like as observed in the data if no signal

Table 7.1: Data and the predicted yields of signal and background in the VBF $\tau_\ell \tau_{\text{had}}$ category after the global fit.

Process/Category	VBF $\tau_\ell \tau_{\text{had}}$		
	All bins	Second to last bin	Last bin
BDT output bin			
$j \rightarrow \tau_{\text{had}}$	1680 ± 50	8.2 ± 0.9	5.2 ± 0.7
$Z \rightarrow \tau\tau$	877 ± 29	7.6 ± 0.9	4.2 ± 0.7
Top	82 ± 15	0.3 ± 0.4	0.5 ± 0.4
$Z \rightarrow \ell\ell$ ($\ell \rightarrow \tau_{\text{had}}$)	54 ± 26	1.0 ± 0.7	0.30 ± 0.28
Diboson	63 ± 11	1.0 ± 0.4	0.48 ± 0.20
ggF $H \rightarrow \tau\tau$	16 ± 6	1.0 ± 0.4	1.2 ± 0.6
VBF $H \rightarrow \tau\tau$	31 ± 8	4.5 ± 1.1	9.1 ± 2.2
$WH \rightarrow \tau\tau$	< 1	< 0.1	< 0.1
$ZH \rightarrow \tau\tau$	< 1	< 0.1	< 0.1
Total background	2760 ± 40	18.1 ± 2.3	10.7 ± 2.7
Total signal	48 ± 12	5.5 ± 1.3	10.3 ± 2.5
Data	2830	22	21

7. RESULTS

were present is calculated using the test statistic $q(0)$. For $m_H = 125.36$ GeV, the observed p_0 is 2.7×10^{-6} , which corresponds to a deviation from the background-only hypothesis of 4.5σ . This can be compared to an expected significance of 3.4σ .

To emphasize the most signal-like regime, two distributions are built from the six categories used in the global fit and shown in Fig. 7.4. First, the signal region bins of the BDT discriminator are re-ordered by $\log_{10}(S/B)$, where S/B is the signal-to-background ratio calculated assuming $\mu = 1.4$ in each bin. The expected signal yield for both $\mu = 1$ and $\mu = 1.4$ is shown, as well as the fitted background yield for the background-only hypothesis. The signal hypothesis is clearly favored. Second, the $m_{\tau\tau}^{\text{MMC}}$ distribution is shown summed across all categories and weighted event-by-event by $\ln(1 + S/B)$, which enhances the events compatible with the signal hypothesis. The excess of events in this mass distribution is consistent with the expectation for a Standard Model Higgs boson with $m_H = 125$ GeV.

7. RESULTS

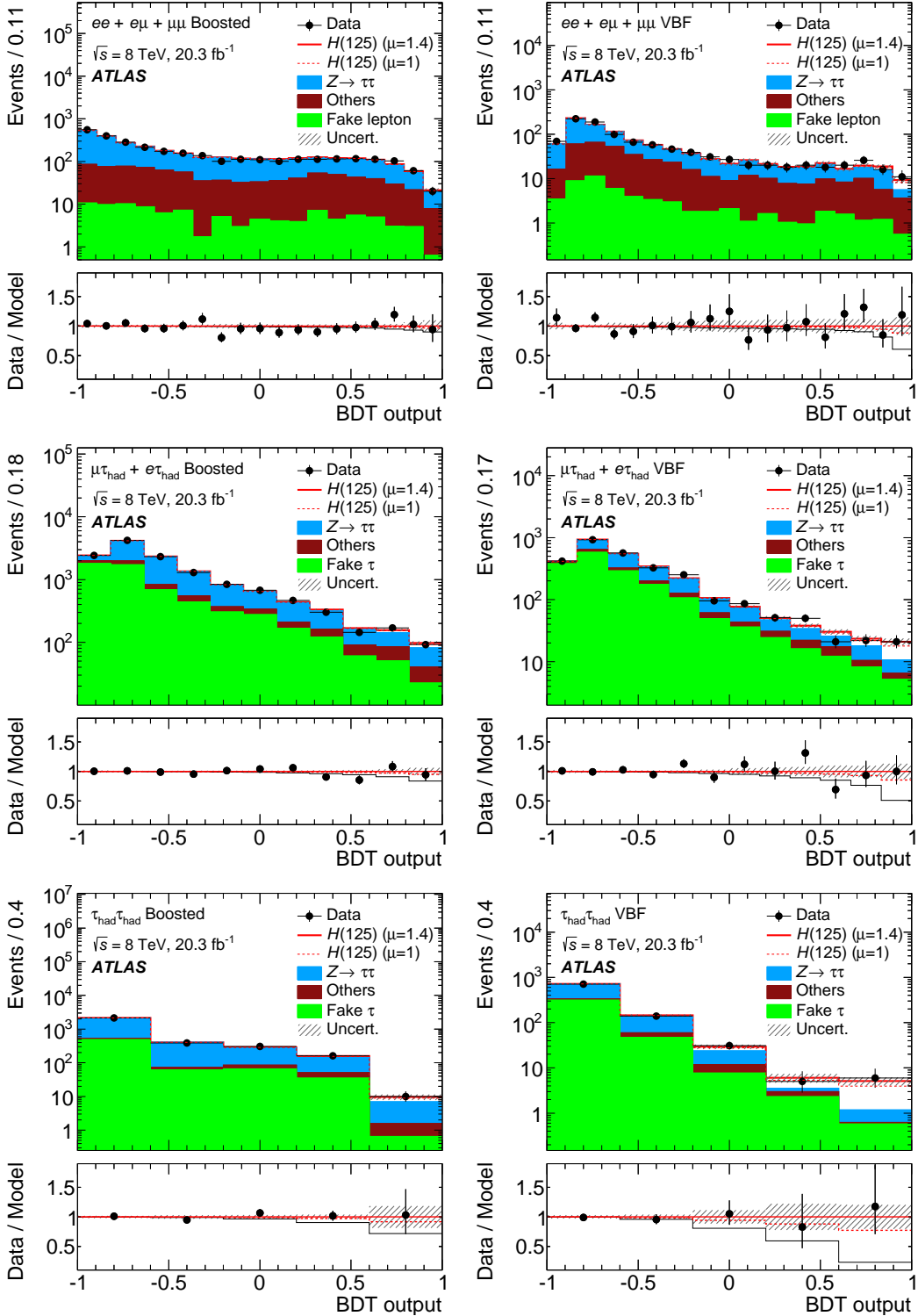


Figure 7.2: Distributions of the 8 TeV BDT discriminants in all six analysis categories after the global fit [2].

7. RESULTS

The dominant uncertainties on the measurement of the signal strength parameters include statistical uncertainties on the data from the signal regions, uncertainties on the jet and tau energy scales, uncertainties on the normalization of the $Z \rightarrow \tau\tau$ and top backgrounds, and theoretical uncertainties. The contributions of each of these significant sources to the uncertainty of the measured signal strength are summarized in Fig. 7.5.

7.3 High score events in data

Event displays of some of the most signal-like events in data in the VBF $H \rightarrow \tau_\ell \tau_{\text{had}}$ and $H \rightarrow \tau_{\text{had}} \tau_{\text{had}}$ analyses are shown in Figs. 7.6 and 7.7.

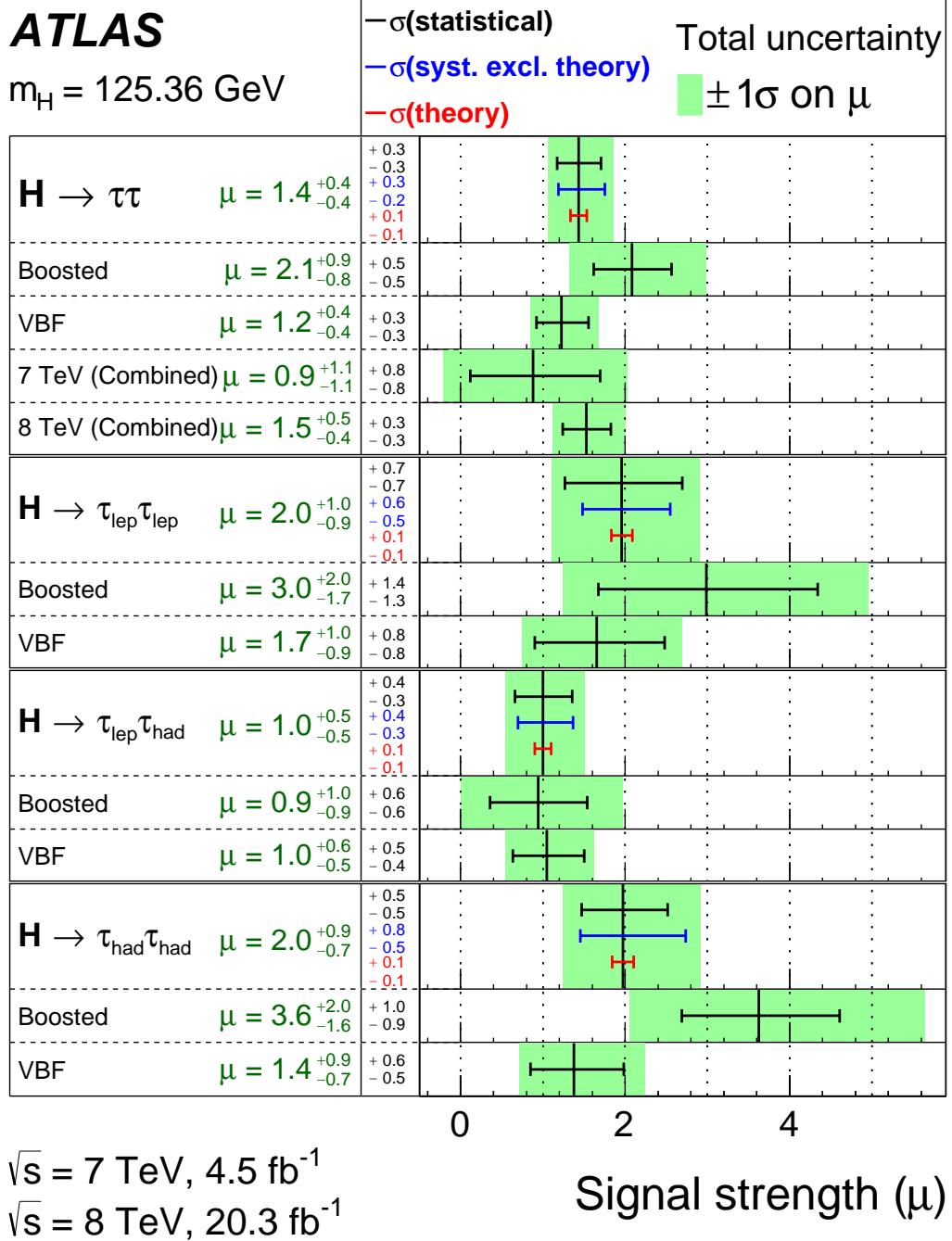


Figure 7.3: The fitted signal strength μ split by category, final state, and data-taking period [2].

7. RESULTS

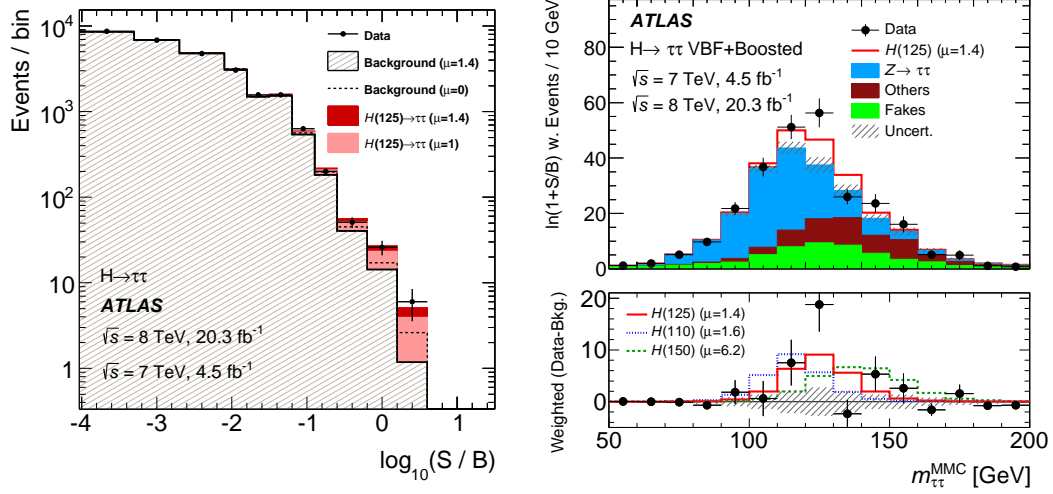


Figure 7.4: Plots of data and prediction which emphasize the most sensitive regions [2]. The individual BDT bins from all six categories are ordered by S/B and plotted on a shared axis (left) and entries in the $m_{\tau\tau}^{\text{MMC}}$ distribution are weighted by $\log(1 + S/B)$ (right).

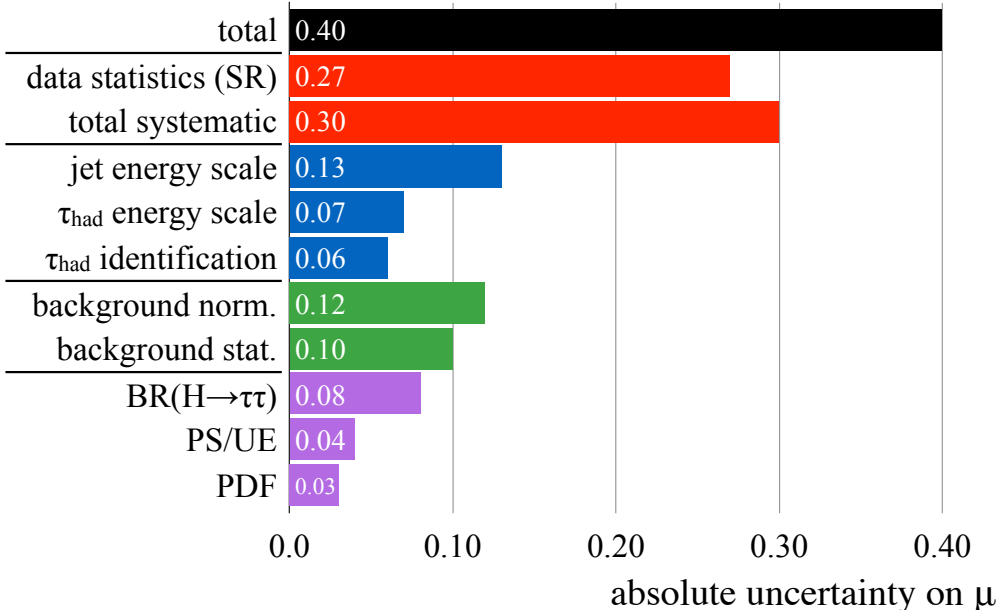


Figure 7.5: Comparison of the impact of the statistical and systematic uncertainties on the absolute uncertainty on μ [2].

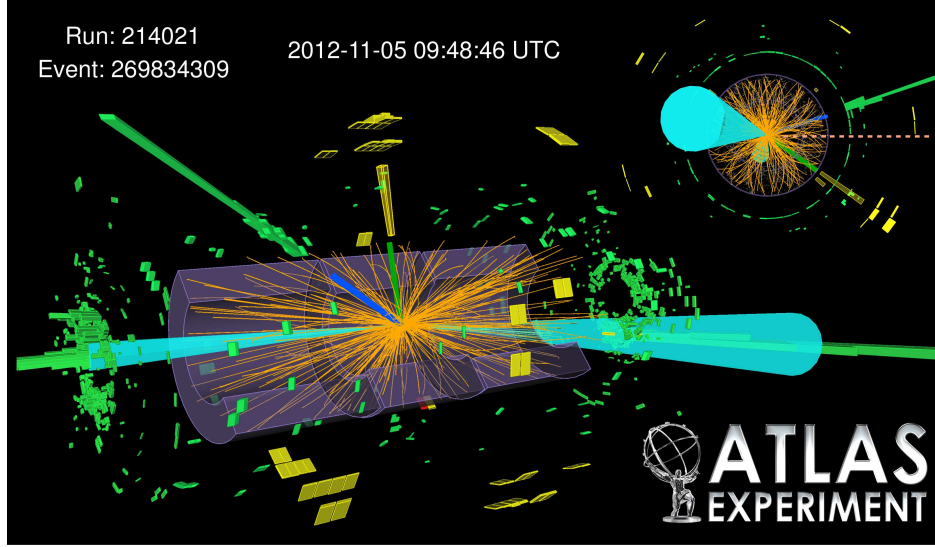


Figure 7.6: Display of one of the most signal-like events in the $H \rightarrow \tau_\ell \tau_{\text{had}}$ VBF category in data [2]. The blue track matched to the green cluster indicates an electron, the green track matched to the yellow cluster indicates a τ_{had} , the pink dotted line indicates the E_T^{miss} in the transverse plane, and the turquoise cones indicates the VBF jets. The reconstructed $m_{\tau\tau}^{\text{MMC}} = 127$ GeV and $m_{\text{jj}} = 1.53$ TeV.

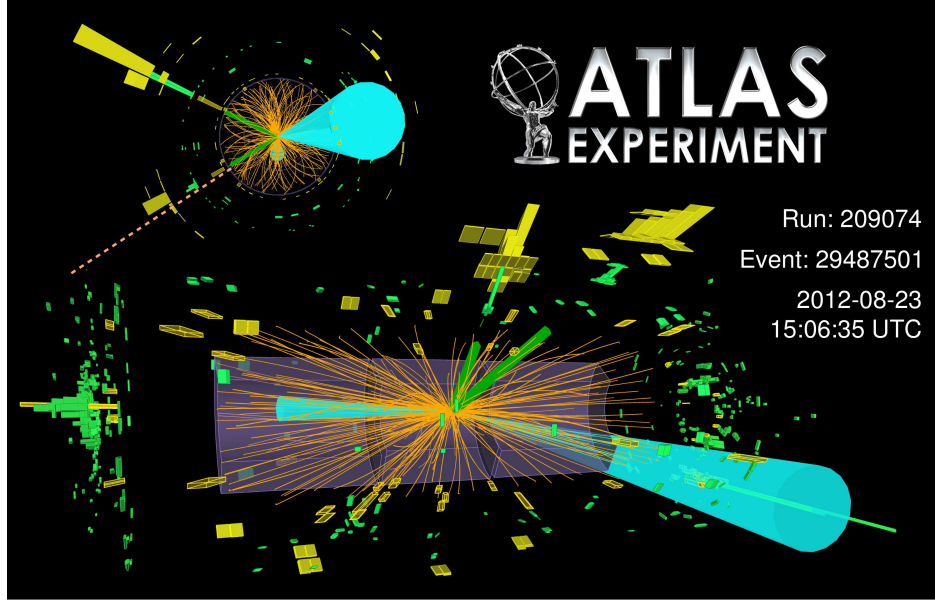


Figure 7.7: Display of one of the most signal-like events in the $H \rightarrow \tau_{\text{had}} \tau_{\text{had}}$ VBF category in data [2]. The green tracks matched to the yellow clusters indicate the τ_{had} , the pink dotted line indicates the E_T^{miss} in the transverse plane, and the turquoise cones indicates the VBF jets. The reconstructed $m_{\tau\tau}^{\text{MMC}} = 123$ GeV and $m_{\text{jj}} = 1.02$ TeV.

CHAPTER 8

Prospects for $H \rightarrow \tau\tau$

Prospects for the $H \rightarrow \tau\tau$ analysis in Run-II and at the HL-LHC are described. Discussion of prospects at the HL-LHC are drawn largely from the recent ATLAS documentation on the topic [111].

8.1 Run-II

In Run-II, the LHC is expected to collide protons with $\sqrt{s} = 13$ TeV, a peak instantaneous luminosity of approximately $1.6 \times 10^{34} \text{ cm}^{-2} \text{ s}^{-1}$, 25 nanosecond bunch spacing, and $\langle \mu \rangle \approx 40$. These data-taking conditions are much harsher than in 2012, as shown in Table 8.1.

The ATLAS L1 trigger rate would increase approximately five-fold if the 2012 trigger menu was ported unchanged to 2015 data-taking conditions [112]. However, the L1 bandwidth is expected to increase from 75 kHz to 100 kHz, much less than this rate increase. The L1 menu must then be adapted to accommodate this.

This is especially true of triggers which rely on τ_{had} since hadronic objects are challenging in the trigger, both in identification and calibration. An unsustainable increase of trigger rate as a function of instantaneous luminosity is shown in Fig. 8.1. Multiple avenues are explored to ensure tenable

Table 8.1: LHC data-taking conditions in 2011 and 2012 compared with the expected data-taking conditions in 2015.

Year of operations	\sqrt{s} [TeV]	peak lumi. [$\text{cm}^{-2} \text{ s}^{-1}$]	bunch spacing [ns]	$\langle \mu \rangle$
2011	7	0.4×10^{34}	50	≈ 10
2012	8	0.8×10^{34}	50	≈ 20
2015	13	1.6×10^{34}	25	≈ 40

8. PROSPECTS FOR $H \rightarrow \tau\tau$

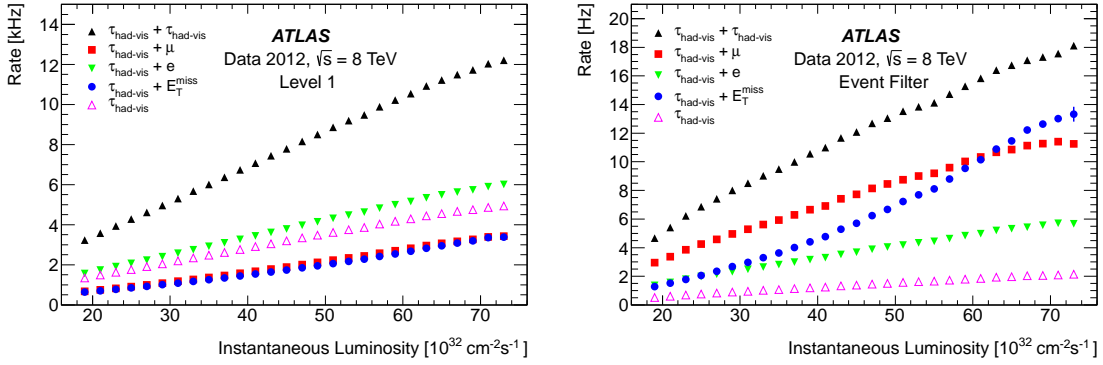


Figure 8.1: Tau trigger rates in 2012 data-taking as a function of instantaneous luminosity for L1 (left) and HLT (right) [1].

trigger rates without significant loss of physics.

8.1.1 Run-I triggers for $H \rightarrow \tau\tau$

In Run-I, only the $H \rightarrow \tau_{\text{had}}\tau_{\text{had}}$ analysis relies on τ_{had} triggers for physics. The $H \rightarrow \tau_\ell\tau_{\text{had}}$ use single lepton triggers with an offline threshold of 26 GeV. $\ell + \tau_{\text{had}}$ triggers are considered but ultimately dropped because they bring additional complication to the analysis without significant improvement in sensitivity. The $H \rightarrow \tau_\ell\tau_\ell$ analysis relies on single and di-lepton triggers. The list of triggers used in 2012 data-taking, and their expected 2015 versions, is shown in Table 8.2 and Table 8.3.

8.1.2 Run-II triggers

Trigger options for Run-II are most critical for the $H \rightarrow \tau_{\text{had}}\tau_{\text{had}}$ since it relies entirely on τ_{had} triggers. The $H \rightarrow \tau_\ell\tau_\ell$ analysis will continue to use single and di-lepton triggers, which enjoy low

Table 8.2: L1 triggers used in the 2012 $H \rightarrow \tau\tau$ analysis, and their expected 2015 versions, grouped by $\tau\tau$ decay channel.

channel	L1, 2012	L1, 2015
$H \rightarrow \tau_{\text{had}}\tau_{\text{had}}$	2TAU11I_TAU15	no di- τ_{had} item planned
$H \rightarrow \tau_e\tau_{\text{had}}$	EM18VH	EM24VHI
$H \rightarrow \tau_\mu\tau_{\text{had}}$	MU20	MU20
$H \rightarrow \tau_e\tau_e$	EM18VH 2EM10VH	EM24VHI 2EM15VH
$H \rightarrow \tau_\mu\tau_\mu$	2MU10	2MU10
$H \rightarrow \tau_e\tau_\mu$	EM10VH_MU6	EM15VH_MU10

thresholds and are among the most high profile triggers, and thus less likely to be cut in case of unexpectedly high rates. The $H \rightarrow \tau_\ell \tau_{\text{had}}$ analysis will continue to use the single lepton trigger, but the potential benefit of recovering events with leptons below the single lepton trigger thresholds could be helpful. Accordingly, only the $H \rightarrow \tau_{\text{had}} \tau_{\text{had}}$ and $H \rightarrow \tau_\ell \tau_{\text{had}}$ analyses are considered for trigger optimizations, with emphasis on $H \rightarrow \tau_{\text{had}} \tau_{\text{had}}$.

8.1.2.1 Object thresholds

The first and simplest option is to raise object thresholds in the trigger. Since the Run-I signal regions only include event topologies with additional jets, triggering on one or two additional jets in the event is considered. To assess the impact of this, the Run-I analysis is re-run but with progressively higher thresholds on the final state objects, and the resulting sensitivity is derived. This is shown in Fig. 8.2.

For both $H \rightarrow \tau_{\text{had}} \tau_{\text{had}}$ and $H \rightarrow \tau_\ell \tau_{\text{had}}$, triggering on the lead jet in the VBF category is promising, and triggering on the sub-lead jet is not. The lowest realistic threshold for triggering on the sub-lead jet is 15 – 20 GeV at L1 (\approx 50 – 60 GeV offline) costs significant sensitivity in both final states. Requiring a second jet would also be inefficient for the boosted category. To trigger on the lead jet, however, an offline threshold of \approx 70 GeV (25 GeV at L1) does not cost significant sensitivity.

For $H \rightarrow \tau_{\text{had}} \tau_{\text{had}}$, raising the threshold on the lead τ_{had} is more promising than raising the threshold on the sub-lead τ_{had} . For $H \rightarrow \tau_\ell \tau_{\text{had}}$, raising the threshold on the τ_{had} is more promising than raising the threshold on the lepton.

8.1.2.2 Topological requirements

A new feature of the L1 trigger in 2015 is the ability to make topological selections, whereas in Run-I, only object multiplicity selections could be made. This topological selection are implemented via the

Table 8.3: HLT triggers used in the 2012 $H \rightarrow \tau\tau$ analysis, and their expected 2015 versions, grouped by $\tau\tau$ decay channel.

channel	HLT, 2012	HLT, 2015
$H \rightarrow \tau_{\text{had}} \tau_{\text{had}}$	<code>tau29Ti_medium1_tau20Ti_medium1</code>	no di- τ_{had} item planned
$H \rightarrow \tau_e \tau_{\text{had}}$	<code>e24vhi_medium1</code>	<code>e28i_tight</code>
$H \rightarrow \tau_\mu \tau_{\text{had}}$	<code>mu24i_tight</code>	<code>mu26i_medium</code>
$H \rightarrow \tau_e \tau_e$	<code>e24vhi_medium1 2e12Tvh_loose1</code>	<code>e28i_tight 2e17_loose</code>
$H \rightarrow \tau_\mu \tau_\mu$	<code>mu18_tight_mu8_EFFS</code>	<code>2mu14</code>
$H \rightarrow \tau_e \tau_\mu$	<code>e12Tvh_medium1_mu8</code>	<code>e17_medium_mu12</code>

8. PROSPECTS FOR $H \rightarrow \tau\tau$

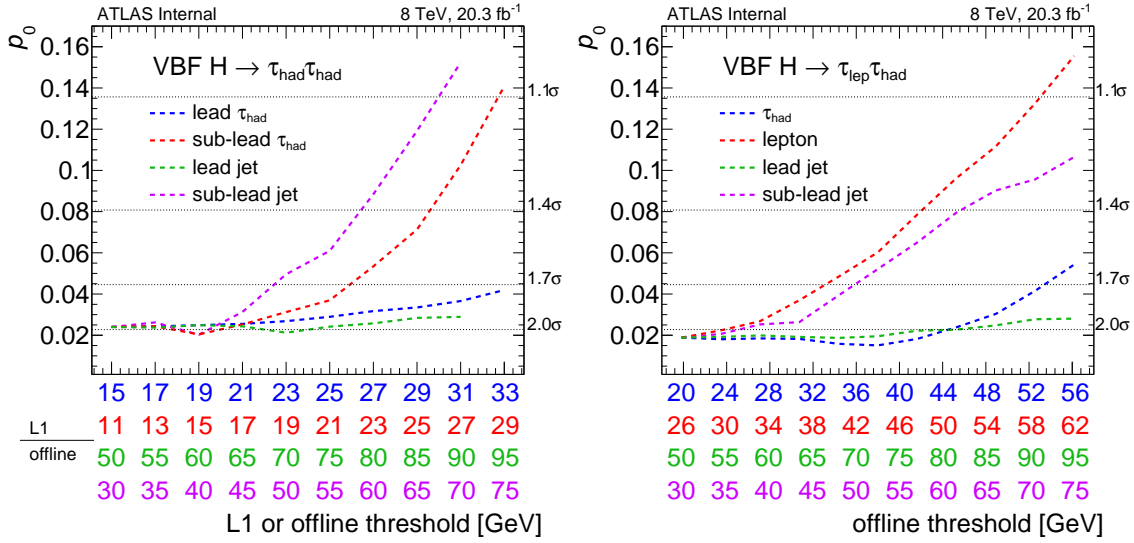


Figure 8.2: Significance (p_0) of the $H \rightarrow \tau\tau$ VBF category in 2012 for the $H \rightarrow \tau_{\text{had}}\tau_{\text{had}}$ (left) and $H \rightarrow \tau_{\ell}\tau_{\text{had}}$ (right) analyses as a function of offline or L1 threshold for various objects.

new L1topo processor [113, 114].

At L1, the dominant background for τ_{had} triggers is QCD di-jet production. Topological selections can be used in various ways to suppress this process, especially in the $H \rightarrow \tau\tau$ signal regions where the $\tau\tau$ system tends to be boosted.

$\Delta\phi(\tau\tau) < X$:

QCD di-jets tend to be produced back-to-back in the transverse plane, and the $\tau\tau$ system tends to have smaller $\Delta\phi$ due to transverse boost of the Z/H .

$\Delta\eta(\tau\tau) < X$:

QCD di-jets tend to be produced broadly in η , and the $\tau\tau$ system tends to have smaller $\Delta\eta$ due to longitudinal boost of the Z/H .

$\Delta R(\tau\tau) < X$:

This combines discriminating power of $\Delta\phi(\tau\tau)$ and $\Delta\eta(\tau\tau)$.

$p_{\text{T}}(\tau\tau) > X$:

QCD di-jet systems tend to be produced at rest in the transverse plane, and the $\tau\tau$ system is usually not due to transverse boost.

$m_{\tau\tau} > X$:

QCD di-jet systems tend to be non-resonant and low- p_{T} , and the $\tau\tau$ system is from Z/H decays.

8. PROSPECTS FOR $H \rightarrow \tau\tau$

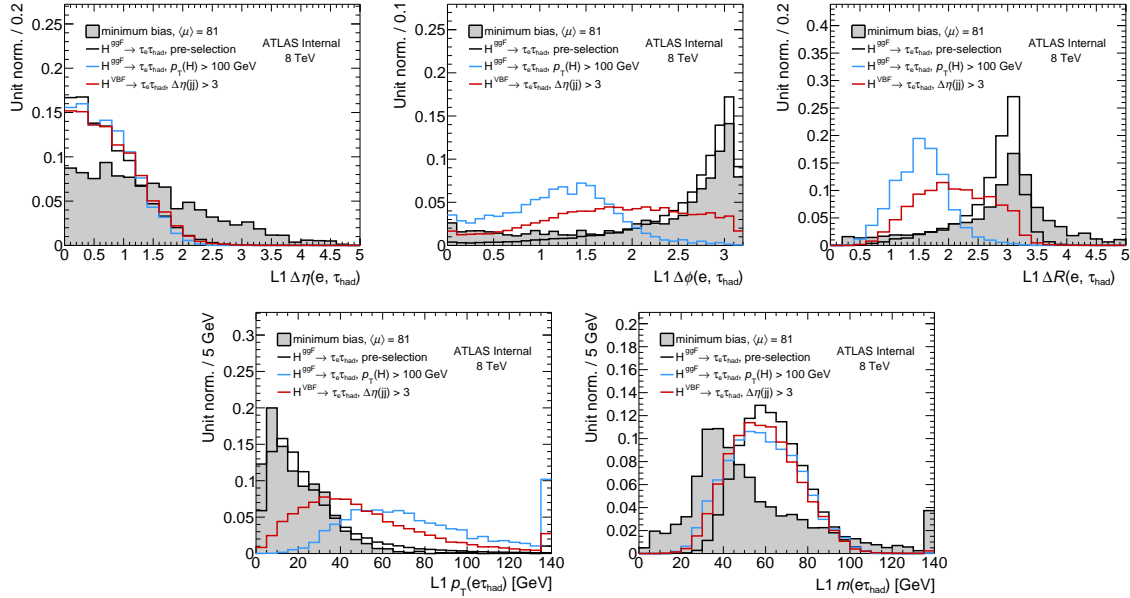


Figure 8.3: Topological distributions at L1 for $H \rightarrow \tau_e \tau_{\text{had}}$ MC versus high-pileup ($\langle \mu \rangle = 81$) minimum bias MC.

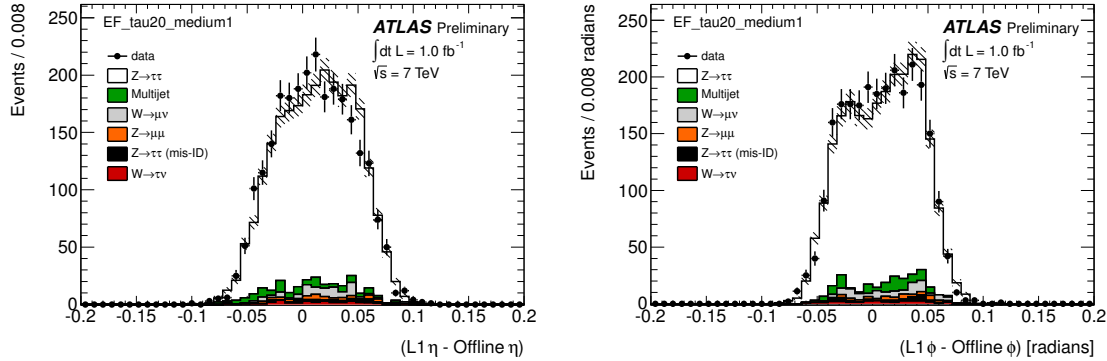


Figure 8.4: L1 angular resolution for τ_{had} in simulation and data [115].

The discriminating power of these variables is shown in Fig. 8.3 for $H \rightarrow \tau_e \tau_{\text{had}}$ MC versus high-pileup minimum bias MC.

Of these options, angular discrimination is appealing because the angular resolution for τ_{had} at L1 is better than momentum resolution, as shown in Fig. 8.4 and Fig. 8.5. Sharper efficiency turn-ons can then be expected at HLT and offline. $\Delta R(\tau\tau) < 2.8$ is ultimately chosen for discrimination because it combines the discriminating power of $\Delta\phi(\tau\tau)$ and $\Delta\eta(\tau\tau)$.

The impact of requiring an additional jet and $\Delta R(\tau\tau) < 2.8$ on the predicted 2015 L1 trigger rate

8. PROSPECTS FOR $H \rightarrow \tau\tau$

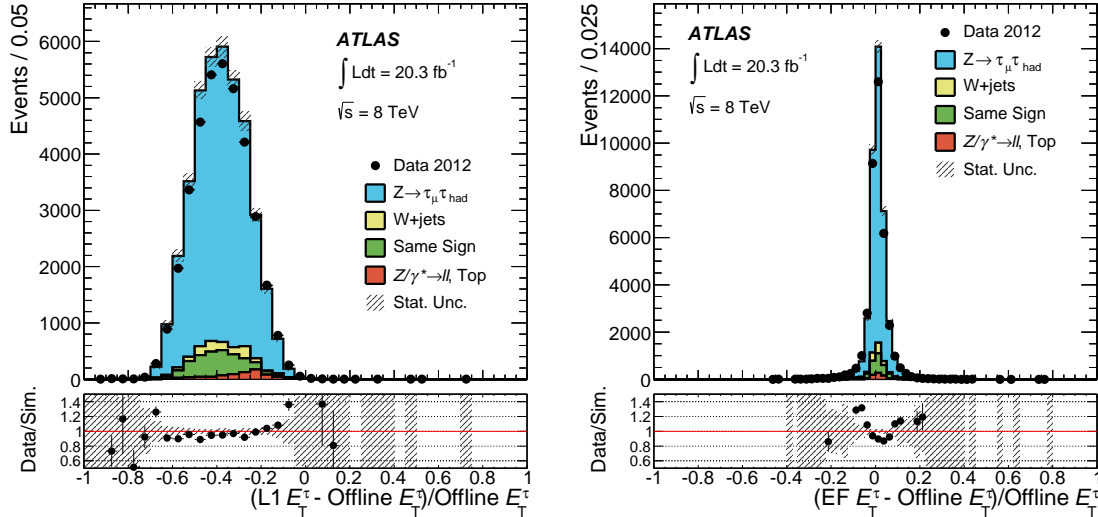


Figure 8.5: Momentum resolution for τ_{had} in simulation and data at L1 (left) and HLT (right). The resolution is significantly improved at HLT [1].

is shown in Table 8.4. A ten-fold reduction of the rate is achieved without significant loss of sensitivity.

8.1.2.3 Gains with $\ell + \tau_{\text{had}}$ triggers

To assess the potential gain in sensitivity of $\ell + \tau_{\text{had}}$ triggers in 2015, the $H \rightarrow \ell \tau_{\text{had}}$ analysis is re-run in the regime below the single lepton trigger threshold with the $\ell + \tau_{\text{had}}$ triggers running in 2012, shown in Table 8.5. Kinematic distributions are shown in Fig. 8.6 and Fig. 8.7, including the final BDT discriminant.

A simple, analytic formula for the discovery significance Z_A [116] gives 0.7σ for the $\ell + \tau_{\text{had}}$ triggered

Table 8.4: L1 trigger items and rate predictions for 2015 data-taking. A baseline L1 menu is used for calculating the unique rate.

L1 item	rate [kHz]	unique rate [kHz]	notes
2TAU11	181	147	$H \rightarrow \tau_{\text{had}}\tau_{\text{had}}$, early 2011
2TAU11I	121	99	$H \rightarrow \tau_{\text{had}}\tau_{\text{had}}$, late 2011
TAU15I TAU11I	96	75	$H \rightarrow \tau_{\text{had}}\tau_{\text{had}}$, 2012
TAU20I TAU11I	69	48	Raise lead τ_{had} p_T
TAU20I TAU12I	61	42	Raise sub-lead τ_{had} p_T
TAU20I TAU12I J25	20	12	Additional jet
TAU20I TAU12I J25 DR2.8	7.8	4.3	$\Delta R(\tau_{\text{had}}\tau_{\text{had}}) < 2.8$

8. PROSPECTS FOR $H \rightarrow \tau\tau$

category. This is not a significant improvement over the single lepton triggered regime.

Table 8.5: L1 and HLT $\ell + \tau_{\text{had}}$ trigger items operating in 2012.

channel	L1	HLT
$H \rightarrow \tau_e \tau_{\text{had}}$	2TAU11I_EM14VH	tau20Ti_medium1_e18vh_medium1
$H \rightarrow \tau_\mu \tau_{\text{had}}$	TAU8_MU10	tau20_medium1_mu15

8. PROSPECTS FOR $H \rightarrow \tau\tau$

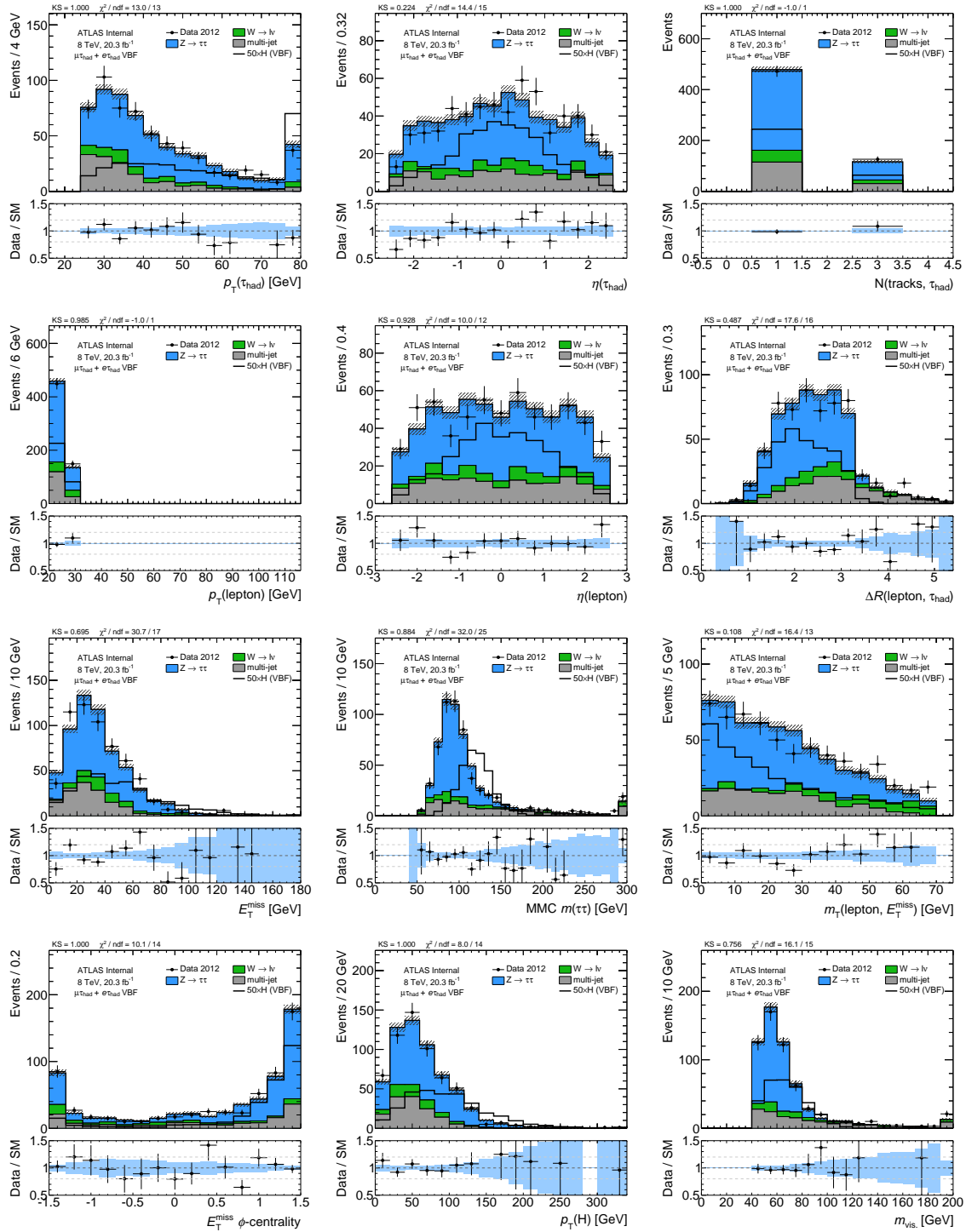


Figure 8.6: Kinematic distributions in the $\ell + \tau_{\text{had}}$ category of the 8 TeV VBF $H \rightarrow \tau_\ell \tau_{\text{had}}$ analysis.

8. PROSPECTS FOR $H \rightarrow \tau\tau$

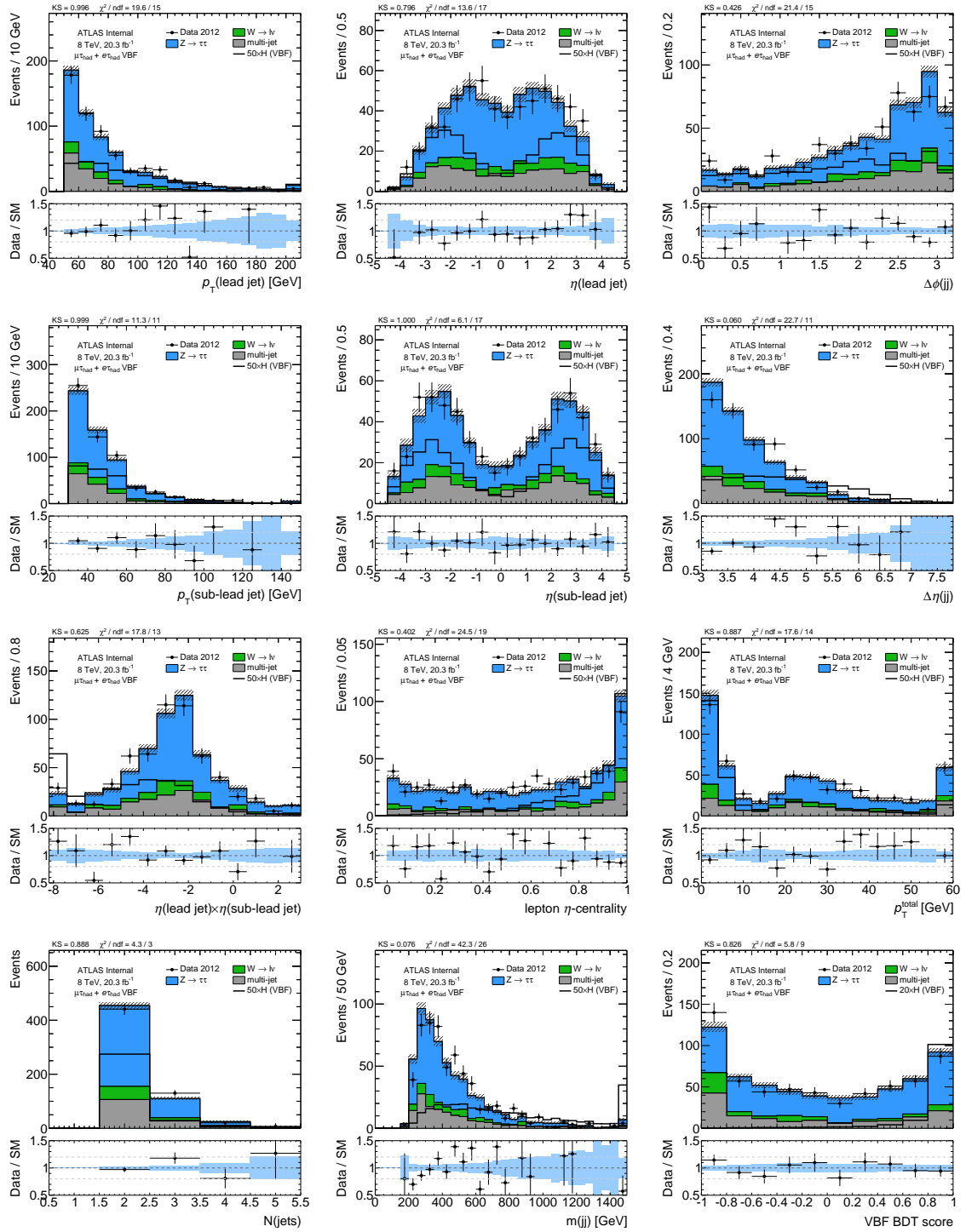


Figure 8.7: Kinematic distributions in the $\ell + \tau_{\text{had}}$ category of the 8 TeV VBF $H \rightarrow \tau\ell\tau_{\text{had}}$ analysis.

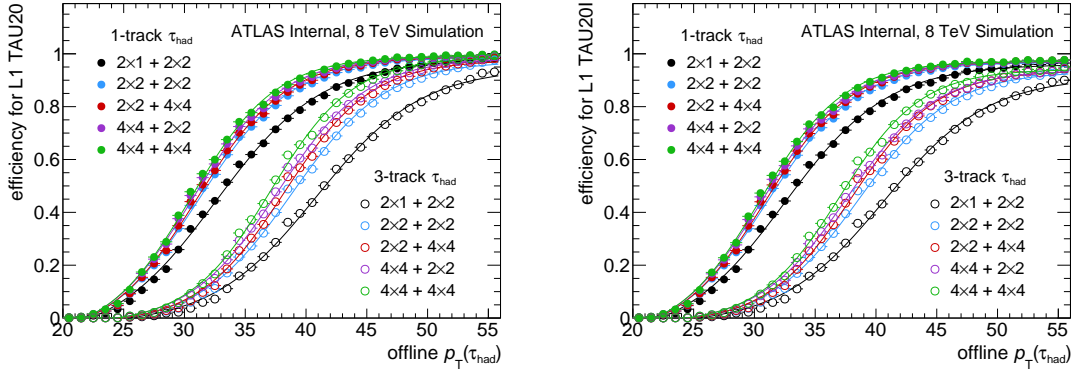


Figure 8.8: Efficiency for firing the 20 GeV L1 τ_{had} trigger as a function of offline $p_T(\tau_{\text{had}})$ for no isolation requirement (left) and the 2012 isolation requirement (right) for various definitions of the L1 τ_{had} item. The current definition (2×1 EM, 2×2 had.) has the slowest efficiency turn-on. Fits are performed with a Fermi-Dirac distribution.

8.1.3 L1 τ_{had}

Updates to the L1 τ_{had} object are also considered. These are explored in hopes of improving the trigger efficiency for τ_{had} generally, without significant rate increases, which could assist all analyses which rely on τ_{had} triggers.

8.1.3.1 Size

The size of the L1 τ_{had} is made larger to check if a sharper efficiency turn-on curve can be gained without significant background contamination. This is especially important for 3-track τ_{had} , which are expected to be wider than 1-track τ_{had} and are observed to have a slower efficiency turn-on curve. The default L1 τ_{had} used in 2012 data-taking is 2×1 in the electromagnetic calorimeter and 2×2 in the hadronic calorimeter.

Efficiency turn-on curves for various L1 τ_{had} definitions are shown in Fig. 8.8 for simulated τ_{had} with and without isolation requirements. A sharper efficiency turn-on is achieved relative to the default definition, as shown in Table 8.6. Since background rates increase non-trivially with larger L1 τ_{had} objects, the default definition will be retained in 2015 data-taking.

8.1.3.2 Isolation

The definition of L1 isolation is also reconsidered for 2015 data-taking. In 2012, a flat cut of $p_T^{\text{L1,iso}} \leq 4$ GeV is used. In 2015, the option of p_T^{L1} -dependent isolation is available. A simple linear dependence

is explored:

$$\text{require } p_T^{\text{L1,iso}} \leq m \times p_T^{\text{L1,iso}} + b \text{ GeV} \quad (8.1)$$

With this definition, the 2012 isolation requirement is $m = 0$ and $b = 4$.

Removing the isolation requirement is considered above $p_T^{\text{L1}} = 60$ GeV. This is equivalent to a logical OR with the lowest unprescaled single τ_{had} trigger, TAU60, and thus will not cost any additional unique rate to the total L1 trigger menu.

The predicted relative rate is shown in Fig. 8.9, with and without isolation at high p_T . An inverse relationship in the rate is observed between offset and slope, as expected. The L1 τ_{had} efficiency is shown in Fig. 8.10 for the isolation requirements which give equal rate. Significant signal efficiency is recovered at high p_T .

8.1.4 Conclusions and contingencies

Despite significantly harsher data-taking conditions in 2015, triggers for the $H \rightarrow \tau_{\text{had}}\tau_{\text{had}}$ and $H \rightarrow \tau_{\ell}\tau_{\text{had}}$ analyses can be adapted to retain physics output with manageable rates and without major loss of generality. The most important adaptations for both channels are requiring an additional high- p_T jet and requiring low $\Delta R(\tau\tau)$. The L1 τ_{had} menu is shown in Table 8.7.

Contingency plans are considered due to the uncertainty of the rate prediction and the uncertainty of the LHC data-taking conditions. If the $H \rightarrow \tau\tau$ section of the τ_{had} L1 menu is asked to reduce its bandwidth consumption, options are available with minor physics losses, such as raising the τ_{had}

Table 8.6: Fits of the efficiency for firing the 20 GeV L1 τ_{had} trigger with a Fermi-Dirac distribution for various definitions of the L1 τ_{had} item. No isolation requirement is made.

τ_{had}	L1 size (EM, had.)	fitted p_T offset [GeV]	fitted sharpness
1-track	2×1, 2×2	32.6	4.43
	2×2, 2×2	31.2	3.87
	2×2, 4×4	31.0	3.72
	4×4, 2×2	30.7	3.67
	4×4, 4×4	30.5	3.52
3-track	2×1, 2×2	41.0	4.47
	2×2, 2×2	38.9	3.93
	2×2, 4×4	38.3	3.65
	4×4, 2×2	37.7	3.71
	4×4, 4×4	37.1	3.42

8. PROSPECTS FOR $H \rightarrow \tau\tau$

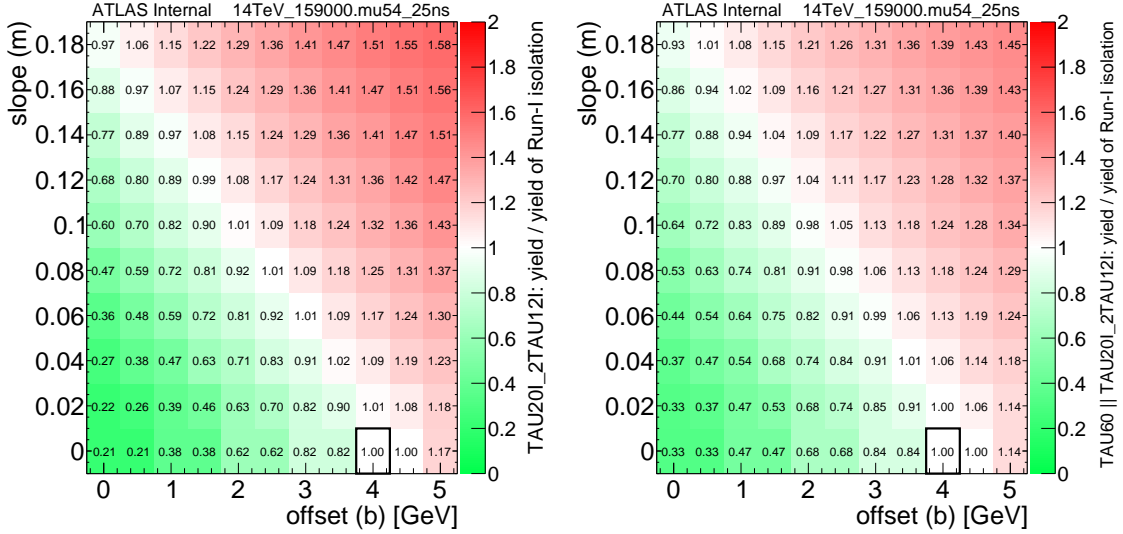


Figure 8.9: L1 rate for the di- τ_{had} trigger in 14 TeV minimum bias MC for various p_T^{L1} -dependent isolation definitions relative to the 2012 definition: $p_T^{\text{L1,iso}} \leq 4$ GeV. Many options give the same rate (white color). The rate is calculated irrespective of the lowest unprescaled single τ_{had} trigger (left) and with a logical OR of it (right).

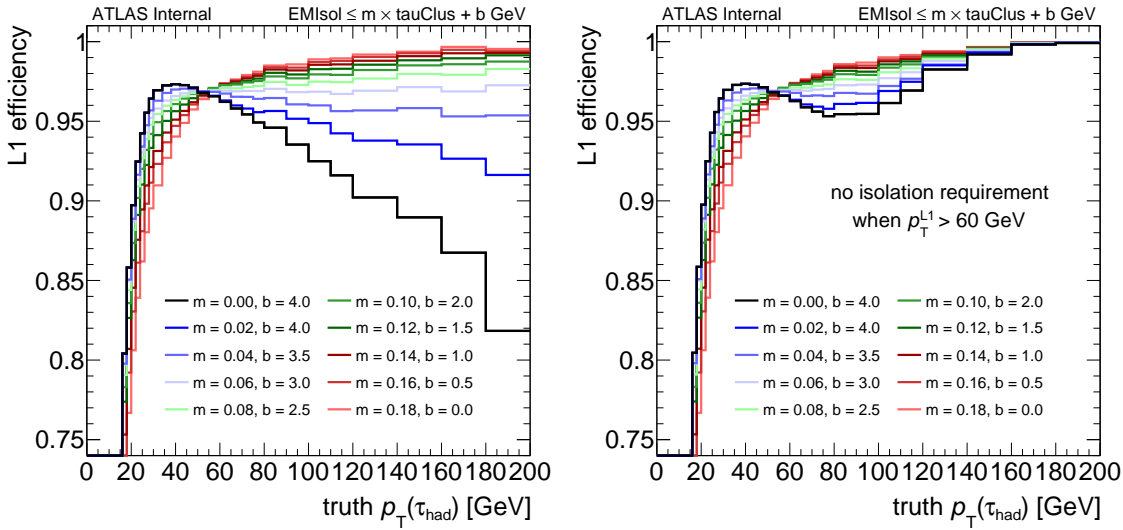


Figure 8.10: Efficiency for firing the L1 τ_{had} trigger for various p_T^{L1} -dependent isolation definitions which have similar rates, as derived from Fig. 8.9. The 2012 definition is the black line. The efficiency is calculated irrespective of the lowest unprescaled single τ_{had} trigger (left) and with a logical OR of it (right).

8. PROSPECTS FOR $H \rightarrow \tau\tau$

threshold of the $\ell + \tau_{\text{had}}$ triggers or raising the jet threshold of all triggers. If additional bandwidth is available, the jet threshold or $\Delta R(\tau\tau)$ requirement can be relaxed. The contingencies are shown in Table 8.8.

8.2 HL-LHC

This section documents projections of the Standard Model $H \rightarrow \tau\tau$ analysis for the ECFA High Luminosity LHC Experiments Workshop 2014 [111]. The projection considers High Luminosity LHC (HL-LHC) running conditions with 14 TeV pp collisions, 3000 fb^{-1} delivered integrated luminosity, and an average number of overlapping pp collisions per bunch-crossing (pile-up) $\langle \mu \rangle = 140$. Only the VBF $\tau_\ell \tau_{\text{had}}$ ($\ell = e, \mu$) analysis category is considered.

This projection is built from the existing Run-I analysis [2] by using the same data samples, Monte Carlo samples, data-driven background estimates, and multivariate analysis (MVA) techniques. It is projected to HL-LHC conditions by adding emulation of the harsher pile-up conditions and scaling the predictions by the ratios of cross-sections and integrated luminosity for HL-LHC versus 2012 conditions. The harsher pile-up conditions impacts jets and E_T^{miss} significantly.

The analysis also considers possible extensions of the tracking volume to investigate the impact of tracking-based rejection of pile-up jets.

Table 8.7: The τ_{had} L1 menu. A baseline L1 menu is used for calculating the unique rate.

signature	target	L1 item	unique rate [kHz]
single τ_{had}	exotics, SUSY	TAU60V	1.6
di- τ_{had}	Higgs, di- H	TAU12I_TAU20I_J25-DR28	3.7
$e + \tau_{\text{had}}$	Higgs	EM15HI_TAU12I_J25-DR28	1.2
$e + \tau_{\text{had}}$	exotics, SUSY	EM15HI_TAU40	0.2
$\mu + \tau_{\text{had}}$	Higgs	TAU12I_MU10_J25-DR28	0.5
$\mu + \tau_{\text{had}}$	exotics, SUSY	TAU20_MU10	0.5
$\tau_{\text{had}} + E_T^{\text{miss}}$	SUSY	TAU20_XE45_J20	0.5
$\tau_{\text{had}} + E_T^{\text{miss}}$	SUSY	TAU12I_TAU20I_XE35	2.1
$\tau_{\text{had}} + E_T^{\text{miss}}$	SUSY	EM15HI_TAU12I_XE35	0.2
$\tau_{\text{had}} + E_T^{\text{miss}}$	SUSY	TAU12I_MU10_XE35	0.0

8.2.1 Selection

The selection of a VBF-like sample for the $\tau_\ell\tau_{\text{had}}$ final state discussed in this note relies on the identification of one lepton (electron or muon), one hadronic tau and at least two jets. Muons are selected if they have transverse momentum higher than 26 GeV and are in the region $|\eta| < 2.4$. Quality criteria on the inner detector track associated to the muon are also applied. Electron candidates are formed from a cluster in the electromagnetic calorimeters (transition regions, $1.37 < |\eta| < 1.52$, are excluded) that is matched with a track reconstructed within the inner detector, $|\eta| < 2.47$. Electrons with a transverse momentum higher than 26 GeV are selected and a `tightPP` working point is used. For both muons and electrons, calorimeter and track-based isolation criteria with similar combined selection efficiency as the LHC Run-I analysis are assumed.

Jets are reconstructed using the anti- k_t algorithm [64] with a radius parameter $R = 0.4$, taking topological clusters in the calorimeters as inputs. Only jets with $|\eta| < 4.5$ are selected in this analysis. The general p_T threshold for jets is 30 GeV, and specific selection of the VBF analysis is mentioned later. Track-based pile-up suppression with jet-vertex fraction (JVF) [66] is applied in the range of the tracking volume ($|\eta^{\text{jet}}| < 2.4$). In the range $|\eta| < 2.5$, b -tagged jets are identified using the MV1 tagging algorithm based on the impact parameter information and on the reconstruction of the displaced vertices of the hadron decays inside the jets [67].

Tau candidates are seeded by anti- k_t [64], $R = 0.4$ jets with $p_T > 20$ GeV whose calorimeter cluster and leading track must satisfy $|\eta| < 2.47$. The Boosted Decision Tree (BDT) tau identification method [1] is used, requiring that the tau candidate passes the `medium` tightness, corresponding to approximately 55-60% efficiency. A dedicated selection to reject fake tau candidates from electrons and muons is applied.

Table 8.8: Contingency options for the $H \rightarrow \tau\tau$ section of the τ_{had} L1 menu. The change in unique rate is with respect to the baseline menu. A baseline L1 menu is used for calculating the unique rate.

scenario	item change	motivation	Δ [kHz]
add rate	3rd TAU20I → TAU15I	slow τ_{had} turn-on	+3.2
	2nd $\Delta R(\tau\tau) < 2.8 \rightarrow 3.0$	ΔR inefficiency for di- H	+2.6
	1st J25 → J20	slow jet turn-on	+0.4
baseline	–	–	–
	1st TAU12I → TAU20I ($\tau_\ell\tau_{\text{had}}$)	small gain with $\ell + \tau_{\text{had}}$ triggers	-1.7
	cut rate 2nd J25 → J30	jet threshold is robust	-2.2
cut rate	3rd TAU20I → TAU25I	τ_{had} threshold is robust	-3.8

8. PROSPECTS FOR $H \rightarrow \tau\tau$

When different objects selected according to the above criteria overlap with each other geometrically (within $\Delta R < 0.2$), only one of them is considered for further analysis. The overlap is resolved by selecting muon, electron, τ_{had} and jet candidates in this order of priority.

The signal events are characterized by true $E_{\text{T}}^{\text{miss}}$ due to the presence of the neutrinos from the tau decays. In this analysis, the $E_{\text{T}}^{\text{miss}}$ reconstruction uses reconstructed high- p_{T} physics objects (electrons, photons, τ_{had} , jets and muons) and a measurement of the soft term, which includes contributions from the underlying event, multi-parton interactions, and physics objects below analysis threshold.

Unless otherwise noted, the topological selection criteria are identical to the Run-I analysis. One lepton and one hadronically decaying tau are required, and there must be at least two jets with a significant separation in η as expected for VBF production. Some additional topological cuts are applied to suppress backgrounds while retaining most of the signal. The VBF category is intentionally defined loosely since the discrimination of signal from background is meant to be handled by the BDTs. The event selection is summarized in Table 8.9.

8.2.2 Emulation of High-Luminosity LHC conditions

The method of pile-up emulation follows the same procedure used by the $H \rightarrow WW^*$ projection for ECFA 2013 [117]. The approach is to port the existing Run-I analysis to HL-LHC conditions by overlaying pile-up jets on the 8 TeV samples, degrading the hard-scatter (HS) jet and $E_{\text{T}}^{\text{miss}}$ resolution, and propagating the impact of this to the analysis.

Table 8.9: Event selection and categorization criteria. The $m_{\text{T}}(\ell, E_{\text{T}}^{\text{miss}})$ requirement is relaxed to avoid signal loss due to the degradation of the $E_{\text{T}}^{\text{miss}}$ resolution at high $\langle \mu \rangle$.

Type	Selection
$\tau_{\ell}\tau_{\text{had}}$ preselection	exactly one identified and isolated lepton (e, μ) exactly one identified tau opposite sign lepton and tau no additional leptons passing loosened identification criteria no jets passing the b -tagging criteria $m_{\text{T}}(\ell, E_{\text{T}}^{\text{miss}}) < 100$ GeV
VBF categorization	leading jet with $p_{\text{T}} > 50$ GeV any additional jet with $p_{\text{T}} > 30$ GeV $ \Delta\eta(\text{lead jet, sub-lead jet}) > 3.0$ $m_{\tau\tau}^{\text{vis.}} > 40$ GeV

8.2.2.1 Performance assumptions

The Run-I triggering thresholds and efficiency are assumed. The ATLAS trigger has many upgrades planned to mitigate the impact of higher instantaneous luminosity, including the New Small Wheel, hardware trackers, and finer L1 EM-calorimeter granularity. Improvements to the L1 granularity will especially improve triggers with electrons and taus, since shower shape variables can be built to discriminate against QCD jets better than existing isolation variables. It is then deemed unnecessary to consider scenarios of significant trigger efficiency loss in detail.

It is also assumed that the lepton and tau reconstruction and identification efficiencies are equivalent to that observed in the 2012 data. This is chosen because the detector upgrades for the HL-LHC aim for achieving a performance similar to Run-I despite the harsher pile-up conditions. Hard-scatter jets from the 8 TeV samples are smeared to emulate the reconstructed jet resolution at HL-LHC conditions [118]. The jet smearing is propagated to the E_T^{miss} calculation. The soft-term resolution of the E_T^{miss} is smeared: 33 MeV per unit of $\langle \mu \rangle$, which is derived from high pile-up Z/γ^* simulation.

8.2.2.2 Pileup emulation

Pileup jets are inserted into the event according to rates recommended by the ATLAS projections [118]. For $\langle \mu \rangle = 140$ and jet $p_T \geq 30$ GeV, the rate is 2.4 additional pile-up jets per event. The kinematics of the inserted pile-up jets are derived from high pile-up Z/γ^* simulation. Templates are built for p_T and η and are then randomly sampled for each inserted pileup jet.

The hard-scattering jets are assumed to have a reconstruction efficiency of the track-confirmation algorithm recommended by the existing ATLAS projections. The pile-up jets are assumed to have the pile-up suppression efficiency of the 2012 JVF algorithm, which is 98% within the tracking volume [66]. No degradation of pile-up jet suppression is assumed because techniques already exist which outperform the JVF tagger. The pile-up suppression is assumed to not depend on p_T and η other than at the boundary of the tracker. The insertion of pileup jets is then propagated to the E_T^{miss} calculation.

A new tracker in the forward region $|\eta| > 2.5$ is being considered for Phase-II ATLAS upgrades. To emulate the impact of pile-up jet suppression with a forward tracker, the analysis is re-run with forward pile-up jet rejection imposed by hand. Since the scope of the forward tracker is uncertain, a range of coverage and performance is considered: coverage of $|\eta| < 3.0, 3.5$, and 4.0 and pile-up jet suppression of 50%, 75%, and 90% with negligible signal (hard-scattering jets) efficiency loss is evaluated. For comparison, a pile-up jet suppression of 90% with negligible signal efficiency loss is comparable to the performance of the JVF tagger within the existing tracker [66].

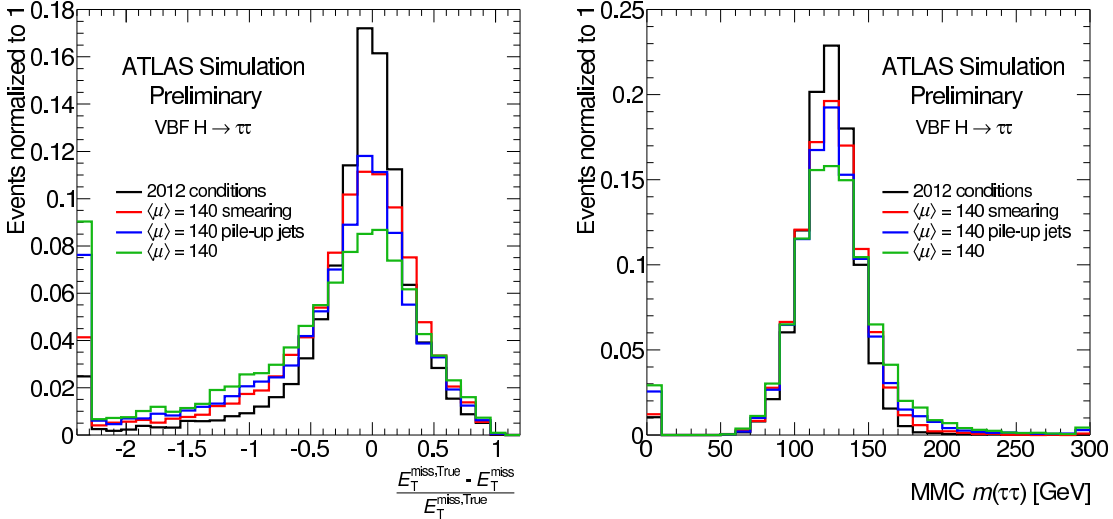


Figure 8.11: Degradation of E_T^{miss} -related observables at HL-LHC conditions for VBF $H \rightarrow \tau\ell\tau_{\text{had}}$: the E_T^{miss} resolution (left) and reconstructed $m_{\tau\tau}^{\text{MMC}}$ (right) [111]. The underflow of the $m_{\tau\tau}^{\text{MMC}}$ shows the fraction of events which fail the mass reconstruction.

The method of randomly inserting pile-up jets into existing events does not consider correlations between pile-up jets. This could be problematic because the p_T imbalance of the event could be overstated, which would propagate to unphysical biases of quantities which are sensitive to balance like E_T^{miss} . The impact of this has been assessed by overlaying entire truth pile-up events onto the existing hard scatter events. The results are comparable.

8.2.2.3 Impact on observables

The VBF $H \rightarrow \tau\tau$ analysis relies on two jets with large $\Delta\eta$ to describe the VBF topology and on E_T^{miss} to describe di- τ decays. The presence of forward pile-up jets can then be expected to degrade the sensitivity of the analysis because they will cause migration of background events into the VBF category, and because they will bias the E_T^{miss} calculation.

The contamination of pile-up jets in the VBF category for the total background is significant. Most events (72%) have a sub-lead pile-up jet, and nearly half (42%) have a lead pile-up jet. These pile-up jets are especially problematic because they are typically forward, thus any event with pile-up lead and sub-lead jets in opposite hemispheres will have $|\eta_{j1} - \eta_{j2}| > 4.8$.

Degradation of the E_T^{miss} and MMC $m(\tau\tau)$ under the high-luminosity conditions is shown in Fig. 8.11 for simulated VBF $H \rightarrow \tau\tau$. Both observables are degraded by jet and E_T^{miss} smearing and by the presence of forward pile-up jets biasing the E_T^{miss} calculation.

8.2.3 Analysis

8.2.3.1 Boosted decision tree training

A multi-variate analysis approach is used by training BDTs to discriminate signal from background. It is trained using all backgrounds scaled to their respective cross-sections against the total (ggF + VBF) signal shapes. The same training parameters and input variables as the Run-I analysis are used, and the input variables are listed in Table 8.10.

BDTs are trained for a variety of forward tracker coverages ($|\eta| < 3$, $|\eta| < 3.5$ and $|\eta| < 4$) and pile-up rejection values (50%, 75% and 90%). Fig. 8.12 shows the efficiency for rejecting the background versus the efficiency for selecting the signal for the scenario of 90% forward pile-up rejection. For a given signal efficiency, the background rejection improves with larger coverage.

8.2.3.2 Kinematic distributions

Predicted signal and background BDT input distributions as well as basic object kinematics are shown in Figures Fig. 8.13, Fig. 8.14 and Fig. 8.15. Signal and background are predicted with the same methods as the Run-I analysis [2], including the data-driven prediction of the dominant $Z \rightarrow \tau\tau$ and fake backgrounds. The resulting BDT score is presented in Figure Fig. 8.16.

8.2.4 Results

Yields for signal and background in the high BDT score bins are shown in Table 8.11. As in the Run-I analyses, $Z \rightarrow \tau\tau$ and fakes are the dominant backgrounds in the most signal-like regime. The binning of the BDT is optimized to maximize the expected sensitivity.

Table 8.10: Discriminating variables used for the BDT training.

Variable	Definition
$\Delta R(\tau_{\text{had}}, \ell)$	Separation of the lepton and τ_{had}
$m_T(\ell, E_T^{\text{miss}})$	Transverse mass of the lepton and E_T^{miss}
$E_T^{\text{miss}}\phi\text{-centrality}$	Centrality of the E_T^{miss} between the lepton and τ_{had}
MMC $m_{\tau\tau}$	$\tau\tau$ mass estimator
$m_{j1,j2}$	Invariant mass of the 2 leading jets
$\eta_{j1} \times \eta_{j2}$	Product of the η s of the two leading jets
$ \eta_{j1} - \eta_{j2} $	Absolute difference η s of the two leading jets
$\ell \eta\text{-centrality}$	Centrality of the lepton between the two leading jets
p_T^{Total}	$ \vec{p}_T^\ell + \vec{p}_T^{\tau_h} + \vec{p}_T^{j1} + \vec{p}_T^{j2} + \vec{E}_T^{\text{miss}} $

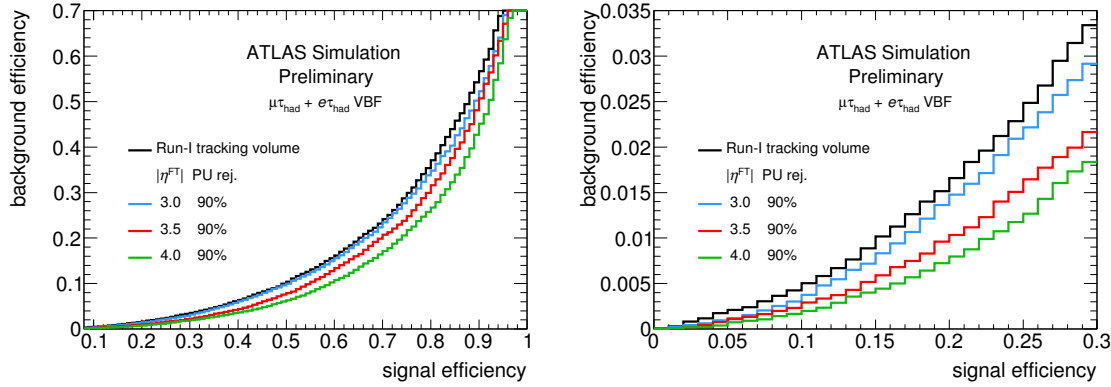


Figure 8.12: Signal efficiency versus background efficiency for scenarios of generic forward tracker coverage and rejection power (left) and zoomed in to lower signal efficiency (right) [111]. A BDT is trained in the VBF category for each scenario.

8.2.4.1 Uncertainties assumptions

When calculating the sensitivity of the analysis, three scenarios of background uncertainties and two scenarios of theory uncertainties are considered. The theory uncertainties are varied from no theory uncertainties to Run-I theory uncertainties, which are as large as 6% (30%) for the VBF (ggF) Higgs production modes [2]. The experimental signal uncertainty is fixed at 5% accounting for experimental sources such as jet energy scale uncertainties. The experimental background uncertainties are varied to 10% and 5% of the prediction, and they are treated as uncorrelated between backgrounds and between bins of the BDT score.

The projected sensitivity is shown in Table 8.12. The two scenarios of background uncertainties

Table 8.11: Yields for signal and background in the VBF category and in the most sensitive BDT bins, as shown in Fig. 8.16.

process	VBF category	third highest bin	second highest bin	highest bin
VBF $H \rightarrow \tau\tau$	8970	114	147	206
ggF $H \rightarrow \tau\tau$	16410	44	46	39
$Z \rightarrow \tau\tau$	1682400	875	720	514
fakes	2959800	205	190	155
$t\bar{t}$	191400	100	20	< 20
other	198600	< 20	< 20	< 20
signal	25380	158	193	245
background	5032200	1180	930	669

8. PROSPECTS FOR $H \rightarrow \tau\tau$

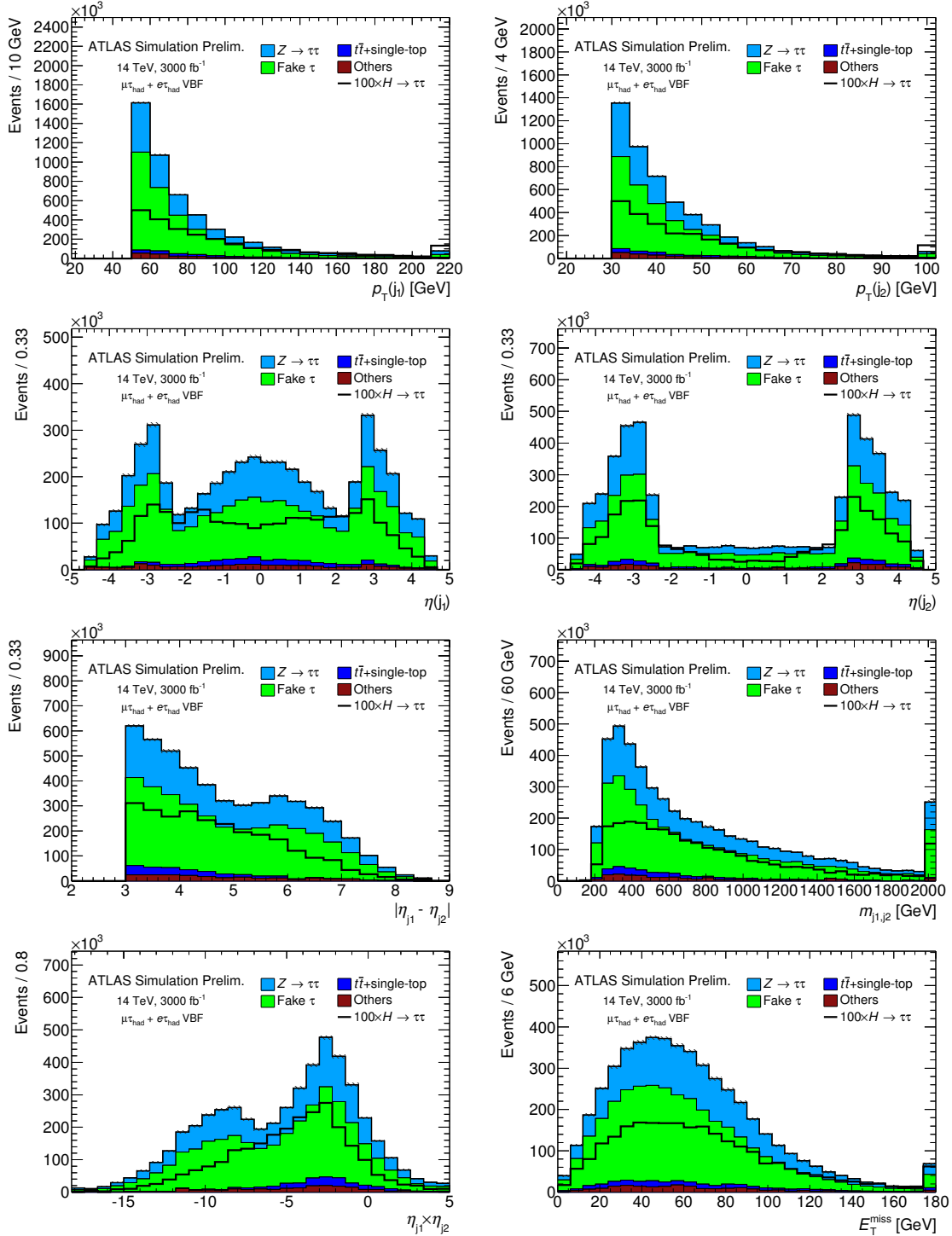


Figure 8.13: Signal and background HL-LHC predictions of (a) leading jet p_T , (b) sub-leading jet p_T , (c) leading jet η , (d) sub-leading jet η , (e) $\Delta\eta_{jj}$, (f) m_{jj} , (g) $\eta_{\text{leadjet}} \times \eta_{\text{sub-leadjet}}$ and (h) E_T^{miss} [111]. The last bin contains the overflow events.

8. PROSPECTS FOR $H \rightarrow \tau\tau$

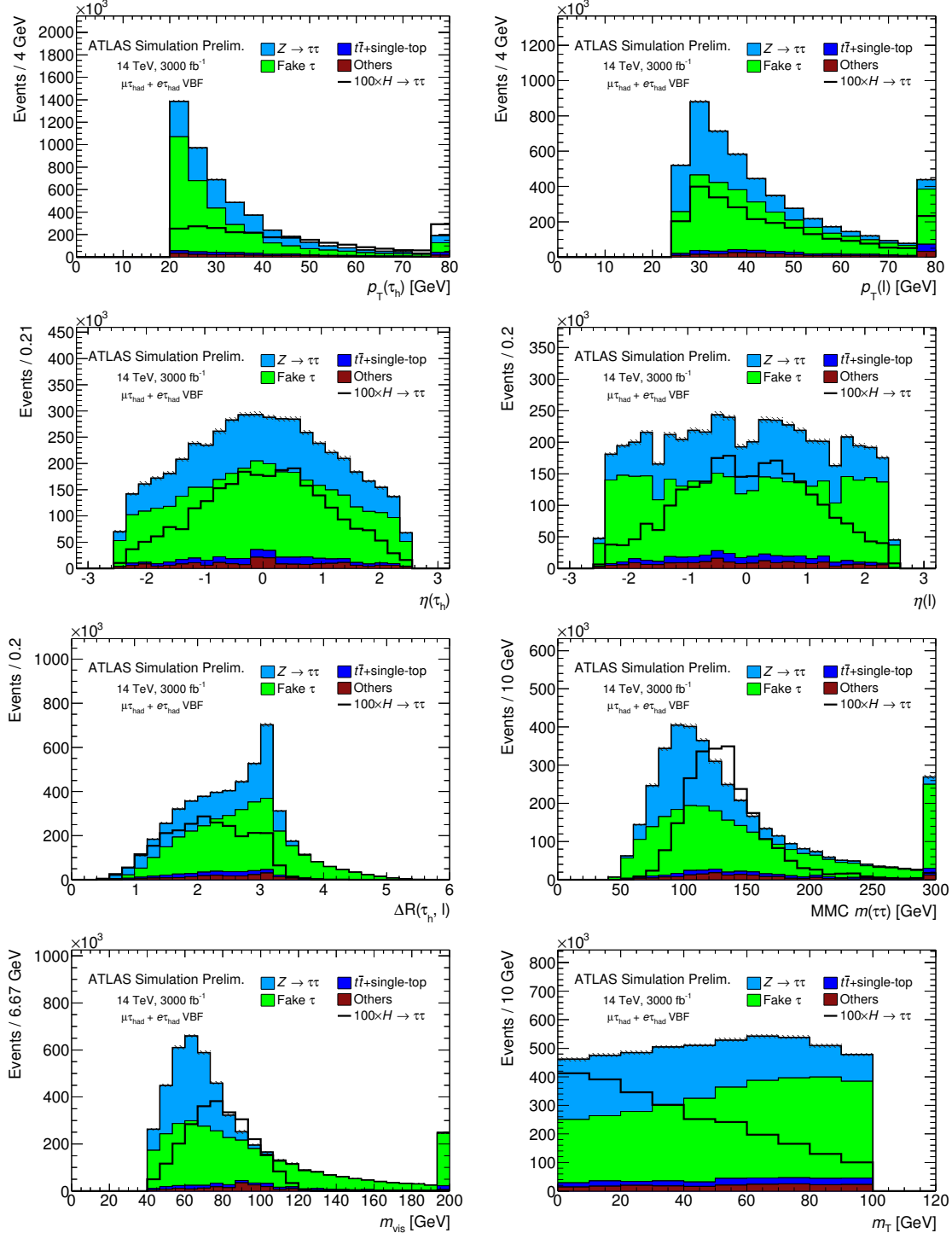


Figure 8.14: Signal and background HL-LHC predictions of (a) $p_T(\tau_{\text{had}})$, (b) $p_T(\text{lepton})$, (c) $\eta(\tau_{\text{had}})$, (d) $\eta(\text{lepton})$, (e) $\Delta R(\tau_{\text{had}}, \text{lepton})$, (f) MMC $m_{\tau\tau}$ and (g) m_{vis} and (h) $m_T(\ell, E_T^{\text{miss}})$ [111]. The last bin contains the overflow events.

8. PROSPECTS FOR $H \rightarrow \tau\tau$

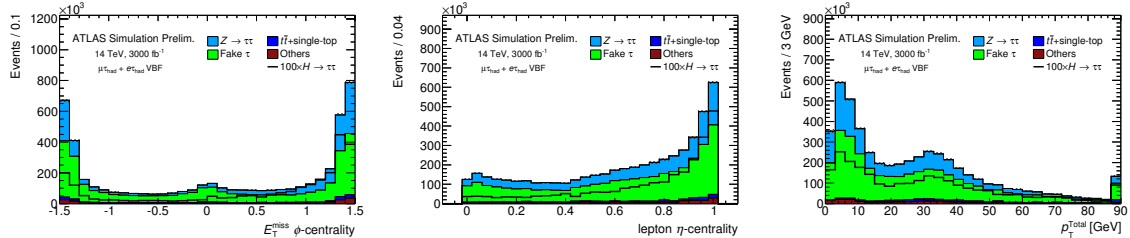


Figure 8.15: Signal and background HL-LHC predictions of (a) E_T^{miss} ϕ -centrality, (b) lepton η -centrality and (c) p_T^{Total} [111]. The last bin contains the overflow events.

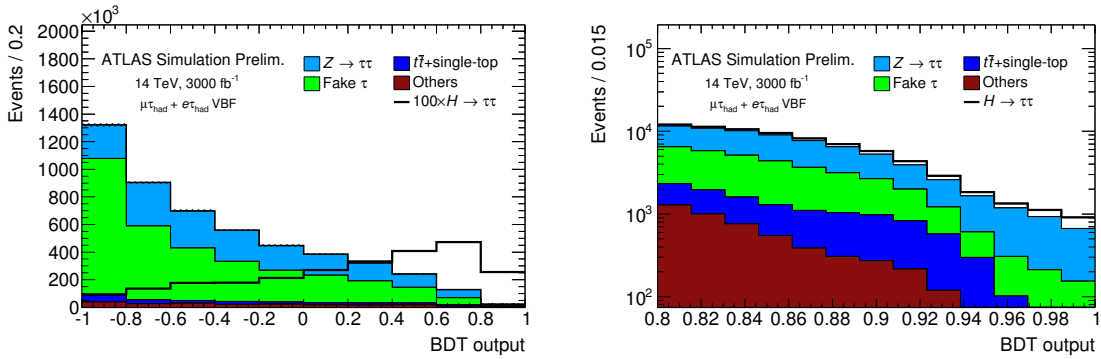


Figure 8.16: Signal and background HL-LHC predictions of the BDT spectrum in the (a) full range and (b) highest bins range [111]. Signal and background are overlaid in (a) and stacked in (b).

and two scenarios of theory uncertainties are shown. The sensitivity of the projection is driven by the uncertainty on the background prediction. For $\sigma_B^{\text{syst.}} = 10\%$, the projected uncertainty on μ with no signal theory uncertainties is 0.24. For $\sigma_B^{\text{syst.}} = 5\%$, this projected uncertainty is 0.13.

The impact of pile-up jet rejection in the forward region is also evaluated as an example of the impact of a forward tracker, and results are given in Table 8.13. Multiple scenarios of $|\eta|$ coverage and pile-up jet rejection are considered. For these scenarios, negligible loss of HS jets to forward pile-up jet rejection is assumed, a 10% systematic uncertainty is assumed for backgrounds, a 5% experimental

Table 8.12: Uncertainty on the signal strength ($\Delta\mu$) for different scenarios of background uncertainties and signal theory uncertainties.

		current $\sigma_S^{\text{theo.}}$	no $\sigma_S^{\text{theo.}}$
$\sigma_B^{\text{syst.}}$	$\sigma_S^{\text{syst.}}$	$\Delta\mu$	$\Delta\mu$
10%	5%	0.25	0.24
5%	5%	0.16	0.13

systematic uncertainty is assumed for signals, and theoretical uncertainties on signals are ignored.

8.2.5 Conclusions

The projection of the Standard Model $H \rightarrow \tau\tau$ analysis to the High Luminosity LHC (HL-LHC) running conditions with 14 TeV pp collisions, 3000 fb^{-1} delivered integrated luminosity, and an average number of overlapping pp collisions $\langle\mu\rangle = 140$ is performed. The VBF $\tau_\ell\tau_{\text{had}}$ ($\ell = e, \mu$) analysis category is considered, and the uncertainty on the signal strength (μ) is projected to be 24% when theory uncertainties are ignored and 10% (5%) background (signal) uncertainties are assumed. The projected uncertainty could be reduced significantly if pile-up jets outside the current tracking volume could be rejected similar to pile-up jet rejection within the tracking volume in 2012. The uncertainty on μ is projected to be 8 – 18% depending on the scenario of forward tracker coverage and pile-up jet rejection.

Table 8.13: Uncertainty on the signal strength ($\Delta\mu$) for different scenarios of forward tracking.

forward pileup jet rejection	50%	75%	90%
forward tracker coverage	$\Delta\mu$		
Run-I tracking volume	0.24		
$ \eta < 3.0$	0.18	0.15	0.14
$ \eta < 3.5$	0.18	0.13	0.11
$ \eta < 4.0$	0.16	0.12	0.08

CHAPTER 9

Conclusions

This thesis described evidence of Higgs boson decays to tau leptons with the ATLAS detector at the LHC, with special emphasis given to the VBF $H \rightarrow \tau_\ell \tau_{\text{had}}$ subset of the analysis. The theoretical context, LHC, and ATLAS experiment were briefly reviewed. The signature of tau leptons at ATLAS was described in detail.

The data in the $H \rightarrow \tau\tau$ analysis correspond to 25 fb^{-1} of proton collisions with $\sqrt{s} = 7$ or 8 TeV . Strong evidence for $H \rightarrow \tau\tau$ is observed (expected) with a 4.5σ (3.4σ) deviation from the background-only hypothesis. The measured signal strength, normalized to the Standard Model expectation, is $1.4^{+0.4}_{-0.4}$, which is consistent with the Standard Model prediction. A limiting factor of the measurement is the size of the available dataset.

Future LHC data-taking campaigns will offer substantially more data and at a higher collision energy, though the harsh conditions present challenges for triggering on τ_{had} and rejecting pileup jets mimicking the VBF signature. The VBF $H \rightarrow \tau_\ell \tau_{\text{had}}$ analysis projects to measure a signal strength uncertainty of 8% with the addition of a high performance, high coverage forward tracker.

APPENDIX A

Control regions for fakes

Comparisons of data with prediction for fakes control regions in the $H \rightarrow \tau\tau$ analysis are shown.

A.1 Same sign CR

A.2 MC SR

A.3 $W \rightarrow \ell\nu_\ell$ CR

A.4 QCD CR

A.5 $Z \rightarrow \ell\ell$ CR

A.6 top CR

A. CONTROL REGIONS FOR FAKES

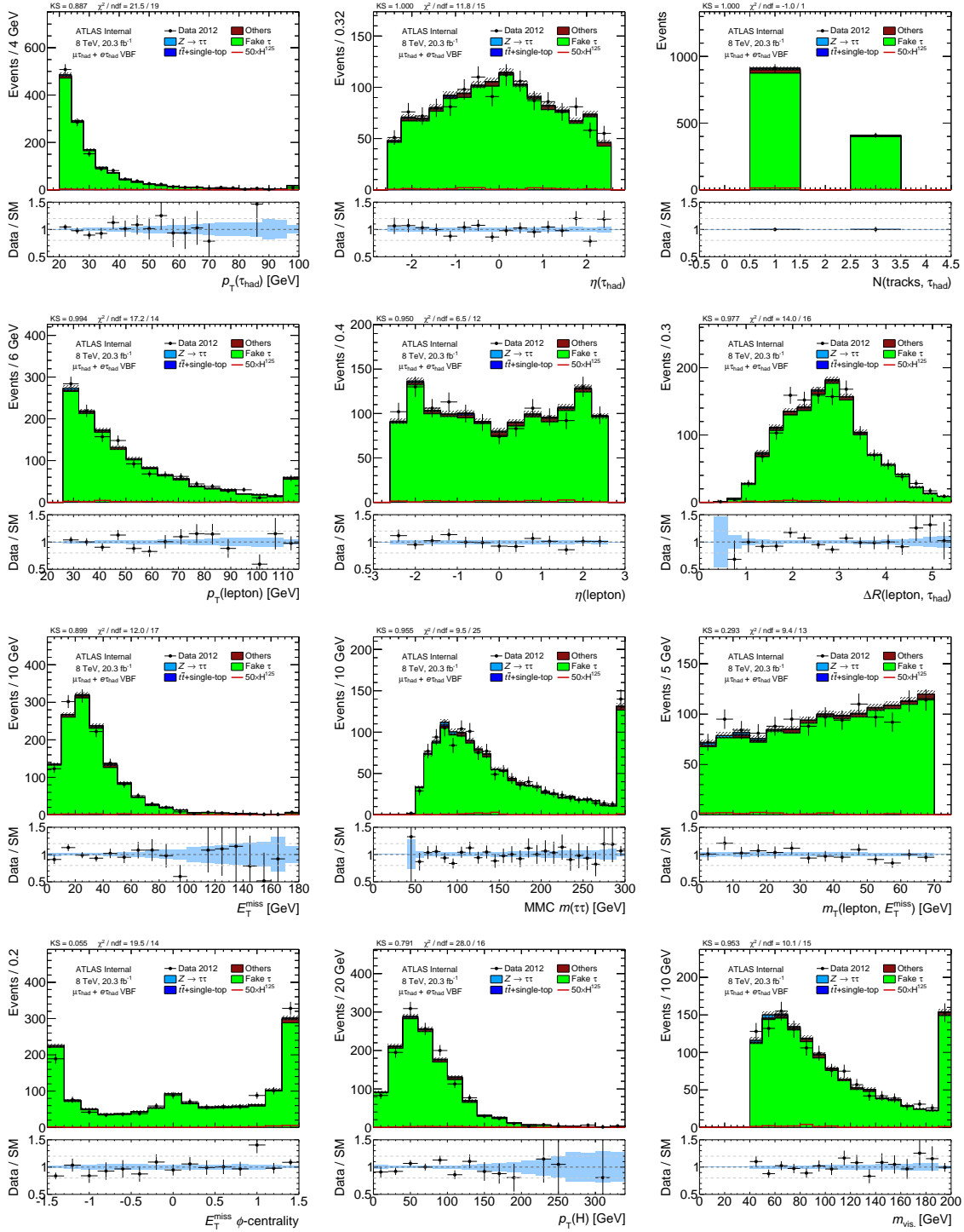


Figure A.1: Comparison of data and $j \rightarrow \tau_{\text{had}}$ prediction in the same sign CR for various event kinematics. Only statistical uncertainties are shown.

A. CONTROL REGIONS FOR FAKES

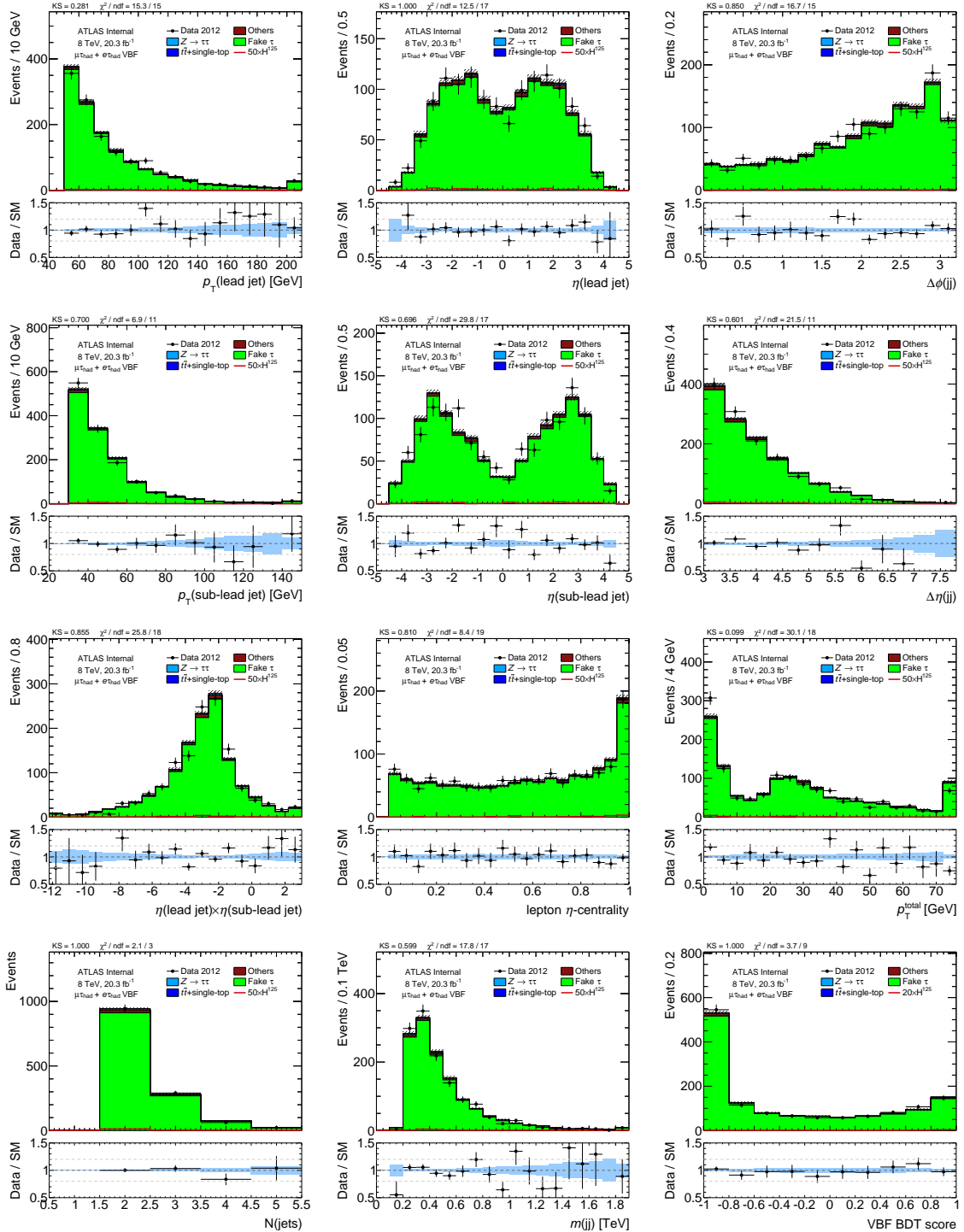


Figure A.2: Comparison of data and $j \rightarrow \tau_{\text{had}}$ prediction in the same sign CR for various event kinematics. Only statistical uncertainties are shown.

A. CONTROL REGIONS FOR FAKES

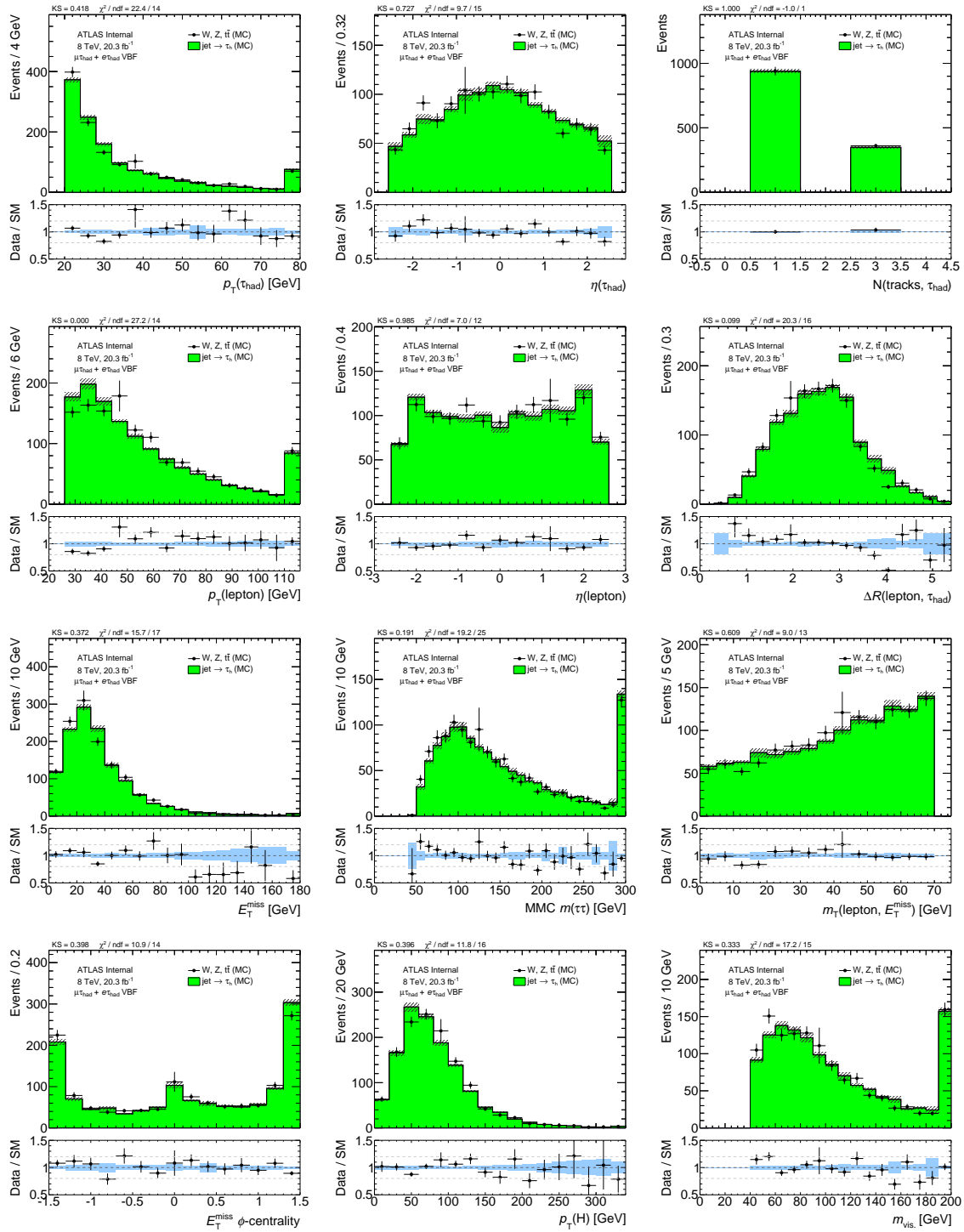


Figure A.3: Comparison of the prediction of identified taus and the $j \rightarrow \tau_h$ prediction, both in simulation, in the signal region for various event kinematics. Only statistical uncertainties are shown.

A. CONTROL REGIONS FOR FAKES

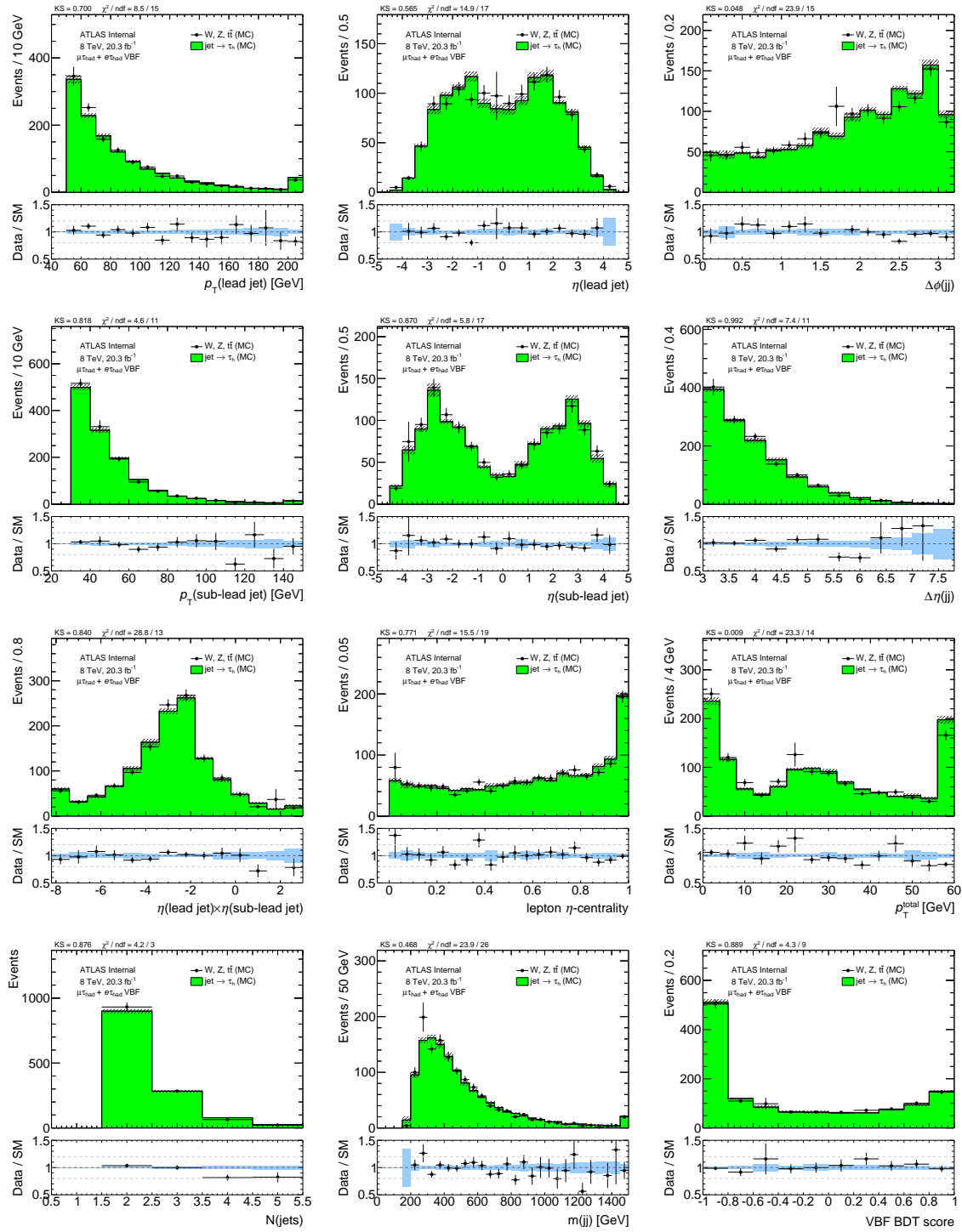


Figure A.4: Comparison of the prediction of identified taus and the $j \rightarrow \tau_{\text{had}}$ prediction, both in simulation, in the signal region for various event kinematics. Only statistical uncertainties are shown.

A. CONTROL REGIONS FOR FAKES

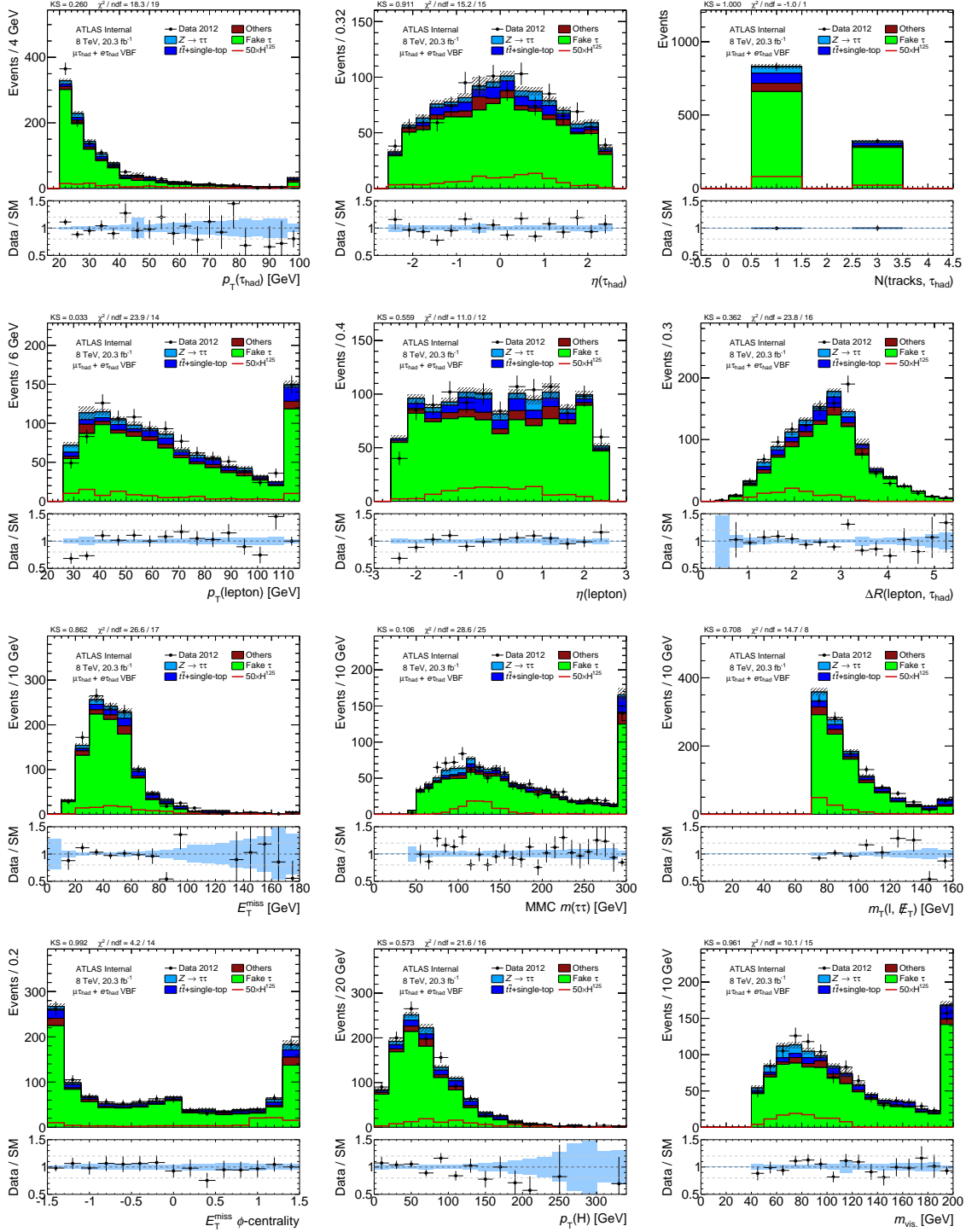


Figure A.5: Comparison of data and $j \rightarrow \tau_{\text{had}}$ prediction in the $W \rightarrow \ell\nu\ell$ CR for various event kinematics. Only statistical uncertainties are shown.

A. CONTROL REGIONS FOR FAKES

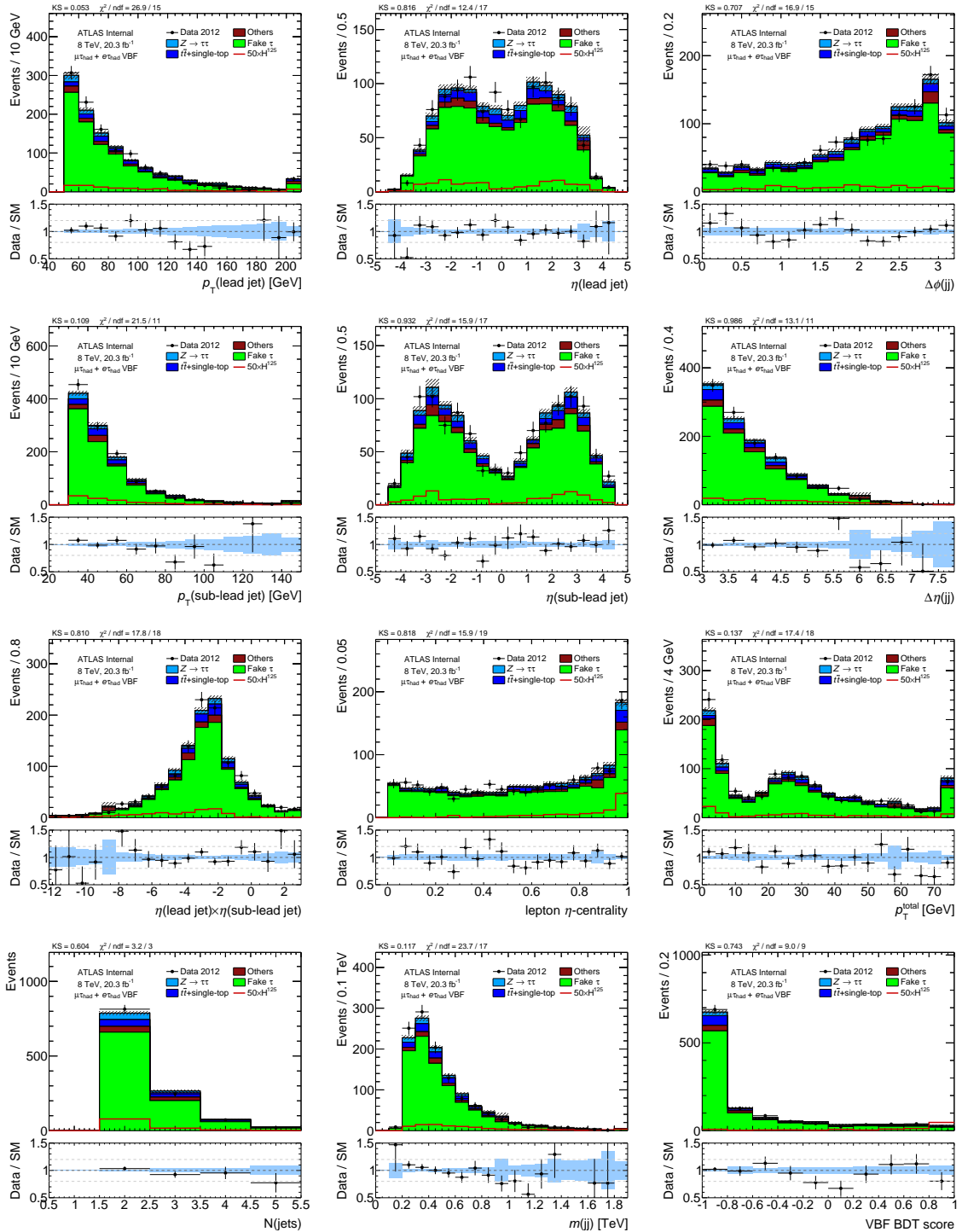


Figure A.6: Comparison of data and $j \rightarrow \tau_{\text{had}}$ prediction in the $W \rightarrow \ell\nu\ell$ CR for various event kinematics. Only statistical uncertainties are shown.

A. CONTROL REGIONS FOR FAKES

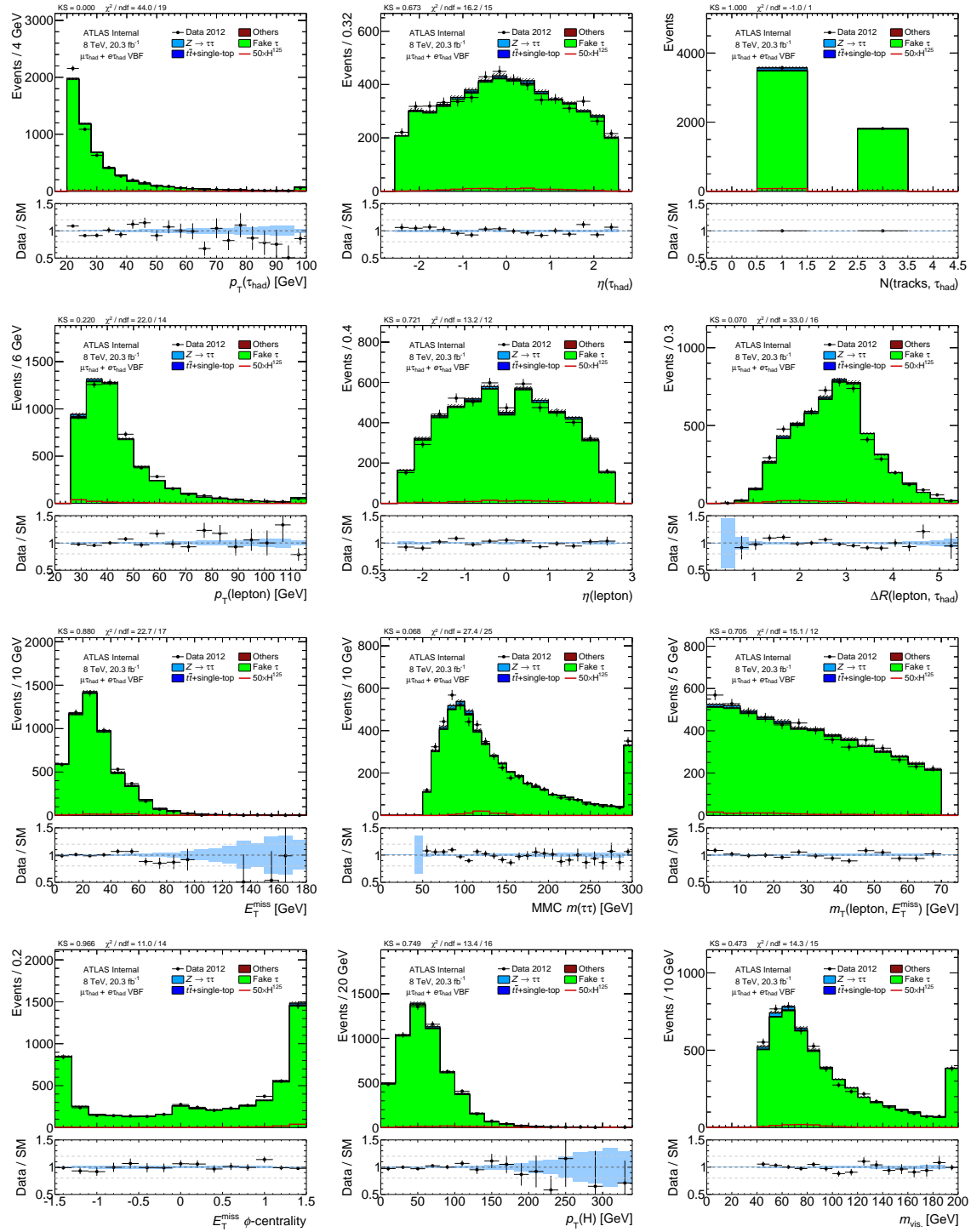


Figure A.7: Comparison of data and $j \rightarrow \tau_{\text{had}}$ prediction in the QCD CR for various event kinematics. Only statistical uncertainties are shown.

A. CONTROL REGIONS FOR FAKES

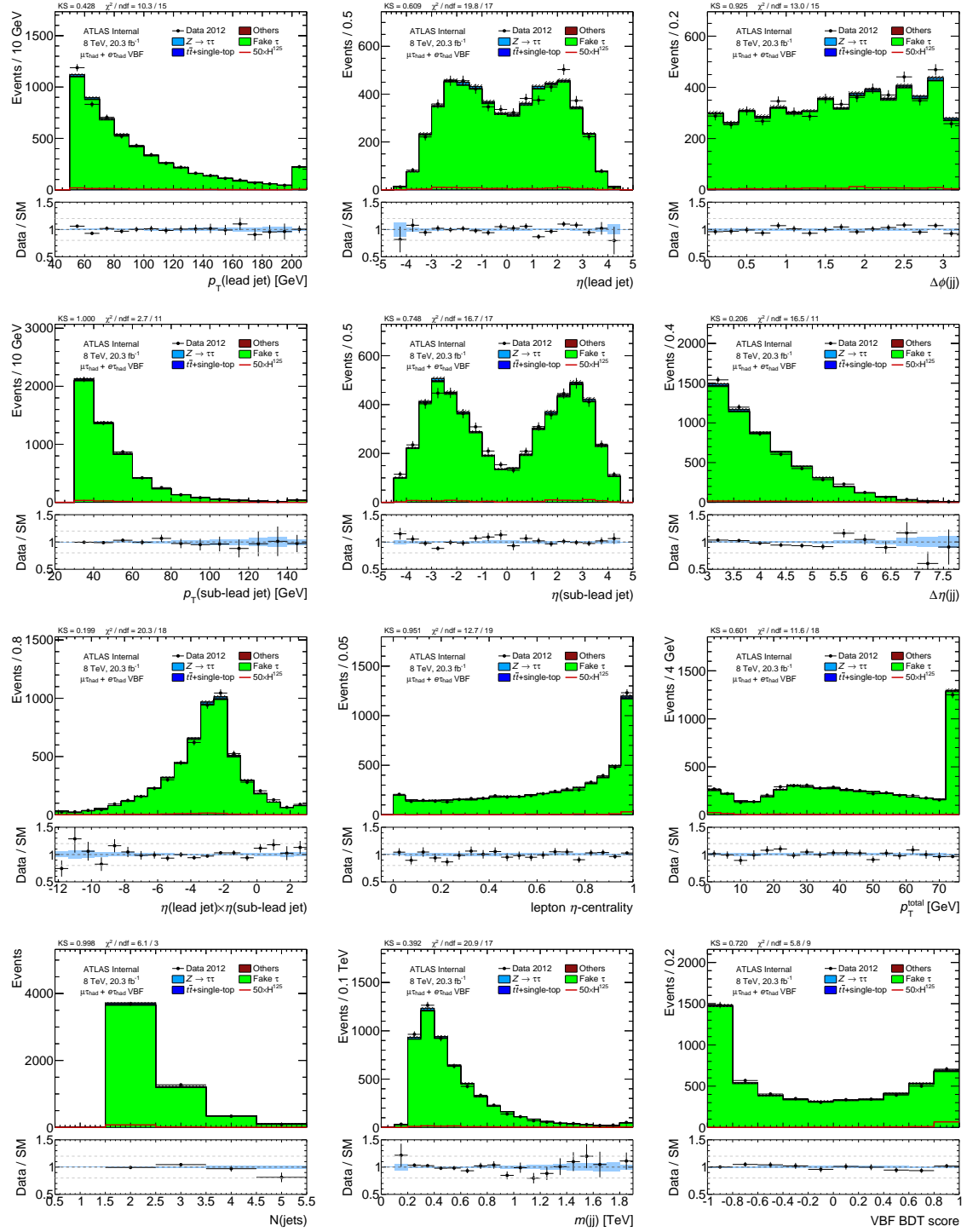


Figure A.8: Comparison of data and $j \rightarrow \tau_{\text{had}}$ prediction in the QCD CR for various event kinematics. Only statistical uncertainties are shown.

A. CONTROL REGIONS FOR FAKES

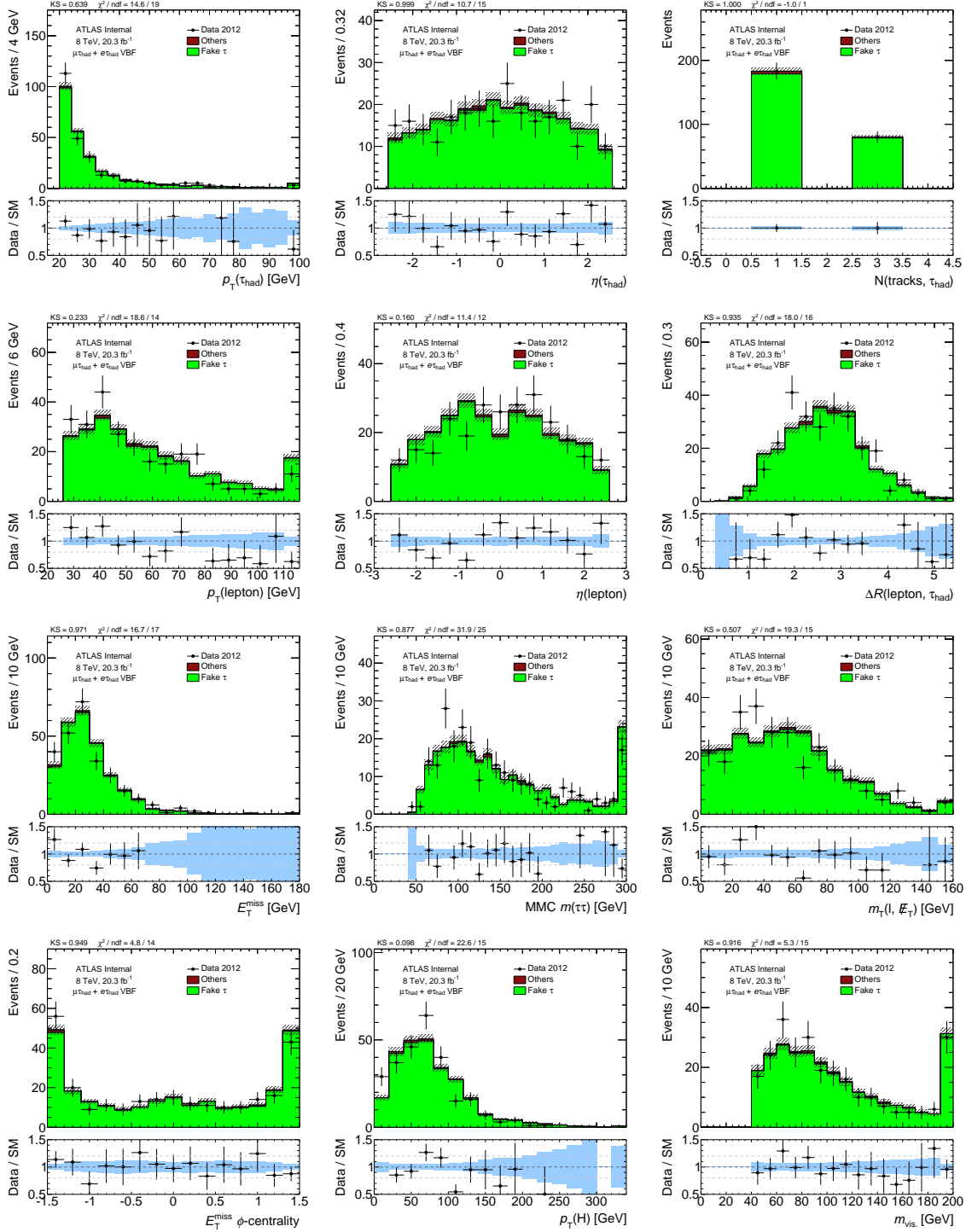


Figure A.9: Comparison of data and $j \rightarrow \tau_{\text{had}}$ prediction in the $Z \rightarrow \ell\ell$ CR for various event kinematics. Only statistical uncertainties are shown.

A. CONTROL REGIONS FOR FAKES

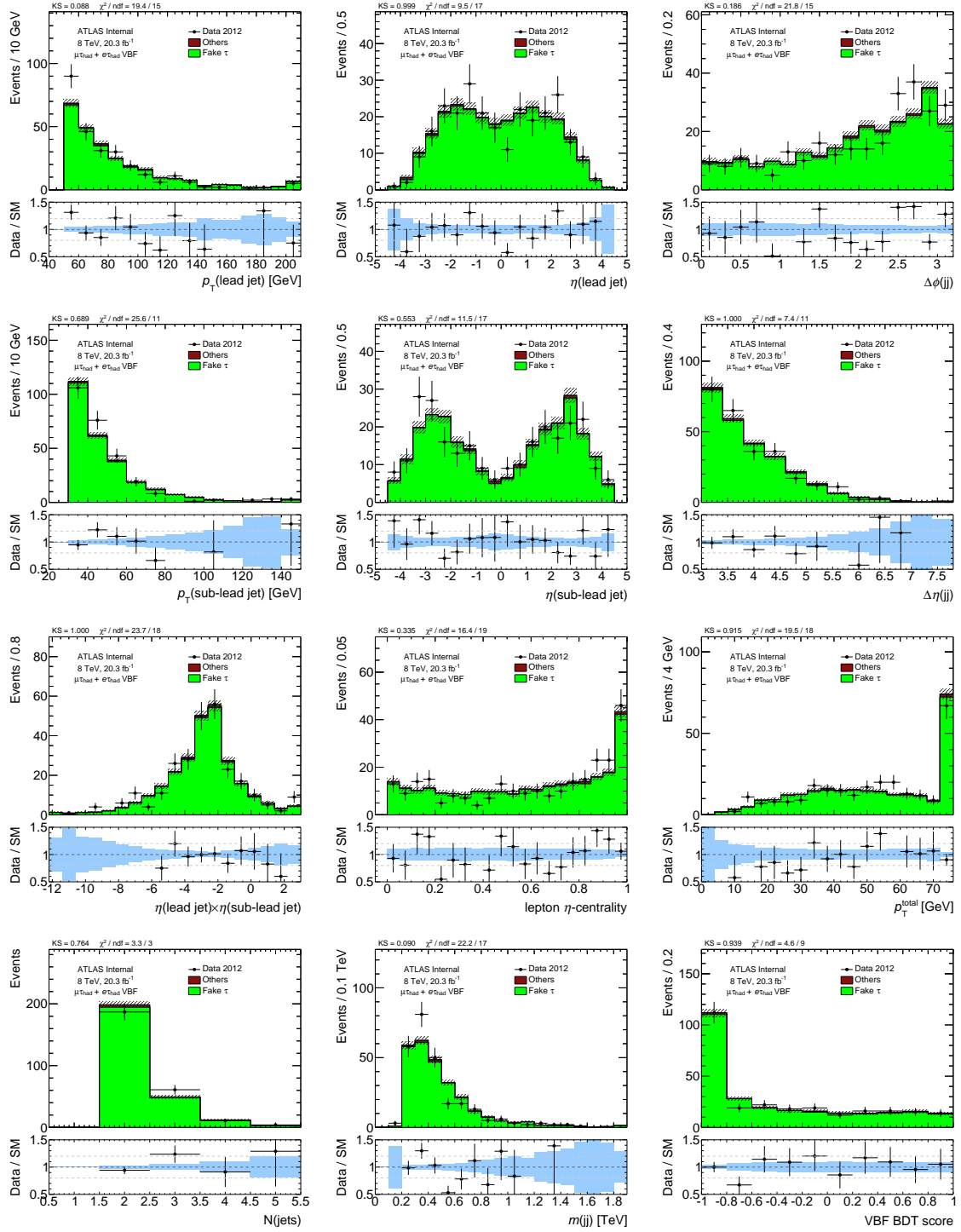


Figure A.10: Comparison of data and $j \rightarrow \tau_{\text{had}}$ prediction in the $Z \rightarrow \ell\ell$ CR for various event kinematics. Only statistical uncertainties are shown.

A. CONTROL REGIONS FOR FAKES

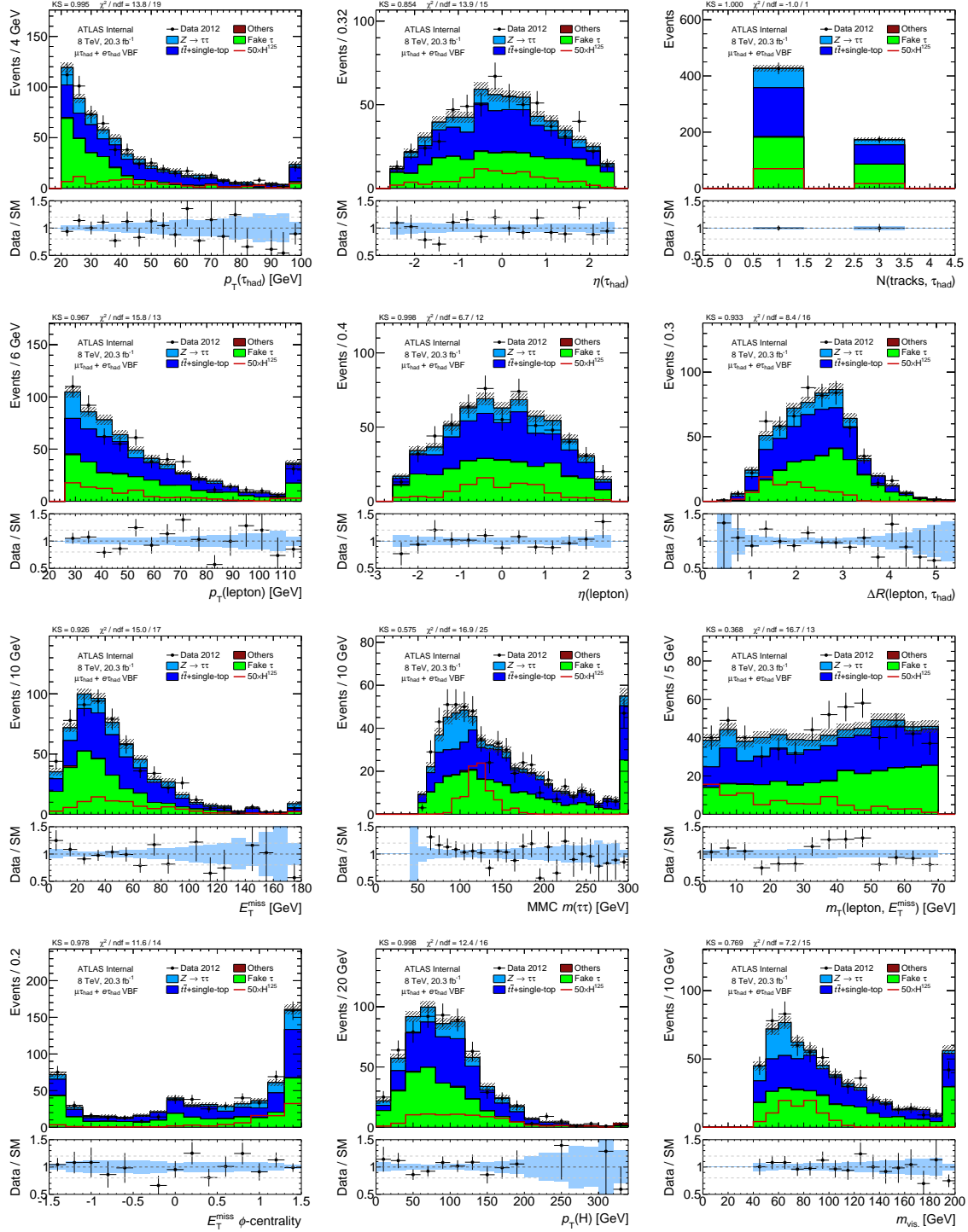


Figure A.11: Comparison of data and $j \rightarrow \tau_{\text{had}}$ prediction in the top CR for various event kinematics. Only statistical uncertainties are shown.

A. CONTROL REGIONS FOR FAKES

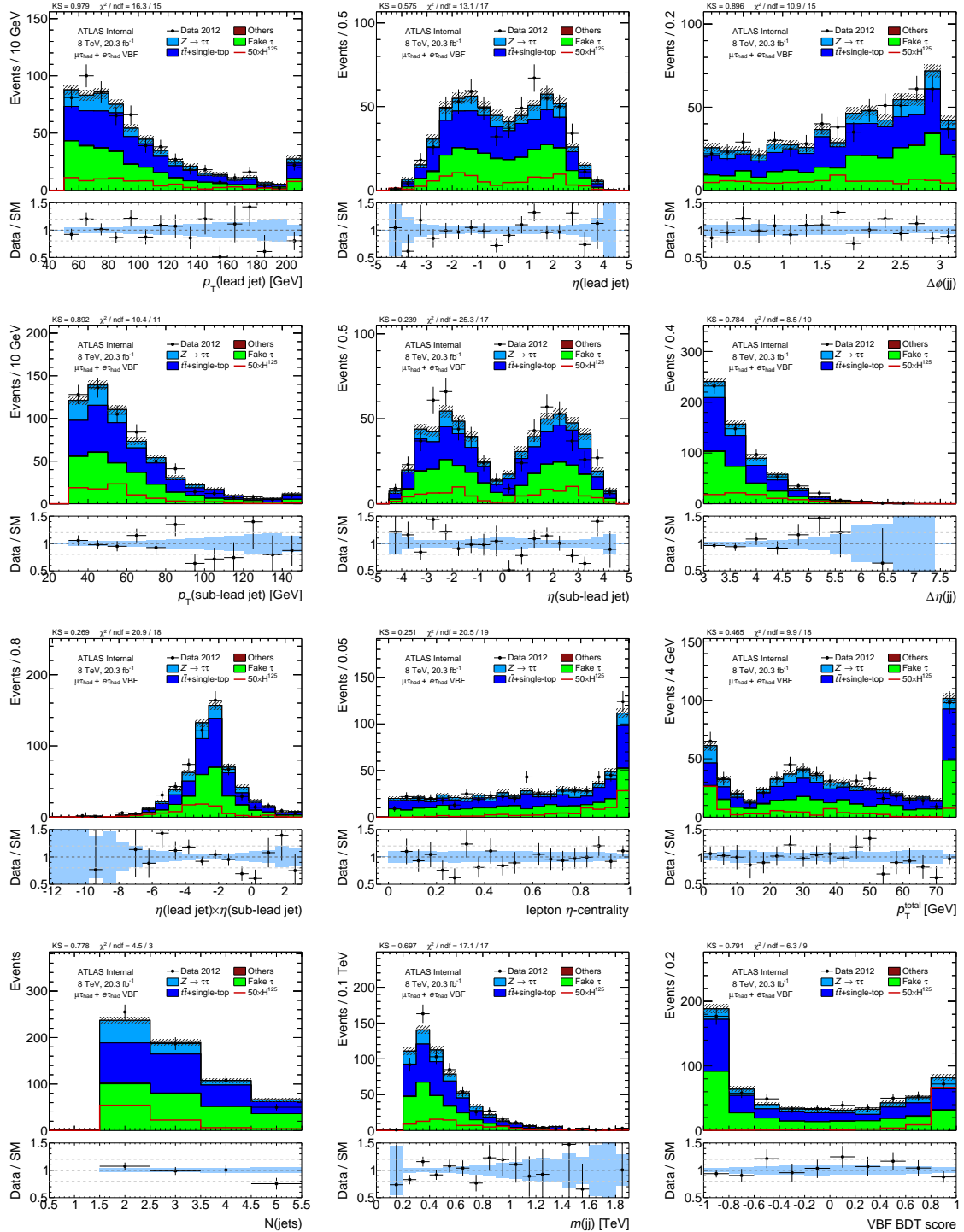


Figure A.12: Comparison of data and $j \rightarrow \tau_{\text{had}}$ prediction in the top CR for various event kinematics. Only statistical uncertainties are shown.

APPENDIX B

Inputs to the τ_{had} BDT identifier

Distributions of τ_{had} (signal) and QCD jets (background) for the BDT identification algorithm are shown.

B. INPUTS TO THE τ_{HAD} BDT IDENTIFIER

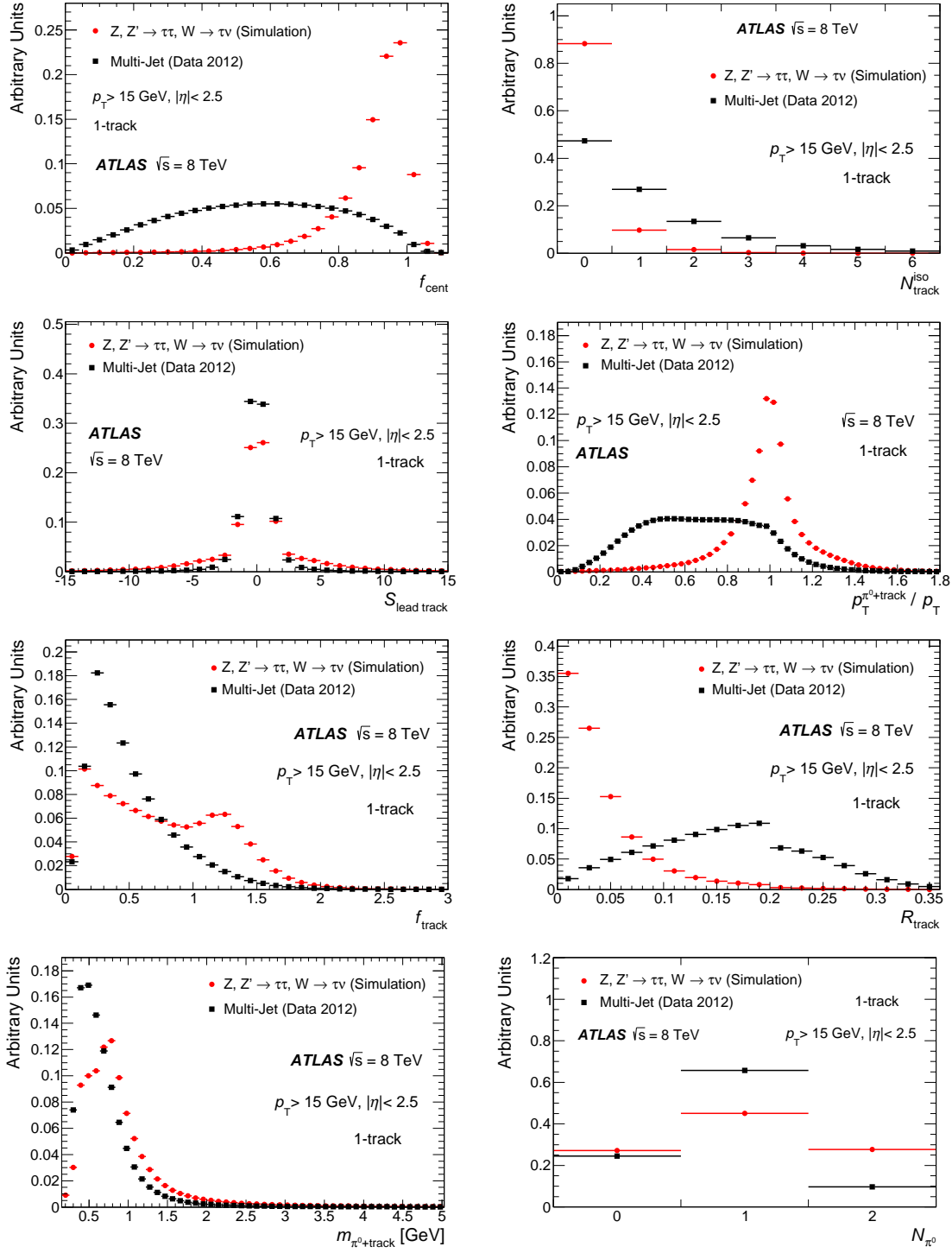


Figure B.1: Signal and background distributions for the full set of the discriminating variables in the 1-track τ_{had} jet discrimination algorithm [1].

B. INPUTS TO THE τ_{HAD} BDT IDENTIFIER

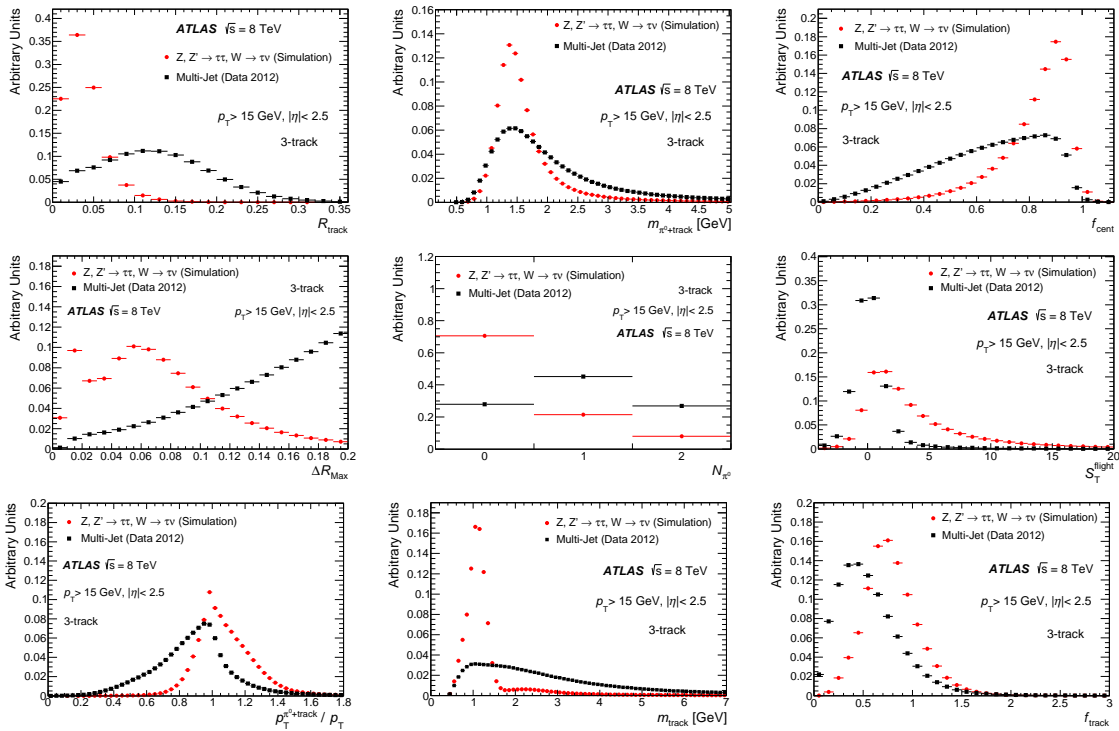


Figure B.2: Signal and background distributions for the full set of the discriminating variables in the 3-track τ_{had} jet discrimination algorithm [1].

APPENDIX C

Performance of $m_{\tau\tau}$ algorithms

Performance of various $m_{\tau\tau}$ reconstruction algorithms are shown. These are inputs to Section 5.5.

C. PERFORMANCE OF $m_{\tau\tau}$ ALGORITHMS

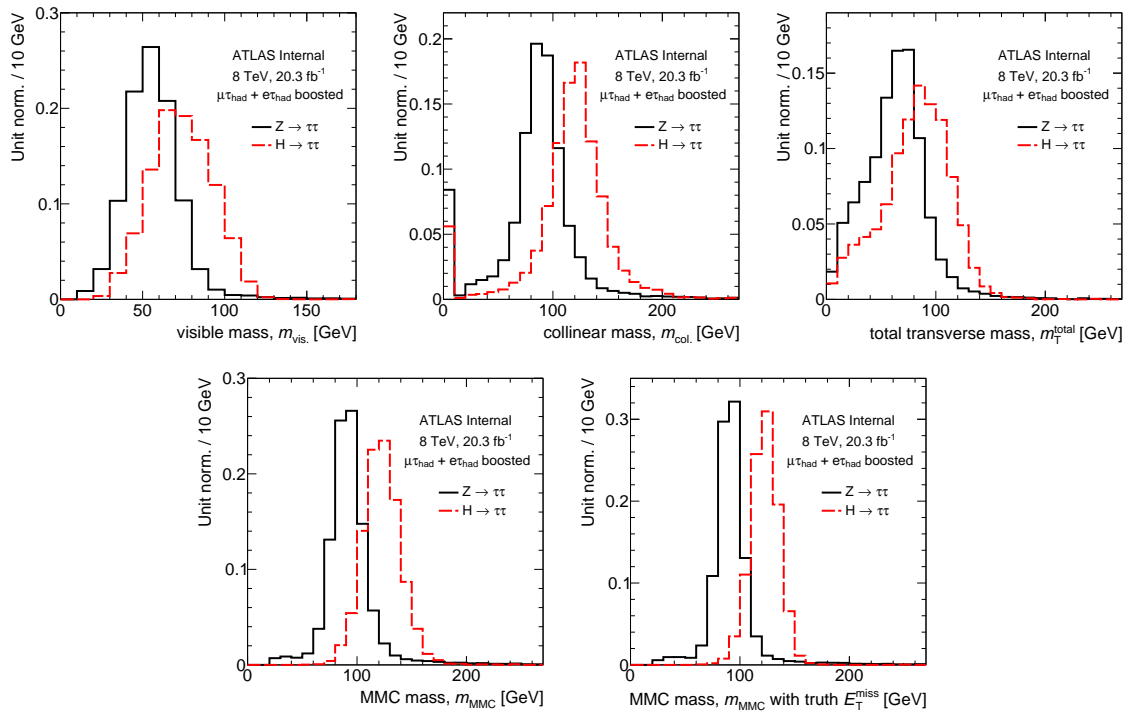


Figure C.1: Simulated predictions of $m_{Z \rightarrow \tau\ell t_{\text{had}}}$ and $m_{H \rightarrow \tau\ell t_{\text{had}}}$ in the boosted category for various $m_{\tau\tau}$ reconstruction algorithms.

C. PERFORMANCE OF $m_{\tau\tau}$ ALGORITHMS

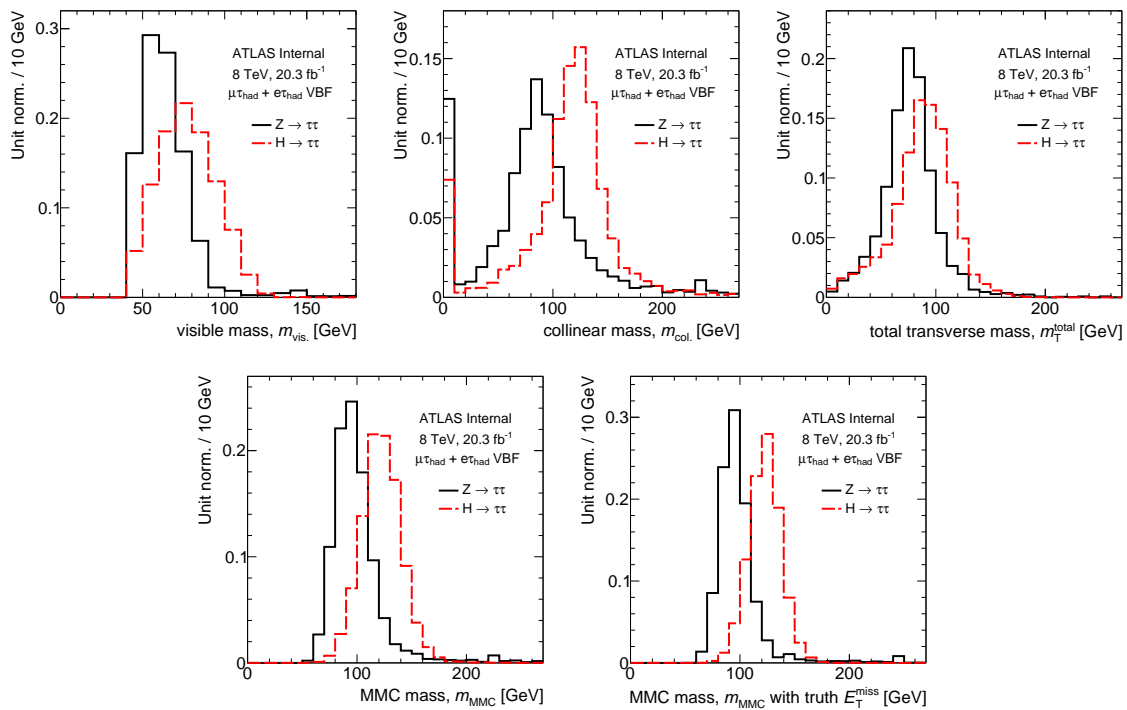


Figure C.2: Simulated predictions of $m_{Z \rightarrow \tau\ell\tau_{\text{had}}}$ and $m_{H \rightarrow \tau\ell\tau_{\text{had}}}$ in the VBF category for various $m_{\tau\tau}$ reconstruction algorithms.

Bibliography

- [1] ATLAS Collaboration, *Identification and energy calibration of hadronically decaying tau leptons with the ATLAS experiment in pp collisions at $\sqrt{s}=8$ TeV*, arXiv:1412.7086 [hep-ex].
PERF-2013-06. Submitted to EPJC. 1, 3.3.3, 4, 4.3, 4.4, 4.5, 4.7, 4.1, 4.8, 4.9, 4.10, 4.11, 4.2, 4.12, 4.13, 4.14, 5.6, 8.1, 8.5, 8.2.1, B.1, B.2
- [2] ATLAS Collaboration, *Evidence for the Higgs-boson Yukawa coupling to tau leptons with the ATLAS detector*, JHEP 117 (2015) , arXiv:1501.04943 [hep-ex]. HIGG-2013-32. 1, 5, 5.1.2, 5.6, 6.4, 6.4.1, 6.24, 6.25, 6.6, 6.26, 7, 7.2, 7.3, 7.4, 7.5, 7.6, 7.7, 8.2, 8.2.3.2, 8.2.4.1
- [3] F. Englert and R. Brout, *Broken symmetry and the mass of gauge vector mesons*, Phys. Rev. Lett. 13 (1964) 321–323. 2.1
- [4] P. Higgs, *Broken symmetries, massless particles and gauge fields*, Physics Letters 12 (1964) 132–133. 2.1
- [5] P. W. Higgs, *Broken symmetries and the masses of gauge bosons*, Phys. Rev. Lett. 13 (1964) 508–509. 2.1
- [6] G. S. Guralnik, C. R. Hagen, and T. W. B. Kibble, *Global conservation laws and massless particles*, Phys. Rev. Lett. 13 (1964) 585–587. 2.1
- [7] S. Glashow, *Partial symmetries of weak interactions*, Nucl.Phys. 22 (1961) 579–588. 2.1
- [8] S. Weinberg, *A Model of Leptons*, Phys. Rev. Lett. 19 (1967) 1264–1266. 2.1
- [9] A. Salam, *Weak and electromagnetic interactions*, Svartholm: Elementary Particle Theory, Proceedings Of The Nobel Symposium Held 1968 At Lerum, Sweden, Stockholm (1968) 367–377. 2.1
- [10] Gargamelle Collaboration, *Search for elastic muon-neutrino electron scattering*, Physics Letters B 46 (1973) 121–124. 2.1
- [11] Gargamelle Collaboration, *Observation of neutrino-like interactions without muon or electron in the gargamelle neutrino experiment*, Physics Letters B 46 (1973) 138–140. 2.1
- [12] Gargamelle Collaboration, *Observation of neutrino-like interactions without muon or electron in the Gargamelle neutrino experiment*, Nuclear Physics B 73 (1974) 1–22. 2.1

BIBLIOGRAPHY

- [13] C. L. Smith and J. Wheater, *Electroweak radiative corrections and the value of $\sin^2\theta_W$* , Physics Letters B **105** (1981) 486–488. 2.1
- [14] A. Sirlin, *Radiative corrections in the $SU(2)_L \times U(1)$ theory: A simple renormalization framework*, Phys. Rev. D **22** (1980) 971. 2.1
- [15] UA1 Collaboration, *Experimental observation of isolated large transverse energy electrons with associated missing energy at $\sqrt{s} = 540$ GeV*, Physics Letters B **122** (1983) 103–116. 2.1
- [16] UA1 Collaboration, *Experimental observation of lepton pairs of invariant mass around 95 GeV/c^2 at the CERN SPS collider*, Physics Letters B **126** (1983) 398–410. 2.1
- [17] UA2 Collaboration, *Observation of single isolated electrons of high transverse momentum in events with missing transverse energy at the CERN pp collider*, Physics Letters B **122** (1983) 476–485. 2.1
- [18] UA2 Collaboration, *Evidence for $Z^0 \rightarrow e^+e^-$ at the CERN pp collider*, Physics Letters B **129** (1983) 130–140. 2.1
- [19] R. Reece and H. Williams, *A search for new physics in high-mass ditau events in the ATLAS detector*. PhD thesis, University of Pennsylvania, 2013. 2.1
- [20] J. Ellis, M. K. Gaillard, and D. V. Nanopoulos, *A phenomenological profile of the Higgs boson*, Nuclear Physics B **106** (1976) 292–340. 2.2
- [21] R. Cahn and S. Dawson, *Production of very massive Higgs bosons*, Physics Letters B **138** (1984) 464. 2.2
- [22] A. Djouadi, J. Kalinowski, and M. Spira, *HDECAY: a Program for Higgs Boson Decays in the Standard Model and its Supersymmetric Extension*, Comput. Phys. Commun. **108** (1998) 56–74, arXiv:9704448 [hep-ph]. 2.2
- [23] LHC Higgs Cross Section Working Group, *Handbook of LHC Higgs Cross Sections: 3. Higgs Properties*, arXiv:1307.1347 [hep-ph]. LHCHXSWG. 2.3
- [24] CERN Press Office, *First results from LEP2*, Press Release, 1996. 2.2
- [25] Fermilab Press Room, *Collider Run II Begins at Fermilab*, Press Release, 2001. 2.2
- [26] ALEPH, DELPHI, L3, OPAL Collaboration, *Search for the Standard Model Higgs Boson at LEP*, Phys. Lett. B **565** (2003) 61–75, arXiv:0306033 [hep-ex]. 2.2, 5.1
- [27] CDF, D0 Collaboration, *Higgs Boson Studies at the Tevatron*, arXiv:1303.6346 [hep-ex]. Submitted to Phys. Rev. D. 2.2, 5.1
- [28] H. Flaecher, M. Goebel, J. Haller, A. Hoecker, K. Moenig, and J. Stelzer, *Revisiting the Global Electroweak Fit of the Standard Model and Beyond with Gfitter*, Eur. Phys. J. **C60** (2009) 543–583, arXiv:0811.0009 [hep-ph]. gfitter/publications. 2.4
- [29] ATLAS Collaboration, *Observation of a New Particle in the Search for the Standard Model Higgs Boson with the ATLAS Detector at the LHC*, Phys. Lett. B **716** (2012) 1–29, arXiv:1207.7214 [hep-ex]. HIGG-2012-27. 2.2, 3.2
- [30] CMS Collaboration, *Observation of a new boson at a mass of 125 GeV with the CMS experiment at the LHC*, Phys. Lett. B **716** (2012) 30, arXiv:1207.7235 [hep-ex]. 2.2

BIBLIOGRAPHY

- [31] *All Nobel Prizes in Physics*, nobelprize.org/nobel_prizes/physics/laureates, 2015. 2.2
- [32] D. Clowe, M. Bradac, A. H. Gonzalez, M. Markevitch, S. W. Randall, C. Jones, and D. Zaritsky, *A direct empirical proof of the existence of dark matter*, *Astrophys. J.* **648** (2006) L109–L113, [arXiv:arXiv:astro-ph/0608407 \[astro-ph\]](https://arxiv.org/abs/arXiv:astro-ph/0608407). 2.3
- [33] Planck Collaboration, *Planck 2013 results. XVI. Cosmological parameters*, *Astronomy and Astrophysics* **571** (2014) A16, [arXiv:1303.5076 \[astro-ph\]](https://arxiv.org/abs/arXiv:1303.5076). 2.3
- [34] N. Arkani-Hamed, S. Dimopoulos, and G. Dvali, *The Hierarchy Problem and New Dimensions at a Millimeter*, *Phys. Lett. B* **429** (1998) 263–272, [arXiv:9803315 \[hep-ph\]](https://arxiv.org/abs/arXiv:9803315). 2.3
- [35] S. P. Martin, *A Supersymmetry Primer*, [arXiv:9709356 \[hep-ph\]](https://arxiv.org/abs/arXiv:9709356). 2.3
- [36] L. Evans and P. Bryant, *LHC Machine*, *Journal of Instrumentation* **3** (2008) S08001. jinst.sissa.it/LHC/. 3.1
- [37] ATLAS Collaboration, *The ATLAS Experiment at the CERN Large Hadron Collider*, *Journal of Instrumentation* **3** (2008) S08003. jinst.sissa.it/LHC/. 3.1, 3.2.1, 3.2.1.1, 3.11, 3.15, 3.3
- [38] CMS Collaboration, *The CMS experiment at the CERN LHC*, *Journal of Instrumentation* **3** (2008) S08004. jinst.sissa.it/LHC/. 3.1
- [39] ALICE Collaboration, *The ALICE experiment at the CERN LHC*, *Journal of Instrumentation* **3** (2008) S08002. jinst.sissa.it/LHC/. 3.1
- [40] LHCb Collaboration, *The LHCb Detector at the LHC*, *Journal of Instrumentation* **3** (2008) S08005. jinst.sissa.it/LHC/. 3.1
- [41] ATLAS Collaboration, *ATLAS Photos*, *Detector Site, Surface*, 2015. 3.1
- [42] CERN, *The Accelerator Complex*, home.web.cern.ch/about/accelerators, 2015. 3.1.1
- [43] C. Lefevre, *LHC: The Guide*, *Brochure*, 2009. 3.2, 3.1
- [44] CERN, *CERN releases analysis of LHC incident*, *CERN Press Release*, 2008. 3.1.2
- [45] CERN, *The first LHC protons run ends with new milestone*, *CERN Press Release*, 2012. 3.1.2
- [46] ATLAS Collaboration, *Luminosity public results*, *LuminosityPublicResults*, 2012. 3.3, 3.4
- [47] W. Stirling, *Tevatron and LHC parton luminosity comparison plots*, <http://www.hep.ph.ic.ac.uk/~wstirlin/plots/plots.html>, 2013. 3.5
- [48] ATLAS Collaboration, *ATLAS Photos*, *Full Detector, CGI*, 2015. 3.6
- [49] ATLAS Collaboration, *Alignment of the ATLAS Inner Detector and its Performance in 2012*, *ATLAS-CONF-2014-047*, 2014. 3.8, 3.2.1.2, 3.2
- [50] ATLAS Collaboration, *Particle Identification Performance of the ATLAS Transition Radiation Tracker*, *ATLAS-CONF-2011-128*, 2011. 3.2.1.1
- [51] ATLAS Collaboration, *Performance of the ATLAS Inner Detector Track and Vertex Reconstruction in the High Pile-Up LHC Environment*, *ATLAS-CONF-2012-042*, 2012. 3.2.1.2, 3.2.1.2

BIBLIOGRAPHY

- [52] ATLAS Collaboration, *Search for anomaly-mediated supersymmetry based on a disappearing-track signature with the ATLAS detector in pp collisions at $\sqrt{s} = 7$ TeV*, *Eur. Phys. J.* **C72** (2011) 1993, arXiv:1202.4847 [hep-ex]. SUSY-2011-14. 3.9
- [53] ATLAS Collaboration, *Performance of primary vertex reconstruction in proton-proton collisions at $\sqrt{s} = 7$ TeV in the ATLAS experiment*, ATLAS-CONF-2010-069, 2010. 3.2.1.2
- [54] ATLAS Collaboration, *Stand-Alone Event Displays*, EventDisplayStandAlone, 2014. 3.10, 3.14, 3.17, 4.6
- [55] S. Menke, *The Electromagnetic Shower Simulator*, <https://www.mppmu.mpg.de/~menke/elss/home.shtml>, 2015. 3.12
- [56] ATLAS Collaboration, *Calorimeter Clustering Algorithms: Description and Performance*, ATL-LARG-PUB-2008-002, 2008. 3.2.2.2
- [57] ATLAS Collaboration, *Determination of the Jet Energy Scale*, ATL-SLIDE-2007-027, 2007. 3.13
- [58] ATLAS Collaboration, *Commissioning of the ATLAS Muon Spectrometer with Cosmic Rays*, *Eur. Phys. J.* **C70** (2010) 875–916, arXiv:1006.4384 [hep-ex]. cds.cern.ch/record/1275998. 3.2.3
- [59] ATLAS Collaboration, *Performance of the ATLAS muon trigger in pp collisions at $\sqrt{s} = 8$ TeV*, arXiv:1408.3179 [hep-ex]. TRIG-2012-03. Submitted to *Eur. Phys. J.* 3.14, 3.3, 3.22
- [60] ATLAS Collaboration, *Measurement of the muon reconstruction performance of the ATLAS detector using 2011 and 2012 LHC proton-proton collision data*, *Eur.Phys.J.* **C74** (2014) 3130, arXiv:1407.3935 [hep-ex]. PERF-2014-05. 3.3.1, 3.16
- [61] ATLAS Collaboration, *Electron efficiency measurements with the ATLAS detector using the 2012 LHC proton-proton collision data*, ATLAS-CONF-2014-032, 2014. 3.3.2, 3.18, 5.3.1
- [62] ATLAS Collaboration, *Measurements of the photon identification efficiency with the ATLAS detector using 4.9 fb^{-1} of pp collision data collected in 2011*, ATLAS-CONF-2012-123, 2012. 3.3.2
- [63] ATLAS Collaboration, *Jet energy measurement and its systematic uncertainty in proton-proton collisions at $\sqrt{s} = 7$ TeV*, *Eur. Phys. J.* **C75** (2014) 17, arXiv:1406.0076 [hep-ex]. PERF-2012-01. 3.3.3
- [64] M. Cacciari, G. P. Salam, and G. Soyez, *The anti- k_t jet clustering algorithm*, *JHEP* **0804** (2008) 063, arXiv:0802.1189 [hep-ph]. 3.3.3, 8.2.1
- [65] ATLAS Collaboration, *Pile-up subtraction and suppression for jets in ATLAS*, ATLAS-CONF-2013-083, 2013. 3.3.3
- [66] ATLAS Collaboration, *Tagging and suppression of pileup jets with the ATLAS detector*, ATLAS-CONF-2014-018, 2014. 3.3.3, 8.2.1, 8.2.2.2
- [67] ATLAS Collaboration, *Calibration of the performance of b-tagging for c and light-flavour jets in the 2012 ATLAS data*, ATLAS-CONF-2014-046, 2014. 3.3.3, 8.2.1
- [68] ATLAS Collaboration, *Performance of the ATLAS Secondary Vertex b-tagging Algorithm in 900 GeV Collision Data*, ATLAS-CONF-2010-004, 2010. 3.19

BIBLIOGRAPHY

- [69] ATLAS Collaboration, *Measurement of the b-tag Efficiency in a Sample of Jets Containing Muons with 5 fb^{-1} of Data from the ATLAS Detector*, [ATLAS-CONF-2012-043](#), 2012. [3.19](#)
- [70] ATLAS Collaboration, *Performance of Missing Transverse Momentum Reconstruction in Proton-Proton Collisions at $\sqrt{s} = 7 \text{ TeV}$ with ATLAS*, [Eur. Phys. J. C72 \(2011\) 1844](#), [arXiv:1108.5602 \[hep-ex\]](#). [PERF-2011-07](#). [3.3.4](#)
- [71] ATLAS Collaboration, *Pile-up Suppression in Missing Transverse Momentum Reconstruction in the ATLAS Experiment in Proton-Proton Collisions at $\sqrt{s} = 8 \text{ TeV}$* , [ATLAS-CONF-2014-019](#), 2014. [3.3.4](#), [3.20](#)
- [72] ATLAS Collaboration, *TriggerOperationPublicResults*, [TriggerOperationPublicResults](#), 2015. [3.3](#)
- [73] ATLAS Collaboration, *Level-1 Trigger Technical Design Report*, <http://atlas.web.cern.ch/Atlas/GROUPS/DAQTRIG/TDR/tdr.html>, 1998. [3.21](#)
- [74] ATLAS Collaboration, *Public Egamma Trigger Plots for Collision Data*, [EgammaTriggerPublicResults](#), 2015. [3.22](#)
- [75] ATLAS Collaboration, *Publications of the ATLAS Collaboration*, [ATLASPublications](#), 2015. [3.5](#)
- [76] ATLAS Collaboration, *Summary plots from the ATLAS Standard Model physics group*, [CombinedSummaryPlots/SM](#), 2015. [3.23](#)
- [77] ATLAS Collaboration, *Performance of the Reconstruction and Identification of Hadronic tau Decays in ATLAS with 2011 Data*, [ATLAS-CONF-2012-142](#), 2012. [4](#), [4.3](#), [4.2](#)
- [78] ATLAS Collaboration, *Identification of Hadronic Decays of Tau Leptons in 2012 Data with the ATLAS Detector*, [ATLAS-CONF-2013-064](#), 2013. [4](#), [4.2](#), [4.14](#)
- [79] ATLAS Collaboration, *Determination of the tau energy scale and the associated systematic uncertainty in proton-proton collisions at $\sqrt(s) = 8 \text{ TeV}$ with the ATLAS detector at the LHC in 2012*, [ATLAS-CONF-2013-044](#), 2013. [4](#)
- [80] M. L. Perl *et al.*, *Evidence for anomalous lepton production in e^+e^- annihilation*, [Phys. Rev. Lett. 35 \(1975\) 1489–1492](#). [4.1](#)
- [81] M. L. Perl *et al.*, *Properties of anomalous $e\mu$ events produced in e^+e^- annihilation*, [Physics Letters B 63 \(1976\) 466–470](#). [4.1](#)
- [82] M. L. Perl *et al.*, *Properties of the proposed tau charged lepton*, [Physics Letters B 70 \(1977\) 487](#). [4.1](#)
- [83] Belle Collaboration, *Measurement of the τ -lepton lifetime at Belle*, [Phys. Rev. Lett. 112 \(2014\) 031801](#), [arXiv:1310.8503 \[hep-ex\]](#). [4.1](#)
- [84] BaBar Collaboration, *Measurements of the τ Mass and Mass Difference of the τ^+ and τ^- at BaBar*, [Phys. Rev. D 80 \(2009\) 092005](#), [arXiv:0909.3562 \[hep-ex\]](#). [4.1](#)
- [85] K. Kodama *et al.*, *Observation of tau neutrino interactions*, [Physics Letters B 504 \(2001\) 218 – 224](#). [4.1](#)
- [86] ALEPH Collaboration, *A precise determination of the number of families with light neutrinos and of the Z boson partial widths*, [Physics Letters B 235 \(1990\) 399–411](#). [4.1](#)

BIBLIOGRAPHY

- [87] J. Beringer *et al.* (Particle Data Group), *The Review of Particle Physics*, Phys.Rev.D **86** (2012) 010001. [4.1](#)
- [88] ATLAS Collaboration, *Local Hadronic Calibration*, ATL-LARG-PUB-2009-001-2, 2008. [4.3.1](#)
- [89] ATLAS Collaboration, *Search for the Standard Model Higgs boson in $H \rightarrow \tau\tau$ decays in proton-proton collisions with the ATLAS detector*, ATL-CONF-2012-160, 2012. [5](#), [6.1.1](#), [6.2.1](#)
- [90] ATLAS Collaboration, *Evidence for Higgs Boson Decays to the $\tau\tau$ Final State with the ATLAS Detector*, ATL-CONF-2013-108, 2013. [5](#)
- [91] The LHC Higgs Cross Section Working Group, *Handbook of LHC Higgs Cross Sections: 3. Higgs Properties*, arXiv:1307.1347 [hep-ex]. [5.1](#)
- [92] ATLAS Collaboration, *Measurement of Higgs boson production in the diphoton decay channel in pp collisions at center-of-mass energies of 7 and 8 TeV with the ATLAS detector*, Phys. Rev. D **90** (2014) 112015, arXiv:1408.7084 [hep-ex]. HIGG-2013-08. [5.1](#), [5.17](#), [5.8](#)
- [93] ATLAS Collaboration, *Measurements of Higgs boson production and couplings in the four-lepton channel in pp collisions at center-of-mass energies of 7 and 8 TeV with the ATLAS detector*, Phys. Rev. D **91** (2014) 012006, arXiv:1408.5191 [hep-ex]. HIGG-2013-21. [5.1](#), [5.17](#), [5.8](#)
- [94] ATLAS Collaboration, *Observation and measurement of Higgs boson decays to WW^* with the ATLAS detector*, arXiv:1412.2641 [hep-ex]. HIGG-2013-13. Submitted to Physical Review D. [5.1](#), [5.6](#), [5.17](#), [5.8](#), [7](#), [7.1](#)
- [95] ATLAS Collaboration, *Search for the bb decay of the Standard Model Higgs boson in associated (W/Z) H production with the ATLAS detector*, JHEP **01** (2014) 069, arXiv:1409.6212 [hep-ex]. HIGG-2013-23. [5.1.1.2](#)
- [96] D. Rainwater, D. Zeppenfeld, and K. Hagiwara, *Searching for $H \rightarrow \tau\tau$ in weak boson fusion at the LHC*, Phys. Rev. D **59** (1998) 014037, arXiv:9808468 [hep-ph]. [5.4.2](#)
- [97] ATLAS Collaboration, *A search for high-mass resonances decaying to $\tau^+\tau^-$ in pp collisions at $\sqrt{s} = 7$ TeV with the ATLAS detector*, Phys. Lett. B **719** (2012) 242–260, arXiv:1210.6604 [hep-ex]. EXOT-2012-03. [5.6](#)
- [98] A. Elagin, P. Murat, A. Pranko, and A. Safonov, *A New Mass Reconstruction Technique for Resonances Decaying to di-tau*, Nucl. Instrum. Methods A **654** (2011) 481–489, arXiv:1012.4686 [hep-ex]. [5.5.1](#)
- [99] ATLAS Collaboration, *Search for neutral MSSM Higgs bosons decaying to $\tau\tau$ pairs in proton-proton collisions at $\sqrt{s} = 7$ TeV with the ATLAS detector*, ATL-CONF-2011-132, 2011. [5.7](#)
- [100] CMS Collaboration, *Evidence for the 125 GeV Higgs boson decaying to a pair of tau leptons*, JHEP **05** (2014) 104, arXiv:1401.5041 [hep-ex]. [5.5.1](#)
- [101] L. Breiman, J. Friedman, C. Stone, and R. Olshen, *Classification and Regression Trees*. Chapman & Hall, 1984. [5.6](#)
- [102] B. P. Roe, H.-J. Yang, J. Zhu, Y. Liu, I. Stancu, and G. McGregor, *Boosted Decision Trees as an Alternative to Artificial Neural Networks for Particle Identification*, Nucl. Instrum. Meth. A **543** (2005) 577–584, arXiv:0408124 [hep-ex]. [5.6](#)

BIBLIOGRAPHY

- [103] ATLAS Collaboration, *Measurement of the Higgs boson couplings in the $\tau\tau$ final state with the ATLAS detector (supporting note)*, ATL-COM-PHYS-2014-170, 2014. **ATLAS Internal.** 6
- [104] ATLAS Collaboration, *Measurement of the Z/γ^* boson transverse momentum distribution in pp collisions at $\sqrt{s} = 7$ TeV with the ATLAS detector*, JHEP **09** (2014) 145, arXiv:1406.3660 [hep-ex]. STDM-2012-23. 6.1
- [105] ATLAS Collaboration, *Measurement of the production cross section of jets in association with a Z boson in pp collisions at $\sqrt{(s)} = 7$ TeV with the ATLAS detector*, JHEP **07** (2013) 032, arXiv:1304.7098 [hep-ex]. STDM-2012-04. 6.2
- [106] Heavy Flavor Averaging Group, *Averages of b -hadron, c -hadron, and τ -lepton properties as of summer 2014*, arXiv:1412.7515 [hep-ex]. 6.1.2
- [107] ATLAS Collaboration, *Search for Standard Model Higgs Boson decaying to di-tau pair with a lepton and hadronic tau in the final state with the ATLAS Detector in 8 TeV Proton-Proton Collisions*, ATL-COM-PHYS-2012-1201, 2012. **ATLAS Internal.** 6.3
- [108] ATLAS Collaboration, *Light-quark and gluon jet discrimination in pp collisions at $\sqrt{s} = 7$ TeV with the ATLAS detector*, Eur. Phys. J. **C74** (2014) 3023, arXiv:1405.6583 [hep-ex]. PERF-2013-02. 6.2.1, 6.6
- [109] ATLAS Collaboration, *Measurements of the W production cross sections in association with jets with the ATLAS detector*, arXiv:1409.8639 [hep-ex]. STDM-2012-24. 6.7
- [110] ATLAS Collaboration, *Search for the Standard Model Higgs boson in the H to $\tau\tau$ decay mode in $\sqrt{(s)} = 7$ TeV pp collisions with ATLAS*, JHEP **070** (2012) , arXiv:1206.5971 [hep-ex]. HIGG-2012-07. 6.2.1
- [111] ATLAS Collaboration, *Studies of the VBF $H \rightarrow \tau_\ell \tau_{had}$ analysis at High Luminosity LHC conditions*, ATL-PHYS-PUB-2014-018, 2014. 8, 8.2, 8.11, 8.12, 8.13, 8.14, 8.15, 8.16
- [112] ATLAS Internal, *Trigger Menu Strategy for Run 2*, ATL-COM-DAQ-2014-054, 2014. 8.1
- [113] ATLAS Collaboration, *Upgrade of the ATLAS Level-1 trigger with an FPGA based Topological Processor*, ATL-DAQ-PROC-2013-039, 2013. 8.1.2.2
- [114] ATLAS Internal, *Physics Uses and Hardware Constraints of the L1 Topological Trigger*, ATL-COM-DAQ-2014-005, 2014. 8.1.2.2
- [115] ATLAS Collaboration, *Tau Trigger Rate Plots for 2011*, ATL-COM-DAQ-2012-001, 2011. 8.4
- [116] G. Cowan, *Discovery sensitivity for a counting experiment with background uncertainty*, <http://www.pp.rhul.ac.uk/~cowan/stat/medsig>, 2012. 8.1.2.3
- [117] ATLAS Collaboration, *Projections for measurements of Higgs boson cross sections, branching ratios and coupling parameters with the ATLAS detector at a HL-LHC*, ATL-PHYS-PUB-2013-014, 2013. 8.2.2
- [118] ATLAS Collaboration, *Performance assumptions for an upgraded ATLAS detector at a High-Luminosity LHC*, ATL-PHYS-PUB-2013-004, 2013. 8.2.2.1, 8.2.2.2